

HYDROGEN ASSISTED CRACKING OF UHSS
FOR MILITARY AEROSPACE APPLICATIONS

Von der Fakultät für Maschinenbau
der Helmut-Schmidt-Universität Hamburg/Universität der Bundeswehr Hamburg
zur Erlangung des akademischen Grades eines Doktor-Ingenieurs
genehmigte

DISSERTATION

vorgelegt von

Benjamin R. Steffens, Maj, USAF
aus Torrejon Air Force Base, Spanien

Hamburg, 2018

Gutachter

Prof. Dr.-Ing. Hans Hoffmeister, ISSV c/o Helmut-Schmidt-University, Hamburg

Prof. Dr.-Ing. Thomas Böllinghaus, BAM, Berlin und OVGU, Magdeburg, Germany

Prof. Dr. Gregory Shoales, CASTLE, USAFA, Colorado Springs, USA

HYDROGEN ASSISTED CRACKING OF UHSS
FOR MILITARY AEROSPACE APPLICATIONS

Doctoral Thesis
submitted to the Faculty

Department of Mechanical Engineering
Helmut Schmidt University
University of the German Federal Armed Forces
Hamburg, Germany

for obtaining the academic degree of
Doktor Ingenieur (Dr. -Ing.)

presented by

Benjamin R. Steffens, Major, USAF

from Torrejon Air Force Base, Spain

Hamburg, 2018

Referees

Prof. Dr.-Ing. Hans Hoffmeister, ISSV c/o Helmut-Schmidt-University, Hamburg

Prof. Dr.-Ing. Thomas Böllinghaus, BAM, Berlin, Germany

Prof. Dr. Gregory Shoales, CASTLE, USAFA, Colorado Springs, USA

Declaration

The views expressed in this thesis are those of the author and do not reflect the official policy or position of the United States Air Force, Department of Defense, or the United States Government. This material is declared a work of the U.S. Government and is not subject to copyright protection in the United States.



Benjamin Steffens, Major, USAF – Hamburg and Berlin, Germany, June 2018

Acknowledgements

The cooperation of several entities, namely the United States Air Force, the Bundesanstalt für Materialforschung und -prüfung (BAM, Berlin) and Helmut Schmidt University in Hamburg had to come together in synergy for this doctoral program to be possible. Through this unprecedented international collaboration of expertise and resources, I have benefited greatly - I will hold my Dr.-Ing. degree with great pride for the rest of my life.

This work would not have been possible without the inspiration from my supervisor, Prof. Dr.-Ing. Thomas Böllinghaus, who encouraged and challenged me through every facet of this doctoral program. I would like to also thank Prof. Dr. Greg Shoales and the CASTLE group for their technical support and expertise during this effort. Additionally, Prof. Dr.-Ing. Hoffmeister and the ISSV team in Hamburg proved to be an excellent advisor and colleagues, respectively.

I would also like to recognize Oded Sobol, Michael Rhode, Tobias Mente and Thora Falkenreck - all fellow BAM colleagues who endured this challenge with me side by side, always motivating me to do my best. I also appreciate all the perspective and support that the colleagues here at BAM have provided me. I have often mentioned that this perspective is as important to me as the subject matter of this work.

Lastly and most especially, I would like to thank my beautiful wife, Ramajana, and our two wonderful children, Anthony and Leila. Words alone cannot express what I owe them for their encouragement and whose patient love enabled me to complete this.

Kurzfassung

Für Flugzeugfahrwerke werden ultra-hochfeste Stähle (engl.: Ultra-High Strength Steels – UHSS) eingesetzt, um sowohl die hohen mechanischen und teilweise stoßartigen Beanspruchungen, aber auch um den Designkriterien des Leichtbaus gerecht zu werden. Die vorhandenen Systeme wurden bisher üblicherweise aus dem Werkstoff AISI 4340, einem niedriglegierten Stahl des Typs 36CrNiMo4 mit der Werkstoffbezeichnung 1.6511 hergestellt. Ein weiterer Werkstoff trägt die Bezeichnung 300M. Hierbei handelt es sich um einen modifizierten Stahl AISI 4340, der zudem mit Silizium und Vanadium legiert ist und einen leicht erhöhten Kohlenstoff- und Molybdängehalt aufweist. Bei beiden Werkstoffen handelt es sich um nach der maschinellen Bearbeitung voll aushärtbare niedriglegierte Stähle, die End-Dehngrenzen von bis zu 2100 MPa erreichen und die Designkriterien bezüglich Festigkeit und Zähigkeit einhalten, aber eine geringe Korrosionsresistenz aufweisen. Deshalb werden solche Werkstoffe üblicherweise mit Cadmium beschichtet und/oder mit Chromat-haltigen Farben ausreichend gegen korrosive Umgebungen geschützt. Diese Art des Korrosionsschutzes ist zwar wirksam, allerdings ist bekannt, dass dadurch Wasserstoff an der Grenzfläche zwischen Substrat und Beschichtung während der industriellen Produktion aufgenommen werden kann. Als zweiter nachteiliger Effekt hat sich zudem herausgestellt, dass die chemische Zusammensetzung die Umwelt und das Personal schädigen kann, sodass die quasi zu einem Anwendungsverbot geführt hat.

Bei dem Stahl mit der kommerziellen Bezeichnung Ferrium S53 handelt es sich um eine inzwischen einsatzfähige Alternative für die herkömmlichen Werkstoffe. Diese neue mit neuesten rechnergestützten Verfahren entwickelte Designlegierung wurde vor allem für den Einsatz in höchstfesten Komponenten und Systemen im Flugzeugbau entwickelt. Der Stahl Ferrium S53 erfüllte oder übertraf sogar alle vorherigen Kriterien, die an Flugzeugfahrwerke gestellt wurden und wies zugleich einen Korrosionswiderstand auf, die die vorherigen Oberflächenbehandlungen unnötig machte. Die Legierung Ferrium S53 weist jedoch ebenfalls eine nahezu vollständig martensitische Mikrostruktur auf, die per se anfällig für eine wasserstoffunterstützte Rissbildung (engl.: Hydrogen Assisted Cracking – HAC) ist – und dies bereits bei verhältnismäßig niedrigen Wasserstoffkonzentrationen.

Quantitative Untersuchungen der wasserstoffabhängigen Materialeigenschaften solcher Werkstoffe für Flugzeugtragwerke wurden bisher allerdings kaum durchgeführt und – wenngleich sie für entsprechend Lebensdaueruntersuchungen der Komponenten essentiell sind. Um ein besseres wissenschaftliches Verständnis bezüglich des Verhaltens dieser Stähle in Flugzeugfahrwerken, die wasserstoffentwickelnden korrosiven Medien ausgesetzt sein können, zu entwickeln, wurden sowohl Proben aus den Werkstoffen im Lieferzustand, als auch insbesondere aus im Einsatz gewesenen Komponenten entnommen.

Aus Unabhängigkeitsgründen wurden die Werkstoffe im Lieferzustand eingekauft, ohne den Verkäufer über die entsprechenden Versuche zu informieren. Der im eingesetzte Werkstoff wurde direkt aus dem Hauptfahrwerk eines Flugzeuges der US Air Force entnommen, das eine Betriebsdauer von mindestens fünf Jahren hatte. Die Proben wurden aus dem Fahrwerk zudem an den am höchsten beanspruchten Stellen entnommen. Basierend auf einer umfangreiche Analyse des derzeitigen Kenntnisstandes zur wasserstoffunterstützten Rissbildung martensitischen Stähle wurde das Versuchsprogramm sorgfältig ausgewählt, indem ein eher multidisziplinärer Ansatz gewählt wurde. Hierbei wurden die Werkstoffe vor allem bisher nicht durchgeführten Versuchsserien unterzogen, in denen die Wirkungen von Wasserstoff auf das mechanische und fraktografische Verhalten im Betrieb untersucht wurden. Hierbei standen Zugversuche mit wasserstoffgesättigten Proben, auch im Vergleich zu dem herkömmlichen Stahl AISI 4340, und unter langsamer Dehnung (Slow Strain Rate Tests – SSRT) im Vordergrund. Die SSRT wurden überwiegend in künstlichem aber auch in natürlichem Meerwasser durchgeführt, teilweise auch bei erhöhten Temperaturen und unter kathodischem Schutz, um das Verhalten des neuen Fahrwerkstahles Ferrium S53 unter extremen Bedingungen in maritimen Umgebungen zu untersuchen und gleichzeitig mögliche einfache Schutzmaßnahmen zu ermitteln. Begleitende Heißgasextraktionen sowie fraktografische und metallografische Analysen lieferten vertiefte Erkenntnisse über das Rissverhalten dieses neuen Werkstoffes unter Präsenz von wasserstoff im martensitischen Gefüge.

Die Untersuchungen an dem bereits mehrere Jahre im Einsatz befindlichen Werkstoff Ferrium S53 sind als weltweit einmalig anzusehen. Sie entsprechen im übrigen dem Ansatz des Programms CASTLE der US Air Force mittels geeigneter Analysen an im Einsatz befindlichen oder außer Dienst gestellten Komponenten und Systemen, präventiv mögliche Schwachstellen und Schäden zu erkennen und diesen entgegenzuwirken.

Die Ergebnisse der Arbeit bestätigen, dass der neue computerdesignte Werkstoff Ferrium S53 gegenüber den herkömmlichen Werkstoffen des Typs AISI 4340 deutlich verbesserte Eigenschaften aufweist, und zwar in allen durchgeführten Analysen.

Unter anderem zeigte sich anhand der Zugversuche mit wasserstoffgesättigten Proben, dass der Stahl Ferrium S53 gegenüber dem Stahl AISI 4340 eine wesentlich bessere Zähigkeit nach etwa derselben Einsatzdauer im Betrieb aufweist, auch wenn Wasserstoff im mmartensitischen Gefüge vorliegt. Auch gegenüber dem Lieferzustand weist der Stahl S53 im gehärteten Zustand eine höhere Zähigkeit auf.

In den SSRT zeigte sich, dass die Phänomenologie einer möglichen Schädigung des Stahles in unter extremem Einsatz in maritimen Klimata, bspw. auf Flugzeugträgern in tropischen Gewässern, grundsätzlich aus vorgehender Lochkorrosion bei recht negativen Potentialen mit nachfolgender wasserstoffunterstützter Spannungsrisskorrosion besteht. Interessanterweise zeigt der Stahl Ferrium S53 im Lieferzustand aufgrund des sehr hohen Anteils an noch vorhandenem Restaustenit unter dieser Schädigungsphänomenologie ein deutlich spröderes interkristallines Verhalten, als der bereits mehrere Jahre im Einsatz gewesene Werkstoff. Darüber hinaus stellte sich heraus, dass ein kathodischer Schutz von ca. $-600\text{mV}(\text{Ag}/\text{AgCl})$ teilweise wirksam gegen Lokalkorrosion (Pitting) und nachfolgende wasserstoffunterstützte Spannungsrisskorrosion sein kann. Gegenüber bisherigen Untersuchungen, die diesen Aspekt nicht in Erwägung gezogen hatten, stellte sich heraus, dass auch ein solcher kathodischer Schutz von einer, wenn auch geringeren Wasserstoffabsorption begleitet wird, die im Langzeitbetrieb beachtet werden sollte. Allerdings zeigte sich in den SSRT ein deutlich besseres Verhalten unter einem solchen kathodischen Schutz heraus, als bei freien Korrosionspotentialen bzw. demgegenüber erhöhten oder abgesenkten Potentialen.

Insgesamt ergibt sich aus den vorliegenden Untersuchungen bezüglich einer möglichen wasserstoffunterstützten Risskorrosion ein deutlich besseres Verhalten des neuen computerdesignten Stahles Ferrium S53 nach einer Nutzungsdauer von mehr als fünf Jahren als im Lieferzustand sowie gegenüber dem herkömmlichen Stahl AISI 4340.

Abstract

Ultra-High Strength Steels (UHSS) are the predominantly used material on aircraft landing gear systems, to combat the high mechanical and partly impacting loads and to match the criteria of light weight design in airplane engineering. Legacy systems have been commonly manufactured from the low alloyed steel AISI 4340, also known as 36CrNiMo4 with the DIN classification number 1.6511. Another material, 300M, has also been widely used in this application – it is a close variant of AISI 4340 steel that has been alloyed with silicon and vanadium. Both alloys represent fully hardenable low alloyed steels which can reach ultimate strengths of about 2100 MPa and that match the design criteria regarding strength and toughness for landing gear applications, but had poor corrosion resistance. Therefore, these materials were commonly cadmium plated and/or painted with chromate paints to protect them against corrosive environments. These surface treatments worked well to protect the components against corrosion, but have been known for potential introduction of hydrogen into the components at the coating-substrate interface due to industrial processes. A second detrimental effect is the environmentally and personally harmful aspects of the chemical compositions of the surface treatments that have virtually prohibited their use.

Ferrium S53, a computationally designed alloy that was tailored specifically for ultra-high strength applications in aerospace systems, has become a viable alternative to the legacy materials. Ferrium S53 met or exceeded all previous criteria for use in landing gear structures while adding an inherent corrosion resistance, which made the previously mentioned surface treatments unnecessary. Ferrium S53 has a highly martensitic microstructure which is susceptible to hydrogen assisted cracking per-se, and this at relative low hydrogen concentration levels.

Quantitative investigations of hydrogen dependent properties of aircraft landing gear materials have only scarcely been carried out in the past, although they are essential for respective component life time assessments. To develop an improved scientific understanding of such steels in landing gear components which can be subjected to corrosive media, samples have been taken from materials in the as-delivered condition and, especially, in the used service-applied condition.

To maintain completely objective test program, the “new barstock” steel was purchased directly from the manufacturer without information about any future testing on the material. The “used component” steel was taken directly from the main landing gear struts of actual U.S. Air Force aircraft with at least 5 years of use. In the case of the “used component” material, selection of where the specimens were extracted would represent the most highly-stressed areas of the component. Based on a substantial analysis of the present state of knowledge regarding hydrogen assisted cracking in martensitic steels, the test program has carefully been selected by following a more multi-disciplinary approach. By such, the materials have been subjected to test series they have not seen up to the present and by which the effects of hydrogen on the mechanical and fractographic behavior in service have been investigated. Among these, a focus has been laid on tensile tests of hydrogen-saturated specimens, also in comparison to the AISI 4340 legacy steel, and on slow strain rate tests (SSRT). The SSRT have been carried out predominantly in artificial but also in natural seawater, partly at elevated temperatures and also at cathodic protection, to evaluate the behavior of the used and service-applied steel Ferrium S53 at extreme conditions in marine environments and to determine potential simple protection measures. Subsequent carrier gas hot extractions, as well as fractographic and metallographic analyses, conveyed in depth results about the cracking behavior of this novel material within presence of hydrogen in the martensitic microstructure.

The investigations of the material Ferrium S53 after several years of service can be regarded as globally unique. They also correspond to the approach used by the CASTLE (Center for Aircraft Structural Life Extension) program, located at the U.S. Air Force Academy, to determine and to counteract potential weaknesses and damages of in-service or retired components or systems by suitable analyses.

The results of the present contribution confirm that the new computer-designed material Ferrium S53 has superior properties as compared to materials of the type AISI 4340, in all analyses that have been carried out. Among other results, it has been shown by the tensile tests with hydrogen-saturated specimens that the Ferrium S53 steel, in contrast to the AISI 4340 steel, has an improved ductility after similar service durations, even if hydrogen is present in the martensitic microstructure. Also in the as-delivered condition, the Ferrium S53 steel has an improved ductility as compared to the AISI 4340 steel.

From SSRT, it turned out that the phenomenology of potential damage of the steel under extreme service in marine climates, as for instance on aircraft carriers in tropical seas, is principally pitting corrosion and subsequent hydrogen assisted stress corrosion cracking. Interestingly, the as-delivered Ferrium S53 steel demonstrated a more brittle intergranular cracking behavior due to the extremely high amount of retained austenite, as compared to the used material with several years of service. Furthermore, a cathodic protection at about $[- 600 \text{ mV (Ag/AgCl)}]$ proved to be partly effective controlling the pitting corrosion and subsequent hydrogen assisted stress corrosion cracking. However, as compared to previous investigations with other materials which did not consider it, it turned out that such a cathodic protection is accompanied by a minor hydrogen absorption which has to be dealt with during long term usage. However, the SSRT showed a much better behavior of the used and service-applied Ferrium S53 steel than at open circuit potentials or respectively increased or decreased potentials.

To sum up, the present investigations exhibit a significantly improved behavior of the novel computer-designed Ferrium S53 steel after a service period of more than five years with respect to potential hydrogen assisted stress corrosion cracking, as compared to the new as-delivered condition and also as compared to the new and used legacy AISI 4340 steel.

Table of Contents

Kurzfassung	IX
Abstract.....	XIII
Table of Contents	XVI
1. Introduction.....	1
2. Literature Review	5
2.1 Aerospace Structures	5
2.1.1 Landing Gear Design	6
2.1.2 Loading and Service Conditions in Application.....	9
2.1.3 Maintenance and Corrosion Prevention	10
2.1.4 Component Service Life.....	13
2.2 Hydrogen Assisted Cracking (HAC)	14
2.2.1. General Phenomenology	15
2.2.1 Hydrogen Transport and Trapping Mechanisms	18
2.2.2 HAC Mechanisms.....	31
2.3. HAC in Martensitic Steels.....	36
2.3.1. High Strength Low Alloyed Steels	36
2.3.2 Heat Resistant Martensitic Low Alloyed Steels.....	39
2.3.3 Martensitic 9 wt.-% Ni Steels.....	44
2.3.4 13% Cr Martensitic Stainless Steels	44
2.3.5 Precipitation Hardening Martensitic Stainless Steels	52
2.3.6 High Alloyed Ni Steels (Maraging Steels).....	53
2.3.7 High Alloyed Martensitic UHSS for Military Aerospace Applications	54
2.3.7.1 Chemical Compositions and Characteristics	54

2.3.7.2 Heat Treatment Techniques	56
2.4 Research Objectives.....	57
3. Experimental Arrangements and Procedures	63
3.1 Materials Investigated.....	63
3.1.1 Specimen Extraction and Preparation	66
3.2 Hydrogen Charging.....	71
3.3 Hydrogen Measurement.....	74
3.4 Tensile Tests.....	75
3.5 Slow Strain Rate Tests	76
3.6 Permeation Experiments	79
4. Results and Discussion	83
4.1 Comparison of “New Production” vs. “Used in Application” Materials.....	83
4.1.1 Initial Hydrogen Concentration of the Test Materials	83
4.2 Hydrogen Charging.....	86
4.2.1 Hydrogen Uptake and Trap Characteristics of Tensile Test Specimens.....	86
4.2.3 Mechanical Properties of the New and Used Materials Dependent on the Hydrogen Concentration	91
4.2.4 Fracture topographies of hydrogen charged tensile test specimens.....	103
4.3 Investigation of UHSS at Environmental Conditions.....	115
4.3.1 SSRT of the S53 Steel in the New As-Delivered Condition	117
4.3.2 SSRT of the S53 Steel in the “Used Component” Service-Applied Condition.....	127
4.3.2.1 Variation of Strain Rate in Artificial Sea Water	127
4.3.2.2 Variation of Strain Rate in Natural Sea Water.....	134
4.3.2.3 Variation of Electrochemical Potential in Artificial Seawater	140
4.3.2.4 Variation of Temperature in Artificial Sea Water.....	150

4.4 Hydrogen Diffusion Kinetics	159
4.4.1 Permeation Test results	159
5. Conclusions and Perspectives	161
References.....	165

1. Introduction

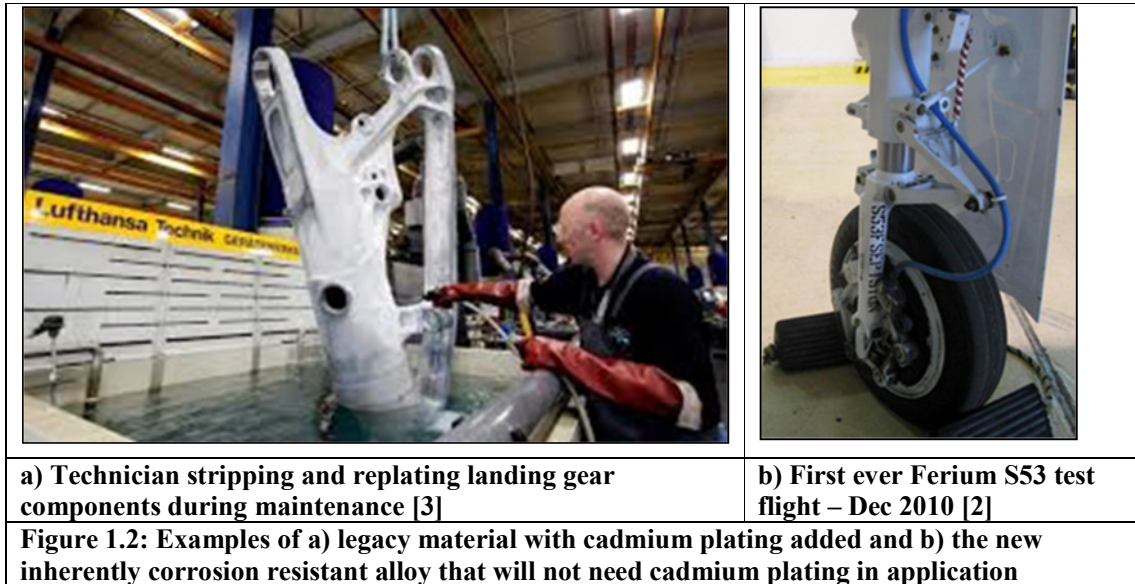
The average age of the U.S. Air Force's fleet of aircraft is 27 years old. Rigorous use in various environments and climatic conditions are typical of any aircraft in this fleet. Intensive testing, maintenance and improvements are made on all flight systems ensure that these aircraft are capable to maintain operational readiness.



Ultra-High Strength Steels (UHSS) are the predominantly used material on aircraft landing gear systems. Legacy systems have been commonly manufactured from AISI 4340 and later 300M for the main load bearing structures. These materials meet the design criteria for strength and toughness for landing gear applications, but have poor corrosion resistance. Therefore, these materials are commonly cadmium plated and painted with chromate paints to protect against environmental corrosive effects. These corrosion inhibiting compounds (CIC) protect against corrosion, but are very environmentally harmful. Additionally, the industrial processes can also potentially introduce hydrogen during the coating process and form a barrier that concentrates the hydrogen atoms at the substrate-plating interface.

Ferrium S53, a high alloyed steel designed and engineered specifically for aerospace systems, is becoming a viable alternative to the low alloyed legacy materials. S53 meets or exceeds all previous criteria for landing gear applications while adding corrosion resistance, which makes the cadmium plating unnecessary and minimized the use of CICs when used in application. This very recently designed alternative alloy is an attractive choice, but it has a highly

martensitic microstructure that can suggest a susceptibility of this material to Hydrogen Assisted Cracking (HAC). Therefore, a thorough investigation of hydrogen degradation effects regarding Ferrium S53 is necessary - considering also the environmental and mechanical conditions replicating aerospace applications.



To begin with, Hydrogen degradation effects were analyzed on AISI 4340 and Ferrium S53 to evaluate their capabilities in aerospace applications. In both cases, new billets of production material and actual used landing gear examples were used for testing. The materials were carefully prepared into specimens by using methods that minimized introducing residual stresses and thermal loading. On the used component materials, the specimens were strategically taken from areas of high stress throughout the component. These specimens were then charged with hydrogen, which concentration was then quantified with the Carrier Hot Gas Extraction (CGHE) method. Following this, experimental testing ranged from standard tensile tests to Slow Strain Rate Testing (SSRT) with simulated environmental effects and finally permeation experiments to evaluate diffusion criteria. After each test, remaining parts were retested using the CGHE process to ensure consistent results. All of the procedures were validated by testing on the AISI 4340 and by crosschecking results with published data.

It is interesting to note that existing studies on S53 and other aerospace UHSS materials have provided little data on investigations with respect to used material that may have experienced aging during service. The main focus of this research was not only to investigate the Ferrium

S53 with regards to hydrogen degradation, but to standardize the qualifying analysis of HAC thresholds for any future steels chosen for military and civilian aerospace applications. By using samples from “new production” material and also “used in application” material, the qualification analysis of the material will not only be useful for meeting current requirements of the airframe, but also be useful for developing service life predictions and maintenance schedules.

2. Literature Review

2.1 Aerospace Structures

In the beginning, airplanes were originally built with the lightweight designs and materials often used in producing bicycles and sailboat rigging. With such lightweight airframes and low-powered propulsion systems, the functionality of the aircraft was limited. After proving itself as an effective observation platform, the aerospace facet of the military was born.

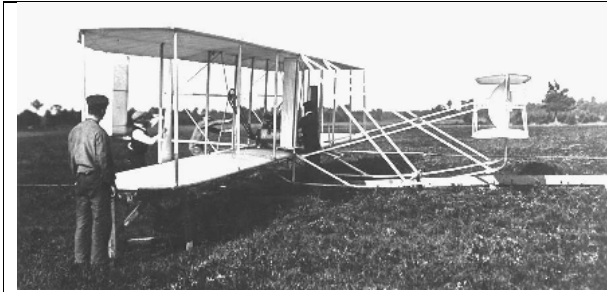


Fig 2.1: Wright Model A – the first powered aircraft ever adopted by the US military in Aug of 1909. Ash wood frame with double layer of stretched fabric over wings and control surfaces. [4]

With the demand and budget of the military, the aerospace industry quickly flourished and both military and civilian variants were soon being used around the world. In quick succession, aircraft became larger, more powerful and effective machines. The aerospace industry was truly at the “cutting edge” of science and engineering, where they were quickly finding and “pushing” the limitations of design.



Fig 2.2: Lockheed SR-71 – a Mach 3+ reconnaissance aircraft that was produced almost completely of titanium. Adopted by US Air Force in 1966. [5]

This strive to “push the limits” of air and space technology has continued through the years, but it has been tempered by the limitations of the materials used for the fabrication of these

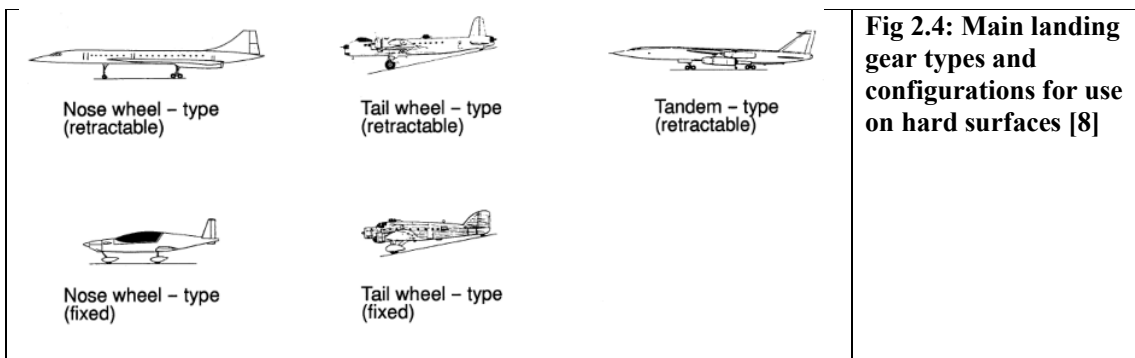
aerospace vehicles. Continued materials research and design are essential for the future of aerospace technology, and all science and engineering in general.



To put this into perspective, the three images (Fig 2.1, Fig 2.2, Fig 2.3) represent the development of aerospace structural design from its inception to current day in roughly 50-year intervals.

2.1.1 Landing Gear Design

The primary function of aircraft landing gear to support the weight of an aircraft during landing and to facilitate movement on the ground. To support the incredible loads from take-off and landing, along with the severe braking loads on the ground and impact loads from deployment in the air [7], the landing gear is tied into the primary load-bearing framework of the aircraft. The placement of the landing gear on the aircraft is a compromise of many factors, some of which are: load capability, stability, aerodynamics, packaging and weight balance.



As shown Fig 2.4, there are two different fundamental types of landing gear: fixed and retractable. Within each type, there are different configurations that each aircraft design dictates the usage of. The lighter and smaller aircraft very commonly have a fixed type landing gear with either a nose-wheel or tail wheel configuration, in particular when airspeeds are low and aerodynamic drag is not a concern. Alternately, larger and faster aircraft almost exclusively use a retractable type of landing gear with various configurations to ensure a more efficient aerodynamic design.

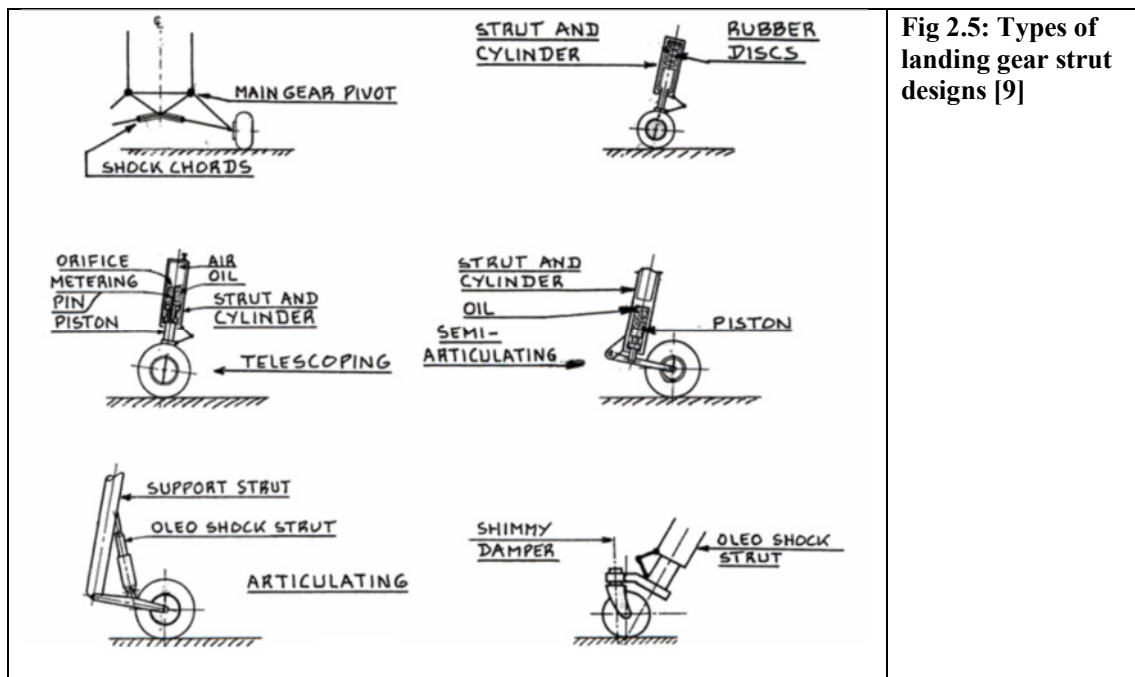
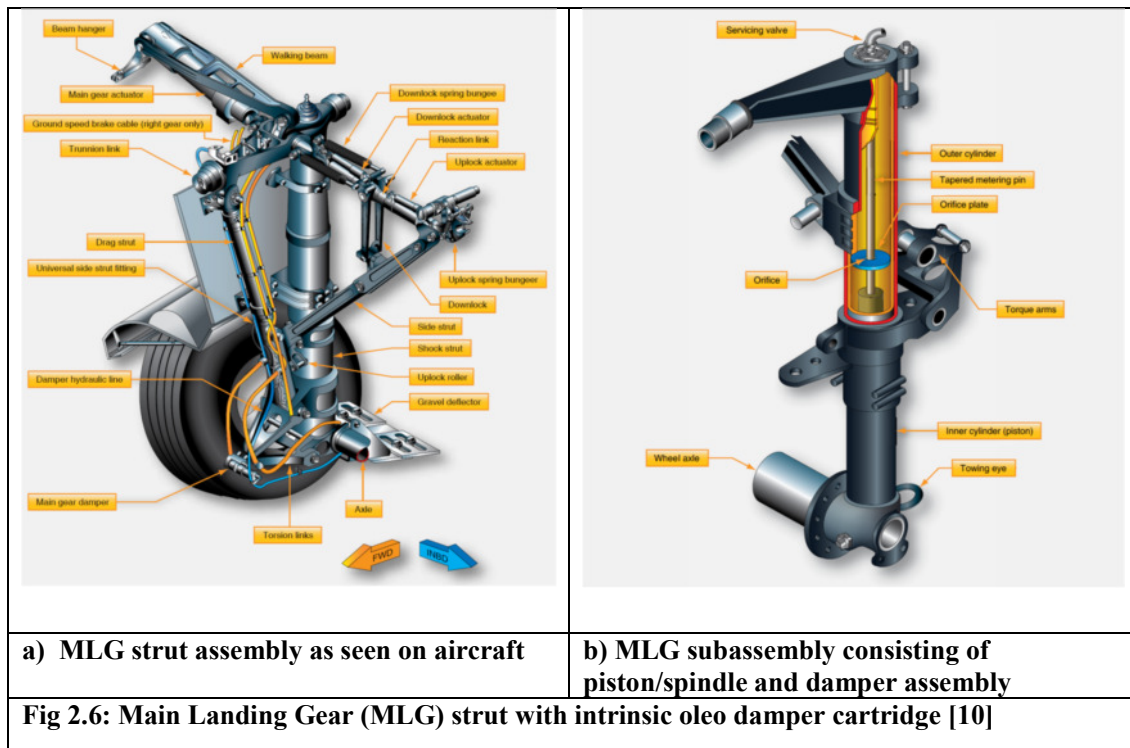


Fig 2.5: Types of landing gear strut designs [9]

The design of the actual strut can vary within the way it is damped and the configuration of the damper. The simplest and most light weight systems comprise of a solid steel swing axle design that is joined to the centerline of the aircraft with shock cords (Fig 2.5). These strut designs are unable to be retracted. From this simple system, the dampers become more complicated and many of the systems incorporate a linkage to make it fold for easier storage when retracted. The systems most common on current military aircraft and civilian passenger aircraft have an intrinsic oleo damper built into the strut unit which has a telescopic action with damper movement. The oleo damper has an air-oil damping circuit (Fig 2.6b) inside the cartridge which works on the principle of limiting an incompressible hydraulic oil flow through an orifice (Fig 2.6b). The “air” used to pressurize the system is always a dry nitrogen to limit corrosion and keep a consistent pressure regardless of altitude. The oleo damper strut design is designed

to dampen the compression of the telescopic strut and limit the rebounding extension – therefore making traverse over a rough surface relatively smooth. The limiting factor of this system is that with long duration use, the oil temperature is increased dramatically which lowers the viscosity of the hydraulic oil and decreases the dampening effects of the strut. Use of synthetic, high-temperature stable, hydraulic oils is used exclusively in all military aircraft to control these temperature degradation effects and also helps control organic growth inside of the wetted hydraulic oil system. It is important to note that many corrosive effects can be caused by organic growth within a hydraulic oil system. [10]



On the sliding surfaces of the MLG piston, a hard chrome-plating, 745-765 HV1, is deposited to mitigate friction and limit wear. The cylinder that the piston slides into has a bronze alloy bushing at the mouth to properly align the outer cylinder and piston concentrically. Similarly, the piston has a bronze alloy bushing in a split-ring design that is mounted into a groove around the circumference of the piston head that is also used to ensure concentric alignment of the strut assembly. The bronze alloy on chrome contact is aided by being wetted by the hydraulic oil which is residing inside of the damper cartridge. [10]

Both aircraft MLG struts that were examined during this contribution were of the same type as that in Fig 2.6.

2.1.2 Loading and Service Conditions in Application

Service in austere conditions with critical mission taskings, military aircraft are often pushed to the edge of the design criteria and sometimes, if not deliberately, past the thresholds of designed performance levels.

With respect to landing gear specifically, the normally recognized modes of loading are [11]:

- Take off – low-impact, shimmy, vibrations, direction corrections
- Retraction – mechanical linkage loads, buffet, drag resistance
- Landing – high-impact, shimmy, vibrations, buffet, direction corrections
- Extension - mechanical linkage loads, buffet, drag resistance
- Taxiing under power – symmetric braking, turning, undulations in taxiway
- Ground support movement – towing, off-axis turns, jerking from tug
- Hangar storage – static load of aircraft and any extras (fuel tanks, armament, electronic sensor pods, etc.)
- Maintenance – installation, removal, jacking of aircraft

Recognized as a mode of significant loading and occasionally overloads on the T-38A supersonic trainer aircraft, was extension at high speed and high altitude which created exceptional loading from drag resistance [7]. In the case study performed by NASA, over a 10,000 N overload was measured during test flights that replicated the maximum speed and altitude allowed for landing gear extension. This flight test experiment resulted in an amendment to the flight procedures of the aircraft when deploying the landing gear. A special component landing gear inspection was also performed on all aircraft in the fleet.

It is normally recognized that the landing gear systems on a military aircraft are designed with a minimum factor of safety of 1.5 [11], which in the case of the NASA study continued to represent loads that exceeded maximum stress for failure.

The theater of operations for most of the combat related missions over the past 30 years has been in arid climates. Iraq, Afghanistan, Iraq (again) and Syria are just some of the locations where aerial missions have been flown. During these 30 years, the two major contributing factors to the deterioration of components have been the abrasive and corrosive effects of sand and the high operational usage of the aircraft. The desert sand, like a very fine talcum powder, was introduced into the smallest crevices. Abrasive wear caused by the sand particulates was quite significant, but when allowed to mix with oil to form an abrasive paste, it greatly increased wear on the mechanical parts. In addition, salts and carbonates found in the sand contributed to the corrosive effects, which when coupled with the abrasive effects wreaked havoc on many mechanical systems used in these environments.

2.1.3 Maintenance and Corrosion Prevention

An example of a finely tuned piece of equipment, aircraft need continued periodic maintenance to perform at peak levels safely. The maintenance involved goes beyond the mechanical inspection and replacement of component parts, but it also refers to the inspection and conditioning of the structures and materials in order to keep them in full mission capable condition for the projected service life of the aircraft.

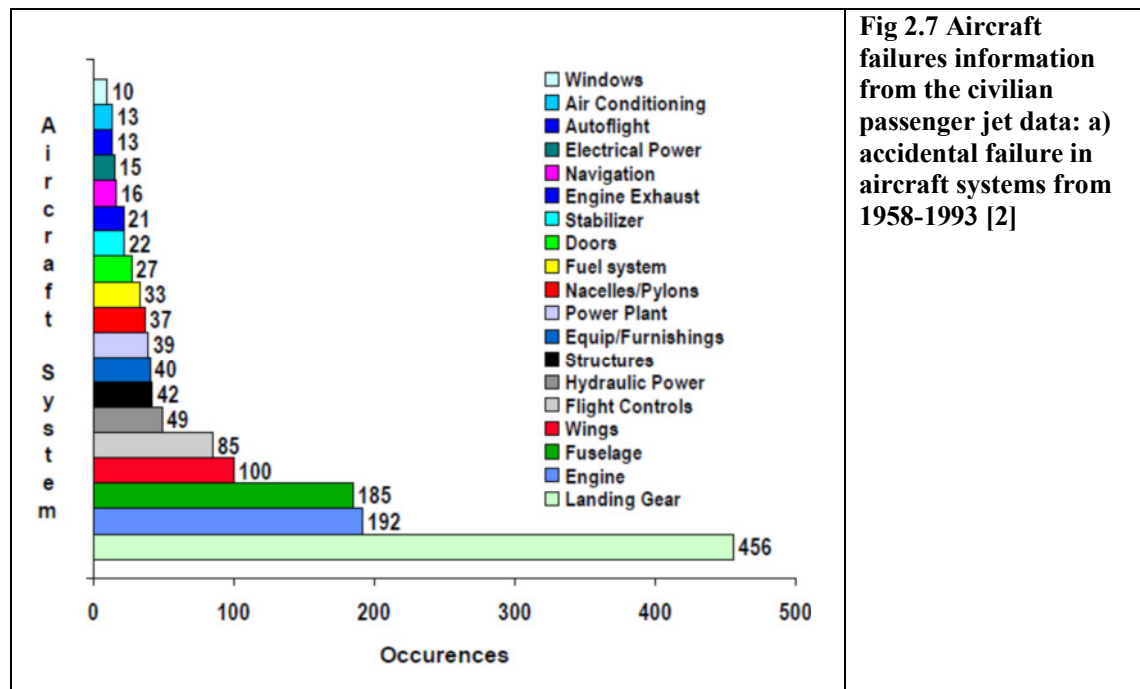


Fig 2.7 Aircraft failures information from the civilian passenger jet data: a) accidental failure in aircraft systems from 1958-1993 [2]

	Percentage of Failures	
	Engineering Components	Aircraft Components
Corrosion	29	16
Fatigue	25	55
Brittle Fracture	16	-
Overload	11	14
High Temperature Corrosion	7	2
SCC/Corrosion Fatigue	6	7
Creep	3	-
Wear/Abrasion/Erosion	3	6

Table 2.1: Chart detailing percentage of failures of each degradation mode in civilian passenger aircraft [12]

Fig 2.7, shows very clearly that landing gear failures are the largest part of the total failures in civilian passenger aircraft. Further study of Table 1 shows that fatigue failures dominates the percentage of failures with 55%. Fatigue is a well-known and studied material failure mode in aerospace materials, which makes it relatively easy to detect where stress-concentrations in the material may be high. Subsequently, the repair procedure for fatigue cracks are also well known and relatively low effort.

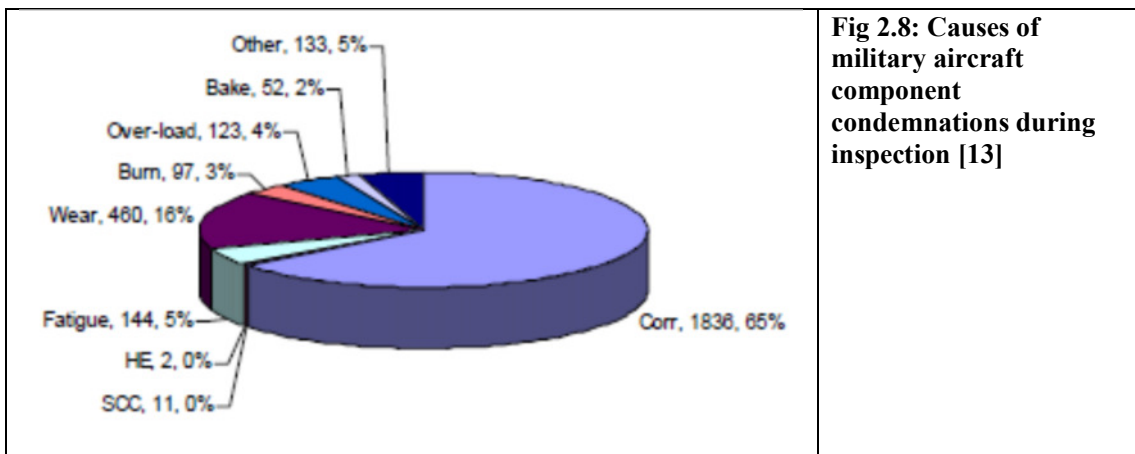


Fig 2.8: Causes of military aircraft component condemnations during inspection [13]

In Fig 2.8, the data specifically targeted military aircraft landing gear systems. Military aircraft commonly fly in adverse conditions and environments that cause the corrosion mode to highly overshadow the fatigue mode. Comparing the civilian and military data (Table 2.1 and Fig 2.8), fatigue in the heavily-used commercial transport aircraft was considerably more prevalent than in the military aircraft. Alternately, the civilian aircraft showed much lower corrosion failure than the military aircraft. Considering the extremely high percentage of condemnations due to corrosion (Fig 2.8), it is not hard to understand why corrosion control is the most expensive military resource program with yearly costs of approximately \$21B [14].

Corrosion type	Effects located	Materials affected
Exfoliation and Intergranular	ribs, spars and joints	mainly Aluminum alloys
Pitting and Crevice	localized areas under skins and coatings, fastener joints, overlaps, under sealant	Aluminum alloys and Steels
Galvanic	Fastener holes, electronics, cable connectors	Dissimilar metal joints
Composite (Resin) Degradation	Galvanic effects at metal/composite joint, resin swelling and/or loss of fiber adhesion	Composite/metal interface
General and Filiform	Under thin coatings	Aluminum alloys and Steels
Stress Corrosion Cracking (SCC)	Stressed components in corrosive areas	Aluminum alloys and Steels
Hydrogen Assisted Cracking (HAC)	Subsurface of material in contact with hydrogen	Mainly high strength steels and Aluminum
Microbial Induced Corrosion (MIC)	Material in contact with bacteria and usually submerged in fluid	Aluminum alloys and Steels
Table 2.2: Corrosion types typical to aircraft - described with usual locations and materials involved [15]		

Corrosion is a broad topic that affects many different materials, both metallic and non-metallic. In Table 2.2, the common corrosion types in aircraft are listed. Preventing corrosion effects can be done with proper preparation of the material and continued maintenance and inspection.

In the past, Corrosion Inhibiting Compounds (CIC), such as thin coatings of Cadmium and/or chromate infused paints, were used to prevent corrosion in materials. These previous solutions were very effective, but have proven to be both harmful to personal health and to the environment. Therefore, new and more environmentally benign techniques have been developed to counter the corrosive effects, which can be found in Table 2.3.

Pretreatments and coatings are major defense against corrosion
Sealant in joints, splices and galvanic couples where possible
Sacrificial metallic coatings for landing gear steels
Ceramic coatings as high temperature corrosion barriers
Temporary protection schemes: Corrosion Protection Coatings, water displacing compounds and wash primers
Frequent equipment washdown with/without corrosion inhibitor in wash/rinse waters
Damage assessment at Aircraft Service Period Adjustment/Programmed Depot Maintenance cycles: select area corrosion inspection at depot level
Table 2.3: Corrosion control techniques [15]

2.1.4 Component Service Life

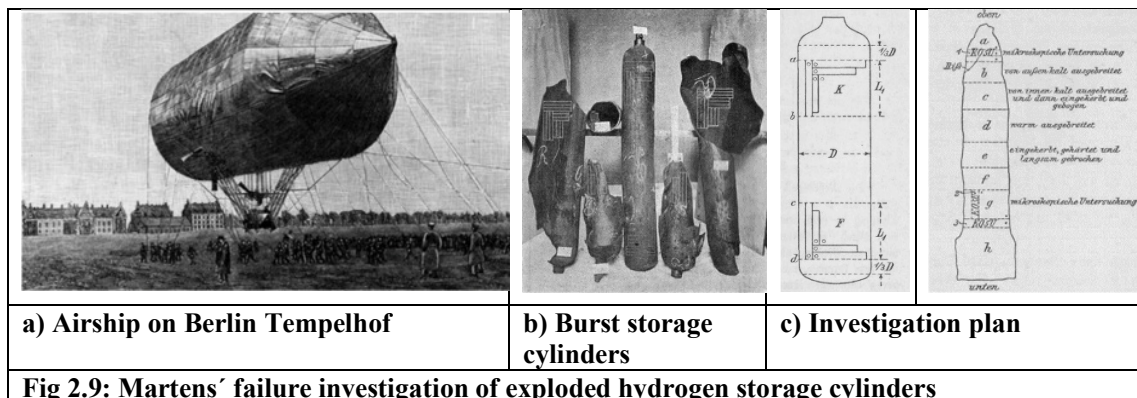
To evaluate component service life, an accurate representation of the service loading condition has to be represented when doing the fracture mechanics analysis. Deviation from the tested service load condition and/or environment will change the expected lifetime assessment. In the late 1980's, NASA proposed a theory and algorithm to predict aircraft structural component service life called the half-cycle theory. This theory was based around predicting the amount of stress cycles necessary to satisfy modeled fatigue-crack growth rates. It upgraded the previously used model by changing the assumption that the amount of crack growth per flight remained constant. As a result, the predicted amount of stress cycles was less than half for the very same component. Of course, to err on the side of safety is good, but the model effectively rendered a component useless in less than half of its previously calculated lifetime, based on theoretical data and boundary conditions. [16]

To achieve a better lifetime assessment, an effort was initiated by the Center for Aircraft Structural Life Extension (CAStLE) to experimentally test service-applied "used components" from aircraft with very well documented flight histories. By instrumenting operational aircraft with strain gauges at all the highly stressed areas, load data was collected and modelled to represent an average load profile for each given airframe analyzed. By using these load profiles on experimental setups replicating the loads of each respective component of interest, low-cycle fatigue tests were run to find cycles to failure data. With many experimental data points throughout each highly instrumented and well documented aircraft, an experimental service life analysis was performed and submitted as the new service life model of the Air Force. This

technique has taken many man hours and several aircraft teardowns to complete, but within its results, it has returned up to and exceeding 100% of previous aircraft service life estimates to the aircraft analyzed. [17]

2.2 Hydrogen Assisted Cracking (HAC)

For nearly 150 years, hydrogen assisted cracking (HAC) has represented a well-known materials degradation phenomenon [18]. One of the most spectacular failure cases might be regarded as the explosion of hydrogen gas storage cylinders on May 25, 1894, which occurred during the late industrialization period in Germany. With respect to modern applications of hydrogen storage as an energy source, it has several times been referred to as precedent failure case for the entire industrial sector. The detailed investigative reports by A. Martens, the first director of today's BAM, the German Federal Institute for Materials Research and Testing in Berlin, Germany, and name-provider for the metallic microstructure martensite, have maintained their importance. The reports by Martens have also attracted attention in the past few years because the publications in 1896 document one of the first and most comprehensive investigations which can be regarded as the prototype exemplar for modern failure analysis. After a revision of the original failure case reports, Boellinghaus et al. [19] concluded that hydrogen assisted cracking had to be considered as primary failure type in the sequence of events leading to the catastrophic scenario in Tempelhof, among some other less-likely origins. In this regard, the explosion on the Tempelhof airfield might represent one of the first and earliest documented failure cases caused by hydrogen degradation of the material. Martens' note at the end of his report that "the investigations should be carried on" can only be emphasized with respect to modern hydrogen transport and storage systems. [20,21]



2.2.1. General Phenomenology

Figure 2.10 provides an overview on the different types of degradation of structural metallic material that might be caused by hydrogen. Blistering and porosity caused by hydrogen are not relevant to the high strength materials covered by the present contribution. Inner and outer hydride formation are also not relevant, since iron based steel alloys with a carbon content below 2 wt.-% cannot form stable hydrides. The steels considered in this contribution also do not contain any noticeable amounts of hydride forming metals, like Mg, Ti or Zr.

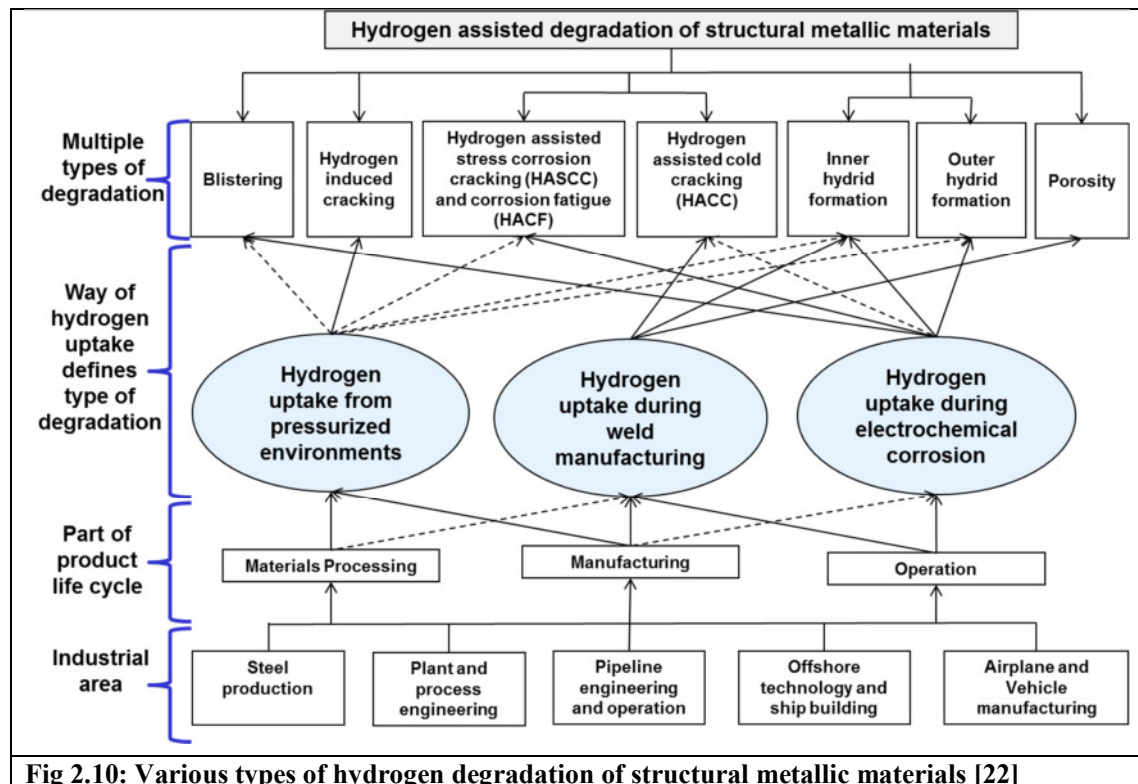
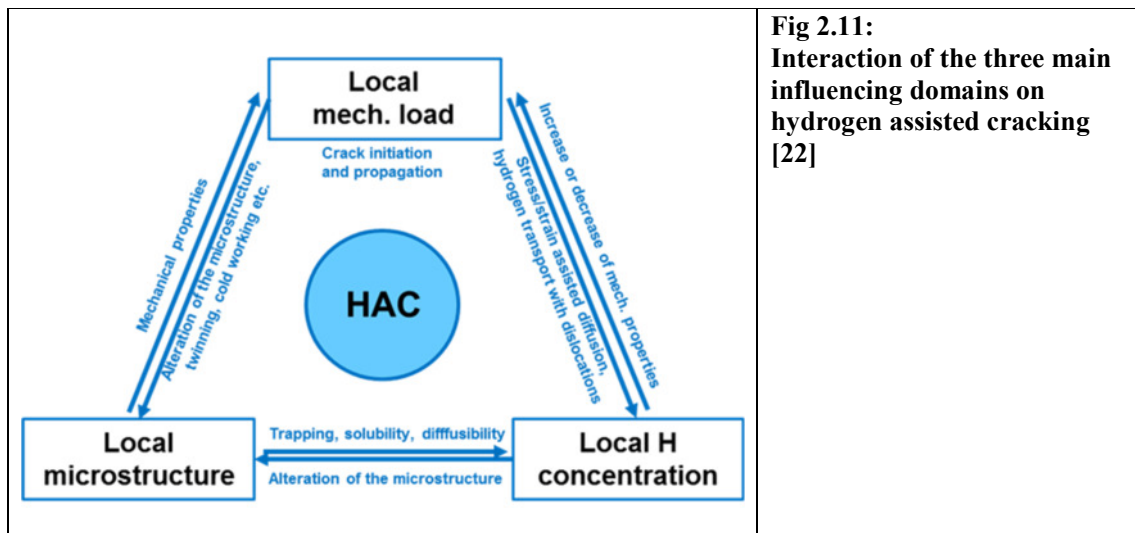


Fig 2.10: Various types of hydrogen degradation of structural metallic materials [22]

Hydrogen induced cracking represents a type of cracking where hydrogen is absorbed by a structural metallic material and may recombine at objects in the microstructure that provide enough space for the recombination process, like the interface between non-metallic inclusions and the surrounding lattice. In this case, the mechanical load required to separate a metallic microstructure is provided by the volumetric change of hydrogen ions absorbed by the material from the hydrogen molecules. Therefore, this type of hydrogen degradation can also be regarded as a special kind of hydrogen assisted cracking. However, occurrence of hydrogen induced cracking is predominantly restricted to soft steels and thus, has limited effects on the high strength steels studied in the present contribution.

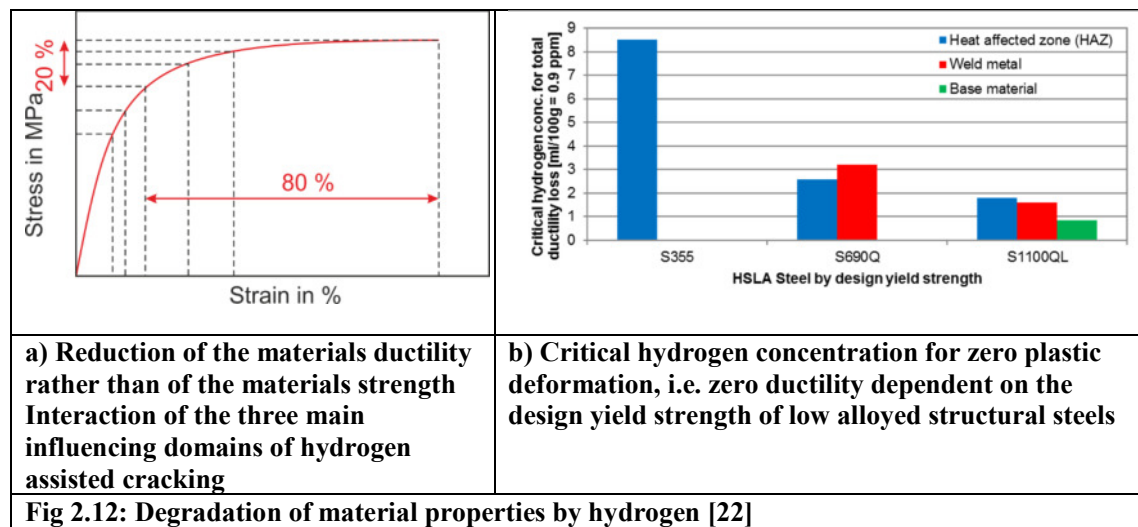
Consequently, only four types of hydrogen assisted cracking exist - they are hydrogen assisted cold cracking (HACC), hydrogen assisted stress corrosion cracking (HASCC), hydrogen assisted corrosion fatigue (HACF) and pressurized hydrogen assisted cracking (PHAC). The way of hydrogen uptake of a structural material defines the type of hydrogen assisted cracking. Arc and laser welding in humid environments, for instance, might cause a dissociation of water in the arc or laser plasma by which hydrogen is absorbed by the liquid weld pool, then causing hydrogen assisted cold cracking in the weld metal or the adjacent heat affected zone. At high hydrogen gas pressures above 200 bar and above 100 °C, hydrogen might also dissociate and cause hydrogen assisted cracking of a structural material, as outlined by the earlier cases by Martens in Chap 2.2. However, the high strength steels investigated here are usually not subjected to high pressure hydrogen gas, and landing gear structures, as outlined previously, are usually not welded. Therefore, HACC and PHAC can be excluded from the present contribution.



To begin with, hydrogen assisted cracking under static loading has been focused on in the present contribution. It must be considered, however, that landing gear might be subjected to impact-like loads in corrosive environments, especially during take-off and landing operations. However, these loads are in the low cycle fatigue regime. As a first approach, the hydrogen assisted stress corrosion cracking under monotonic static loads has been concentrated on in the present thesis. Of course, the basic dependence of the mechanical properties of the landing gear steels on the hydrogen concentration that might be absorbed during service operation has also been investigated in depth, to provide a basic understanding of HAC in such steels. As a further

approach, investigation of the low cycle HACF behavior of these materials has been kept in consideration as well, but is going far beyond the frame of the present contribution.

The general phenomenology of all four types of HAC can quite easily be described by the local interaction between a mechanical load, the hydrogen concentration and the microstructure. In other words, if a certain local combination of a mechanical load and a hydrogen concentration exceeds the tolerable limit of the local microstructure, then a risk for hydrogen assisted cracking in the local microstructure is encountered (Figure 2.11).



In general, hydrogen is reducing the mechanical properties of a structural metallic material, steels, predominantly by reducing the ductility and lesser by a reduction in strength. This is illustrated by Figure 2.12a. Commonly, the technical stress strain diagram of material evaluated by tensile testing is initially affected by hydrogen in terms of reducing the necking capabilities. Such behavior usually becomes quite apparent, even at lower concentration levels absorbed in the material. With high strength steels, this effect of reduction in ductility can become even more pronounced. Another point regarding the technical stress-strain curve is that the uniform deformation capabilities between the yield strength and the ultimate tensile strength (UTS) are reduced. For example, high strength steels with increased hydrogen concentrations will not even reach their UTS determined in an inert environment, like air, for instance. A critical hydrogen concentration, which represents total reduction of ductility, is when steel does not show any deformation capabilities any more. In this case, the material will fail at yield strength – or it can be understood that yield strength and UTS have the same value. This hydrogen concentration

will mark the total embrittlement of a steel and has been identified for the base material, the heat affected zone and the weld metal, for conventional weldable structural steels used in the European and Asian regions, Figure 2.4b. Here, should be understood that 1 ml/100 g Fe equals approximately 0.9 ppm of hydrogen dissolved in the material. With a typical structural steel used for offshore oil and gas platform frames and for wind mill towers, it will only exhibit zero ductility with hydrogen concentrations far above 10 ppm. However, this is not the case in the heat affected zone, where such steels will still behave as intended, even if hydrogen has been introduced. However, when the design yield strength of such structural steels is doubled to about 700 MPa (S 690) or even tripled to about 1100 MPa (S1100), then these materials exhibit a more martensitic base microstructure that will react very negatively with absorbed hydrogen. In other words, the S1100 steel base material can have totally brittle failure when hydrogen concentrations beyond 2 ppm are introduced into such microstructures. To sum up, the diagram shows that an increasing amount of martensite in the steel will reduce its tolerance against hydrogen in the microstructure. For this reason and because landing gear steels represent martensitic steels, a literature review about HAC in martensitic steels has been included in the present contribution.

2.2.1 Hydrogen Transport and Trapping Mechanisms

Before going into details of HAC in martensitic steels, the metallurgical mechanisms regarding HAC have to be addressed. With respect to Figure 2.12a, the phenomenon of HAC in steels cannot be explained with one metallurgical mechanisms alone, as already commented by Hirth more than 35 years ago [23]. However, the reason for this is that the various interactions of the major local influences: microstructure (in this case martensite), mechanical load (in this case monotonic tension) and hydrogen concentration have to be considered. Moreover, most of the mechanisms only reflect one or two interactions. For instance, mechanisms regarding hydrogen uptake do predominantly account for the interaction between microstructure and hydrogen concentration and only to a lesser extent to the local mechanical load. This is to a much lesser extent the fact regarding the mechanisms for hydrogen trapping and enhancing the transport in the various microstructures. This must be considered to understand not only trapping of hydrogen in a plastic strain field at crack tips, but also the enhanced hydrogen transport in such regions by dislocations.

To sum this up, the main categories associated with HAC and specifically the hydrogen transport processes and mechanisms regarding the hydrogen cracking processes. These will be addressed briefly in the following sections:

Mechanisms of Hydrogen Transport:

The transport of hydrogen in the solid metal can be divided into three steps: hydrogen uptake, hydrogen transport in the microstructure and effusion of hydrogen. The individual sub-steps are linked to different boundary conditions. The conditions for hydrogen uptake into the metal and for diffusion and effusion are described in more detail below.

Hydrogen uptake and solubility:

Landing gear steels will only be subjected to aqueous environments, usually variations of marine brines, from which hydrogen could be incorporated into the microstructure. Hydrogen uptake from these environments can essentially be described by three sub steps which include: the transport of hydrogen ions from the surrounding medium to the metal surface, the adsorption of hydrogen at the surface and the absorption of hydrogen into the metal [24], Equation (2.1):



However, there is also the possibility that two adsorbed hydrogen atoms recombine to molecular hydrogen and desorb from the metal surface. This process can be described by the Volmer Tafel mechanism, Equation (2.2), or the Volmer-Heyrowsky mechanism, Equation (2.3).

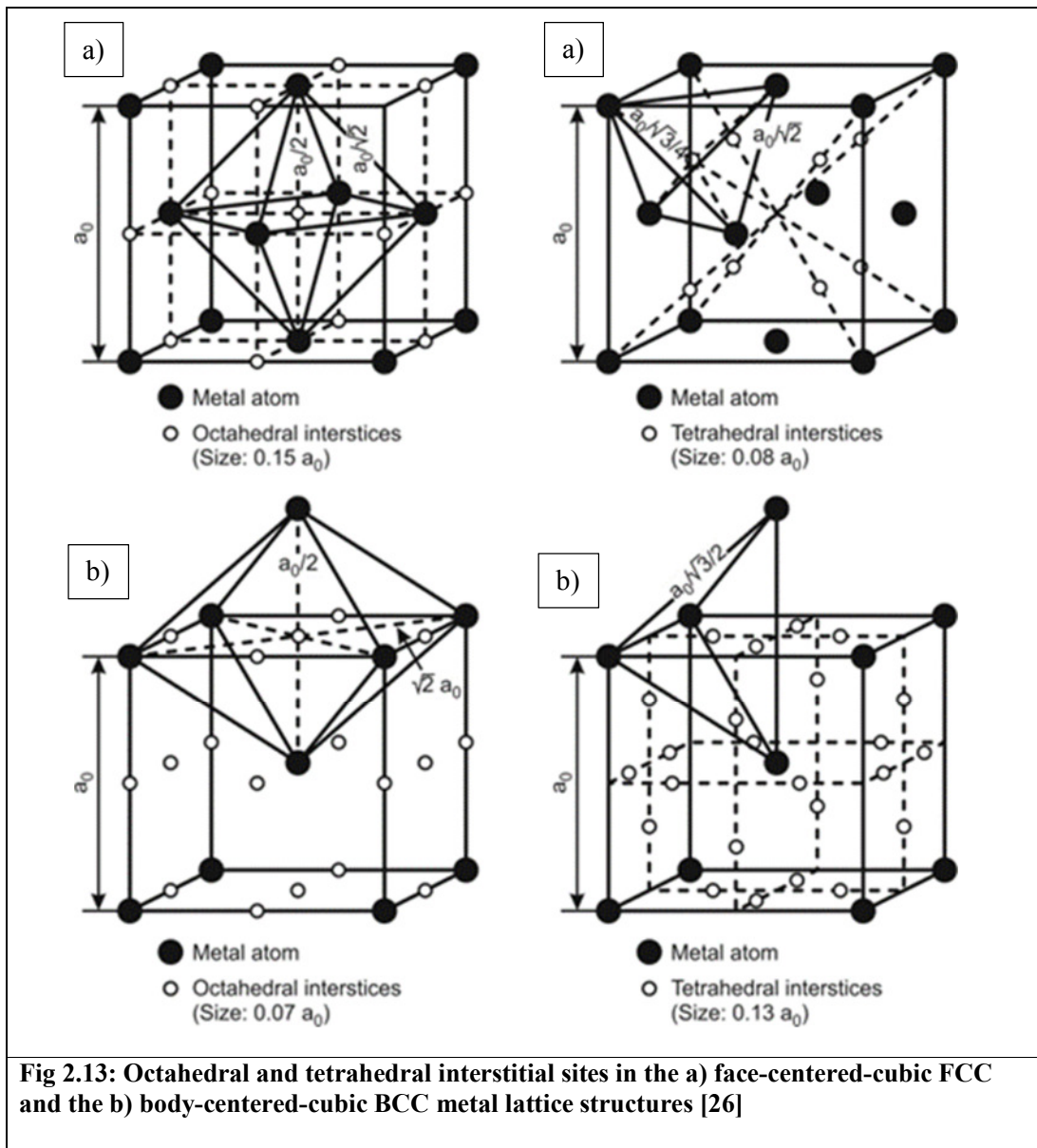


This recombination of hydrogen ions at the metal surface may be suppressed by the presence of promoters, e.g. H_2S [84], As_2O_3 , cyanides and other compounds with elements of the V and VI main group of the periodic table (P, As, Sb, S, Se, Te) [24, 25].

In this context, it has to be considered that Sievert's law which can be simplified by Equation (2.4).

$$HD = k \cdot \sqrt{p_{H_2}} \quad \text{with} \quad k = e^{\frac{\Delta G}{RT}} \quad (\text{ppm}), \quad (2.4)$$

with HD: Hydrogen concentration in the metal, ΔG : Reaction enthalpy, R: Ideal gas constant and T: Absolute temperature.



This represents only the uptake of diatomic gaseous hydrogen in a solid metal lattice and cannot be applied to hydrogen taken up from corrosive environments [24].

For a more detailed description of the hydrogen uptake from different media and methods for the mathematical description of the processes, it is referred to in the work of Boellinghaus and Mente [24, 25].

The absorbed atomic hydrogen is interstitially dissolved in the metal as the smallest chemical element on the interstitial sites, thus forming mixed crystals [24, 25]. Figure 2.13 shows the tetrahedral and octahedral interstices for a face-centered cubic (FCC) and body-centered cubic (BCC) crystal lattice. In the FCC lattice, hydrogen is preferentially dissolved on the tetrahedral interstices and in the BCC lattice in the octahedral interstices [24].

The different occupation of the interstitial spaces in the two crystal forms results from the space available for the hydrogen. In the cubic face-centered crystal lattice, the octahedral interstices and, in the cubic body-centered crystal lattice, the tetrahedral interstitial sites provide more space for the incorporation of hydrogen. By using the lattice parameters for BCC lattices ($a_0 \sim 2.87 \text{ \AA}$) and FCC lattices ($a_0 \sim 3.65 \text{ \AA}$), the value for the tetrahedral interstitials in the BCC lattice is $\sim 0.37 \text{ \AA}$ and for the octahedral sites in the FCC lattice has a value of $\sim 0.55 \text{ \AA}$. Thus, there is more space for the incorporation of hydrogen in the FCC lattice, which explains the larger solubility in the FCC lattice as compared to that of the bcc lattice. However, due to the higher packing density in the four-atom FCC crystal, as opposed to the 2 atoms per cubic unit cell BCC lattice, the diffusivity of hydrogen in the BCC lattice is higher. Martensite represents a tetragonally elongated bcc lattice and the considerations above for BCC apply to the martensitic microstructure as well, with some minor restrictions.

Beyond these observations, Oriani [27] found that atomic hydrogen releases its valence electron to the 3d shell of the iron atom and is present as a proton in the metal lattice. This interaction leads to a change in the electronic charge density and the electrical resistance. The electrical resistance changes due to lattice distortion caused by the repulsion of the hydrogen protons due to positively charged metal ions [27]. By Baranovski et al. [28] it was found that the incorporation of the hydrogen atom in a BCC martensitic lattice causes a volume expansion of

the lattice of about 3 \AA^3 . Furthermore, Fukai [29] reports that the change in volume of the lattice depends on the occupation of the tetrahedral and octahedral sites, and that the occupation of the tetrahedral interstitial sites usually causes a larger volume expansion and therefore a greater strain of the crystal lattice. For a pure crystal lattice, the solubility for hydrogen can be described very well with these considerations. However, in real industrial alloys, like martensitic steels, the solubility for hydrogen can be much higher, since vacancies, dislocations, and foreign atoms create additional space for hydrogen. Grain and phase boundaries also provide additional space for the storage of hydrogen [24, 30, 31].

Internal Hydrogen Transport

For hydrogen transport inside a metallic microstructure, diffusion represents the driving force. Diffusion determines the amount and velocity of hydrogen, which is ultimately responsible for the damage in the microstructure [24].

The diffusion of hydrogen is the relative movement of the hydrogen atoms through the interstices in the crystal lattice. Mathematically, this movement is described by Fick's laws. The first Fick's law describes the stream of hydrogen in the crystal lattice proportional to the concentration gradient, Equation (2.5):

$$J = -D\nabla C = -\left(D_x \frac{\partial C}{\partial x} + D_y \frac{\partial C}{\partial y} + D_z \frac{\partial C}{\partial z}\right), \quad (2.5)$$

with J: hydrogen flux, D: proportionality factor (diffusion coefficient or diffusivity) and ∇C : gradient vector of concentration. The gradient ∇C indicates the direction of the largest concentration change and points in the opposite direction from the vector J. The material flow J represents the number of particles which diffuse through a surface perpendicular to the diffusion flow J within a certain time. When considering the diffusion in only one spatial direction, it becomes:

$$J_x = -D_x \frac{\partial C}{\partial x}, \quad (2.6)$$

with $\frac{\partial C}{\partial x}$: Local concentration gradient.

Fick's First Law is analogous to the heat conduction, Equation (2.7):

$$\mathbf{J}_q = -\kappa \nabla T, \quad (2.7)$$

with \mathbf{J}_q : heat flow, κ : thermal conductivity and T : temperature.

Fick's first law applies only to the case of spatially stationary diffusion, therefore the concentration gradient $\partial C/\partial x$ remains constant during diffusion. In order to describe a time-varying diffusion, possibly due to concentration compensation, the concentration varies as a function of location and time and the continuity equation must be taken into account [32]. The thermal change of the concentration in the crystal lattice corresponds to the divergence of the hydrogen current, as represented by Equation (2.8):

$$-\nabla \cdot \mathbf{J} = -\left(\frac{\partial J_x}{\partial x} + \frac{\partial J_y}{\partial y} + \frac{\partial J_z}{\partial z}\right) = \frac{\partial C}{\partial t}. \quad (2.8)$$

Inserting the first Fick's law (Equation (2.9)) into the equation of continuity (Equation (2.8)) gives Fick's second law, also called the diffusion equation [32], Equation (2.9):

$$\frac{\partial C}{\partial t} = \nabla \cdot (D \nabla C) = -\nabla \cdot \mathbf{J}. \quad (2.9)$$

Fick's law represents a non-homogeneous second-order differential equation. If the diffusion coefficient depends on the concentration, this equation is nonlinear [32]. When the diffusion coefficient is independent of the concentration, Equation (2.9) simplifies to:

$$\frac{\partial C}{\partial t} = D \Delta C = D \left(\frac{\partial^2 C}{\partial x^2} + \frac{\partial^2 C}{\partial y^2} + \frac{\partial^2 C}{\partial z^2} \right). \quad (2.10)$$

Equation (2.10) is a second-order differential equation to represent the concentration field $C(x, y, z, t)$, with the Laplace operator Δ .

In all equations, D represents the diffusion constant (diffusion coefficient or diffusivity), which characterizes the rate of diffusion. The diffusion coefficient can be described by the Arrhenius relation [32], which reflects the strong temperature dependence of diffusivity, Equation (2.11):

$$D = D_0 \cdot e^{-\frac{E_A}{k_B T}}, \quad (2.11)$$

with D_0 : material-dependent constant (lattice diffusion coefficient in the ideal lattice) and $e^{-\frac{E_A}{k_B T}}$, the Boltzmann factor, which determines the probability of particles detected to perform a change of location according to a specific mechanism, with E_A : Activation energy, k_B : Boltzmann constant and T : Absolute temperature.

To change the location of a hydrogen ion in the metallic microstructure, a certain activation energy E_A must be applied. Völkl and Alefeld [33] identified an average value of $D_0 = 7.5 \cdot 10^{-4} \text{ cm}^2 \cdot \text{s}^{-1}$ and an activation energy of $E_A = 6.658 \text{ kJ} \cdot \text{mol}^{-1}$ ($U = 0.105 \text{ eV}$) for the lattice diffusion of hydrogen into α -iron. In addition, the diffusion coefficient for pure α -iron can be determined for the temperature range from room temperature to the transition temperature in γ -iron. The authors explain that the diffusion coefficient begins to scatter strongly for temperatures below 250° C and this is due to the diffusion-inhibiting influences in the crystal lattice (hydrogen traps).

However, previous observations on the laws of diffusion are only valid for the diffusion of hydrogen in a defect-free crystal lattice. Realistically, the crystal lattice in a production metal alloy is mostly heterogeneous and has numerous different lattice defects, which can hinder or accelerate the migration of hydrogen through the lattice. These processes are referred to trapping or enhancing mechanisms.

As mentioned previously, the diffusion coefficient of hydrogen in BCC lattices or martensitic microstructures is several orders of magnitude higher than in FCC lattices. This is due to the different packing density of the cells and the size of the interstitial sites.

Most polycrystalline metal alloys have a heterogeneous microstructure and their crystal lattice is interspersed with lattice defects. In this setting, these lattice irregularities are usually called

traps [24], since they can capture and bind hydrogen. This action is referred to as trapping mechanisms. Pressouyre [34] classified different hydrogen traps by the binding energies:

- Point defects: vacancies, substitution or foreign atoms
- Line defects: screw or line dislocations, node of three grain boundaries
- 2D defects: grain, phase or twin boundaries, particle-matrix interfaces, inner surfaces
- 3D defects: volume defects such as voids, micropores, microcracks or particles.

By trapping hydrogen, the diffusion through the lattice is slowed down. McNabb and Foster [35], Oriani, [36] and McLellan [37] distinguish hydrogen traps by an energy difference between the trap ($E_{B\text{ trap}}$) and the energy level of the grid (E_{grid}). It is assumed that the hydrogen in the lattice is locally in equilibrium with the hydrogen in the traps. This allows the trapped hydrogen in traps to escape by supplying a sufficiently high activation energy $E_{A\text{ trap}}$ and therefore again take part in the lattice diffusion. The authors McNabb and Foster [35] differ in their thoughts between trapped hydrogen or alternately, deep trapped hydrogen. An overview of the mathematical models for the detection of diffusion-inhibiting effects has been provided by Böllinghaus [24]. Pressouyre [34] further classifies the three different types of traps depending on the activation energy needed for escape.

Very deeply trapped hydrogen that cannot be released at higher temperatures and needs a very-high activation energy to break away, is usually called irreversibly trapped hydrogen. Another name for it is residual hydrogen. In the work of Maroef et al. [38] the residual hydrogen is divided into reversibly and irreversibly trapped hydrogen as a function of the activation energy. The irreversibly trapped hydrogen has an activation energy of $E_A \geq 60 \text{ kJ / mol}$ ($U \geq 0.62 \text{ eV}$) [38]. However, if hydrogen is bound so-called irreversibly within a certain temperature range, this does not mean that it might be escaping from such traps under special circumstances during the service life of a metallic component and therefore, residual or irreversibly trapped hydrogen cannot be considered a zero risk for cracking. Moreover, the binding energy of -60 kJ/mole is not enough to hold hydrogen in place, especially if the material is globally strained and the microstructure is locally strained during service in the plastic region.

It is important to note, dislocations are assumed sometimes to bind interstitial atoms such as hydrogen in the dormant state [39]. However, due to a corresponding stress on the material,

dislocations begin to migrate through the crystal lattice. The hydrogen can be transported with it depending on the dislocation velocity [40] and, may also be escaping from trapping sites.

There are different schools of thought when concerning grain boundaries as trapping sites [41]. For one thing, they are often assigned to hydrogen traps [23,34,38] because they represent a grid irregularity and thus provide increased space for hydrogen. On the other hand, they can also be paths of increased hydrogen diffusion [32,42]. However, the acceleration and inhibition of hydrogen diffusion depends on the geometry of the grain boundary and the amount of precipitates within the grain boundary [43-45]. Yazdipour et al. [44, 45] and Dadfarnia et al. [46] show by numerical calculations that the diffusion coefficient of a single crystal as compared to a fine-grained polycrystalline material only slightly increases and then decreases again sharply with decreasing grain size. The authors argue that this behavior is due to the increase in grain boundary area per unit volume. They further discuss that as the grains get smaller, there is an increase in the number of potential hydrogen traps. Chou and Tsai [47] found improved resistance to hydrogen-assisted cracking in their SSRT experiments as the particle size decreased for a duplex steel. The authors justify this behavior by the decrease of the diffusion speed and an increased accumulation of hydrogen at grain boundaries. In general, the authors note a decrease in ductility with increasing particle size. Alternately, it is unanimously argued that phase boundaries, especially inclusion-lattice phase boundaries on carbides and nitrides act as traps [41,48-50].

The classification of hydrogen traps according to their activation energies allows the consideration of trapping effects in the Arrhenius relationship (Equation (2.11)) [51]. Using this equation, diffusion bands can be created for the diffusion coefficients in which diffusion-inhibiting effects are recorded [41, 52]. The upper limits are the unconstrained hydrogen diffusion and the lower limits describe the worst case, i.e., delayed trapping in deep traps. As a result, it is also possible to calculate trapping in numerical calculations via an effective diffusion coefficient D_{eff} , which includes the corresponding activation energies of the respective trap types [24]. Martensite represents an austenite decomposition microstructure - the scatter band for such steels can be applied regarding the diffusion coefficient in martensitic steels (Figure 2.14).

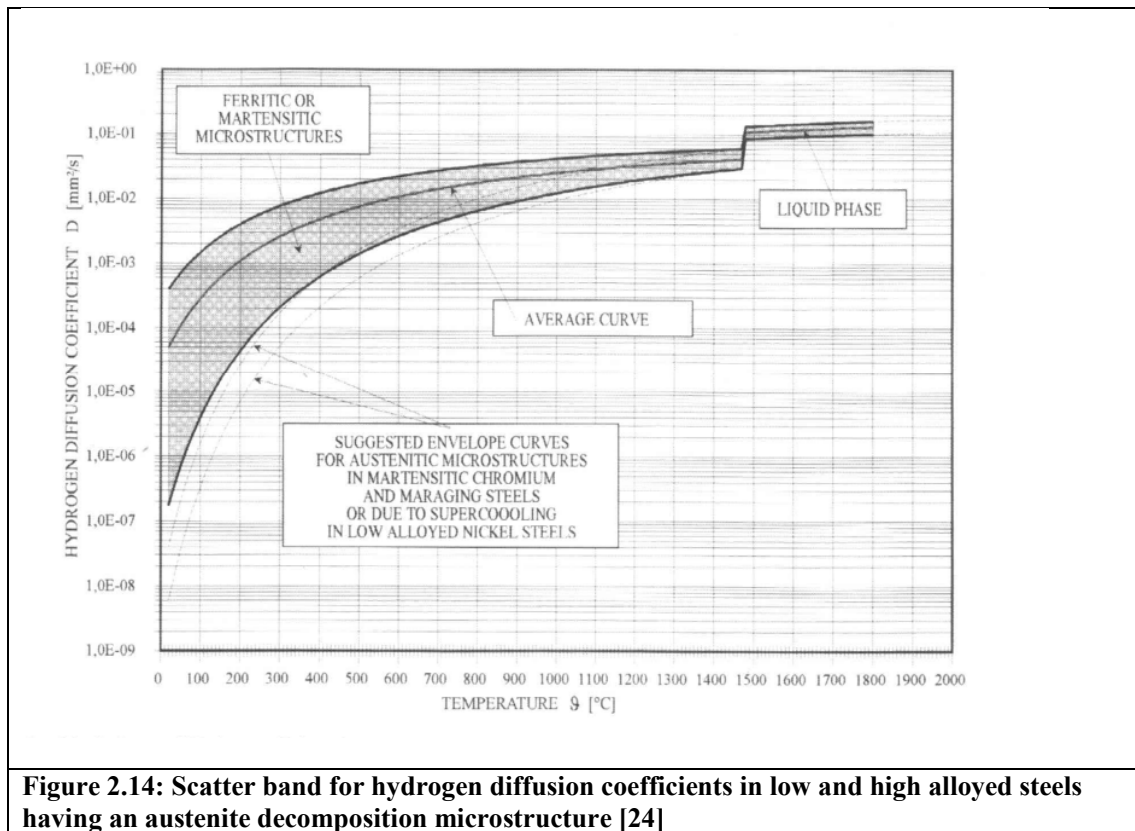


Figure 2.14: Scatter band for hydrogen diffusion coefficients in low and high alloyed steels having an austenite decomposition microstructure [24]

In addition to the diffusion-delaying effects of hydrogen traps, there are also theories for accelerated hydrogen diffusion in the literature. For example, it is assumed that high strains or deformations due to the width of the crystal lattice can promote hydrogen diffusion [53-59] and that hydrogen follows not only a concentration gradient but also a strain or strain gradient [24]. According to Böllinghaus [12], the detection of such effects can take place via the extension of Fick's law around a second potential field. This is the only way to mathematically describe the accumulation of hydrogen above the initial concentration associated with enhancement effects [24].

Another form of enhancement, much discussed in the literature, is accompanied by the plastic deformation of the material. Associated with plastic deformation are the formation and migration of dislocations. As already described above, hydrogen can be trapped at dislocations as a Cottrell cloud [39]. For example, Trojano [60] noted that hydrogen accumulates in the plastic zone before cracking, thus contributing to the damage of the material. In the work of Kiuchi and McLellan [61], a model is suggested that the hydrogen can be transported faster on both sides of the displacement at a certain distance to the displacement.

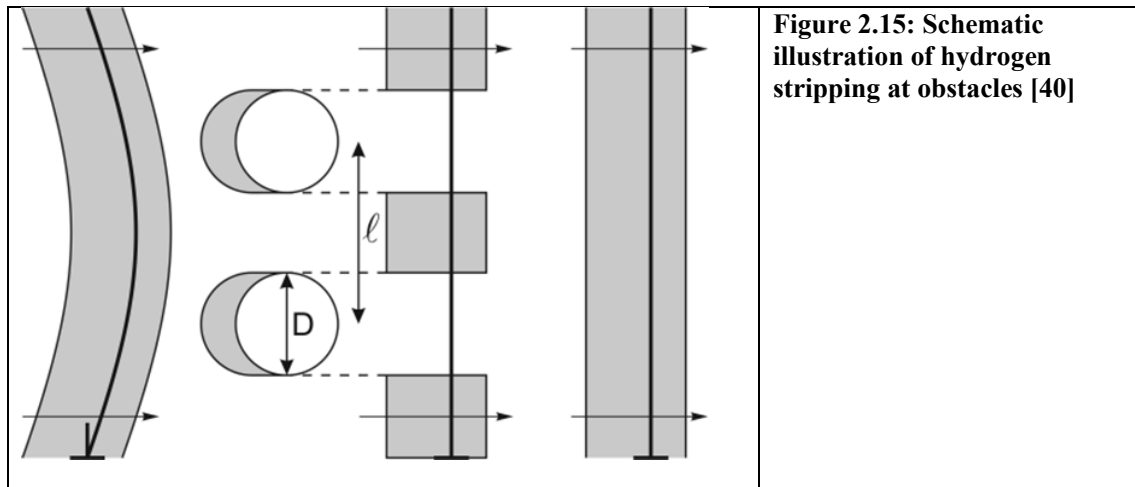


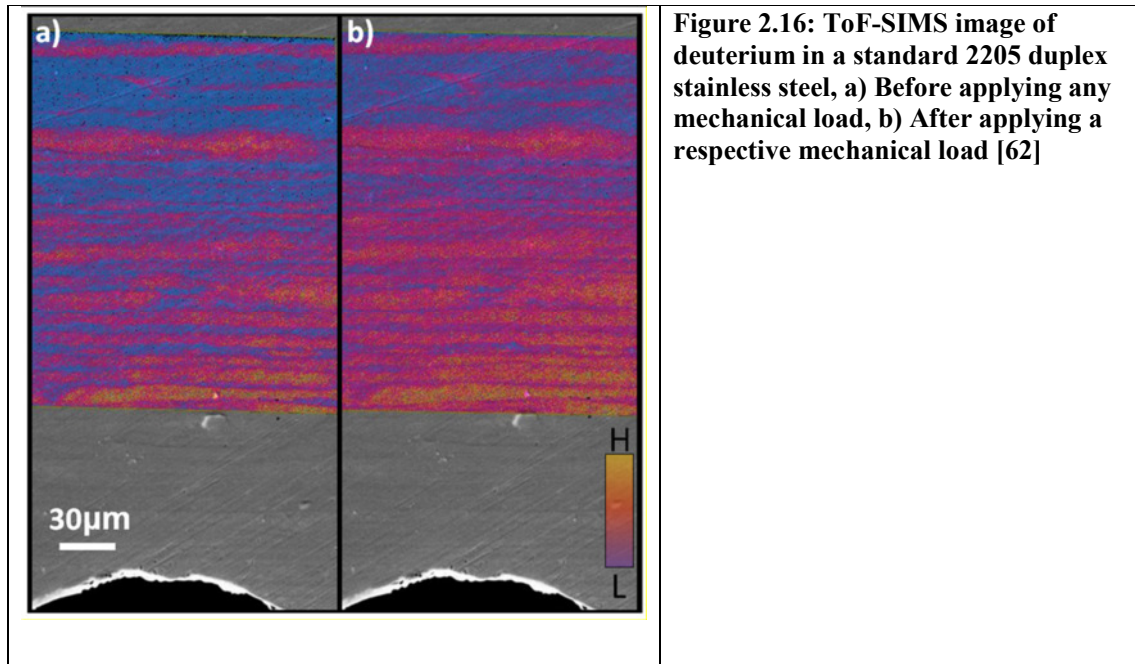
Figure 2.15: Schematic illustration of hydrogen stripping at obstacles [40]

In addition to these effects, Tien et al. [40] described the transport of hydrogen with the dislocations. According to the authors, an accumulation of hydrogen in the structure takes place when the hydrogen is released from the dislocation. This can be done by exceeding a critical velocity, extinction, or interaction of the translocation with hydrogen traps [40]. If the hydrogen is stripped off at a reversible hydrogen trap, it is possible that another dislocation can take up this hydrogen again and transport it further. The maximum radius for such interaction is given by Tien et al. [40] with thirty times the Burgers vector b . The amount of hydrogen transported can be described by a Boltzmann equation, similar to the diffusion coefficient (Equation (2.16)), with hydrogen bonding energy at dislocations. The mechanism of stripping and reuptake of hydrogen is referred to as "dislocation sweeping" [40] and is shown schematically in Figure 2.15 using the example of particles in the crystal lattice.

Experimental evidence of the hydrogen transport by dislocations has been provided by Louthan et al. [63]. Evidence of the increased hydrogen concentration in a local strain field of a crack has just recently been provided by Sobol et al. by the measurement of deuterium via secondary ion mass spectroscopy (ToF-SIMS) (Figure 2.16)

Birnbaum and Sofronis [64] introduced the cracking mechanism Hydrogen Enhanced Local Plasticity (HELP) based on the interaction of hydrogen with dislocations, which describes the local excitation of the dislocation activity by hydrogen. Performing them in-situ investigations with a transmission electron microscope (TEM), they were able to determine experimentally

that dislocations migrate faster without increasing the external mechanical stress by loading the material with hydrogen. If the hydrogen is removed again, the dislocation movement slows down again. The facilitated dislocation movement is caused by a local reduction of the yield stress and thus leads to a local softening [64].



On the other hand, the authors also explain that hardening could be observed for corrosion resistant steels, and this is due to localization of dislocation glide on a few slip planes. In addition to influencing the movement of dislocations by hydrogen, the authors also noted a facilitated reformation of dislocations by hydrogen [64]. Robertson [65] investigates the effect of hydrogen on the dislocation motion and describes the interactions described (Hardening and Softening) as well as experimentally demonstrating the facilitated dislocation movement under the influence of hydrogen.

In addition to the above-mentioned effects of accelerated hydrogen diffusion, there are other effects that can contribute to a rapid enrichment of the structure with hydrogen. For example, a phase transformation can cause a supersaturation of hydrogen. This type of enrichment of a microstructure is often observed during welding [24,66-68]. The solubility in the lattice is many times greater at higher temperatures. Thus, after cooling and possibly conversion, there may be

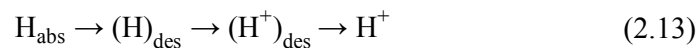
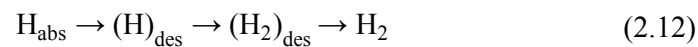
an increased hydrogen concentration which either leads to pore formation or which is trapped in a supersaturated microstructure in hydrogen traps.

Also conceivable is a phase transformation of austenite into martensite. Austenite has a higher solubility through the FCC lattice than the distorted BCC cell of the α' -martensite. In addition, martensite is more sensitive than austenite to degradation of mechanical properties by hydrogen, [69, 70] and austenite decomposition may result in hydrogen-saturated martensite.

It has to be considered with respect to the present contribution, that martensitic landing gear steels are extensively processed before application and, should be provided in the strengthened fully martensitic microstructure. However, as will be shown in the subsequent chapters, especially the S53 steel in the new as-delivered bar-stock condition contains up to 40% of retained austenite for which exactly these aspects might apply.

For a more detailed overview of the mathematical modelling of trapping and enhancement of hydrogen in metallic microstructures it is referred to the thesis of Böllinghaus [24].

The effusion of hydrogen is very important in avoiding hydrogen-assisted material damage. By releasing the hydrogen to the environment, the hydrogen in the structure can be reduced and thus the risk of hydrogen-assisted material damage can be reduced. The effusion of hydrogen proceeds in three steps in analogy to hydrogen uptake [24]. The absorbed hydrogen is transported by diffusion to the metal surface and desorbed. The desorbed, atomic hydrogen can either be released directly into the surrounding gaseous medium or recombination into molecular hydrogen takes place before desorption, as shown by Equation (2.12). When released into a liquid medium, the hydrogen on the metal surface is oxidized or ionized to release an electron, and then it can be converted into the electrolyte [24], Equation (2.13).



Also in these processes there is the possibility of recombination of the hydrogen at the metal surface according to the Volmer panel or Volmer-Heyrovsky mechanism.

The release of hydrogen into the environment, like hydrogen uptake, can be influenced by various boundary conditions. For example, desorption sites on the metal surface can be occupied by other elements, such as oxygen [71]. In addition, other factors such as surface roughness [71], temperature [72] or surface reactions leading to an oxide layer [73,74] are important for effusion. Kiuchi and McLellan [61] consider the surface as a deep trap and consider this by means of a correspondingly high activation energy for the diffusion coefficient. In addition, the surfaces may be coated with oxide or passive layers, which makes hydrogen leakage difficult [71- 74].

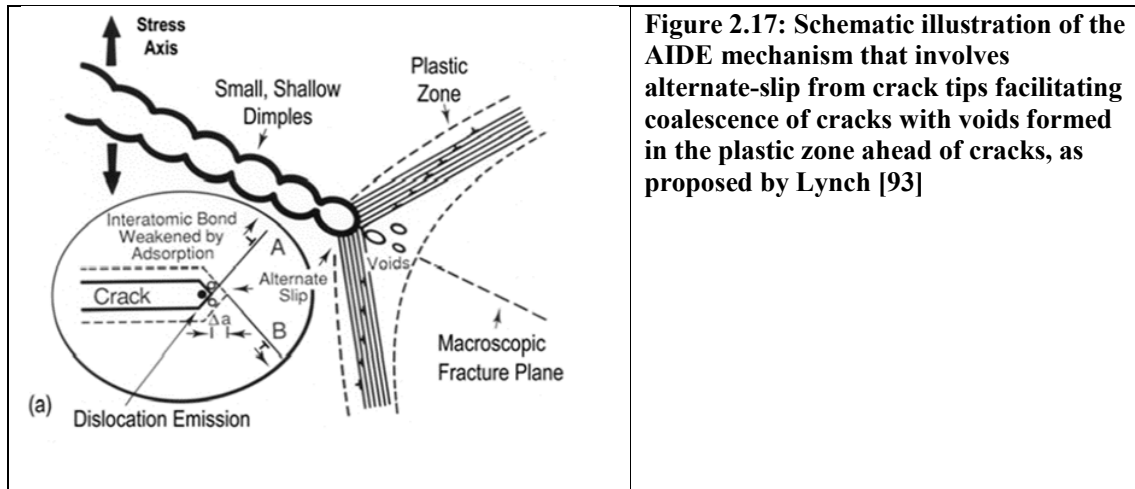
2.2.2 HAC Mechanisms

After introduction of the pressure theory by Zapfe and Sims [75] in the forties, a variety of mechanisms and theories have been proposed to explain the failure of technical metallic components at respective mechanical loads and in the presence of significant hydrogen concentrations in a specific metallic microstructure. After Hirth [23] in eighties, most of the mechanisms discussed in the past 50 years have been reviewed more recently by Robertson [76]. Interestingly, quite a few previous and old-fashioned theories and mechanisms have already been disregarded by Robertson. As already mentioned, the formation of hydrides can be excluded in the steels investigated for this contribution can also be excluded. The remaining mechanisms of proposed more recently are the following:

- Hydrogen enhanced de-cohesion [22, 77, 78-81]
- Hydrogen-enhanced localized plasticity [60, 82-85]
- High hydrogen pressure bubble or void [86, 87]
- Hydrogen-induced reduction in surface energy [88, 89]
- Hydrogen-enhanced dislocation ejection from the surface or near surface region [90]
- Hydrogen- and deformation-assisted vacancy production [91]
- Hydrogen-triggered ductile to brittle transition [75, 92]
- Hydrogen- and strain-induced phase transformations [93,94]
- Reactants and hydrogen [95]

There are still many controversies and disagreements regarding the various mechanisms. However, in the discussions around the hydrogen conferences every four years, there is a

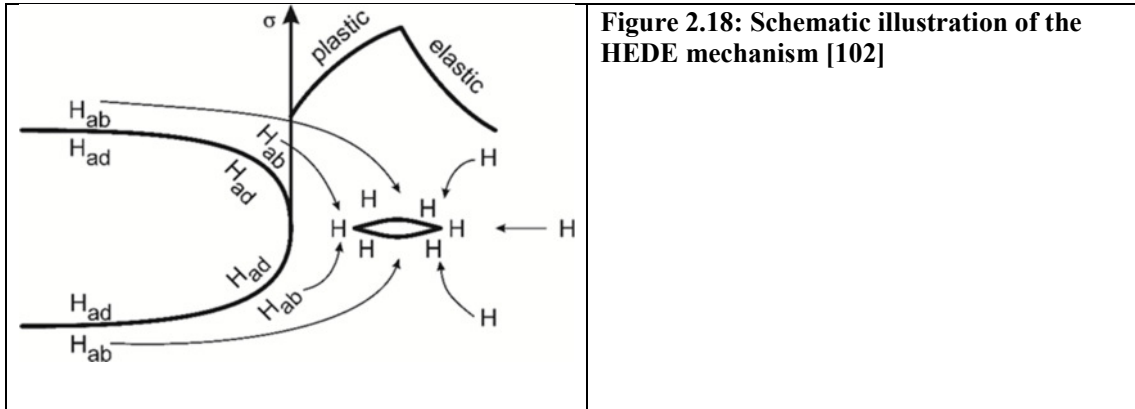
common understanding that the most important mechanisms of hydrogen assisted cracking are adsorption induced dislocation emission (AIDE) [96, 97], hydrogen enhanced de-cohesion



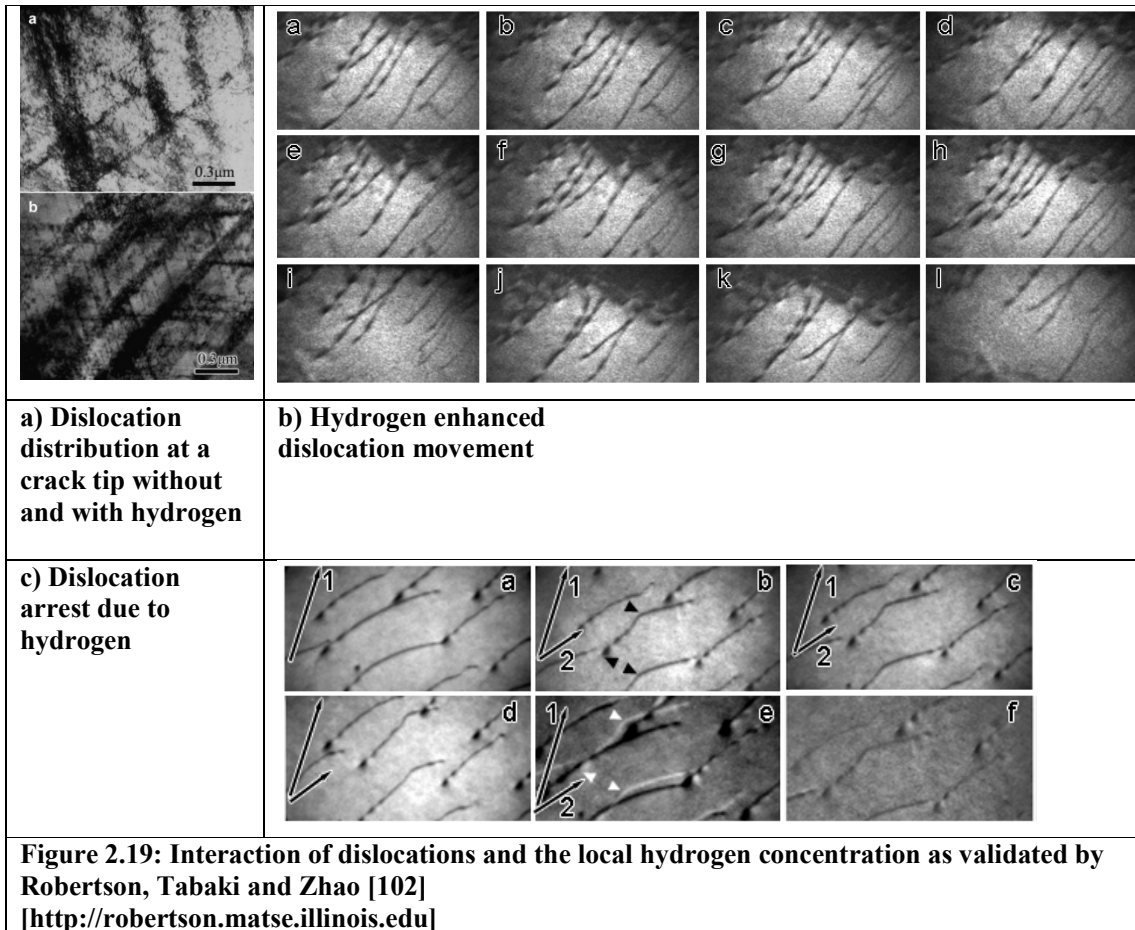
(HEDE) [77] and hydrogen enhanced localized plasticity (HELP). [70, 82, 98-101] Additional to these, in the frame of this contribution, any hydrogen related phase transformations, particularly those from austenite into martensite and perhaps the old pressure theory by Zapffe and Sims [75] has to be revisited, if it comes to the formation of so-called fish-eyes.

The AIDE mechanism has first been proposed by Lynch [93]. It is anticipated that hydrogen has to be first adsorbed near a crack tip. The adsorption of hydrogen results in subsequent formation of dislocations [110]. The formation and emission of dislocations from the crack tip affects the mechanical properties under further plastic deformation. By applying a mechanical load, the dislocations can easily move away from the crack tip. During nucleation of dislocations, a core is formed by shearing of several atomic layers. Another part of this process is the formation of micro voids ahead of the crack tip as well as nucleation and growth of voids at second phase particles. It is assumed that the process is accompanied by the absorption of hydrogen that weakens the interatomic bonds in the range of several atomic layers (Figure 2.17).

The HEDE mechanism appears to be more simplistic as had first been proposed by Troiano [60] and Oriani [36] in the 1960's, since the current existing theories were unable to explain some of the early experiments with hydrogenated samples under mechanical load. The HEDE mechanism can be described in a way that a solute hydrogen atom in the metallic matrix can



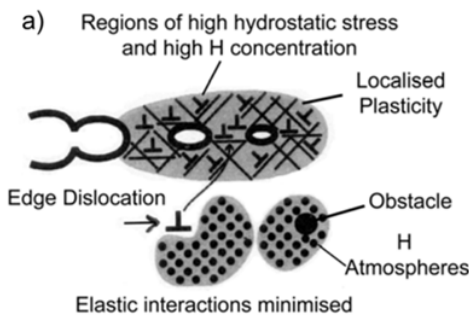
share its electron to the 3d-orbitals of the neighbor iron atoms and remain as a proton in the matrix. As a result, the electron density increases locally and the cohesive force between the metal atoms is reduced allowing the propagation of the crack under a reduced mechanical load. Figure 2.18 represents a simplified schematic illustration of this mechanism.



The HELP mechanism is based on the two contradictory hardening and softening effects of hydrogen in different alloys, reported by Nelson in 1983 [104] and was first proposed by Sirois [105] and Sofronis [79]. However, it represents the only hydrogen assisted cracking mechanism that has been at least partly proven by in-situ experiments utilizing transmission electron microscopy (TEM), as for instance by Tabata et. al. [88]. Generally, the HELP process explains the interaction of dislocations with hydrogen. It is assumed that a certain concentration of hydrogen is dissolved in front of the in the crack tip, i.e. in the region of stresses and strains concentrated ahead of the crack tip or a notch. During the emission or propagation of a dislocation by global and local strains and stresses, hydrogen can enhance locally the dislocation activity, i.e. the emission and propagation rate, at lower stresses and strains. In other words, dislocations surrounded by a hydrogen cloud will move faster than ones without it when a similar shear stress is applied on the material. To keep up such activation and to continue the propagation rate, the dislocations must carry the hydrogen with them. As a result, the local hydrogen concentration is driven by the motion of dislocations and the obtained fracture has a local ductile failure with a brittle appearance on the macroscopic scale. Tabata et al. [88] conducted several in-situ experiments by environmental TEM to compare the effect of vacuum and H₂ on a mechanically pure iron sample. These experiments showed that dislocations nucleation and movement are facilitated under the hydrogen environment.

However, hydrogen can also retard the dislocation activity and reduce the interactions between defects and precipitates. Dislocation emission and the HELP mechanism are illustrated in the Figures 2.19 and 2.20.

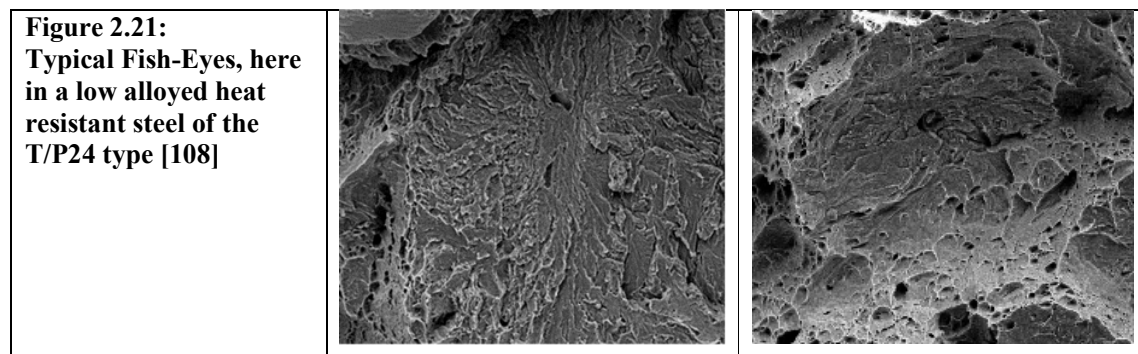
Figure 2.20:
Schematic illustration of
the HELP mechanism
[106]



In general, the HELP mechanism can be summarized in explaining softening, i.e. a hydrogen enhanced deformation of the microstructure by an increased dislocation activity with respect to

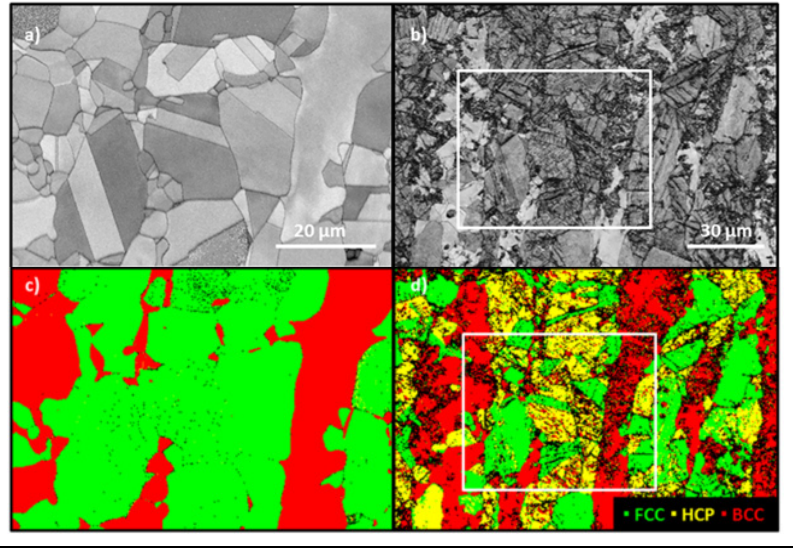
emission and propagation. It also explains a hardening effect by hydrogen, by hydrogen reducing the dislocation velocity by formation of Cottrell clouds or even blocking of dislocations and thus, hydrogen retards the deformation.

According to the old pressure theory of Zapffe and Sims, the recombination of hydrogen in a trap of metallic microstructure might cause a very high pressure that might cause blisters and cracks. Quite recently, this has been validated by Kircheim [108] and provides a specific explanation for the formation of so-called fish-eyes at precipitates and inclusions in a steel microstructure. However, fish-eyes occur normally in steels having a lower strength, as for instance because of hydrogen cold cracking of fine grained structural steels during welding (Figure 2.21).



High hydrogen concentrations in an austenitic microstructure can produce large lattice distortions and thus, might initiate a phase transformation from austenite into martensite. Two kinds of martensite can form in the austenitic phase: α' (BCC) and ϵ (HCP). It has to be mentioned that this phenomenon is also discussed controversially in the literature, but Han et al. ¹¹⁸ showed that the common austenitic stainless steels of the AISI type 304 and 316 might be subjected to a martensitic phase transformation at hydrogen charging. Much more recently, such effects by hydrogen have been observed by ToF-SIMS, HR-SEM and EBSD in a duplex stainless steel [62] (Figure 2.22). Considering that the steel S53 contains up to 40% of retained austenite, such effects by hydrogen are considered at least at this point. However, it should also be emphasized that in the strengthened condition, air plane landing gear steels are usually and should be fully martensitic.

Figure 2.22:
Martensite transformation of the austenite phase in a duplex stainless steel observed by EBSD, a), c) Before charging, b), d) After charging [62]

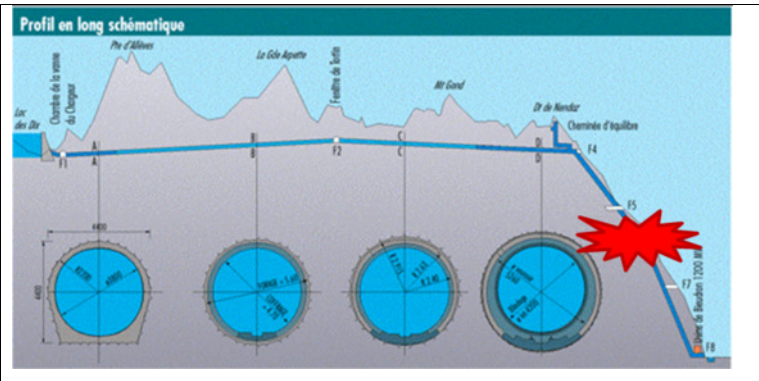


2.3. HAC in Martensitic Steels

2.3.1. High Strength Low Alloyed Steels

To achieve a considerable strength in low alloyed steels for structural applications, such steels are either quenched and tempered (QL grades) or are thermos-mechanically controlled processed (TMCP grades). While steels with a strength of up to 1000 MPa might still contain some bainite, like the S960 class, this amount is more and more reduced to further increase the strength of such steels. Usually, HSLA steels with a strength level of and above 1100 MPa are fully martensitic. After a spectacular failure case at a hydro power station in the Mount Blanc area Cleuson-Dixence near the French-Swiss border (Figure 2.23), considerable effort

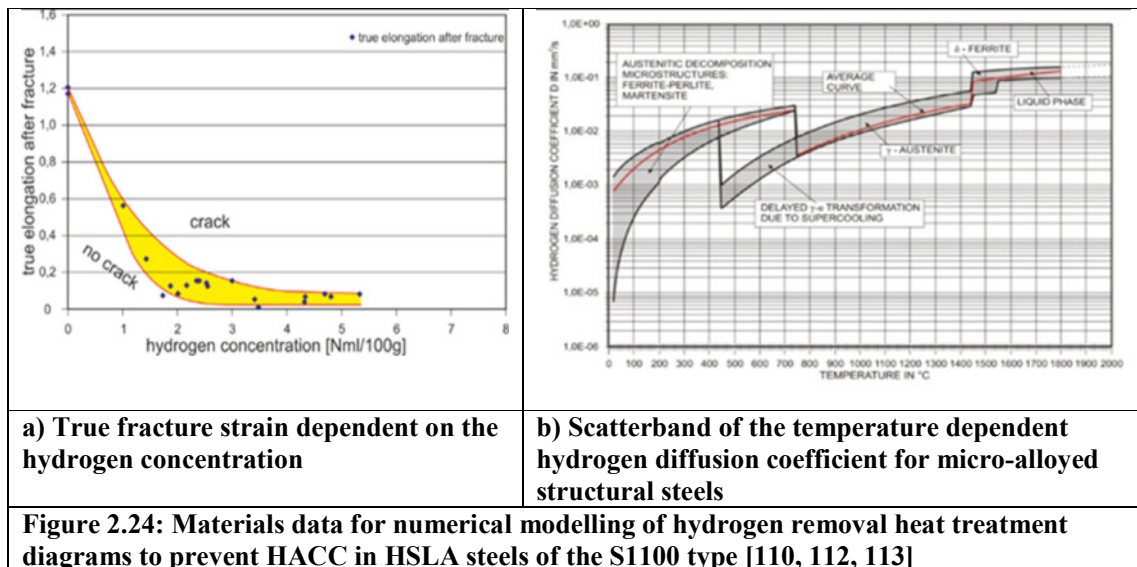
Figure 2.23:
Schematic illustration of a failure case by HAC of a welded downhill pipe at a hydro power plant in Switzerland made of the steel S890, causing several fatalities, loss of energy production and damming the river Rhone [22]



has been undertaken to particularly prevent hydrogen assisted cold cracking in such steels during welding. Steels of this type with yield strengths above 1100 MPa are increasingly

considered as materials for welded cantilevers of automobile cranes. Thus, the principal hydrogen tolerance of such steels against hydrogen dissolved in such microstructures has been investigated comprehensively. Figure 2.24a shows the hydrogen concentration dependent true fracture strain of such a martensitic structural steel microstructure and Figure 2.24b the scatter band of the temperature dependent hydrogen diffusion coefficients.

The hydrogen dependent true fracture strain has been taken as respective crack initiation and propagation criterion for respective numerical analyses to develop easy to handle diagrams for hydrogen removal heat treatment (HRHT) after welding, as a very sufficient measure to prevent cold cracking during automotive crane production, for instance. Figure 2.24a shows such a diagram for S1100 butt welds and Figure 2.24b shows various weld joint types that have been modelled for developing of such HRHT diagrams.



Parallel to HSLA steels of the structural steel series S XXXX, a series of Armour Steels has been developed in Europe. Such steels consist of a hard and high strength martensitic microstructure for improved crash, ballistic and blast threat resistance. Such steels usually have a carbon content of 0.15 wt.-% and are QL steels. Recently, welds made of such fully martensitic steels have been compared to the above-mentioned S XXXX series with respect to their blast resistance [114].

As another concept, HSLA steels in the US have been developed based on several AISI series which represent steels that are quenched and tempered (QT) to the desired strength level. This includes a wide variety of annealing or otherwise called heat-treatable steels, as for instance the typical steel AISI 4140, known in the European markets as the steel 42CrMoV (1.7225). However, in the frame of this thesis it is concentrated on the frame of this contribution on the conventional landing steel AISI 4340, known in the European markets as the steel 36CrNiMo4 (1.6582). This steel also represents a QT material, thus a heat-treatable steel that is widely applied in mechanical, automotive and aircraft engineering. It can be QT-strengthened with yield strength up to 1300 MPa. For landing gear applications in military aircraft, usually a modified and Si alloyed variant of this material is used.

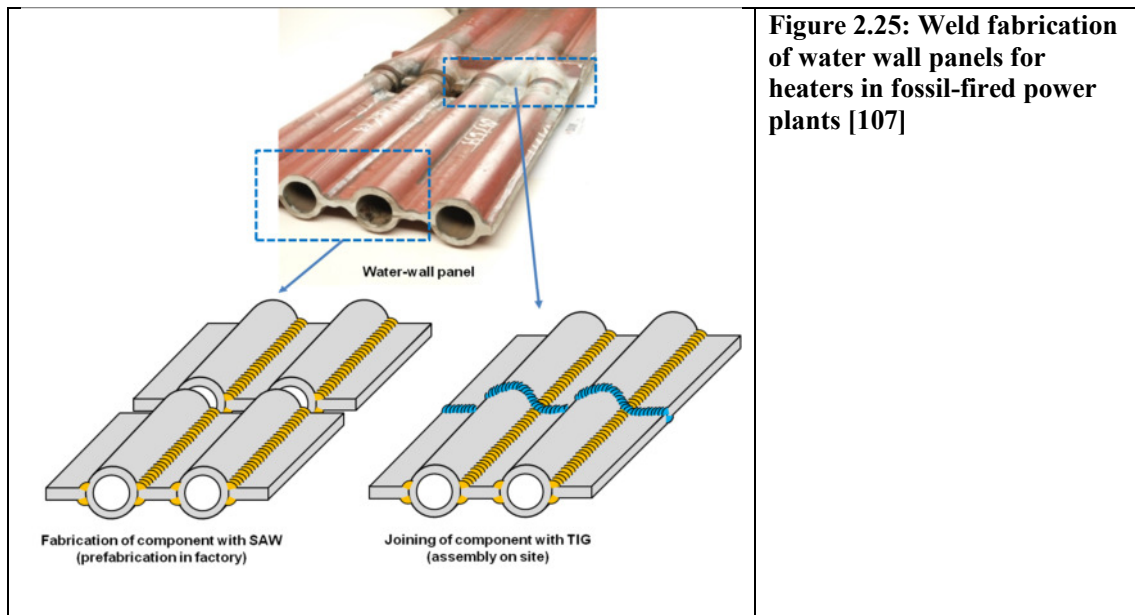
Landing gear components, with this high strength, are usually not welded to avoid any soft zones by undesired heat treatment of the high strength base materials in the heat affected zone. Another reason is that respective filler materials for such welds are usually not available in such strength categories above the 1000 MPa level. To this respect, landing gear components made of the 4340 steel and its variants will probably not be subjected to a hydrogen assisted cold cracking risk during or delayed after welding.

However, it is well known, that small amounts of hydrogen traced into the material from in aqueous environments, like from splash water already during washing, but by corrosion in Cl-containing marine applications, might entail a severe loss of ductility. For such reasons, these materials are usually given a low temperature heat cycle over a long period of time to extract any easily reversibly trapped hydrogen.

The 4340 steel variants used in the military aircraft regime consist of a strengthened and fully martensitic microstructure. Therefore, it must be ensured that such materials will not experience any risk of hydrogen assisted cracking. As it is well known that the 4340 steel is by no means corrosion-resistant, due to a far lower than 10.5 wt.-% Cr content of about 1.5 wt.-%, it is usually Cd-plated after production of the landing gear components.

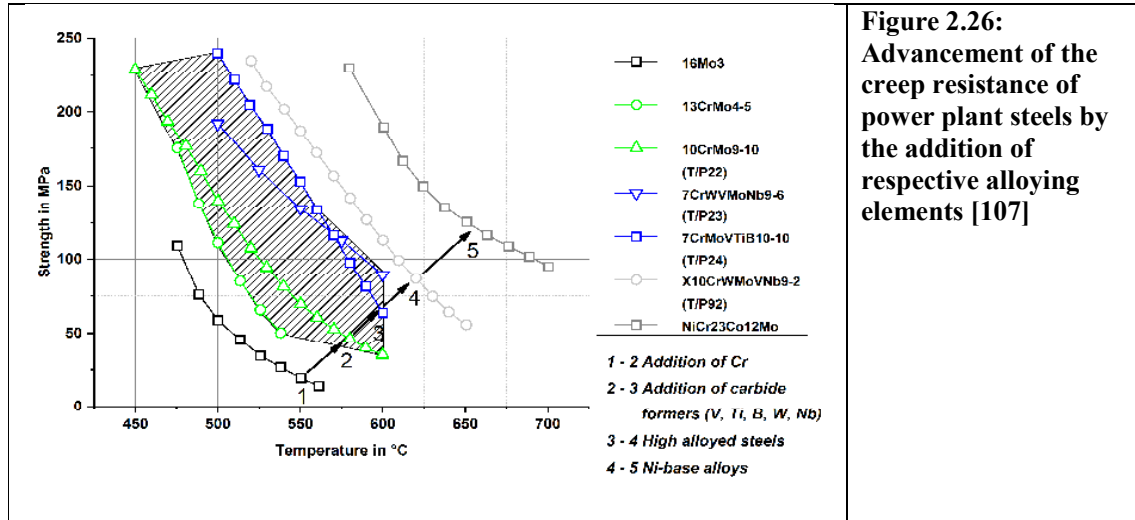
2.3.2 Heat Resistant Martensitic Low Alloyed Steels

Martensitic low alloyed steels with some heat resistance have predominantly been developed for fossil-fired power plant components. One region where these steels are applied are tube walls for the heaters, like it is shown in Figure 2.25. Parts of such tube walls are prefabricated and then assembled on-site. These low alloyed steels have a Cr content of around 9% and are predominantly applied for creep resistant parts. Such steel are more than 50 years on the market and covered usually application ranges with temperatures of up 550 °C. However, since a couple of years, in particular in the European sector, such steels experienced the greatest challenges ever since. For increased efficiency of conventional power plants, the steam parameters of the heaters were increased to about 600 °C and 290 bar. In addition, due to the development of renewable energy applications, the heaters should have been designed for temperature cycling, i.e. to tolerate many shut-down and start-up cycles in conventional power plants serving as a back-up for the renewable energy [107].



This entailed a demand for new more creep resistant steels which are named T24/P24. In contrast to previously applied grades of the T/P 22 types 10 CrMo 9 10 such new grades had a more complex alloying concept namely where 7CrMoVTiB 10 10 steels. Figure 2.26 shows the whole development of creep resistant steels in the energy sector with the final goal to get with such low alloyed variants even beyond the application range of the new 9 wt.-% Cr steels of the T/P92 (X10CrWMoVNb 9 2).

It has to mentioned that the applied steel grades have to withstand increased corrosion loads during the component life-time due to the elevated temperatures and aggressive media like high temperature steam or smoke gas.

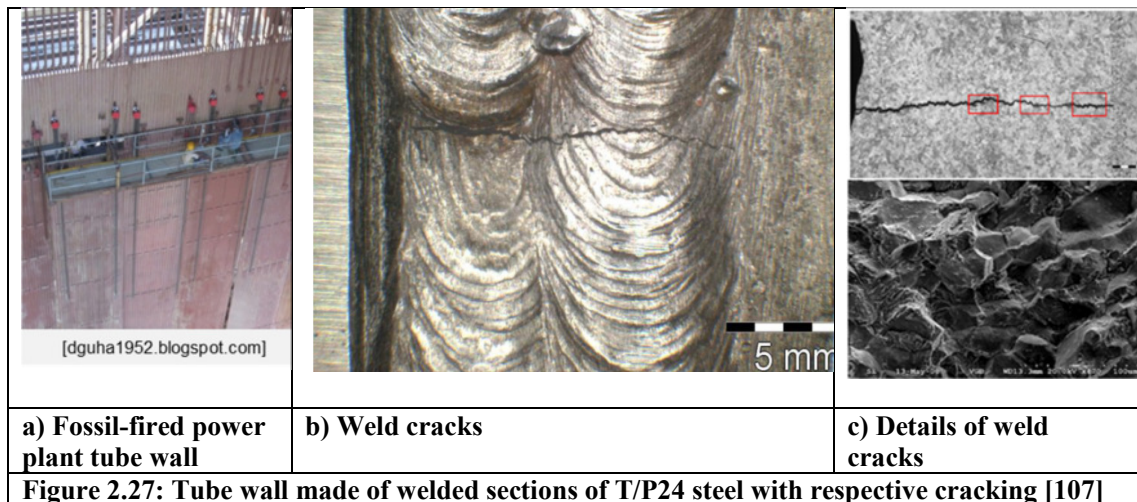


However, in case of water-wall panels the component has to face two different in-service corrosion loads at elevated temperatures. The first is corrosion at high temperatures in the combustion chamber due to forming chemical compounds in the flue gas such as H_2S [107] or SO_2 . These corrosion reactions mainly occur on the fire-side of the power plant components. The second is steam oxidization inside the tubes due to the transported hot live steam. This can result in a formation oxide layers which reduced tube thickness and increasing stress. This means that predominantly chemical corrosion resistance must be taken into account regarding the service application of such steels.

However, additionally, electrochemical corrosion in the lower temperature range ($<200^\circ C$) can occur in pressurized water in with the risk of hydrogen uptake [107]. It has also to be mentioned that additionally to the power plants, low alloyed Cr-Mo steels are applied for example in oil or petrol refining industry. In this case, the steel grades are highly prone for hydrogen uptake as example due to H_2S [107].

About 10 years ago there have been spectacular failure cases all over Europe with respect to the start-up and first-time application of T/P24 steels in the elder fossil-fired power plant

generation. The steels were used for the welded heater tube walls replacing conventional boilers for advanced pressures and higher temperatures. However, extensive weld cracking appeared, some time with thousands of cracks in one tube wall, in the years between 2008 and 2012. It turned out that such failures only occurred in plants where the tube walls had been cycled several times and much undesired in the lower temperature regime ($< 200\text{ }^{\circ}\text{C}$). Therefore, the failure of the tube walls was predominantly HASCC due to hydrogen uptake in aqueous environments without the chance to build up a protective hematite layer on the tube walls by starting-up these sections quickly through the lower into higher temperature regimes. Instead, the cycling through the lower temperature regimes entailed production of high hydrogen amounts at the surface due to the non-complete hydrolysis and formation of a dense hematite layer on the surface (Figure 2.27).



Detailed studies have been thus undertaken to compare the principal HAC resistance at lower temperatures in aqueous environments of the new T/P24 generation with the conventional steels of the T/P22 type, by which the new tube walls have immediately been replaced. These revealed a significant ductility loss, if hydrogen is present in the steel microstructure, independent of the steel grade. For comparison, Figure 2.28 shows the fracture topographies and hydrogen concentration dependent true fracture strain as well as the tensile properties for both base materials, i.e. the T/P22 and the T/P24 grade [22]. While the tensile properties, yield strength and ultimate tensile strength have been less affected by hydrogen, evidently the true fracture strain is very much decreasing at already considerably low hydrogen concentrations in 1 to 4 ppm range. The fracture topography also turns from ductile MVC to a brittle transgranular

cleavage-like mode with increasing hydrogen concentrations. Interestingly the conventional steel T/P 22 showed a significantly lower ductility in terms of the true fracture strain at hydrogen concentration levels of and above 2 ppm. While the new steel T/P24 still showed a

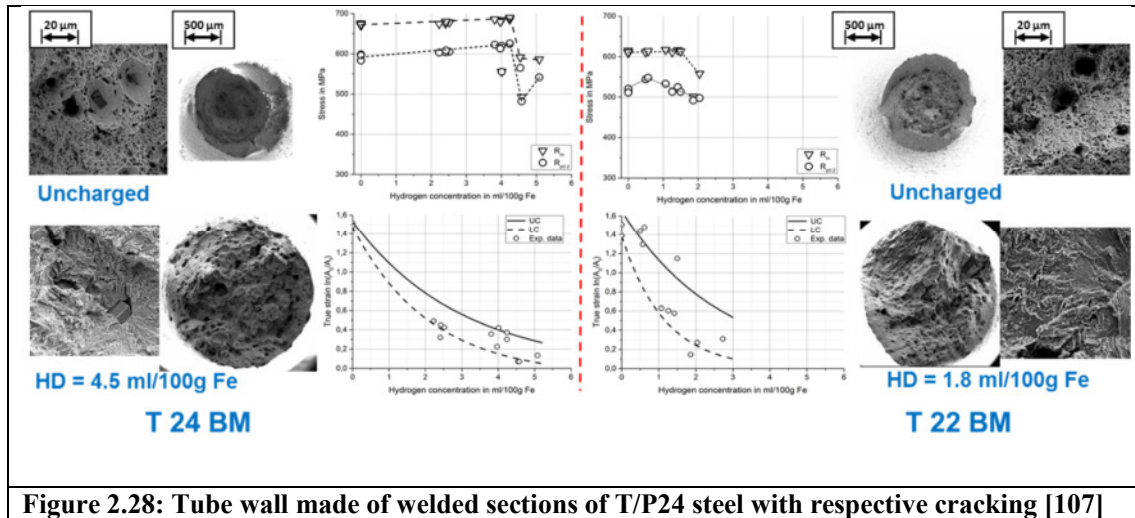
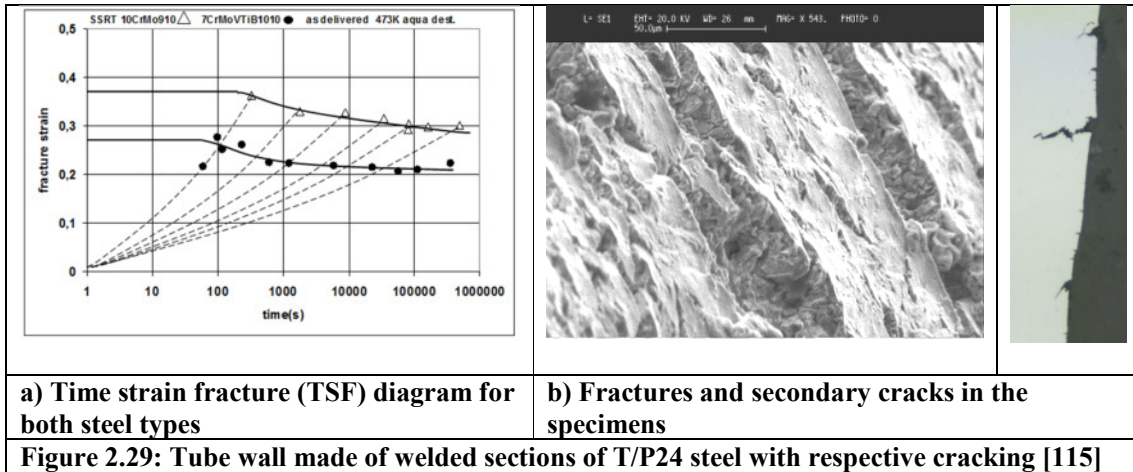


Figure 2.28: Tube wall made of welded sections of T/P24 steel with respective cracking [107]

true fracture strain of about 0.4 at 2 ppm hydrogen dissolved in the microstructure, the steel T/P22 showed only values of about 0.2 to 0.3.

Such hydrogen dependent material properties represent very valuable crack criteria also for numerical modelling of HAC and for respective life time assessments of technical components. However, in addition to the determination of such hydrogen dependent material properties, also slow strain rate tests (SSRT) with both base materials have been carried out in water at 200 °C in distilled water, in order to simulate the materials behavior in most realistic environments. Figure 2.29a shows the respective time strain fracture diagrams for both steels. The new steel shows a lower tolerance with respect to the total strain level in such environments. However, the ductility loss with respect to the gradient of the fracture strain with increasing exposure and loading time is much higher by the elder steel T/P22. Figure 2.29b just shows some cracks and side cracks of a respective SSRT specimen of the T/P24 steel. In total the fracture topographies were very similar to those observed at original failure parts which emphasizes that SSRT in such environments are quite realistic tests. Additionally, crack chemistry modelling then confirmed that hydrogen is introduced into the materials during start-up at temperatures up to 200 °C without establishment of a stable magnetite layer on the surface. This together confirmed also that the failure phenomenology is HASCC in such materials at lower



temperatures and by no means any SCC by slip dissolution or some else not verified but frequently proposed damage mechanism [115].

The results also show that the steel T/P24 is more tolerant to environments providing the conditions for hydrogen uptake than anticipated and does not comply with such a high ductility loss as the steel T/P22. This means that the replacement of the T/P24 steels in the fossil-fired power plant heaters by the previous steel T/P22 was not necessary.

In general, it should be concluded from these considerations that new advanced materials are sometimes blamed wrongly when the real failure root represents a wrong service operation. the replacement of an advanced steel after the first failures should not happen without a decent failure and material investigation [22].

Among the heat-resistant martensitic Cr steels, also 9% Cr steels of the type P91 must be mentioned, although such steels have usually a ferritic-martensitic and mainly not a fully martensitic microstructure. They might also contain about 1 wt.-% Mo. Marchetti et al. [116] investigated the influence of specific hydrogen concentrations on the mechanical behavior of such steels with SSRT and found that the brittle topography on the fracture surface strongly depends on the sub-surface concentration by which hydrogen is entering the material. They also assume hydrogen dislocation interactions.

2.3.3 Martensitic 9 wt.-% Ni Steels

The natural change from ductile to brittle behavior through a temperature range characteristic of most ferritic materials prevents their use below approximately -101 °C. Thus, martensitic low-carbon 9 wt.-% Ni steels have been developed to maintain a sufficient ductility, as for instance for pressure vessels. Such steels have been recognized by the ASME Code for cryogenic applications since 1954 and has been widely used for storage of oxygen, nitrogen and other liquefied gases in competition with other stainless steels, especially austenitic stainless steels. 9 wt.-% Ni steels are also heat-treatable and thus, belong to the category of martensitic QT steels. [117]

However, such steels might be extremely prone to hydrogen assisted cracking, in particular HASCC, if subjected to H₂S-containing environments. Investigations of such steels have been carried out by Vollmer [118] and they found out that their cracking resistance in sour service applications can only be improved by reduction of the hardness. Such general proposals have later been expounded upon by Bowers et al. [119], who excluded the hardness of a steel as a criterion to assess the susceptibility against hydrogen assisted cracking. The latter must be regarded as one of the most important findings with respect to standardization. However, to improve the HAC-resistance of 9 wt.-% Ni steels, the authors suggest increasing the Ti content, since this element suppresses the development of non-annealed martensite in the respective microstructure. Also, an addition of Mo might improve the HAC-resistance. The proposal by Vollmer [118] that cold deformation of such steels is increasing the susceptibility for HAC has not been supported by Bowers et al. [119] who also underwent the dilemma suggesting a strength reduction instead an improved ductility for a better HAC resistance. Following Hudgins [120], the susceptibility of 9 wt.-% Ni steels can be reduced at higher temperatures, since their ductility is increasing and other electrolytic reactions take place with H₂S.

2.3.4 13% Cr Martensitic Stainless Steels

Martensitic stainless steels with a Cr content of around 13 wt.-% have particularly been developed for oil and gas production. These materials can be divided in conventional variants with a medium and higher carbon content and low carbon (LC) to extremely low carbon (ELC) types with a Ni content of up to 6.5 wt.-% and a Mo content of up to 2.5 wt.-%.

Conventional 13 wt.-% Cr steels have been used since the 70ies on- and offshore for down well applications and also for tubes and pipelines, in many applications also welded. However, immense service experience is existing regarding this type of steels. Also, spectacular failure cases have been reported from the oil and gas fields in Canada, Texas, and the Gulf of Mexico [121-124]. It is thus well-known that components made of such materials might fail by HAC under sour service applications, thus predominantly HASCC. The sour service resistance and the respective HASCC resistance of 13 wt.-% Cr steels has thus been investigated embracingly, specifically by small scale go-no-go tests like the constant load test or the C-ring test [125].

Additionally, it is well-known that the high strength variants of this steel type might suffer from HAC even in H₂S-free environments [129]. Some of those failure cases have been reported by Alkire and Ciaraldi [123] who also recommend a hardness limitation of such steels. According to Hudgins [128] and Tanimura [130], conventional 13 wt.-% Cr steels might become even more prone than low alloyed martensitic steels.

However, Bonis and Crolet [126] confirm, based on 16 years of experience, that 13 wt.-% Cr steels are more resistant against cracking in sour service environments than originally expected. Generally, a recommendation to reduce the hardness of such materials below 22 HRC is existing [127], but this is based on laboratory tests and, does by no means account for the mechanisms of HAC [119]. No need to emphasize that such reduced hardness levels may never be achieved for landing gear steels, regardless which type of martensitic steel would be selected. However, the recommendations by others to increase the Cr content to improve the HASCC resistance of such steels is important to be considered also for landing gear applications of any type of Cr-containing high strength steel. According to Hudgins [128], an improvement of the HASCC resistance is achieved by increasing the Cr-content to 18 wt.-%. As reason it is proposed that Cr reduces the hydrogen diffusivity in such materials what has been confirmed elsewhere. [52] Also by Asano et al. [131] it has been assumed that the hydrogen interactions with dislocations are increasing at increased Cr contents and that this might reduce the HAC risk. At the same time, Hudgins [128] proposed that an increased Cr content might entail a lower hydrogen concentration offered at the surface, since it is produced less during the corrosion reactions. However, this does by no means correlate to the mechanisms of pitting or crevice corrosion where a huge amount of hydrogen ions is produced by respective hydrolysis in the propagated state.

In this context, Treseder [121] found out that an increasing Cl concentration in the environment might cause a higher susceptibility to HASCC of 13 wt.-% Cr steels, in contrast to low alloyed steels, since the passivation of the high alloyed martensitic Cr steels will be reduced significantly by Cr ions in the aqueous environment. It can only be emphasized at this point that 13 wt.-% Cr steels are by no means prone to intergranular corrosion in Cl environments. Particularly not in the annealed state due to a very dense mesh of Cr carbides distributed alongside the martensite laths and, to a lower extent, alongside the former austenite grains [24].

Highest HASCC susceptibility exists for this type of steels in the quenched state [129] and thus, they are used predominantly in the quenched and tempered state. Annealing twice at 607 °C and 677 °C significantly improves the HASCC resistance as reported by Kane et al. [132], also showing the hardness and the strength of such materials does not correlate directly with the HASCC resistance.

Ishizawa et al. [140] claim that the formation of coarse globular carbides increases the HASCC resistance of particularly the type AISI 420. This is confirmed by Klein [133] who found a higher HASCC resistance of the steel AISI 420 versus the steel AISI 410 when the yield strength is restricted below 621 MPa. Tanimura [140] claims that such better resistance of the steel AISI 420 is caused by a formation of finer grains and that the carbides reduce grain growth during production.

Since such steels completely transform into martensite, the HASCC resistance is nearly not influenced by the cooling rate during production [133,134], but by the height of the (re-) austenization temperature. Vitale and Ebert [134], for instance, found out that the steel AISI 410 has a much finer grain size, if austenized at 900 °C instead of 982 °C and thus has a significantly improved HASCC resistance.

The results by Watkins and von Rosenberg [135] as well as of Yoshitake et al. [136] showed drastically that high alloyed martensitic stainless steels with 13 wt.-% Cr have to be subjected to a suitable heat treatment after welding to improve the HASCC resistance of the weld to that level of the base material.

Intergranular HASCC is a classic example for a combination of anodic metal dissolution and hydrogen assisted cracking of this steel types. Among others, this has been shown by Turnbull et al. [101] in respective slow strain rate tests (SSRT). They found intergranular fracture topographies with early onset pitting and crack propagation alongside the former austenite grains, while towards the specimen center this fracture topographies changed more towards transgranular fracture. Such fracture behavior has been confirmed by many others, among those Ishizawa et al. [140] and Gonzalez-Rodriguez et al. [139]. Ishizawa et al. [140] also remarked that the intergranular fracture depends on the size of the former austenite grains. Also at real components such transgranular HASCC has been observed. It has to be assumed that the intergranular crack propagation is favored by the oxygen, pH value and potential depletion inside the propagating crack, often initiated at a pit and acting as propagating crevice [24]. This phenomenology of HASCC in martensitic stainless steels of the 13 wt.-% Cr types has been widely investigated and meanwhile, there is a common agreement that even in oxidizing environments immediately after a passive film breakdown pitting corrosion might be initiated which then turns also quickly into HASCC, due to the separation of the anodic and, in particular, cathodic partial reactions in the pit from those of the bulk solution, causing respective hydrogen production inside the pit that is absorbed in the surrounding microstructure. This type of pitting and subsequent HASCC can occur even in non-sour service, but Cl containing solutions, i.e. in marine environments. It has also to be emphasized in this context that El Shawesh and El Agdel [141] have provided quantitative results showing that the ductility of these steels is reduced, if a cathodic potential is applied in marine environments, i.e. if these are cathodically protected.

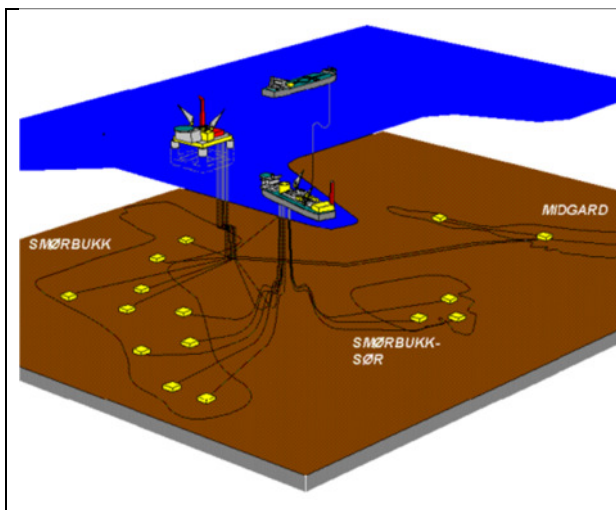


Figure 2.30: Schematic illustration of the AASGARD Field in the North Sea for application of supermartensitic stainless steels as flow line material [24]

Newer supermartensitic stainless steels (SMSS) represent advanced 13 wt.-% Cr steels which are alloyed with Ni up to 6.5 wt.-% and Mo up to 2.5 wt.-%. For better weldability and ductility, the carbon content of such steels is reduced to below 0.02 wt.-% (LC – low carbon) and to below 0.01 wt.-% (ELC – extra low carbon). These materials have increasingly been applied as materials for welded flow lines in the oil and gas fields of the North Sea since the mid 90ies [142], as shown in Figure 2.30. The materials have extensively been investigated with respect to their HASCC in mild sour environments and most of the results of the over 50 studies reported in literature are based on small scale go-no-go tests and have been assigned to the diagrams in Figure 2.30. In the diagrams all relevant investigations up to the end of the 1990s have been compiled which were carried out in up to 10% NaCl solutions at a constant load between 80 and 100% of the yield strength, pressures of up to 10 bar and room temperature. Literature results of SRRT are separately exhibited.

It can be summarized that a change in the CO₂ portion in the solution at H₂S presence is only directly effective with respect to the result by just reducing the pH, but is not influencing the phenomenology of HASCC. However, although the specimen types are very different, the results show a clear tendency. The diagrams confirm that the tolerance fields of *Non- Sour Service* for low alloyed steels is matched by SMSS which are also partly resistant to HASCC in slightly sour service.

However, subsequent SSRT of SMSS evidently showed that SMSS might fail under sour service conditions by two specific sequences [24]. Both sequences with respective fracture topographies have been assigned to the Figure 2.31. Sequence 1 can be described as a total sulfide film coverage on the specimen surface. By the sulfide film formation at lower pH in severe sour service, hydrogen ions are produced that can be directly introduced into the material. The SSRT specimen showed a very small ductility, if at all. The fracture topography has been usually starting intergranular at the outer surface and became more transgranular towards the center of the specimen. No ductile dimple fracture by micro void coalescence (MVC) has been observed. The potential during such tests was fairly at -500 mV-SCE.

As a second sequence, pitting has been developed on the specimen surface at somewhat higher pH. In this context, it must be considered that the bulk potential was still quite low and ranged between -100 and -300 mV-SCE.

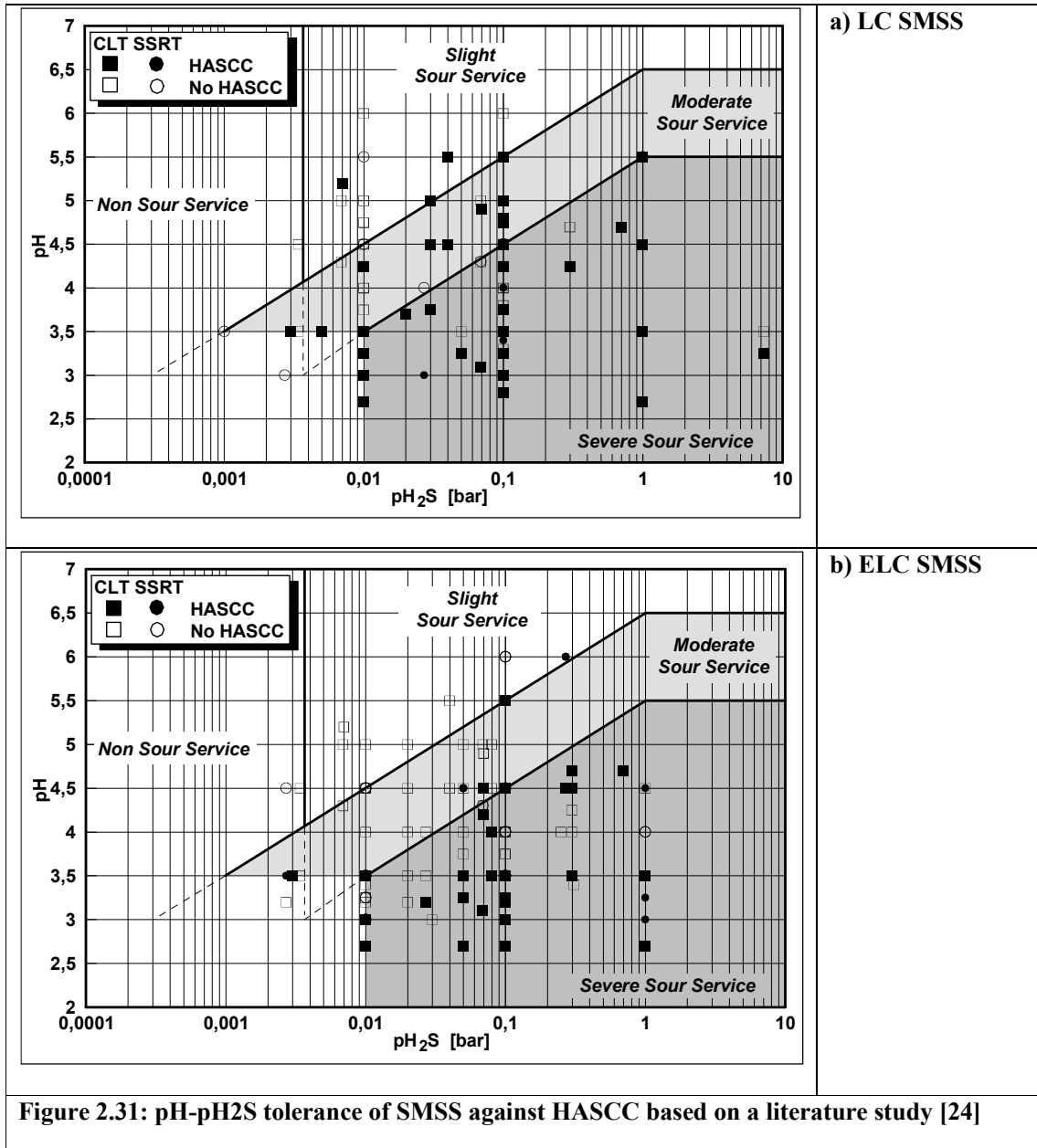


Figure 2.31: pH-pH₂S tolerance of SMSS against HASCC based on a literature study [24]

However, HASCC always was initiated inside the pits which turned black by a sulfide film inside, indicating a similarly low pH as observed for the first sequence (Fig 2.32). Cracking

usually started from inside the pit then also intergranular and then turned into transgranular cracking and finally, the ligament shows some shear dimples or even MVC.

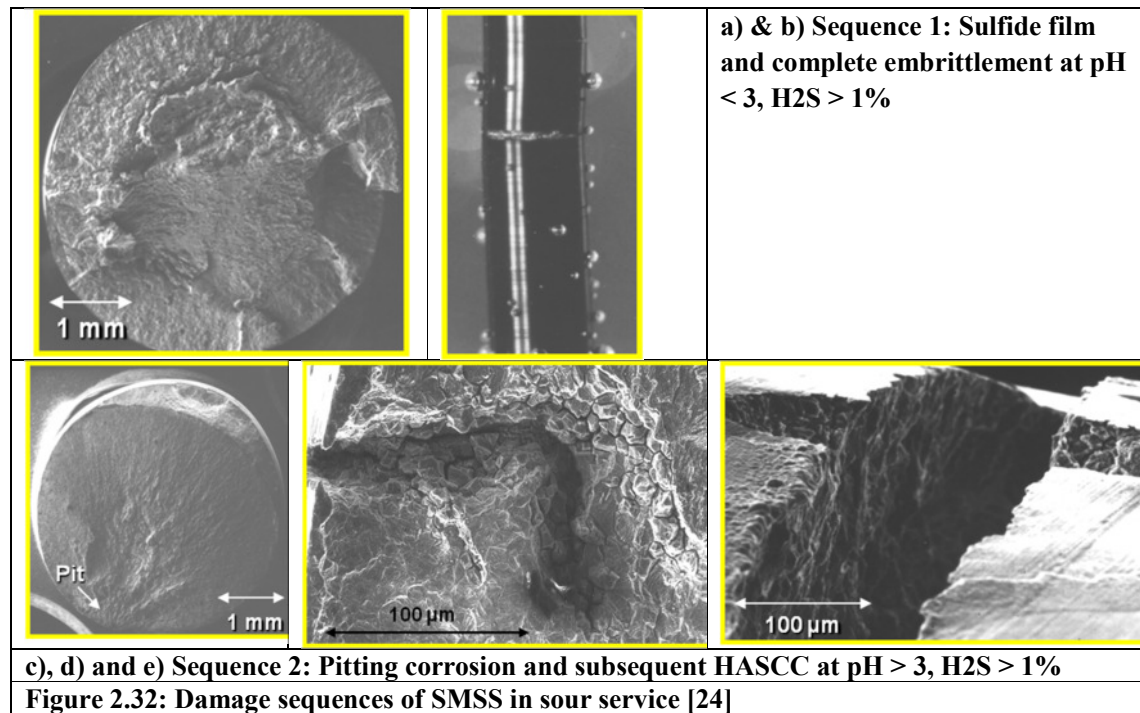
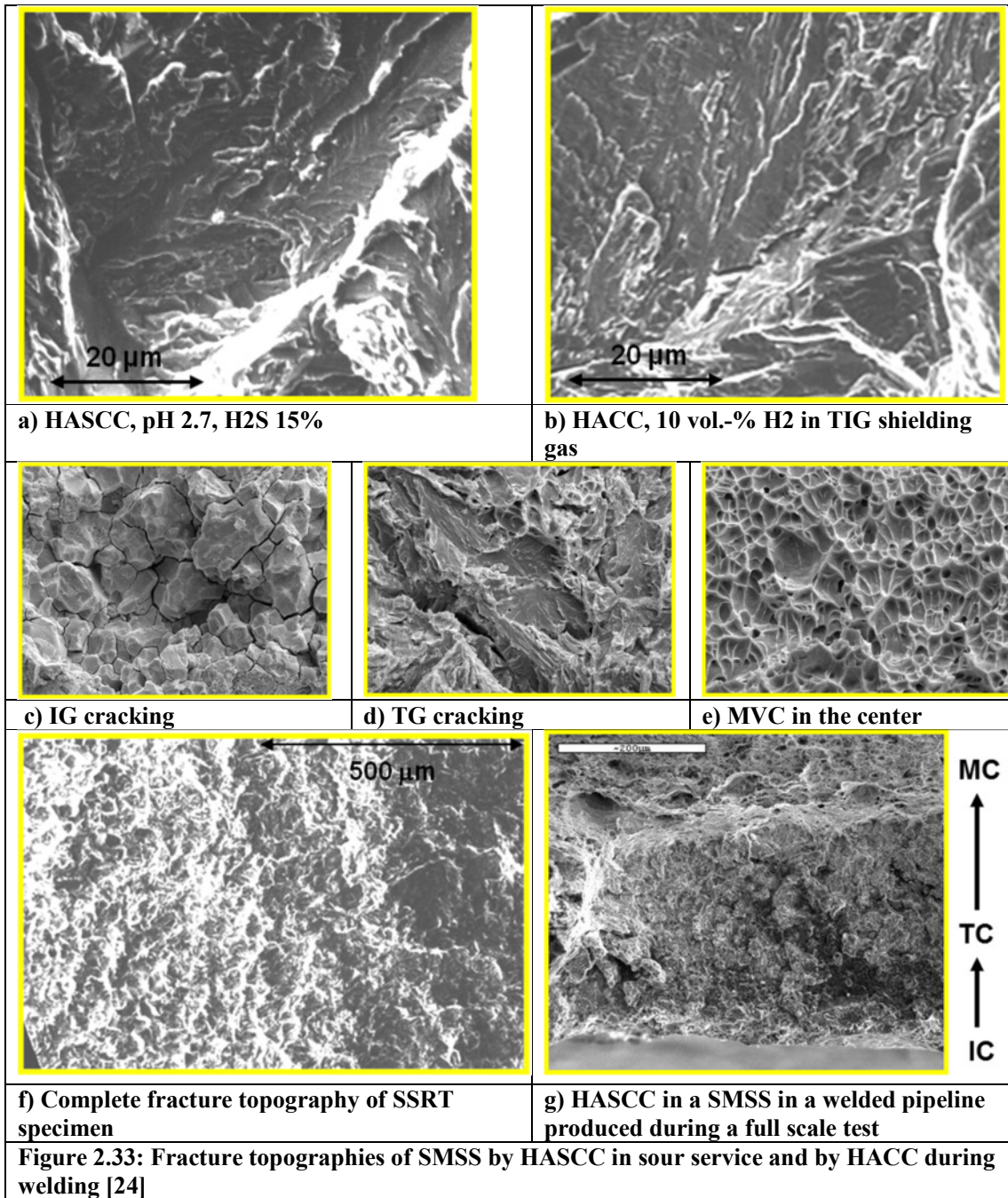


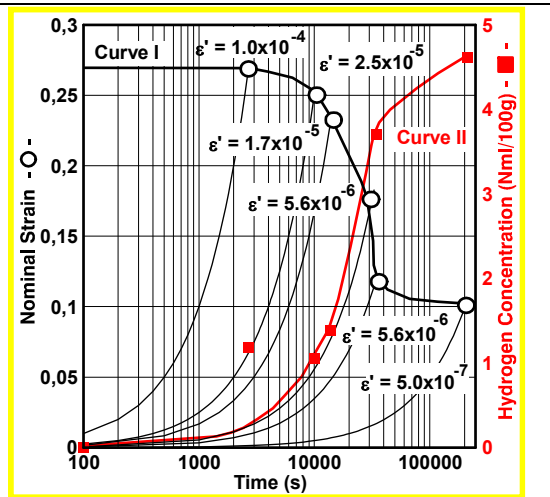
Figure 2.33 shows some typical fracture topographies for SMSS tested in full scale tests, but also by SSRT and during welding. From a comparison of the Figures 2.33a and 2.33b it becomes very clear that the fracture topography occurring by HACC during welding and by HASCC in sour service is quite similar and is exhibiting transgranular fracture of the quasi-cleavage type. This means, as in any kind of martensitic steel, that the fracture topography is only dependent on the hydrogen concentration in the microstructure, but not by the way how the hydrogen entered the microstructure. As shown by the Figures 2.33c to 2.33e, hydrogen assisted cracking in such materials always developed from intergranular cracking at relatively high hydrogen concentrations at the specimen or sample margins towards transgranular mostly cleavage-like cracking with increasing crack length and stresses and strains in the vicinity of the crack tip favoring cleavage towards ductile dimple-like cracking by micro void coalescence at low hydrogen concentrations or under no presence of hydrogen.



A typical evaluation diagram for the resistance of a material against HASCC is represented by so-called time strain fracture diagrams, as shown in Figure 2.34. In such diagrams the nominal or technical strain at fracture is plotted versus the time to fracture. It can be seen from such diagrams that a sufficiently low strain rate should be applied in the SSRT to show a degradation of the ductility in terms of the fracture strain by hydrogen. As shown by Figure 2.34, at high

strain rates of 10^{-4} s^{-1} , no reduction of ductility takes place, while at sufficiently low strain rates below 10^{-6} s^{-1} , evidently this strain is not any more reduced. Parallel, the hydrogen concentrations measured as an average in the gage length of the specimens is increasing. The connection of the various points is giving the failure curve of the respective local microstructure. Such diagram also allows a rough assessment service life time assessment. If the accumulated strain in a HAC relevant region in a real component having is exceeding the failure curve for the same microstructure, a risk for HAC is provided, if hydrogen might be taken up in the same or a similar environment.

Figure 2.34: Typical time strain fracture diagram for a SMSS subjected to 1% saturated NACE TM 0177-96 solution [24]



2.3.5 Precipitation Hardening Martensitic Stainless Steels

Precipitation hardening steels have been developed for applications especially in the mechanical engineering and aerospace sector as high-performance material for gears, valves and other engine components, high strength shafts and also to some extent as turbine blades or molding dies or even nuclear waste casks. A special application of these materials are pump shafts and wells for off- and onshore multiphase pumps in oil- and gas production as well as in geothermal power.

Precipitation hardening steels contain Cr and Ni to provide an optimized property range. Like the conventional martensitic Cr steels and SMSS, they can be heat treated to achieve high strength levels at a good corrosion resistance. The high tensile strengths of precipitation hardening stainless steels are achieved, if the martensitic microstructure has a number of precipitates after the heat treatment. Hardening can be achieved by addition of Cu, Al, Ti, Nb

and Mo. The most well-known precipitation hardening steel is the steel 17-4 PH which has about 17 wt.-% Cr and 4 wt.-% Ni. It also contains about 4 wt.-% Cu and 0.3 wt.-% Nb. The advantage of such steels is that they are supplied in a solution heat-treated condition which is quite well machinable. After fabrication of the respective parts, the material single heat-treatable to increase the strength of the material. This is known as ageing or age-hardening. As it is carried out at low temperature, the component undergoes no distortion. Precipitation hardening steels are categorized into three groups based on their final microstructures after the heat treatment, i.e. martensitic (17-4 PH), semi-austenitic (17-7 PH) and austenitic (A-286). Only the martensitic alloys are taken into consideration in the frame of this contribution. They have predominantly an austenitic microstructure at annealing temperatures of around 1040 to 1065 °C. Upon cooling to room temperature, they undergo a transformation that changes the austenite to martensite. Precipitation hardening martensitic Cr steels might also become prone to HAC in certain aqueous environments, particularly in sour service conditions. Several failure cases have been reported regarding a precipitation hardening steel with up to 17.5 wt.-% Cr and up to 5.5 wt.-% Ni, however, at severe sour service conditions. Vitale [134] indicates that also the Cl concentration in the environment has a significant influence on the HAC risk of these steels. Also in H₂S-free marine environments, these steels can be cathodic protected only within a very limited potential range, due to their HAC-susceptibility.

2.3.6 High Alloyed Ni Steels (Maraging Steels)

Into the group of high alloyed martensitic steels fall also martensitic steels that contain up to 25 wt.-% Ni, 8 wt.-% Co and 5 wt.-% Mo. The yield strength of such alloys is shifted by precipitation hardening in such alloys up to 2200 MPa, based on the precipitation hardening with Ni₃Mo or Ni₃Ti. These maraging steels also might become prone to HAC, specifically to HASCC in aqueous solutions Phelps [24], in particular in marine environments, if their yield strength is increased above 1700 MPa by respective heat treatment. Marsh and Gerberich [129] emphasize that HASCC is one of the main damage phenomena for such materials which are, however, less HAC susceptible than low alloyed variants having a similar strength, as for instance the steel 4340.

The addition of Co leads to a reduction of the former austenite grain size and thus, improves the resistance against HAC [129]. Crack propagation rates increase with decreasing annealing temperatures in such materials. The chemical composition on the grain boundaries also

influences the type crack propagation, which might be either transgranular at higher precipitation or intergranular at lower precipitation temperatures [129]. Welds have been identified as to be HAC susceptible in the weld metal with cracks usually arrested in the base material by Phelps [24].

2.3.7 High Alloyed Martensitic UHSS for Military Aerospace Applications

High strength steels with high corrosion resistance have been in continuous development since 1960's. Most of the materials developed during these years were refined to a higher performance level from a previous alloy by slight changes to the chemical composition or by a change in the industrial processing and then testing was performed on them. The development process was very Edisonian, fundamentally. Alternately, the development of these steels has become much more refined and applications based with the advent of computational material design.

2.3.7.1 Chemical Compositions and Characteristics

AerMet 100

C	Co	Cr	Ni	Mo	Fe
0.23	13.40	3.10	11.10	1.20	Bal

AerMet® 100 is a alloy that has been designed to have properties of excellent hardness and strength combined with exceptional ductility and toughness. AerMet 100 is used in applications that require high fracture toughness and excellent resistance to stress corrosion cracking and fatigue. After heat treatment processing, AerMet 100 has a lath martensite matrix with a nano-scale dispersion of strengthening carbides and a very small amount of precipitated austenite due to cryogenic processing.

Ferrium M54

C	Co	Cr	Ni	Mo	W	V	Fe
0.30	7	1	10	2	1.3	0.1	Bal

Ferrium M54 was designed as a lower-cost, drop-in replacement for AerMet 100. While not a corrosion-resistant alloy, M54 does offer a unique combination of very high toughness

and ultra-high-strength for industrial applications such as where 4340 is currently used. TEM characterization by Wang *et al.* indicates that the general microstructure of Ferrium M54 is near-identical to AerMet 100. The matrix is comprised of lath martensite with an average width of 0.1 – 0.25 μm [75, 2].

Ferrium S53

C	Co	Cr	Ni	Mo	W	V	Fe
0.21	14	10	5.5	2	1	0.3	Bal

Ferrium S53 is a new computationally-designed, ultra-high strength steel that provides significantly greater strength, corrosion resistance, SCC resistance, and corrosion fatigue resistance than existing alternative steels such as 4340 and 300M. It provides: much greater resistance to general corrosion and to stress corrosion cracking (SCC); excellent resistance to fatigue and to corrosion fatigue; and high hardenability. Its resistance to general corrosion is similar to that of 440C stainless steel, but it has much greater fracture toughness. S53 steel is double vacuum melted (i.e., vacuum induction melted and then vacuum arc remelted or "VIM/VAR") for high purity, leading to much greater fatigue strength [2].

Custom 465

C	Co	Cr	Ni	Mo	Ti	V	Fe
.02 max	-----	11	10.75	0.75	1.50	-----	Bal

Custom 465 is a premium melted, martensitic, age-hardenable stainless steel alloy. This material was designed with improved tensile strength, fracture toughness and improved fabricability and excellent resistance to stress corrosion cracking. It has been used in the medical industry, oil and gas drilling, aerospace components, marine equipment, firearms and hand tools [2].

Ferrium PH48S

C	Co	Cr	Ni	Mo	Ti	Al	Fe
-----	7.0	11.5	9.0	1.4	0.6	0.4	Bal

Ferrium PH48S, a castable and forgeable corrosion-resistant high strength steel designed to offer increased toughness and stress corrosion cracking (SCC) resistance as compared to

commercially available stainless steel alloys. A goal of this military contracted material, was to replace cast titanium components with cast stainless steel components for section thicknesses up to 3” and reduce dissimilar metal connections, with the benefit of lower costs at equivalent specific strength compared to titanium. It had proven to have substantially higher resistance to stress corrosion cracking and hydrogen assisted cracking over Custom 465 [2].

2.3.7.2 Heat Treatment Techniques

Vacuum oil quenching offers various environmental and economic benefits over traditional hardening techniques in controlled atmosphere furnaces. Ideally, the vacuum furnaces are leak tight, which assures surface chemistry is precise and the decarburization and high-temperature oxidation problems often associated with traditional controlled-atmosphere heat treating can be minimized. This technique also allows producers of aircraft landing gear to finish machine critical surfaces on these components prior to heat treating. This in turn, reduces final machining costs when the part is in the hardened condition.

A significant reason that the high alloyed materials perform so well in the “used component” service-applied condition is that the material is very carefully heat treated, as per Table 2-4, and tempered to precisely attain the hardness, strength and microstructural qualities that are required for application.

	Form	Austentization	Temper	Yield Strength	Ultimate Tensile Strength	Hardness RH _c
Aermet 100	15 cm Ø Forging	885°C 1hr / OQ / LN ₂	482°C 5 hr	1725	1965	54
Ferrium M54	1.4 cm Ø Bar	1060°C 1hr / OQ / DI	516°C 10 hr	1720	2020	54
Ferrium S53	1.4 cm Ø Bar	1085°C 1hr / OQ / DI	501°C 3 hr / WQ / DI / 482°C 12 hr / AC	1550	1985	54
Custom 465	1.9 cm Ø Bar	982°C 1hr / OQ / DI	482°C 4 hr / AC	1700	1810	51
Ferrium PH48S	10 cm Ø Forging	825°C 1hr / OQ / LN ₂	482°C 2 hr / AC	1585	1585	49
OQ: Oil Quench, LN2: Liquid Nitrogen Quench, WQ: Water Quench, DI: Dry Ice Quench						
Table 2.4: Heat treatment and mechanical behavior of selected aerospace steels [2]						

2.4 Research Objectives

The literature study has shown that all martensitic steels have some susceptibility to HAC. The main research objective in the present contribution is thus to show the general HAC resistance of the new design alloy S53 in the used service-applied condition.

For designing such a research approach, the main streams of research and development in HAC have to be taken into consideration. In the years between 1970 and 2000, R&D with respect to HAC was very much oriented towards clarification of the respective mechanisms, as shown in the literature survey. When the international scientific community concluded that not a single mechanism might be able to explain and clarify the phenomenon, especially since 2000, but partly already earlier since the eighties with a focus on industrial application, R&D was concentrating more on the phenomenology of HAC. However, in the recent years more inter- or to say cross-disciplinary approaches have been established and followed, as for instance the investigation of hydrogen distributions with more advanced high-resolution imaging techniques. However, such cross-disciplinary techniques have not always to be such highly complicated and, for instance, the tensile testing of hydrogen charged specimens represents already a cross-disciplinary approach and involves metallurgical, mechanical and materials engineering as well as electrochemistry.

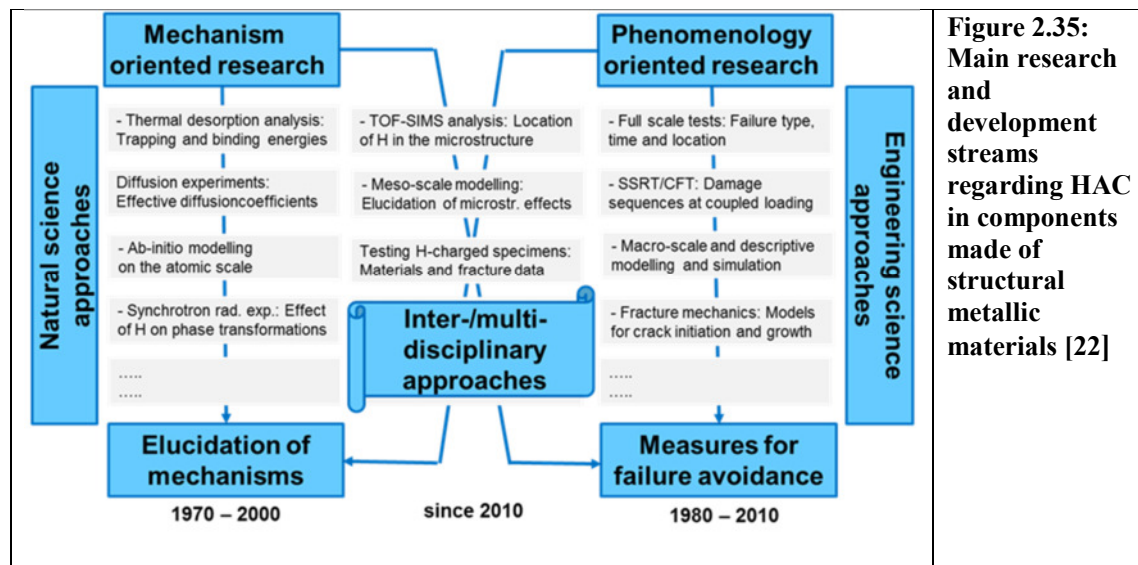


Figure 2.35: Main research and development streams regarding HAC in components made of structural metallic materials [22]

To take the first approach and, especially, to gain the above mentioned more detailed insight into the resistance of the new landing gear steel S53 against HAC, a mixed cross-disciplinary and a conventional phenomenological approach has been followed by predominantly conducting tensile testing of hydrogen charged specimens and by respective slow strain rate tests (SSRT).

Several additional partial objectives have been identified which are listed here:

1. Clarification of the service and loading conditions in real landing gear applications

As typical conventional landing gear material the steel AISI 4340 has been identified and will be investigated here in comparison to the new design alloy S53. Such material will be subjected various mechanical loading types and various corrosive environments. Since the loads subjected to the landing gear are always a combination of tension, compression and torsion – it is easier to test for the lowest threshold for failure with mechanical loading applied. In application, landing gear will most likely fail in bending, which has components of tension and compression. In compression, there really is no issue with the material buckling due to its extreme strength and design. Therefore, a tensile mode test is the most accurate representation of worst case loading – specifically while in corrosive environments. To sum up, considering military aircraft applications, marine environments should be considered as worst-case scenarios, in particular the exposure of the unprotected (coated) materials to seawater in splash water regions.

2. Determination of the principal hydrogen dependent material properties

The master procedure for such goals are to tensile tests of completely hydrogen charged specimens. Good experience with such procedure have been made in previous contributions with respect to the determination of hydrogen dependent material properties of low alloyed martensitic steels of the S100 type (Section 2.3.1), low alloyed martensitic heat resistant steels (Section 2.3.2), supermartensitic stainless steels (Section 2.3.4). The procedure should be applied similarly to the high strength landing gear steels. As shown in the literature survey, hydrogen degrades the mechanical properties more in terms of ductility than in terms of

strength. Thus, the ductility relevant parameters dependent on the hydrogen concentration in the materials must be paid special attention to.

Determination of the hydrogen dependent material properties provides a very good comparison of the mechanical behavior of the landing gear steels versus the so far investigated martensitic steels. Furthermore, such hydrogen dependent material properties will provide a profound data basis in terms of cracking criteria for later numerical simulations and for assessment of the necessity to conduct large scale tests.

Although the main focus of the present contribution lies on the determination of the hydrogen dependent mechanical properties of the used and service-applied steel S53, respective properties have also to be determined for this steel in the new as-delivered condition for comparison. Similarly, such values must be compared to the new and also service-applied conventional steel AISI 4340.

Determination of such properties should be accompanied by an embracing fractography to learn more about the real failure behavior of such materials, if they might be hydrogen charged in any other type of environment. This also gives the opportunity for back-reflection from later failure analyses, if necessary.

In addition to such tests, also the hydrogen degassing characteristics should be investigated to find hints for potential trapping of hydrogen, as also outlined in the literature review.

3. SSRT of the new landing gear steel S53

As mentioned above, the worst-case scenario with respect to military aircraft applications, evidently the exposure of the unprotected material to seawater should be considered regarding the environmental conditions. As shown in the literature review and as mentioned above, hydrogen degradation of metallic materials occurs less in terms of strength, much more in terms of ductility. For this reason, additional straining in seawater must be considered and thus, an approach by conducting SSRT has been selected.

SSRT are by no means short term tests and thus, to restrict the number of tests, these experiments have been completely focus on testing the new landing gear steel S53. Later SSRT

going far beyond the frame of the present contribution might have perhaps to show the behavior of the conventional steel 4340 for comparison.

Most of the SSRT have been concentrated on the used service-applied landing gear steel S53 that has been in service for about five years. It can only be emphasized that such testing on used landing gear material, especially the novel steel S53, has been carried out for the first time. However, the as-delivered version of the S53 steel should be investigated for comparison.

The SSRT have the main goals to identify the failure sequence of such high strength materials in comparison to other martensitic steels, as for instance high alloyed 13 wt.-% Cr steels, in comparison. Also, the various fracture topographies must be investigated in comparison to other martensitic steel types.

Considering the literature study regarding SMSS, the slow strain rate test is providing five significant advantages:

- A. The test duration is much shorter as compared to 720 h constant load tests. At a strain rate of $1 \cdot 10^{-6}$ 1/s for the specimen type defined in the NACE standard TM 0177-96 method A, for instance, such test period is reduced to less than one tenth for low carbon martensitic stainless steels, if the material behaves completely ductile.
- B. Straining of the material is performed in a controlled way as compared to uncontrolled strains occurring during loading and due to creep in constant load tests.
- C. Environmental and, specifically hydrogen degradation can be better identified by the reduction in strength and/or in ductility of the test material.
- D. The metallurgical mechanisms of material failure can be more extensively investigated. For low carbon martensitic stainless steels, any absorption of hydrogen can be verified by carrier gas hot extraction after SSRT and hydrogen degradation can be visualized by the fracture topography of the specimens in the SEM, which, naturally, requires complete fracture of the test piece.
- E. The straining of a small-scale test piece is providing consistent information on material behavior which can subsequently be processed by FEM analysis for life time assessment of realistic components and structures.

Of course, the fracture topography of the SSRT specimens has to be investigated in comparison to that of the hydrogen charged specimens and has also to be compared to that of other martensitic passivating steels. In addition, the hydrogen degassing characteristics of the SSRT specimens have to be investigated to compare perhaps different trapping behavior of the steel in the as-delivered as compared to the service-applied condition.

4. Identify measures for the material compatibility for application

Finally, one particular goal of the present contribution is to identify hints and measures for future service applications of the novel Ferrum S53 steel. For this, the previously identified hydrogen degradation behavior will provide valuable input. Additionally, the performance under seawater exposure will provide indispensable information for further and future applications in marine climates.

3. Experimental Arrangements and Procedures

3.1 Materials Investigated

Two Ultra High Strength Steel (UHSS) materials used specifically for landing gear applications were investigated. The first, AISI 4340 is a low-alloyed legacy steel that has been commonly used in aircraft landing gear for the past 60 years. The second, Ferrium S53 is a high-alloyed “engineered” steel that has been specifically designed for use in aerospace applications with emphasis on landing gear. The two types differ by the heat treatment condition of the steel and inherent alloy composition, respectively. The “new” condition material was purchased directly from Carpenter Latrobe Specialty Metals in the form of 1 inch round bar and 2 inch round bar. The “used” condition material came from actual main landing gear (MLG) components that had been exposed to the service loads and environmental effects of use in application.

Table 3-1: Chemical composition of AISI 4340 steels (wt.-%, Fe balance) by OES

Grade	C	Ni	Mo	Mn	Si	Cr	Co	W	V
AISI 4340 Nominal	.40	1.80	.25	.75	0.30	0.80	N/A	N/A	N/A
AISI 4340 “New”	0.40	1.62	0.27	0.73	0.32	0.81	0.023	< 0.04	0.003
AISI 4340 “Used”	0.38	1.60	0.21	0.78	0.21	0.80	N/A	N/A	N/A

Table 3-2: Chemical composition of Ferrium S53 steels (wt.-%, Fe balance) by OES

Grade	C	Ni	Mo	Mn	Si	Cr	Co	W	V
Ferrium S53 Nominal	0.21	5.50	2.00	N/A	N/A	10.0	14.0	1.00	0.30
Ferrium S53 “New”	0.21	5.71	2.04	N/A	N/A	10.0	13.52	1.06	0.32
Ferrium S53 “Used”	0.18	5.77	1.94	N/A	N/A	10.43	13.75	1.03	0.29

Figure 3-1 and 3-2 show the microstructures of the two steels investigated in the as-delivered normalized and annealed state. As can be seen from the micrographs, 4340 exhibits a typical microstructure mixture of lamellar pearlite (vermicular striped areas) and ferrite (bright areas). In contrast, S53 has a lath martensitic microstructure with carbide precipitations (M2C)

embedded in a coarse matrix that also contains austenite from the normalizing and annealing process at the steel manufacturer.

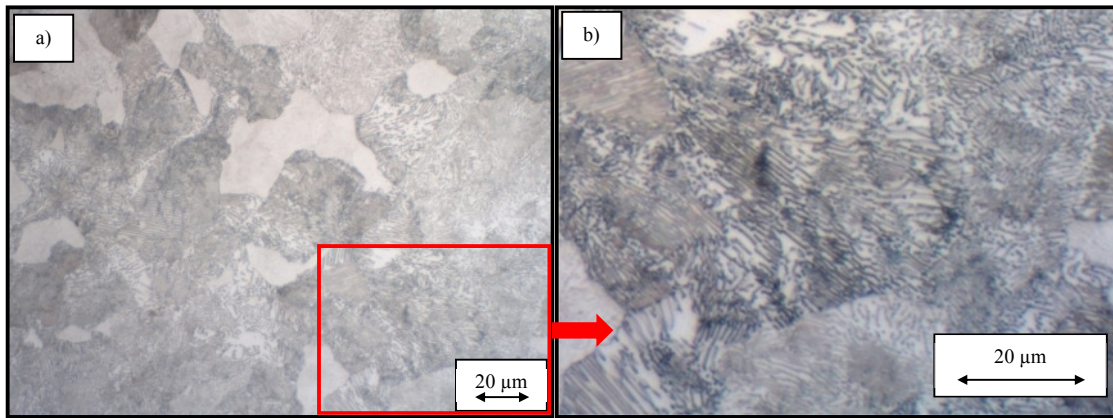


Fig 3-1: a) AISI 4340 “new barstock”, b) AISI 4340 “new barstock” increased magnification

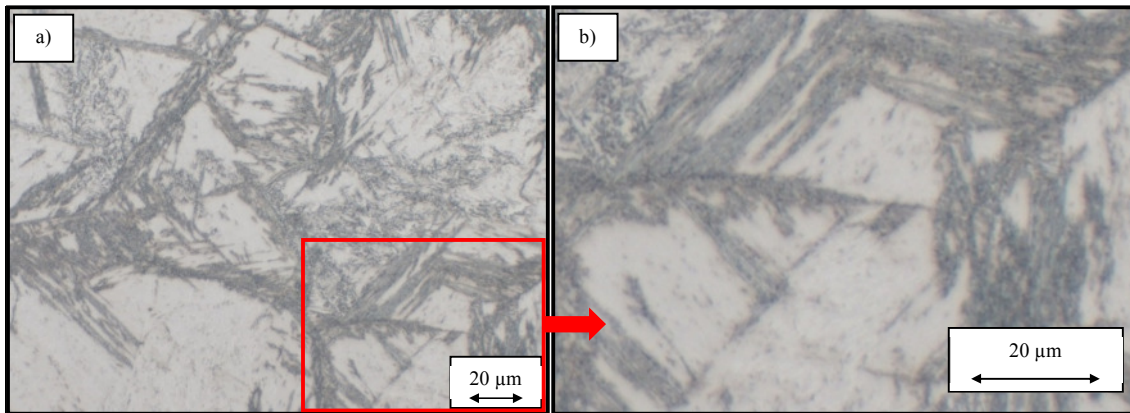


Fig 3-2: a) Ferrium S53 “new barstock”, b) Ferrium S53 “new barstock” increased magnification

Figures 3-3 and 3-4 illustrate the microstructures of the two steels investigated in the heat-treated state that is required to achieve the desired mechanical properties for use in application. Notable from both micrographs is the substantial grain refinement and homogeneous microcarbide formation. [24]

Shown in Fig 3-5, S53 “new barstock” was examined to establish the amount of austenite present prior to heat treatment. In this image, the FCC microstructure is shown in red and BCC is shown in green. From this image, we can graphically approximate an austenitic (FCC) area of 20-25% on the cross-section.

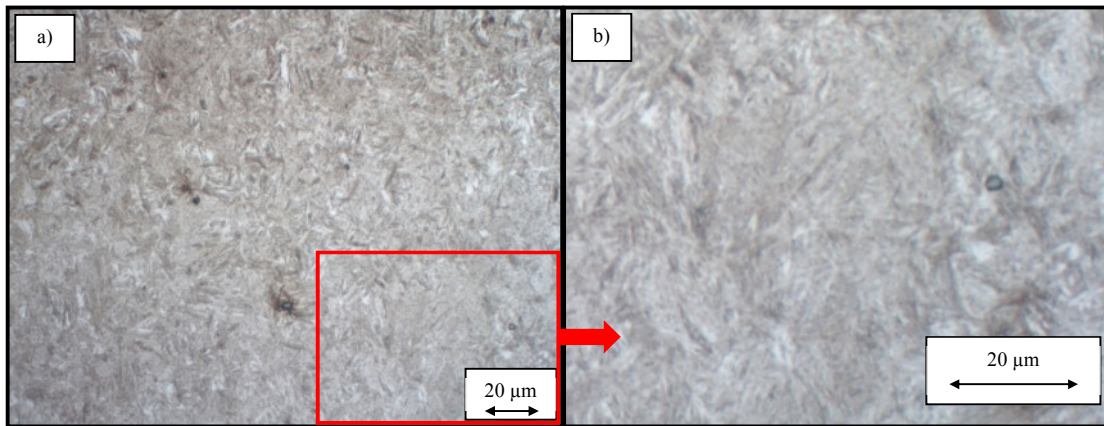


Fig 3-3: a) AISI 4340 “used component”, b) AISI 4340 “used component” higher magnification

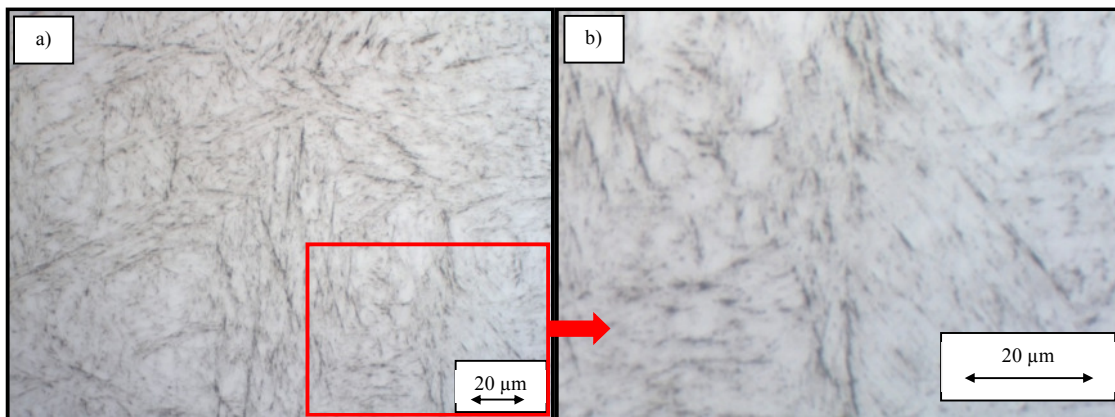


Fig 3-4: a) Ferrium S53 “used component”, b) Ferrium S53 “used component” hi magnification

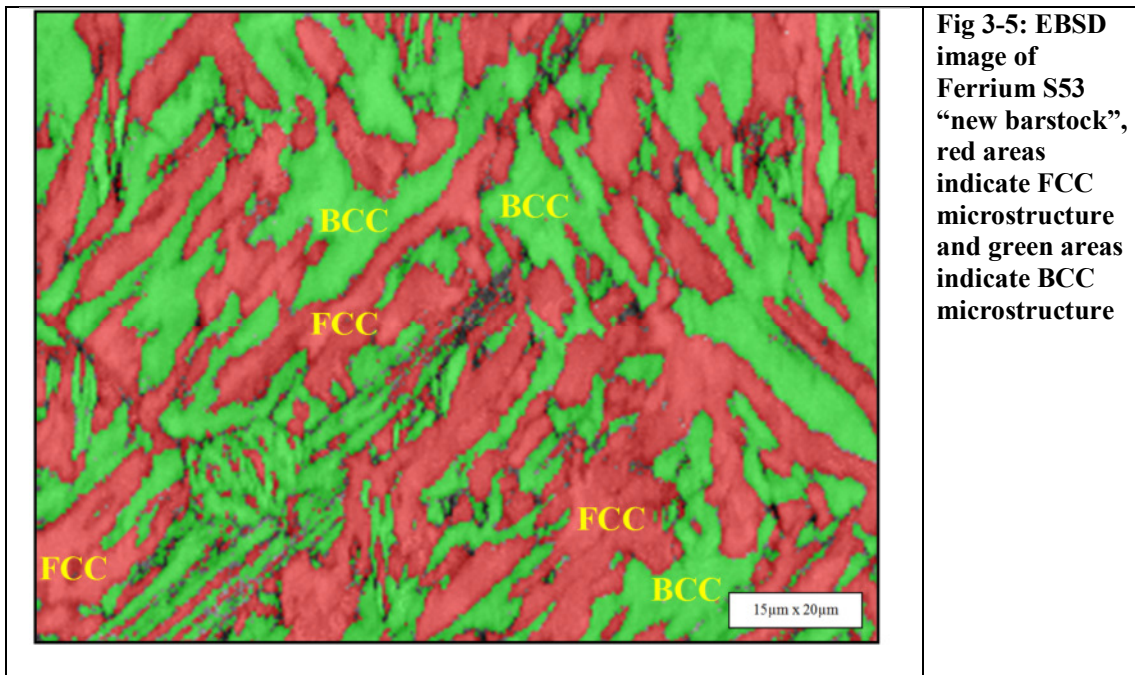


Fig 3-5: EBSD image of Ferrium S53 “new barstock”, red areas indicate FCC microstructure and green areas indicate BCC microstructure

Repeating the EBSD imaging on the Ferrium S53 “used component” material netted a maximum value of less than 2% retained austenite, indicating almost complete transformation of the microstructure to martensite from its unique heat-treatment and cryogenic tempering cycles. [2]

Table 3-3: Material properties evaluated from tensile testing

Grade	Yield Strength (MPa)	Tensile Strength (MPa)	Hardness (HV1)	Reduction in Area (%)	Fracture Strain A5 (%)
AISI 4340 “New barstock”	527	766	233	42.7	19.8
AISI 4340 “Used component”	1624	1855	565	48.3	7.9
Ferrium S53 “New barstock”	828	1091	352	33.8	14.6
Ferrium S53 “Used component”	1758	1977	610	54.7	9.7

In addition to completely different microstructures, the comparison of the “new barstock” materials to the “used component” also provided completely different material properties. Both of the materials in the “used component” state netted much higher hardness and strength than in “new barstock” state, as shown in Table 3-3.

3.1.1 Specimen Extraction and Preparation

To extract the specimens necessary for all of the experimental work done during this study, it was imperative to impart the minimum amount of thermal stress onto the specimens. To minimize this, electro-discharge machining (EDM) practices were followed throughout the specimen harvesting. The subsequent operations necessary for surface preparation and threading also were always done under flood cooling with particular attention to minimize thermal stresses.



Fig 3-6: Specimen extraction from Northrop T-38 Talon – Primary supersonic jet trainer of US Air Force: a) Overview of aircraft, b) MLG close-up, c) Actual MLG as received

In Fig 3-8 and Fig 3-9, specimens were taken to establish whether the chrome plating process on the piston stanchion tube had introduced any hydrogen at the plating-substrate interface. These (10mm x 20mm x full wall thickness) specimens were extracted using a water jet operation to keep the heat input to a minimum. They were then analyzed using the Carrier Gas Hot Extraction method which is explained in section 3.3.

To specifically investigate the areas of the component that experienced the highest service loads and representative stresses, a detailed map (Fig 3-10) of the MLG knuckle (spindle to piston stanchion tube interface) was created to harvest the specimens from these identified areas. This was done by matching the necessary cross-section measurement with available component thickness.



Fig 3-7 Specimen extraction from Fairchild Republic A-10 Thunderbolt II – Close air support combat aircraft of USAF: a) Overview of aircraft, b) MLG close-up, c) Actual MLG as received

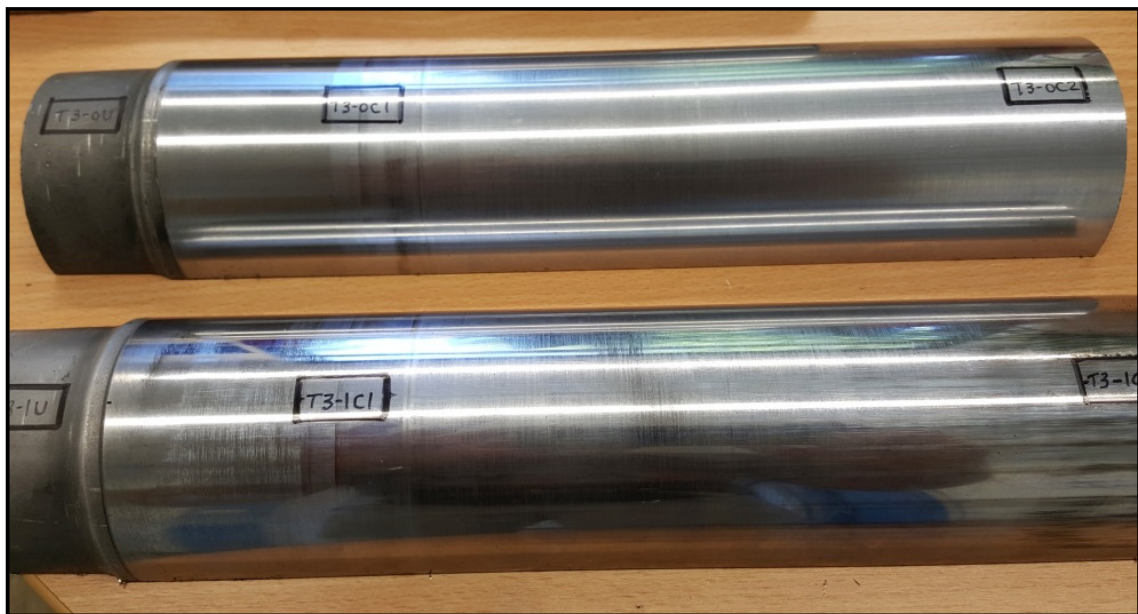


Fig 3-8: T-38 aircraft 4340 MLG piston stanchion tube indicating specimen extraction sites



Fig 3-9: A-10 aircraft S53 MLG piston stanchion tube indicating specimen extraction sites

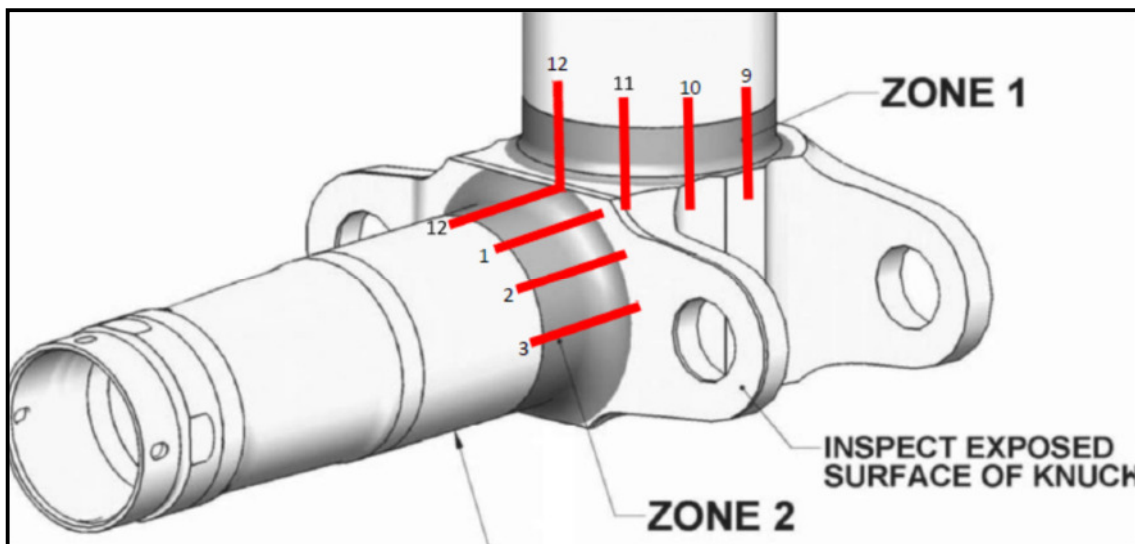


Fig 3-10: Specimen extraction schematic highlighting the highest service load areas

Due to the fact that these components are actual aerospace items and designed for a minimum weight while maintaining factor of safety, this specimen harvesting was very challenging. A review of the identified areas was carried out with the expertise of the staff from the Center for Aircraft Structural Life Extension (CASTLE) to confirm that the areas of interest were ideal for testing.

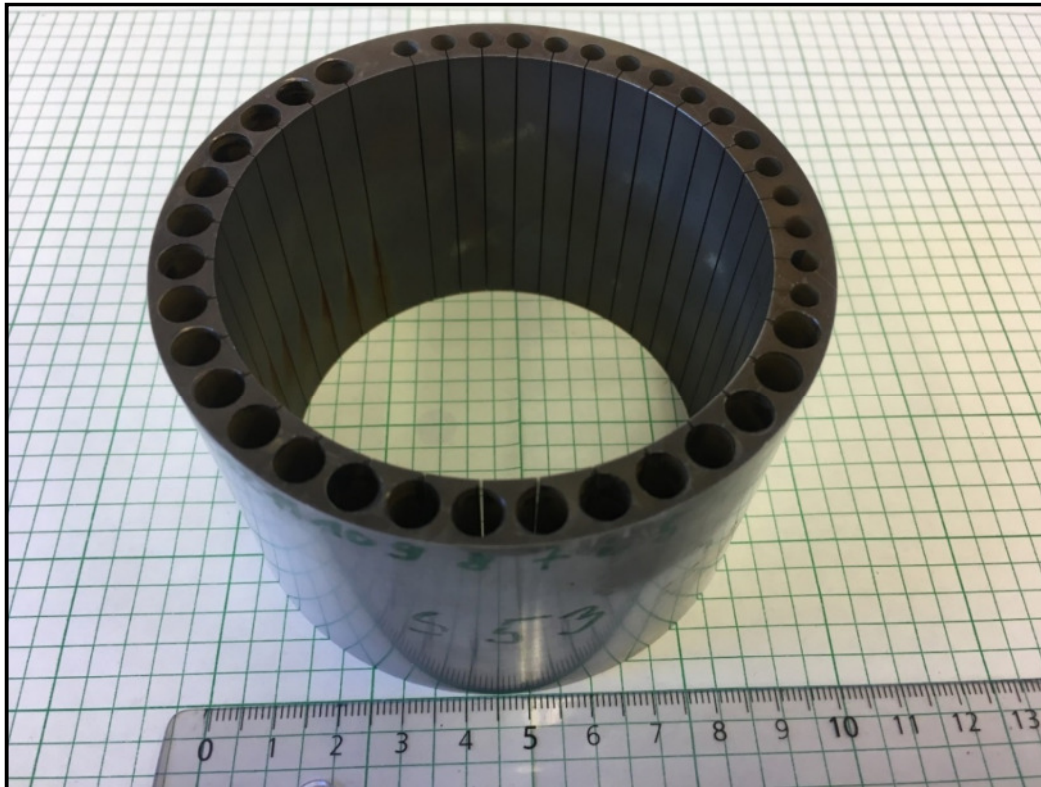


Fig 3-11: Actual area of specimen extraction from spindle section (Zone 2 on Fig 3-10)

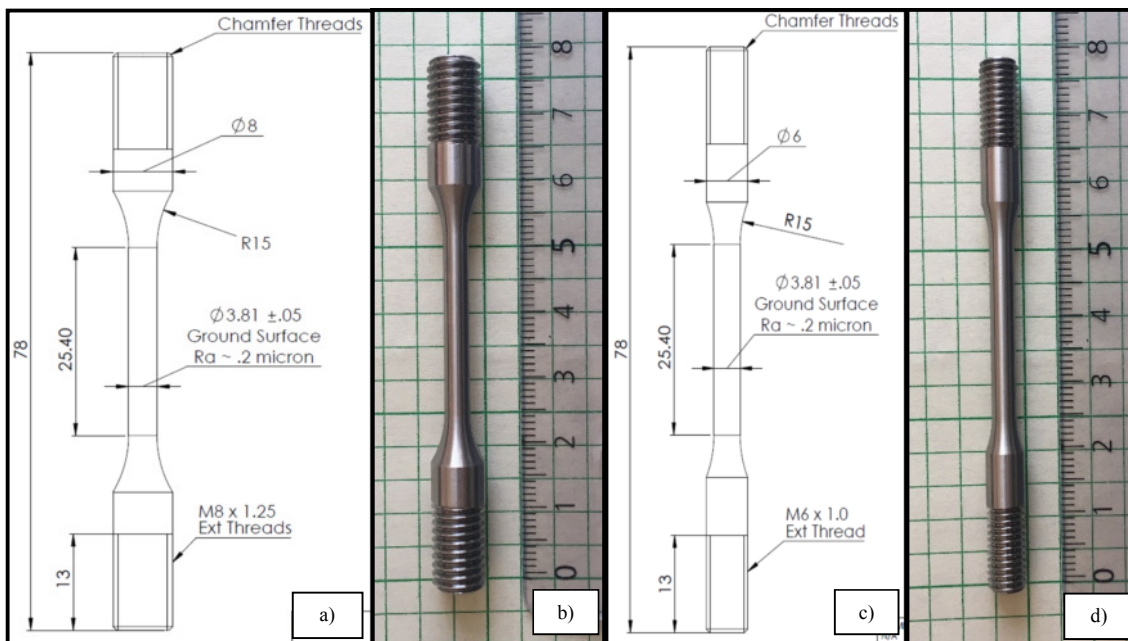


Fig 3-12: Redesign of subscale specimen used for Slow Strain Rate Testing: a)NACE TM0177 subscale schematic, b)NACE TM0177 actual part, c)Modified NACE TM0177 subscale with M6 thread connections and 6mm overall diameter, d)Modified NACE TM0177 actual part

Limitations can be seen in Fig 3-11 where the wall thickness of the spindle was only just sufficient to extract the samples. Specimen designs were modified as a solution to the challenge of taking material from the used components where the component thickness was less than the required specimen size. Fig 3-12 illustrates that the NACE TM0177 subscale specimen was redesigned from M8 threaded connections to M6 threaded connections in order to address this challenge. The tooling in the testing apparatus also had to be modified to accept these modified specimens.

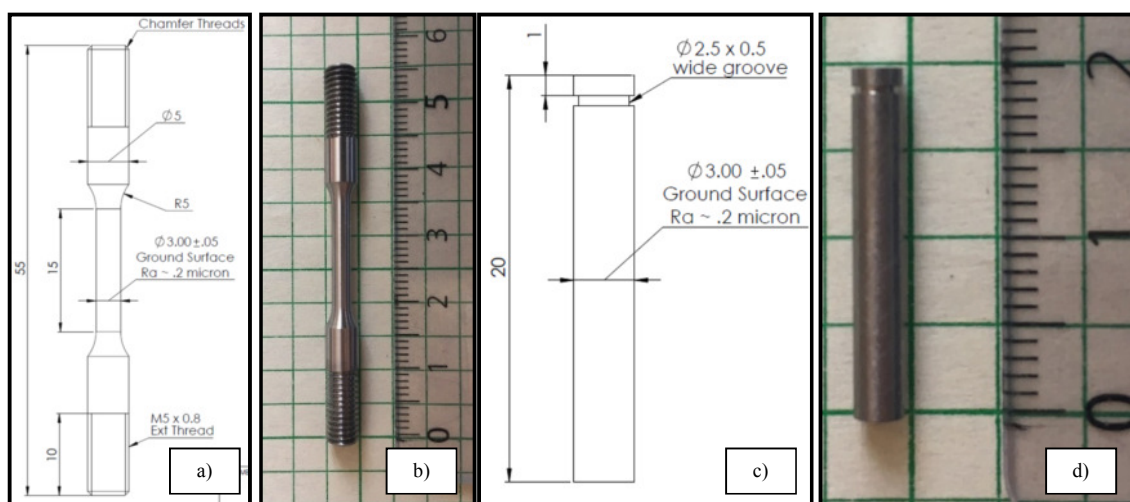


Fig 3-13: Specimens used for hydrogen charging experiments: a) 3mm diameter tensile specimen, b) 3mm diameter concentration evaluator specimen

3.2 Hydrogen Charging

In order to introduce hydrogen into the investigated material in specific concentrations, an electro-chemical method of hydrogen charging was used. The standard electrolytic solution used for all of the charging in this study consisted of 0.1 M H_2SO_4 (Sulfuric Acid) and 0.05 M $NaAsO_2$ (Sodium Arsenite) dissolved homogeneously into an aqueous solution. The Sulfuric Acid in the solution provided the hydronium ions that are used to charge the material. The Sodium Arsenite functions as a recombination inhibitor, keeping the hydrogen in ion form rather than recombining into molecular hydrogen (H_2).

Illustrated in Fig 3-14, the specimens were introduced into the solution in a custom made 3-port, borosilicate glass vessel with a liquid volume of 1L. The three top ports provide a via for: the charged specimens which connect with a platinum wire that was wrapped around them, a

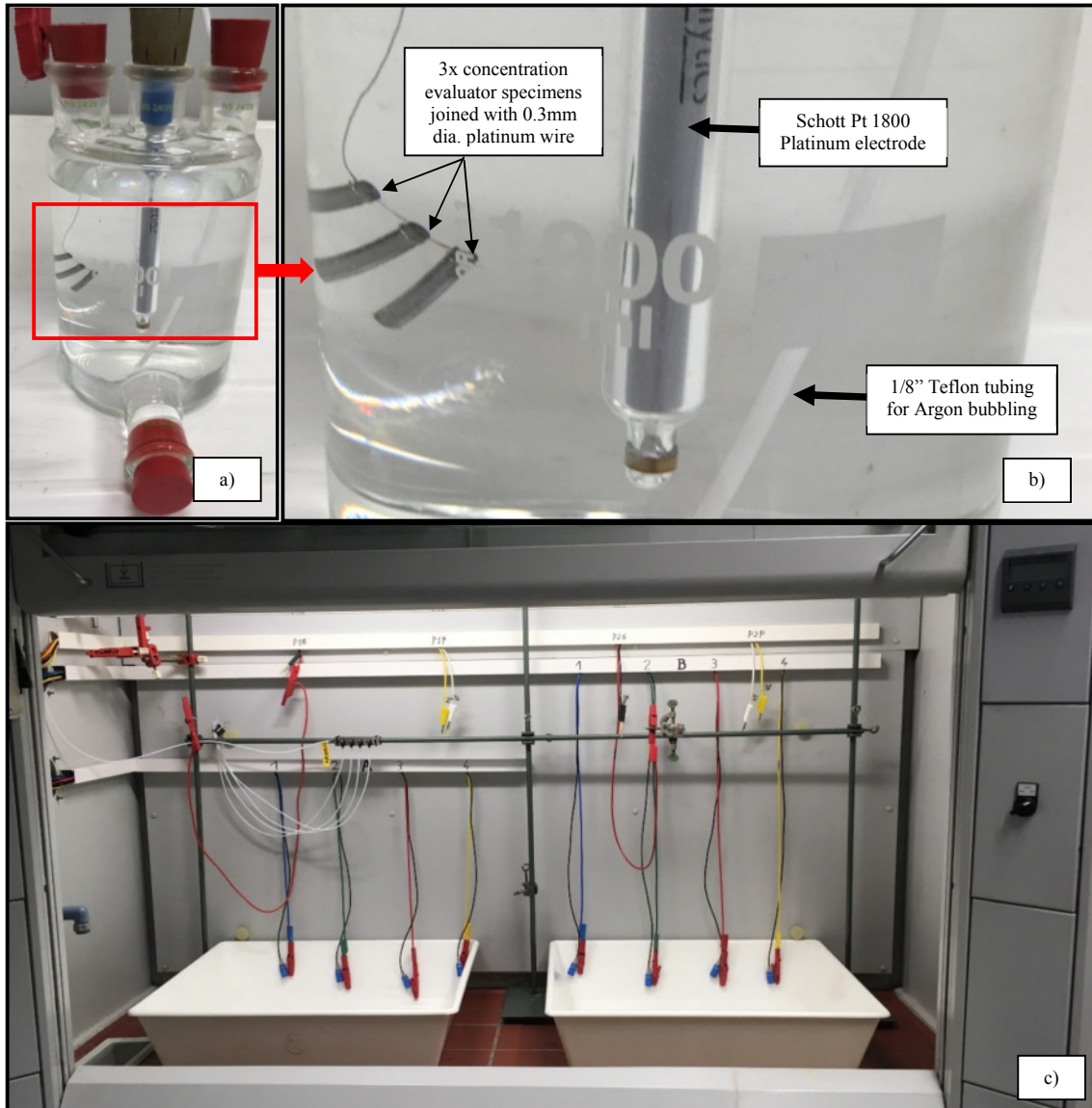


Fig 3-14: a) Custom 1L borosilicate glass vessel used for charging experiments, b) red-box area magnified to indicate the specimens, the Pt 1800 electrode and the Teflon tube for argon gas, c) chemical hood for charging procedures, note argon manifold and series of 4 tubes

platinum electrode (Pt 1800 Schott) which represented the counter electrode and the Teflon tube that introduced the Argon gas that was bubbled into the solution during charging. The specimens act as the working electrode (cathode) and the Pt 1800 acts as the counter electrode (anode). All charging experiments were conducted under a hood (Fig 3-14c) with proper ventilation and chemical safety protocols.

Before introducing the specimens into the solution for charging, the surface of each specimen was lightly abraded in a random pattern. A 3M Scotch-Brite Hand Pad 7447 which is a general-

purpose abrasive pad that would replicate the surface conditions produced by cleaning and maintenance by aerospace technicians. This surface treatment was applied to all of the different types of specimens that supported this research.

The Bank Elektronik Wenking TG97 Potentiostat/Galvanostat (Fig 3-15) was used exclusively during the process of electrochemical charging of the specimens. For charging, the Bank TG97 was used in galvanostatic mode with a variation between 0.3 mA/cm^2 and 50 mA/cm^2 current densities and durations of 24 hours to 120 hours to achieve the desired hydrogen concentrations. At very low current densities ($<1.0 \text{ mA/cm}^2$) the specimens would develop corrosion on the surface that was detrimental to the charging procedure. This was avoided by slowly bubbling Argon gas into the solution which effectively extracted any dissolved oxygen from the electrolyte and thus eliminated this effect. [107] The charging time was varied to find out the required time to achieve consistent concentrations in the gage length of the specimens. Subsequently, charging for 120 h was found to be sufficient to achieve complete saturation with a homogeneous concentration. This has been checked by simple solutions of Fick's second law for cylindrical specimens [9] and has also been validated by consistent fracture surfaces of the electrochemically charged tensile specimens.



Fig 3-15: a) Bank Elektronik TG97 Potentiostat/Galvanostat, b) charging tensile specimens in the same manner as the concentration evaluator specimens, c) array of TG97's in corrosion lab

After charging, all of the specimens are immediately placed in a storage dewar of liquid nitrogen at -196 degrees C to limit the hydrogen effusion from the sample until a hydrogen concentration analysis can be performed.

3.3 Hydrogen Measurement

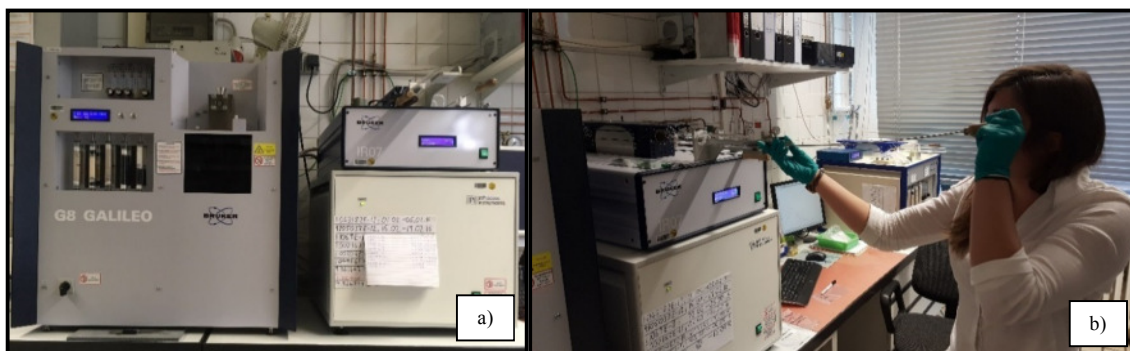


Fig 3-16: a) Bruker G8 Galileo with IR07 infra-red furnace and InProcess Instruments mass spectrometer, b) a colleague inserts the specimen into the quartz tube that is heated by the IR furnace for gas extraction

The quantitative hydrogen analysis was done by using the carrier gas hot extraction (CGHE) method. A hydrogen analyzer (G8 GALILEO from Bruker Elementals) with an additional mass spectrometer (ESD100 from IPI) was used. The resolution of the equipment was approximately +/- 10 ppb per gram of specimen weight, allowing a much higher accuracy than commonly used thermal conductivity devices [107]. In order to achieve repeatable results with minimal effects from inconsistencies from hydrogen effusion or evaporation from the specimens during setup, a strict timetable was followed during the CGHE procedure. First, the specimen was removed from the LN₂ dewar where it has been in a cryogenic state since the electrochemical charging. It was then massed on a Mettler XP205 scale (± 1 mg). Immediately after, it was warmed to room temperature in acetone for 30 sec. It was then blotted dry on laboratory wipes and given a nitrogen air blast to dislodge any remaining acetone (another 30 sec). At this point, a total of 60 seconds from when the specimen exited the liquid nitrogen, the specimen was inserted into the quartz tube that allows the infrared heater to begin its program from 25 °C to 900 °C at a 0.5 K/sec temperature ramp rate. After total degassing, the total hydrogen amount was calculated via specimen weight in parts per million (ppm).

The 3 mm diameter concentration evaluator specimens of all materials researched were used for the charging and later CGHE process for establishing set parameters to achieve specific HDs. To corroborate the HD values of the 3 mm concentration evaluator specimens, one half of each of the tensile specimens was analyzed with the CGHE process as a forensic step to ensure that hydrogen concentrations adhered to the set parameters found previously.

To assess the quantity of hydrogen inside of the component at the time of teardown, specimens were taken from throughout the component and tested using the CGHE method to establish a baseline and also to investigate other possible hydrogen sources.

3.4 Tensile Tests

Mechanical testing of uncharged and charged tensile specimens, as shown in Fig. 3-16, was carried out on an Instron 4505 50 kN load frame. An extensometer was only fitted to the uncharged specimens due to the brittle failure of the charged specimens. Instead, the true strain was calculated in accordance to previous investigations [107]. The tests were performed at a cross head speed of 1 mm·min⁻¹.



Fig 3-16: Instron 4505 50kN load frame with gimbal on upper head to ensure only axial loading – tensile specimen mounted and undergoing severe necking prior to fracture

Similar to the CGHE process, a strict timetable was followed. Immediately after the specimen was removed from the liquid N₂, it was prepared by warm up for 30 seconds in acetone, dried on laboratory wipes and mounted on the machine, which all normally took approximately 60 s. One half of each fractured tensile specimen was then immediately stored in liquid nitrogen and later sectioned and analyzed with the CGHE process. Since the whole tensile testing process took less than 300 s, the outgassing of hydrogen could have affected only a distance of less than 50 μm in depth from the surface, as calculated by simple of Fick's second law solutions [24]. The material properties could thus be directly related to the measured hydrogen concentration in the respective specimens. The other half of the specimen was used for determination of the fracture topography via SEM.

3.5 Slow Strain Rate Tests

The high-precision load frame was built by Cormet of Finland with a load limit of 25kN for slow strain rate test (SSRT) experiments, and a load limit of 100kN for use with low cycle fatigue (LCF) experiments. The machine has a screw-driven load train with a 250 to 1 gear reduction to provide the low strain rates that were necessary for this testing. In this research effort, only the SSRT portion was used which had a capability for strain measurements from 10^{-3} to 10^{-7} 1/sec strain rates with the NACE TM0177 subscale specimens. Slower strain rates are theoretically possible, but the step-wise functions of the rotary encoders are then visible in the data which precludes the testing at strain rates lower than 10^{-7} 1/sec. All of the SSRT experiments supporting this research were conducted at strain rates of 10^{-5} to 10^{-7} 1/sec strain rate.

The SSRT machine has provisions to introduce dry laboratory air or Argon gas to be bubbled into the test cell during runs. The dry lab air is introduced by an aquarium bubbler unit which the flow can be throttled infinitely. The Argon gas is provided by a remotely connected bottle of Argon 4.6 purity gas also fitted with an infinitely adjustable throttle valve. The bubbling of dry lab air would provide a slight stirring effect of the solution and also introduce molecular oxygen into the solution. Alternately, the bubbling of Argon gas would also provide the stirring effect, but would extract any molecular oxygen in the solution.

An AXIS P1365 Mk II network camera (Fig 3-17) was fitted to the framework of the SSRT machine to record images of the specimen during the test. The camera was able to be remotely

accessed with full control from off-site. A Bank Elektronik Wenking TG97 Potentiostat/Galvanostat was used to: monitor the open circuit potential (OCP) during OCP SSRT experiments, and to introduce a potential into the solution during SSRT experiments where cathodic protection was being evaluated.

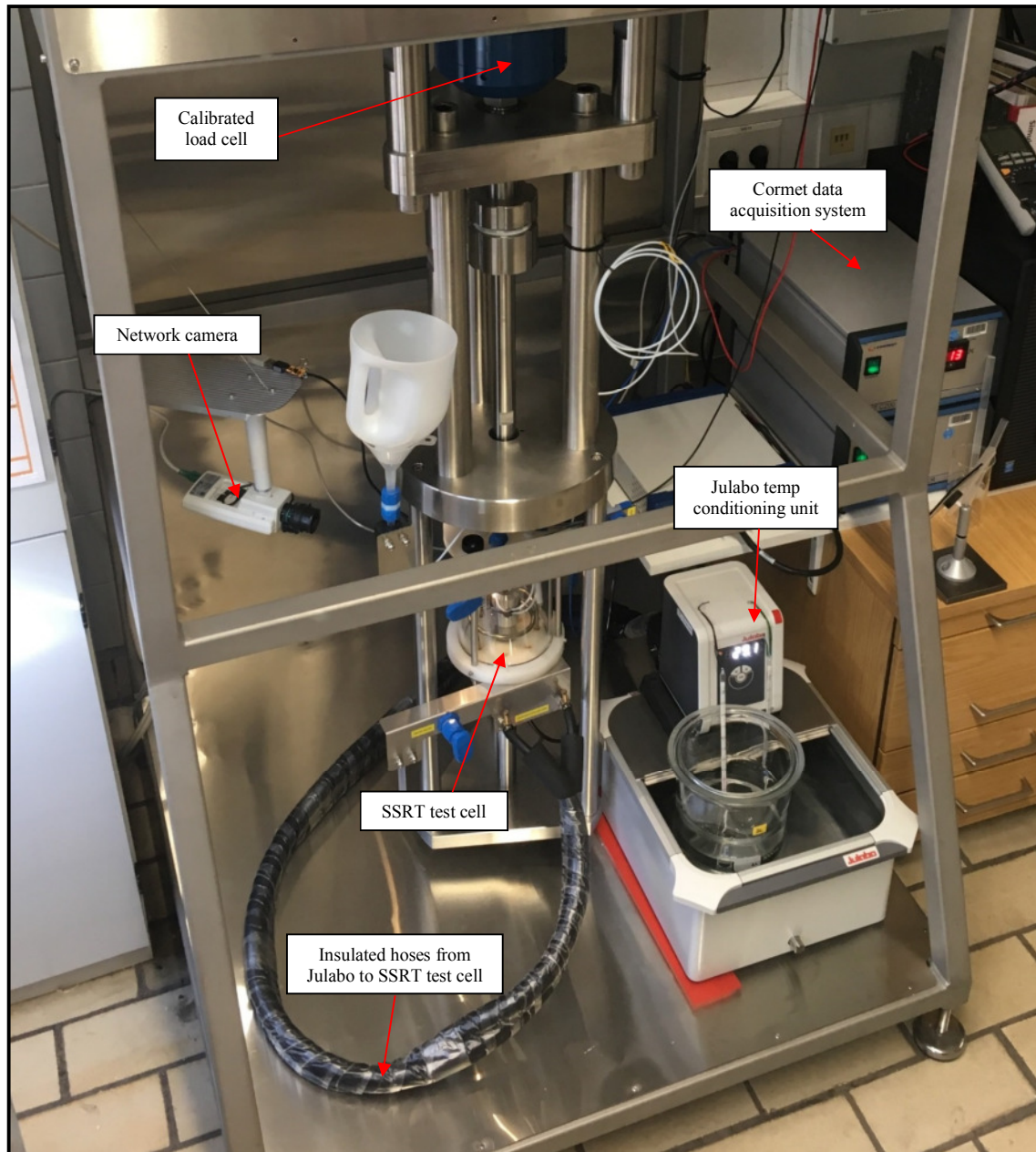


Fig 3-17: Front view of the Cormet high-precision load frame.

A Julabo Corio CD temperature conditioning unit (Fig 3-18a) was used to perform SSRT experiments at higher temperatures by heating a reservoir of distilled water from room temperature to up to 80 deg C. The heated water is pumped through insulated hoses into the heating coil of the SSRT machine and then back to the reservoir of the temperature conditioning unit in a loop. The standard temperature in the lab is 21 deg C, which is controlled by the air-conditioning unit for the laboratory.

According to NACE TM0284 testing standards, the solution that was used in the test cell was a simulated seawater prepared to the ASTM D1141 standard specifications. All used reagents were analytical grade. This netted a 3.5% sodium chloride (NaCl) solution that when used, was adjusted to a pH level of 8.2 ± 2 in all SSRT experiments. The simulated seawater (simsea) was stored in a 20L carboy that was kept away from any light sources and was decanted into a 4L glass dewar in preparation for each experiment.

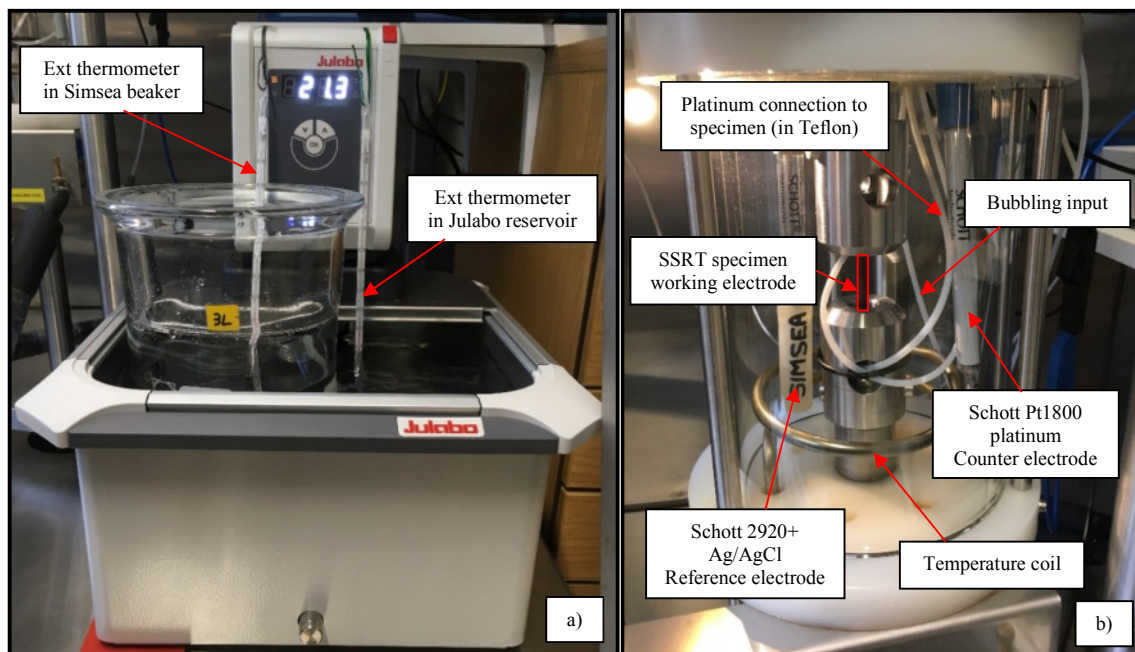


Fig 3-18: a) Julabo Corio CD temperature conditioning unit with a 4L beaker containing 2L simulated seawater being heated inside of the reservoir while the SSRT coil is also being heated, b) SSRT test cell with components identified

Each SSRT experiment consisted of several segments of preparation. To begin with, the specimen had to be prepared by cleaning in acetone and conditioning the surface with the 3M Scotch-Brite general purpose abrasive pad. After a subsequent cleaning in acetone and drying

off with dry nitrogen gas, the specimen was inserted into the SSRT machine and pre-tensioned to 50N. After this, a 2L volume of Simsea was drawn from the large 20L carboy and adjusted in pH to 8.2 ± 2 . If the test was to be run at increased test cell temperature, the Julabo temperature conditioning unit would be initiated and the Simsea beaker would be introduced into the reservoir to warm up with the fluid from the system. Also, if the test was to be run with a set potential or run OCP, the Bank TG97 potentiostat would have to be set to support that. Finally the camera would be prepared for taking the footage of the test. To trigger the test: when the fluid/Simsea reached the proper temperature - the dewar would be emptied into the test cell, the Bank TG97 would be energized, the SSRT machine program would be started, and the camera would be toggled, all being done as expeditiously as possible. After the test, one specimen half was saved for further CGHE analysis and the other specimen half was used for metallography/SEM imaging.

3.6 Permeation Experiments

A Devanathan cell arrangement was used to conduct the permeation experiments for this research [107]. Fig 3-xx shows the experimental setup, which consisted of two custom made 3 port 500mL borosilicate glass vessels that also shared a single port at the bottom of the sidewall. Between these 2 individual vessel ports is where the permeation specimen lies. At this junction point, there are 2 Teflon adaptors that interface with the tapered holes in the individual ports but also have a face connection that is sealed with two 16mm diameter by 1.5mm thick Viton o-rings. The steel clamping plates have two M5 threaded bolts that can be finger tightened to provide enough seal at the o-ring to prevent any fluid leakage at the specimen joining surfaces.

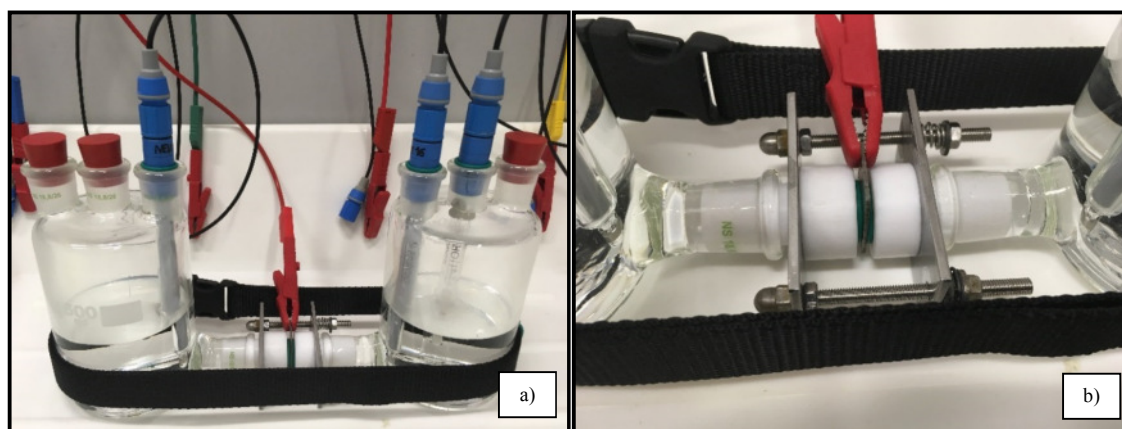


Fig 3-19: a) Devanathan cell configuration with anodic cell (left) and cathodic cell (right) b) close up of Teflon adaptors and o-ring seal junction with specimen

The nylon 25mm strap keeps the cells together by ensuring that the tapered connections with the Teflon adaptors are held in place.

The specimen geometry is a simple 20mm x 30mm piece of material that is .5mm thick. This thickness can be varied due to the material being tested. It is dependent on the time necessary for the hydrogen ions from the charged electrolyte from one vessel to transfer through the membrane (specimen) into the vessel of the hydrogen detection cell on the exit side. The specimen is oversize in one direction to facilitate the clamping of the alligator clip that connects the anodic galvanostat, the cathodic potentiostat, and the specimen. The surface preparation of the specimen begins with using a gradually finer and finer wet/dry aluminum oxide sandpaper until the surface is very good (ca. 0.5 $\mu\text{m Ra}$). After reaching this surface roughness, the same 3M Scotch-Brite random light abrading was performed to make the surface the same as that of all of the other tested specimens.

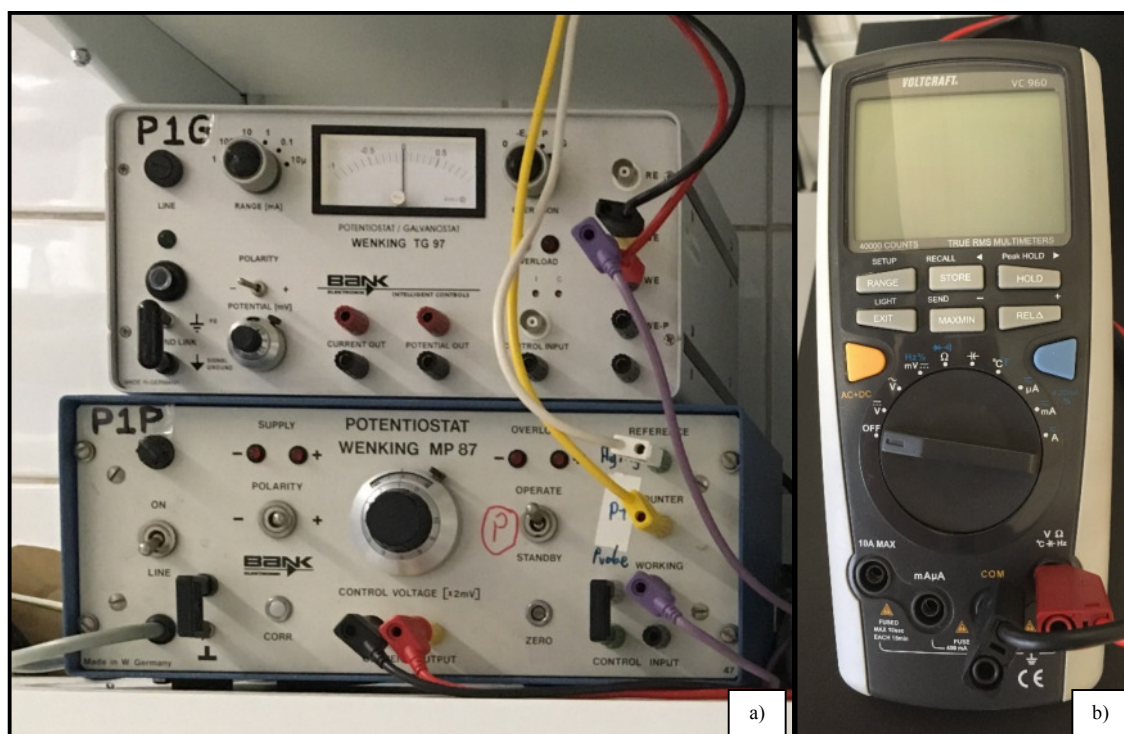


Fig 3-20: Electronic apparatus for permeation, a) Bank MP87 potentiostat and Bank TG97 potentiostat/galvanostat, b) Volcraft VC960 multimeter with data recording function

To begin the experiment, the specimen is installed between the two cells. After this, the detection cell (cathodic) was filled with 250 mL of .1M NaOH solution. The potentiostat (Fig 3-20a), a Bank Elektroniks Wenking MP87 that is hooked to this cell is energized to -205mV vs SCE. The detector (Fig 3-20b) that is measuring the μA of current in the cell is sampling at 1 data point every second and recording the data into a file on the computer. The test runs until the signal reaches a baselined steady-state. After this, 250mL of the electrolyte that is explained in the charging section (section 3-3) is poured into the anodic cell and the Bank Elektroniks TG97 galvanostat is energized and set to produce 30 mA/cm² across the surface area of the specimen. The test is run until the detector increases and then reaches steady state again.

4. Results and Discussion

4.1 Comparison of “New Production” vs. “Used in Application” Materials

4.1.1 Initial Hydrogen Concentration of the Test Materials

The new barstock materials, i.e. the steels 4340N and S53N have been degassed up to 850 °C as shown in the experimental section. No hydrogen has been detected in the as delivered steel S53N. However, the “new barstock” 4340N material exhibited some small hydrogen concentration levels ranging between 0.2 and 0.7 ppm, which are at the approximate measurement certainty limits of 0.1 ppm of the hydrogen degassing equipment.

In contrast, some amounts of hydrogen have been found in the as-used materials. As shown in Figure 4.1, the initial concentration in the used Cd-free, but still Cr-coated 4340 steel has been 1.2 ppm, while quite lower concentrations of around 0.7 ppm have been detected in the Pd-coated and Cr-plated material. A comparison of the respective degassing curves shown in Figure 4.2 reveals that the Cd-coated material (Figures 4.2c and 4.2e) shows a second hydrogen release peak at a temperature of about 550 °C, while the non-Cd-coated material (Figure 4.2a) does not show this second peak. Such a second peak in the degassing curve, particularly at elevated temperatures, represents an indication for some trapped hydrogen. However, since the specimen have been degassed up to 850 °C and no other peak occurred at even higher temperatures, this portion is in comparison to the main hydrogen release only reversibly trapped.

Although for a more detailed analysis of the kind of trap corresponding to this temperature and binding energy slower degassing with a smaller heating rate might be helpful, it can tentatively be concluded that such hydrogen has been trapped at the interface between the Cd-coating and the substrate, since such a second hydrogen release peak has not been found in the Cd-free material. It should be noticed in this context that trapping of hydrogen at Cd-coatings has been reported earlier and thus, represents a well-known phenomenon.

Since no irreversibly trapped, i.e. deeply bound, hydrogen has been detected in this material, it has to be anticipated that the hydrogen detected in the “used component” 4340U material has been taken up during long-term service. It could be assumed that such hydrogen

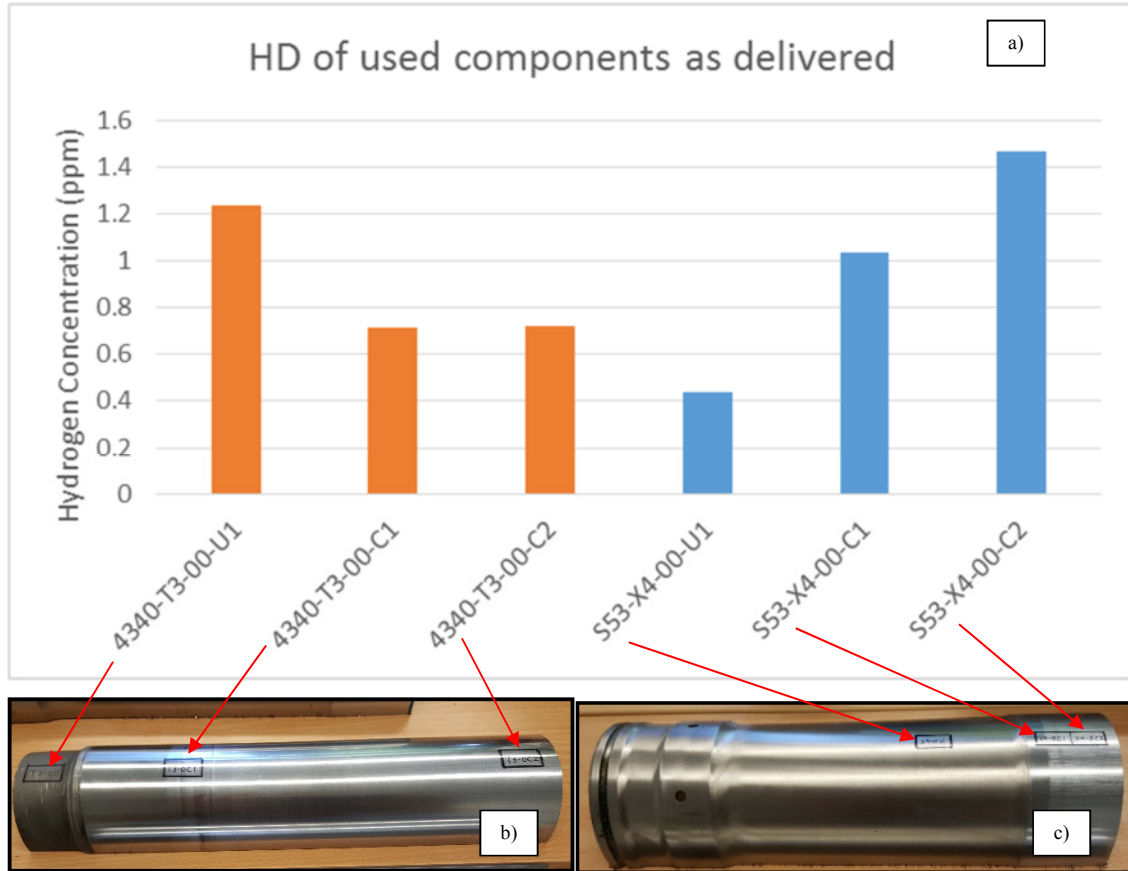


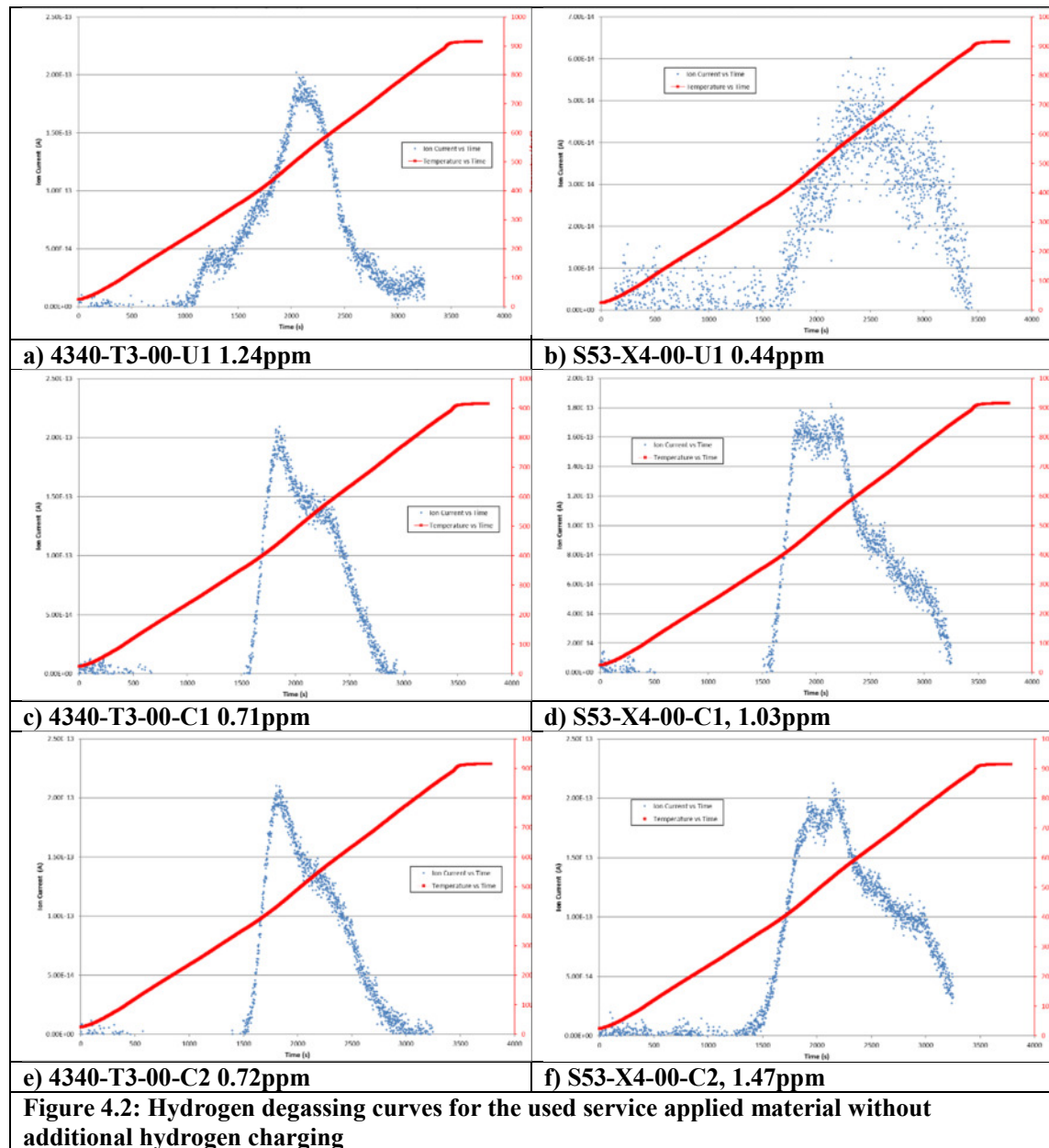
Figure 4.1: a) Hydrogen concentrations in used material, b)4340 used material extraction sites, c) S53 used material extraction sites

concentration might have been quite higher, since the material experienced some lay-over time after demounting of several months, i.e. it underwent also some time to release hydrogen.

In the context of the Cd-free materials it should be considered that all the material has been also Cr-plated prior to the Cd-coating and thus, that the measured hydrogen portion in the Cd-free material might also have been introduced during the Cr-plating and might have been released from the respective interface between the Cr-plating and the substrate.

To sum this up, the Cd-coating might have prevented some hydrogen uptake during service, since the Cd-coated specimen contained only up to 60% of the concentration measured in the

uncoated material. But, the Cd-coating evidently acts as a sink (reservoir) hydrogen at the coating-substrate interface.



Cd-coating, it might thus also entail a safety risk. The latter is entailed by trapping hydrogen at the interface which might not be released over a long time, but instead with a good opportunity to enter the high strength substrate and initiate cracking.

In contrast to the at least Cr-plated 4340 steel, relatively low hydrogen concentrations have been measured in the used S53 steel without any coating or plating. However, similarly high hydrogen concentrations have been found in the Cr-plated service-applied S53 steel.

From the degassing curves, it can be derived that the blank S53 steel as well as the Cr-plated material exhibit a not very pronounced second hydrogen release peak, corresponding to a temperature of 700 °C, i.e. at a somewhat higher temperature range as the second peak has been found in the 4340 material. But, since the non-plated S53 specimens also exhibited such a second peak and since the Cr-plated AISI 4340 material did not exhibit such a second hydrogen release peak, it should be accepted that this peak in the S53 does not stand in correlation to any hydrogen release from an interface between the Cr-plating and the substrate. It has thus to be anticipated that hydrogen is trapped internally at some site of the S53 microstructure. Again, it should be accepted that the hydrogen is only reversibly trapped in the S53 microstructure, since the release temperature is still lower than what is usually found for deeper hydrogen traps, i.e. ranges at temperatures still quite below 850 °C. Additionally, it is, if at all, only a very small portion of hydrogen that is trapped in the used service-applied steel S53. It has also to be anticipated that such hydrogen has been taken up during service, since for S53, at least, recommendations exist for hydrogen bake out (191 °C for application dependent times of up to 23 hrs - SAE AMS 2759/9). It should be mentioned in this context that such hydrogen removal heat treatment procedures have their limitations with respect to annealing the material and lowering the strength.

4.2 Hydrogen Charging

4.2.1 Hydrogen Uptake and Trap Characteristics of Tensile Test Specimens

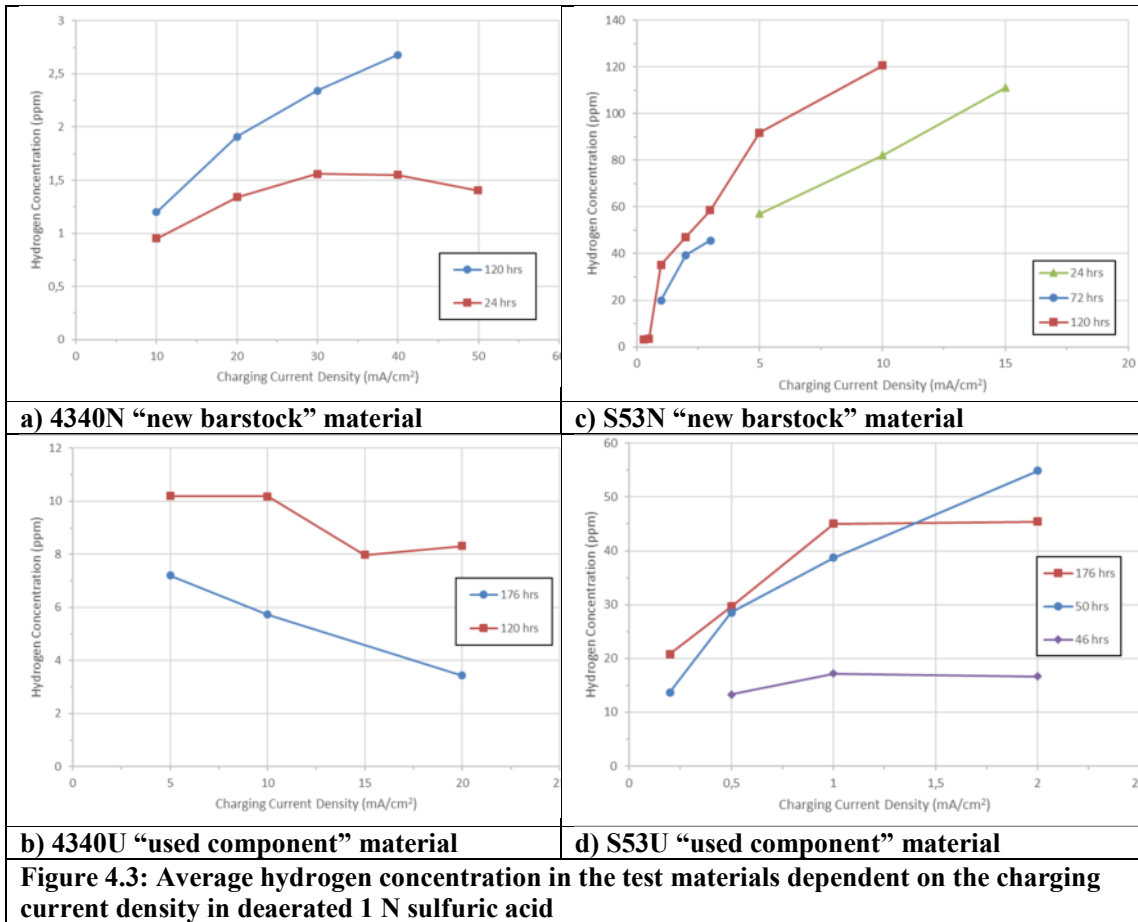
All materials used and new were tensile tested as delivered and no hydrogen removal heat treatment has been performed on purpose to check if there is any HAC related tendency of the used materials.

The materials have been cathodic charged with hydrogen, as outlined in the experimental section. Here, under the Argon bubbling and respective deaerating, different current densities will provide different hydrogen amounts offered at the surface that are then absorbed to a certain extent by the material. The exposure time will then lead to respective saturation of the

specimens. By a pre-calculation via simple solutions of Fick's second law it has been evaluated that charging times above 100 hours, should be sufficient to completely saturate the specimens. For most of the specimens, a charging time of 176 hours, i.e. more than seven days, has thus been selected to ascertain that the specimens have been completely saturated with hydrogen. The respective current density over this period then provides different amounts of hydrogen offered the specimen surface, thus providing different absorbed subsurface concentrations leading to complete saturation of the specimen over above mentioned period of about one week. This roughly means that the charging time entails saturation of the specimens, while the current density reveals different hydrogen concentration levels of the specimens.

Figure 4.3 illustrates the absorbed hydrogen concentration (HD) versus charging current density for the defined times for 4340 and S53 in the new-barstock and in the used service-applied condition. Already from these plots it becomes very evident that the hydrogen solubility in the two steel microstructures is significantly different. While hydrogen can homogeneously be dissolved in the new-barstock low alloyed steel 4340 only in concentrations up to 2.5 ppm (Figure 4.3a), the high alloyed new-barstock S53 can absorb 120 ppm and, as shown in experiments not considered here, also up to 150 ppm (Figure 4.3c). This is actually an indication for a significant trapping capacity of the microstructure. Since the S53 studied here has a chemical composition comparable to another investigated ultra-high strength steel of this type [6], it might tentatively be assumed that predominantly the carbide precipitates, but also the austenite phase and respective trapping at the austenite-martensite interface represent the origin for such high hydrogen solubility.

As also can be seen by comparing the Figures 4.3a and 4.3b, the steel 4340 evidently can solute more hydrogen in the used service-applied condition than in the state delivered as new barstock material. Achievement of somewhat higher concentrations at shorter charging durations of the samples of the "used component" 4340U steel should be attributed to the fact that no Ar purging has been carried out during charging of those samples entailing an uncontrolled oxygen content in the solution. This also might have been the reason why hydrogen is taken up in lower concentrations with increasing charging current density in these specimens.



However, all S53 specimens have been hydrogen charged under Ar purging which entailed more consistent electrochemical conditions for the hydrogen adsorption and absorption process. A comparison of the Figures 4.3c and 4.3d shows that significantly higher hydrogen concentrations can be dissolved by the “new barstock” S53N steel, as compared to the service-applied condition S53U. It should be mentioned in this context that the new S53N material contains up to 40% of retained austenite which might act as a hydrogen sink, in particular at the martensite-austenite interfaces. However, the main reason for the significantly lower hydrogen concentrations in the S53U steel is given by charging this material with an order of magnitude lower current densities which had the intention to investigate the materials property degradation of this material more in detail for presumed uptake of hydrogen at lower concentration levels during service.

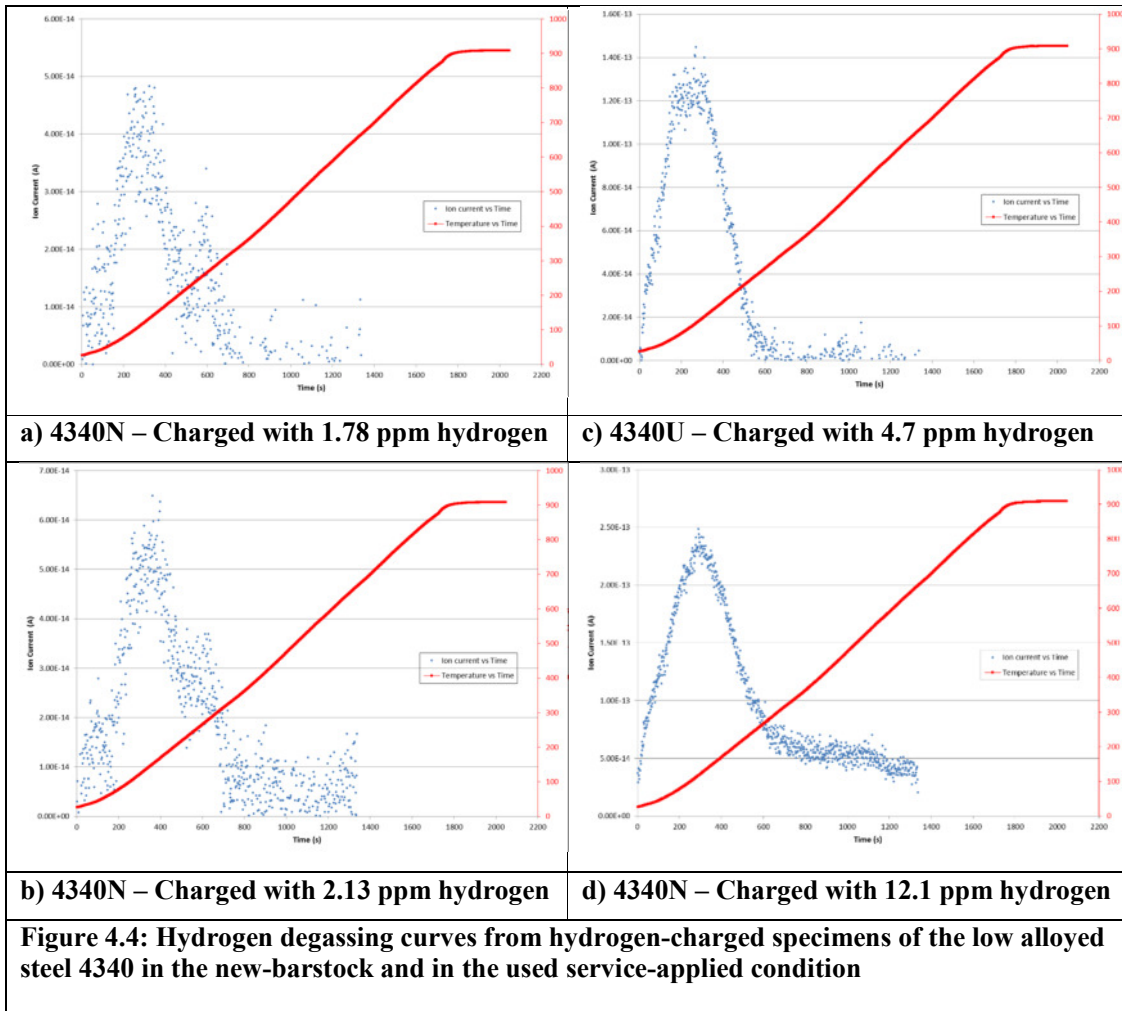


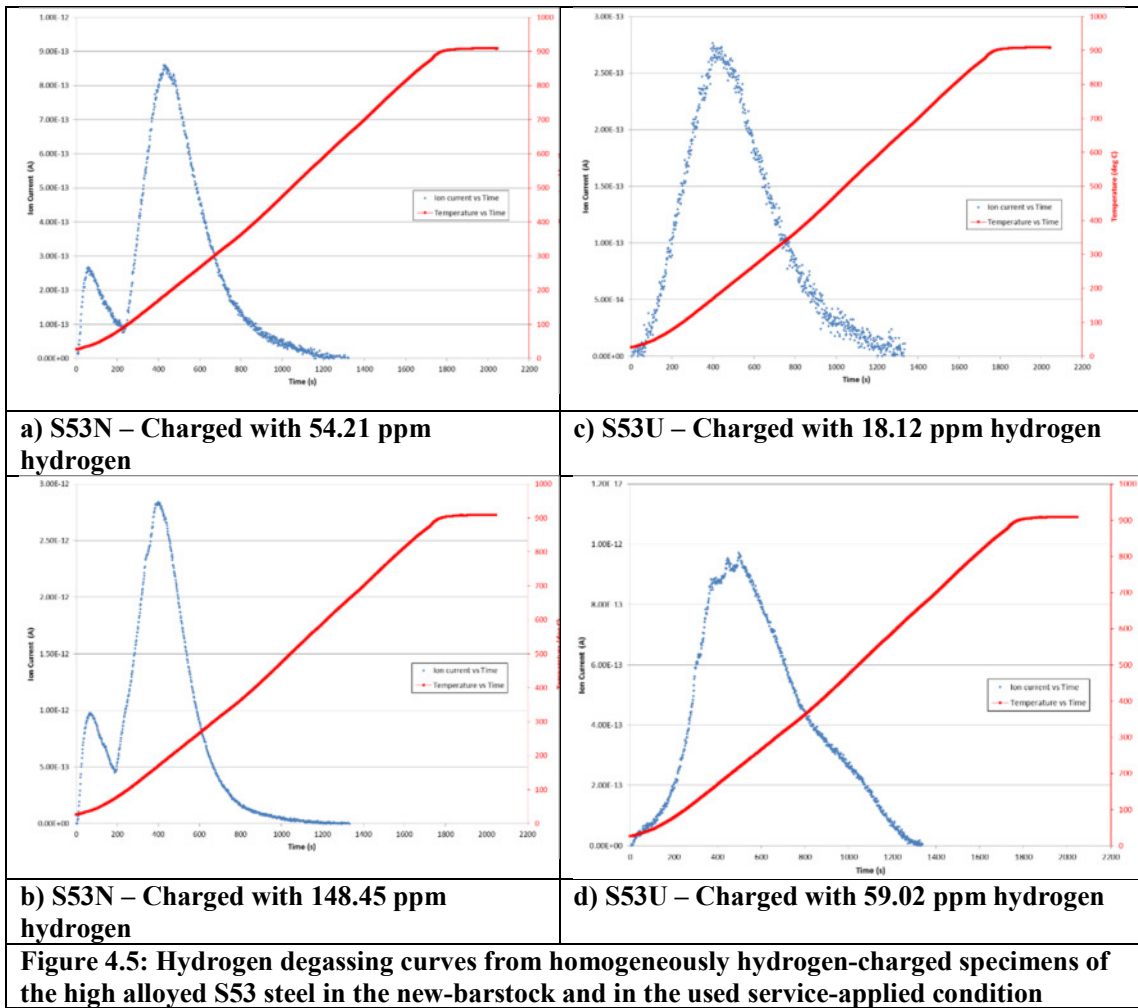
Figure 4.4 shows exemplary hydrogen degassing curves of some hydrogen-charged specimens of the steel 4340 in the new (Figures 4.4a and 4.4b) and in the used service-applied condition (Figure 4.4c and 4.4d). Although the data points show some scatter for the fairly low hydrogen concentrations dissolved in the new 4340 steel, it can be derived that particularly the new material seems to exhibit a second peak during hydrogen degassing. While the first peak corresponds to a degassing temperature of 200 °C, the second peak corresponds to about 300 °C. It can thus be anticipated that the main peak at 200 °C corresponds to the release of hydrogen from the martensitic lattice, while the second peak indicates some very slight trapping. The degassing curves, particularly at such scatter, do perhaps not allow a thorough thermal desorption analysis.

However, the fact that second peaks occurs only at lower temperatures and no additional hydrogen release peak has been observed at higher temperatures of up to 900 °C indicates that, if at all, no deep trapping of hydrogen occurred in the electrochemically charged steel 4340 in the new bar-stock condition.

As already mentioned above, the Figures 4.4c and 4.4d in comparison to the plots shown in the Figures 4.4a and 4.4b reveal that the steel 4340 can evidently absorb up to about five times higher hydrogen concentrations in the used service-applied condition. Generally, it can be seen from these plots that the degassing curves become clearly much smoother and better evaluable, if respectively more hydrogen has been absorbed in the specimens. The degassing curves of the used 4340 steel (Figures 4c and 4d) show some smaller hydrogen release peaks in the temperature range between 400 and 500 °C, indicating some slightly deeper trapping in the steel 4340 in the used service-applied condition as compared to the new bar-stock material. However, also in this condition the steel did not exhibit any further peaks during hydrogen degassing at higher temperatures.

To sum this up, the hydrogen degassing curves reveal that electrochemically charged hydrogen is not deeply trapped in the steel 4340 in the new and the used condition. It can thus be anticipated that hydrogen entering such material electrochemically is only reversibly trapped, if at all. This, in turn, allows using overall diffusion coefficients and application of Fick's Second Law for any calculations of hydrogen transport in this martensitic low alloyed steel.

Some exemplary hydrogen degassing curves for the new as well as the service-applied S53 steel are summarized in Figure 4.5. By comparison of the curves for the new S53N material (figures 4.5a and 4.5b) with those for the used material (Figure 4.5c and 4.5d) it becomes evident that the new steel always showed a very pronounced second hydrogen release peak that was even higher than the first peak. The fact that the second peak is related to only a slightly temperature of about 200 °C as compared to the first peak at about 50 to 100 °C and no further peaks occurred at any temperature of the whole heating regime up to 900 °C clearly indicates that no irreversible trapping of hydrogen occurs in the steel S53, not in the "new barstock" and not in the "used component" condition. This and the fact that no significant amounts of retained austenite have been detected in the service-applied steel S53U allow the tentative conclusion that the second hydrogen release peak is exhibiting the hydrogen release from the austenite



phase. As indicated by the comparatively high peak, the austenite evidently solutes more hydrogen than the martensite phase in this material.

4.2.3 Mechanical Properties of the New and Used Materials Dependent on the Hydrogen Concentration

Figure 4.6 shows exemplarily the stress-strain diagram for the “new barstock” S53N steel to show how the yield strength ($YS_{0.2}$), evaluated by the 0.2% offset method and the ultimate tensile strength (UTS) have been determined. Regarding the deformation capabilities and respective ductility characterizing parameters not the technical fracture as indicated in the diagram, but the dimensionless true fracture strain and the reduction in area have been determined by the common formulas given in literature [111].

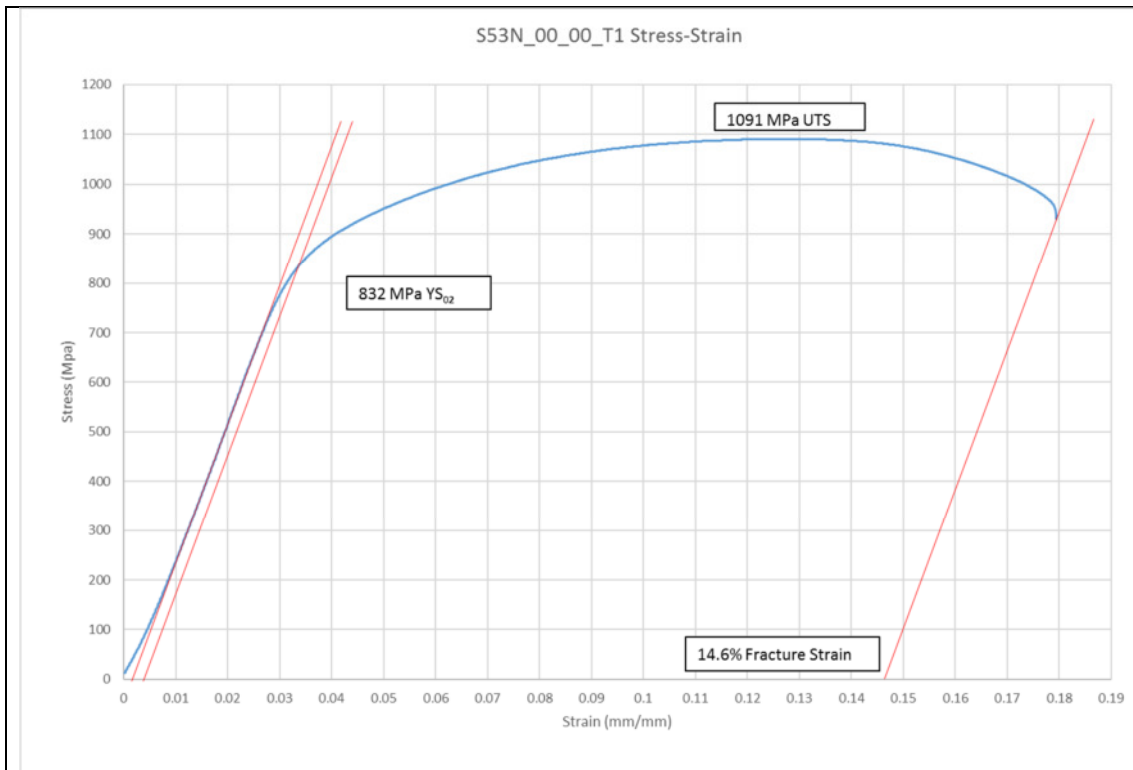


Figure 4.6: Evaluation of material properties exemplarily shown for the S53N new barstock material tensile test diagram

As an overview, the Figure 4.7 shows the compilation of stress-strains diagrams for all 4340 steel test specimens hydrogen-charged at various concentration levels. Already from these technical these stress-strain curves it can be clearly seen that increasing hydrogen concentrations in the materials – as for most metallic materials and particularly in steels – considerably reduce the ductility in terms of fracture strain and to a much lesser and in sometimes even no extent reduce the properties in terms of strength. However, in the new steel 4340, a slight increase of the strength, i.e. the yield strength can be seen with hydrogen concentrations above 1 to 2 ppm (Figure 4.7a). Similar to previous observations by others, this can be attributed to reaching the solubility limit inside the lattice and to the assembly / trapping of hydrogen in the vicinity of dislocations, i.e. blocking dislocations and thus increasing the strength to a limited extent. A similar effect, here mostly with a pronounced Portevin-LeChatelier effect, has been reported by nitrogen in bcc steels [111]. It can thus be anticipated that the same, although to a much lesser extent, occurs in the martensitic microstructure of the new steel 4340N, particularly by considering that the lattice solubility of martensite at room temperature ranges at the same level of 2 ppm.

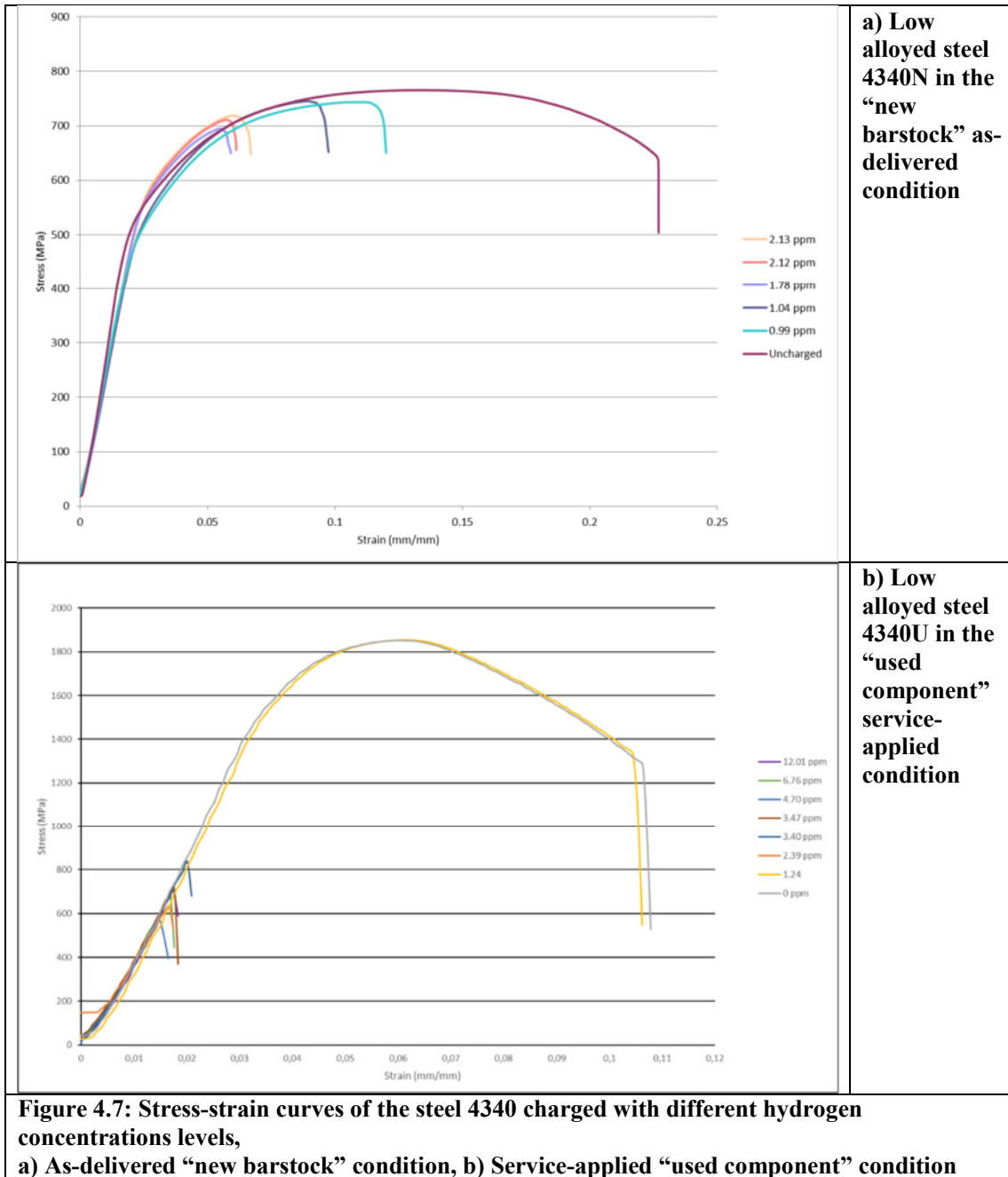
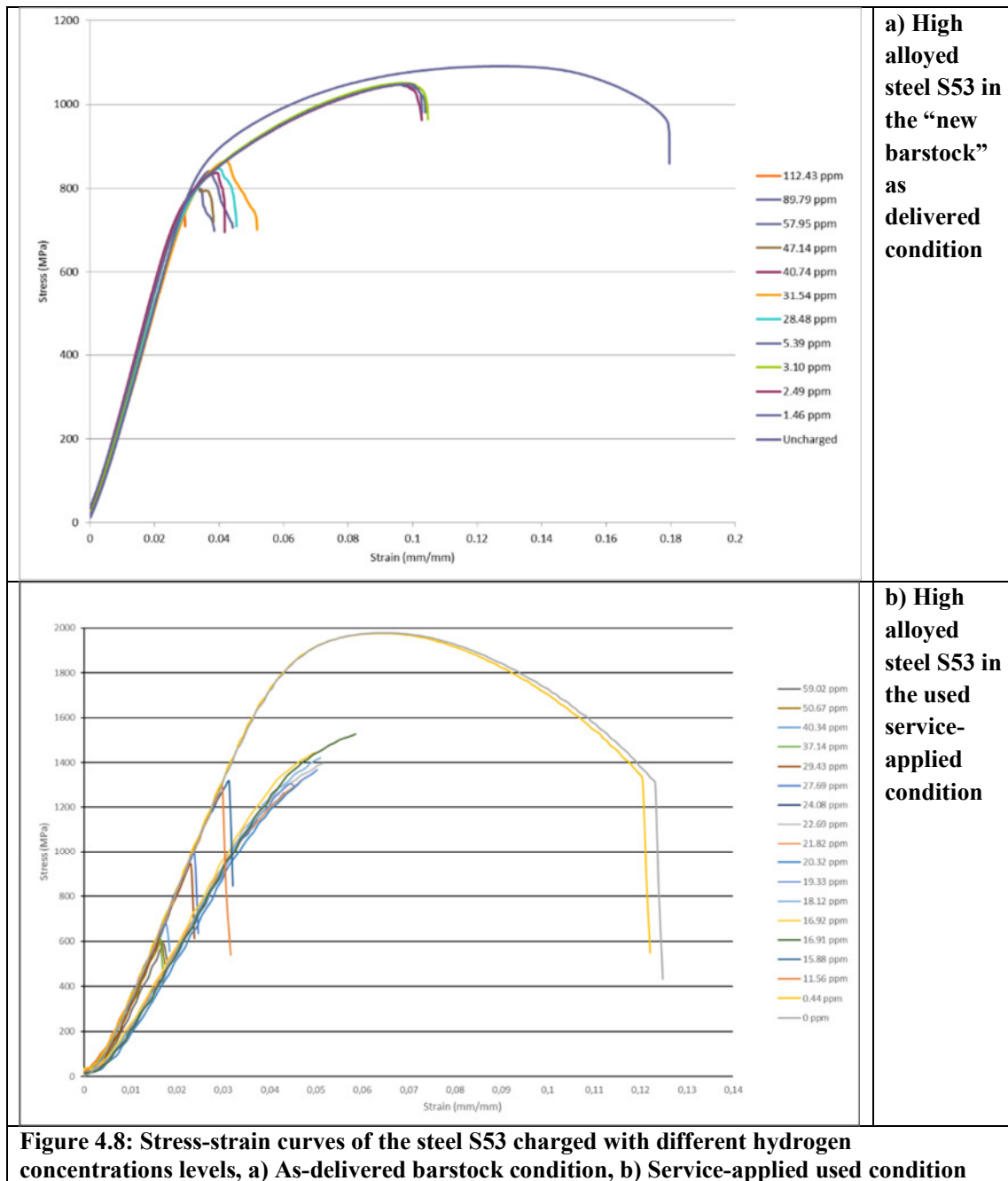


Figure 4.7: Stress-strain curves of the steel 4340 charged with different hydrogen concentrations levels, a) As-delivered “new barstock” condition, b) Service-applied “used component” condition

It should be emphasized, the low alloyed steel 4340 N in the as-delivered condition does probably not match the criteria for a landing gear steel at all. In contrast, the real service-applied steel 4340U exhibits about three times higher strength levels (Figure 4.7b) which are nearly in the same range than those of the new and used high alloyed steel S53. However, the steel 4340 experiences also in the used condition a severe reduction of ductility, as indicated by the stress-strain curves of the hydrogen charged specimens. Also, with increasing hydrogen

concentrations, no strength increase could be observed and not even the original yield strength of this material could be achieved.



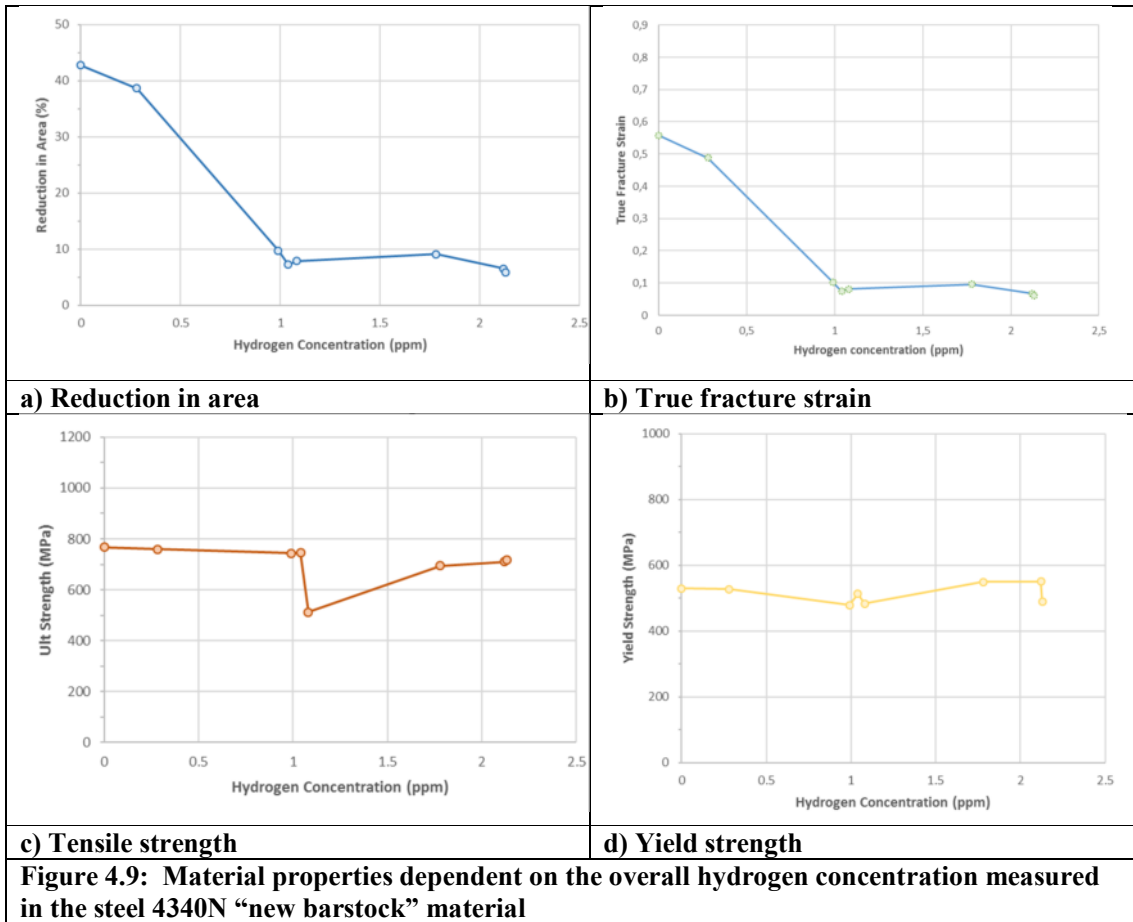
In comparison to the low alloyed steel 4340, Figure 4.8 shows the stress-strain curves for the steel S53 charged with hydrogen at various concentration levels. A comparison of the two charts shows quite clearly that also the service-applied steel S53U has a much higher strength than the

new-barstock material S53N. In addition, the strength level of the service-applied material S53U (Figure 4.8b) is even higher than that of the used lower alloyed landing gear steel 4340U (Figure 4.7b). The steel S53 also does not show any strength increases at lower hydrogen concentration levels, as observed in the as-delivered low alloyed steel 4340N. While with increasing hydrogen concentrations at least the original yield strength level is still reached in the as-delivered new steel S53N this is by no means the case for this alloy in the service-applied condition S53U. The smaller gradients of some stress-strain curves in Figure 4.8b have been caused by the fact that these tests have been carried out with another tensile test machine, as compared to the previous ones (Figures 4.7 and 4.8), which had a different compliance of the mounting devices versus the tensile test specimens, i.e. the mounting devices of the second machine have been less stiff than those of the first machine. This, however, does not have any influence on the test results with respect to the mechanical properties determined here.

For practical service applications, it should be realized at this point that both materials, i.e. the low alloyed steel 4340 as well as the high alloyed steel S53, can not only lose ductility with increasing dissolved hydrogen concentrations, but might not even achieve their original design yield strength level. It can already be stated at this point that any hydrogen uptake during production and service of landing gear components manufactured from these materials should be avoided under all circumstances.

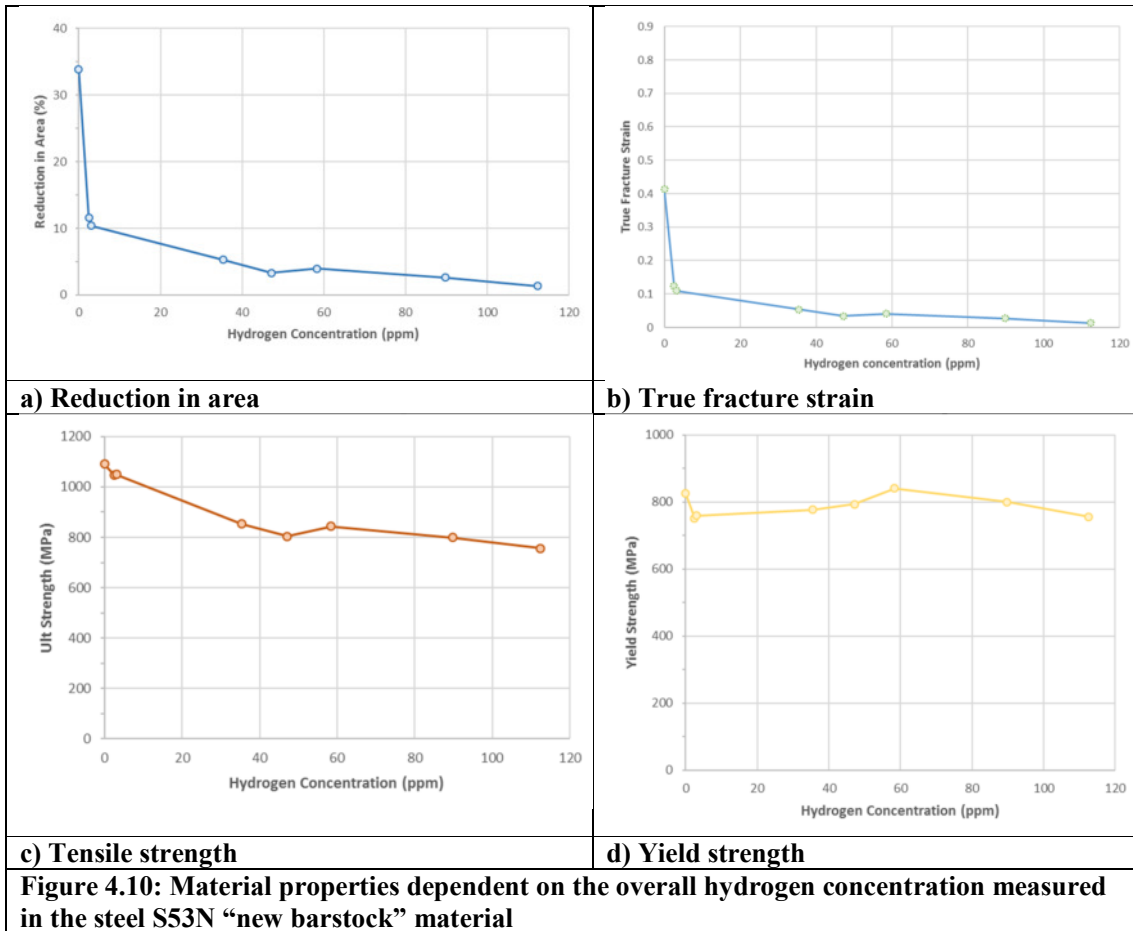
However, to determine the hydrogen concentration limits that these landing gear materials do tolerate, particularly in the service-applied condition, the respective material properties have been assigned to the following Figures 4.9 to 4.13 dependent on the hydrogen concentration in all four materials tested, i.e. 4340 in the new and used as well as S53 in the new and used state. This is relevant as crack criterion for crack propagation calculations, as for instance numerical analyses based on the finite element method [25].

At around 1 ppm, fracture of the specimens appeared immediately after yielding, as also indicated by a significant drop of the tensile strength (Figure 4.9c). It can also be seen that between 1 and 2 ppm (approx. lattice solubility of hydrogen in bcc iron), the yield strength and the tensile strength was slightly increasing (Figure 4.9d) again, however without reaching the tensile strength level of the uncharged material.



Such effects of hydrogen on the tensile properties associated with the above mentioned significant ductility loss can be attributed to respective hydrogen dislocation interactions and associated solid solution strengthening. This is a commonly observed phenomenon in bcc alloys with a pronounced yield point [4, 8].

In general, the higher alloyed new material, S53, seems to be slightly more tolerant to hydrogen with respect to any ductility losses, although having a considerable higher yield and tensile strength. For instance, at a hydrogen concentration of about 2 ppm, the reduction in area still ranges at about 11% in the new design alloy (Figure 4.10a), while it already is reduced to about 6% (Figure 4.19a) in the conventional steel 4340N in the as-delivered “new barstock” condition. It should be mentioned in this context that the area reduction represents a quite common materials property parameter to describe behavior of materials subjected to saline and/or hydrogenizing environments.



However, consistently, the true fracture strain still ranged about 0.11 or 11% in the S53N material (Figure 4.10b), while it was degraded already to about 7% in the 4340N steel. Similar to the 4340N steel, necking was also present in the S53N material - but not occurring at hydrogen concentrations above 2 ppm.

But, a totally ductility loss in terms of fracture at yielding was detected in the S53N material only at very high hydrogen concentrations above 20 ppm, i.e. this material becomes totally brittle only at hydrogen concentrations above 25 ppm. However, at considerably high concentrations, $HD \geq 30$ ppm, the reduction in area in S53N was substantially lower, equal to and below 5% and with this, ranged below the values obtained for the conventional 4340N material.

Also remarkable, it appears that no increase in yield strength at hydrogen concentrations of about 2 ppm has been observed in the S53N material. Instead it decreased slightly (Figure

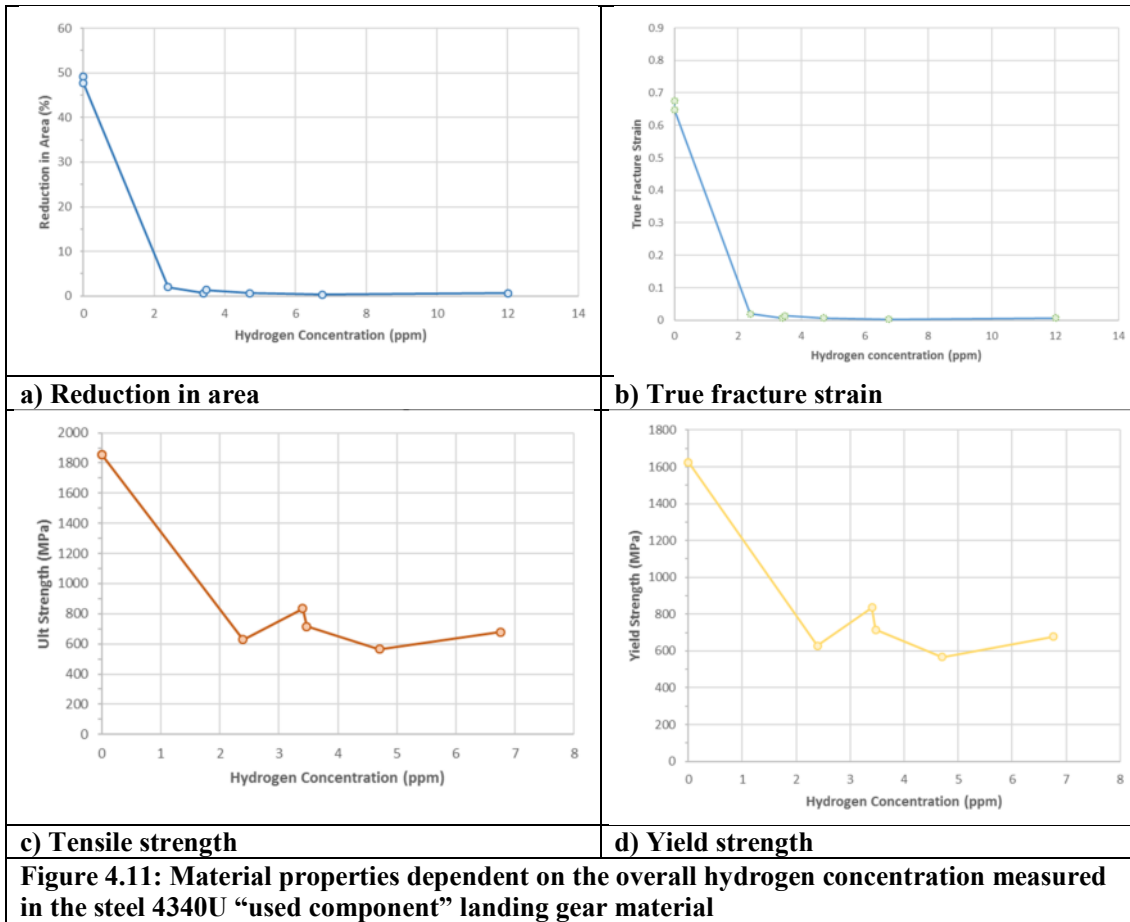
4.19d). However, there has been observed a slight increase with increasing the hydrogen concentration to significantly high values of about 60 ppm, followed by a slight decrease towards considerably extreme concentrations above 110 ppm. To sum this up, hydrogen causes a slightly lower degradation of ductility in the as delivered condition the S53N material which has also a much higher yield strength than the as delivered 4340N material.

For the first time, used landing gear material in terms of the commonly applied steel 4340 has been investigated with respect to its hydrogen concentration dependent material properties. Again, it should be emphasized that this material in the condition as tested here, is very frequently used for military as well as civil airplane landing gear. A comparison of the Figure 4.11 to Figure 4.9 immediately reveals that the used steel shows in the uncharged condition a much, i.e. about three times, higher yield strength, as compared to the as-delivered “new bar-stock” condition. was registered for the used 4340U steel, as compared to the “new bar-stock” material. Remarkably, also the ductility of the used steel has been considerably higher than that of the “new bar-stock” material, as can be drawn from a comparison of the Figures 4.11a to 4.9a and 4.11b to 4.9b, respectively. For instance, the true fracture strain has been evaluated in the used material ranging at about 0.65 or 65% while it ranges at about 0.55 or 55% for the new bar-stock material.

It can only be emphasized that in reality, for application as landing gear material, the steel has evidently been heat treated, i.e. quenched and tempered, in a very suitable way with significantly improved mechanical properties.

However, hydrogen severely degrades the improved material properties of this steel. At concentrations ranging slightly above 2 ppm the reduction on area and, much more prominent as crack nucleation and propagation criterion, the true fracture strain are both reduced to about 2%. This means, the steel 4340 in the heat treated and used condition behaves much less tolerant to any absorbed hydrogen, although exhibiting much better ductility properties in the uncharged condition.

Remarkably, not only the tensile strength (Figure 4.11c), but also the yield strength (Figure 4.11d) is significantly reduced, if hydrogen concentrations above 2 ppm have been absorbed. It should be emphasized that such drastic degradation of the material properties even below the

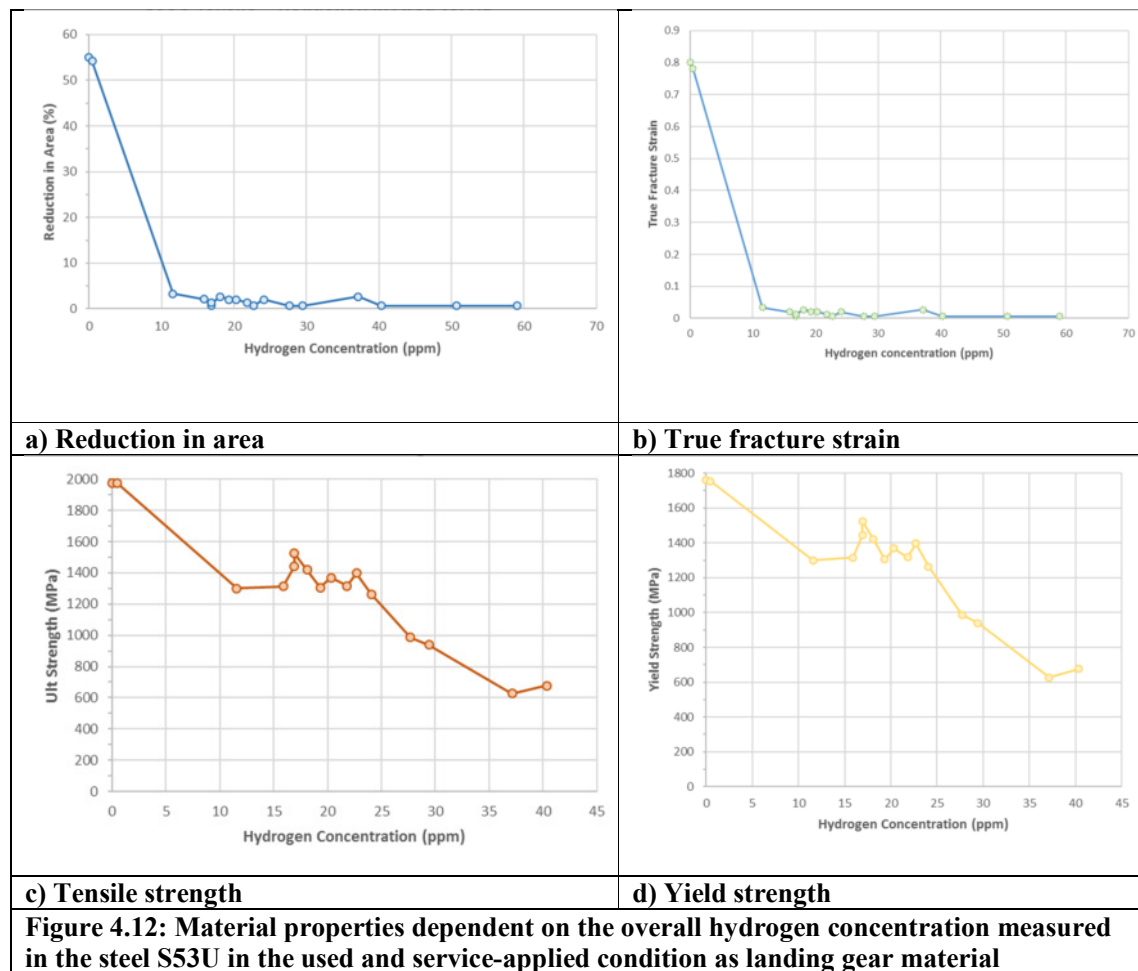


yield strength in the uncharged state have not yet been observed in any martensitic steel microstructure.

Both strength properties, not only the tensile strength, but also and in a similar way the yield strength are reduced to about 50%, if hydrogen is introduced into these microstructures in concentrations above 2 ppm. For practical use as landing gear material, regardless in the military or in the civil aviation, any absorption of hydrogen during production and/or service has thus and under any circumstances to be avoided. However, as shown in the diagrams in Figure 4.10, up to a hydrogen concentration of around 1.4 ppm measured in the used material, the service-applied steel 4340 does not show any significant degradation of mechanical properties. But above 1.5 ppm towards concentrations above 2 ppm a drastic decrease of mechanical properties, particularly the ductility related values reduction in area and true fracture strain has been determined. That means that only a slight increase of the hydrogen concentration by 0.5 ppm above 1.5 ppm might cause a severe drop of the mechanical

properties, particularly in terms of ductility. It should be emphasized from the knowledge about several types of martensitic steels, that particularly by an increase from 1.5 above 2 ppm such materials might get prone to HAC and exhibit such drastic reduction of the material properties.

Regarding real service applications, slight differences in the hydrogen tolerance of a material below 2 ppm cannot be managed properly. This accounts particularly to the Cd-coating which is known to provide hydrogen sinks at the interface the Cd-coating and the substrate. In other words, if hydrogen is released even in small concentrations from such coatings into the matrix of the substrate this might entail a severe risk for HAC. In addition to any environmentally related restrictions during its application, the Cd-coating of the high strength 4340 steel might thus additionally increase the cracking risk of such steels.



Not only for a better environmental compliance, but also to avoid any HAC risk associated by hydrogen release from the interface between the such coatings and the substrate it is beneficial to design the landing gear components by using materials that do not need any Pd-coatings. Evaluation of the hydrogen dependent mechanical properties of such materials is thus essential.

For such reasons, the dependence of the tensile properties on the dissolved hydrogen concentration has been investigated in detail for the alternative S53 material in the used condition and is summarized by the diagrams shown in Figure 4.12.

From these diagrams, consistent to the results of charging of the tensile test specimens, it can be seen that the S53 steel also in the used and application heat treated and very high strength condition solutes much more hydrogen than the 4340 steel.

In the non-charged condition, similar to the low alloyed 4340 steel, the S53 steel shows in the processed and service-applied state a significant increase in ductility. As a comparison between the diagrams in the Figures 4.12a and 4.12a as well as in the Figures 4.12b and 4.12b reveals, the ductility of the service applied S53 steel in the uncharged state is 55% as compared to 32% with the new barstock material concerning the reduction in area and even reaches a value of about 0.78 or 78% regarding the true fracture strain, as compared to 0.42 or 42% of the new barstock material.

Generally, hydrogen affects the mechanical properties of steels more in terms of ductility than in strength. It is thus quite remarkable that the ductility of the S53U steel is also much higher than that of the up to now widely applied 4340 steel. From a comparison of the Figures 4.12a and 4.12b to the Figures 4.10a and 4.10b, it becomes evident, that the reduction in area reaches 55% in the S53U, but only 48% in the 4340U steel. As most relevant crack initiation and propagation criterion, the significantly high true fracture strain of 0.78 (78%) in the non-hydrogen-charged S53U material is also not matched by the commonly applied steel 4340U and ranges at 0.68 (68%), if it is also not charged with hydrogen.

Despite ductility and strength are usually antithetic material properties in steels, it has to be emphasized that also the tensile and the yield strength of the actually applied steel S53U

(Figures 4.12c and 4.12d) range at much higher values, i.e. have been nearly doubled in comparison to the new barstock material (Figures 4.10c and 4.10d).

Both used materials, 4340U and S53U, achieve thus ultra-high strength levels. In comparison to the low alloyed variant (Figures 4.11c and Figure 4.11d) the tensile and the yield strength of the S53U (Figures 4.12c and 4.12d) are even nearly 200 MPa higher in the uncharged condition.

It cannot be denied that hydrogen dissolved in the applied S53U steel significantly degrades the mechanical properties, similarly to the three other materials, i.e. S53 in the new and 4340 in the new and used state. Like the used 4340U steel, also the service applied S53U material does not show any degradation of the mechanical properties, in particular not in ductility, at the lower hydrogen concentrations of 0.45 up to 1.2 ppm measured in the service-used state. The ductility in terms of the reduction in area (Figure 4.12a) as well as of the true fracture strain (Figure 4.12b) is reduced to about 3% for both parameters, however, only at quite high hydrogen concentrations above the 10 ppm level. In comparison, the service applied low alloyed steel 4340 experiences such low ductility of about 2% already at five times lower hydrogen concentrations in the range of 2 ppm (Figures 4.10a and 4.11b).

As to be expected from such low ductility values, the five-year service applied S53U steel did not show any necking with increasing hydrogen concentrations. The tensile strength is reduced to the yield strength at hydrogen concentrations above 10 ppm which can be derived from a comparison of the respective plots in the Figures 4.12a and 4.12b. Interestingly, in the new-barstock S53N steel, this is the case only at considerably higher hydrogen concentrations above 45 ppm. However, it has to be taken into account that the yield and tensile strength of the S53N material range at about 50% of that for the service applied S53U steel.

Similar to the used 4340U steel, above a certain hydrogen concentration the service applied S53U steel does not even reach its original yield strength of about 1800 MPa. Again, this value ranges at far higher concentrations above 10 ppm as compared to the 2 ppm for the 4340U steel.

Both service-used steels seem to maintain their strength level of a certain hydrogen concentration range. While this is the case between 2 and about 7 ppm for the low alloyed 4340U variant, this concentration range covers between 10 and 22 ppm for the high alloyed S53U steel. At hydrogen concentrations around 17 ppm, a slight strengthening effect visible by

an increase of the yield strength (Figure 4.12b) could be observed, however, at still coincident yield and tensile strength (Figures 4.12a and 4.12b). At even higher hydrogen concentration levels above 25 ppm the strength of the S53U steel is further reduced to about 700 MPa at 40 ppm which is, interestingly, the strength level observed in the S53 new barstock material at a similar hydrogen concentration.

Summarizing the fundamental effects of hydrogen on the material properties in this section, it can generally be stated that the new as well as the service-used S53 steel achieves higher strength levels than the low alloyed material 4340 in the new as well as used state. Additionally, the S53 steel exhibits a considerably higher ductility in both, the new-barstock and service-applied, processing conditions than the low alloyed steel 4340. This higher ductility should be regarded as a major reserve of the S53 steel regarding any hydrogen related degradation of material properties as compared to the 4340 steel.

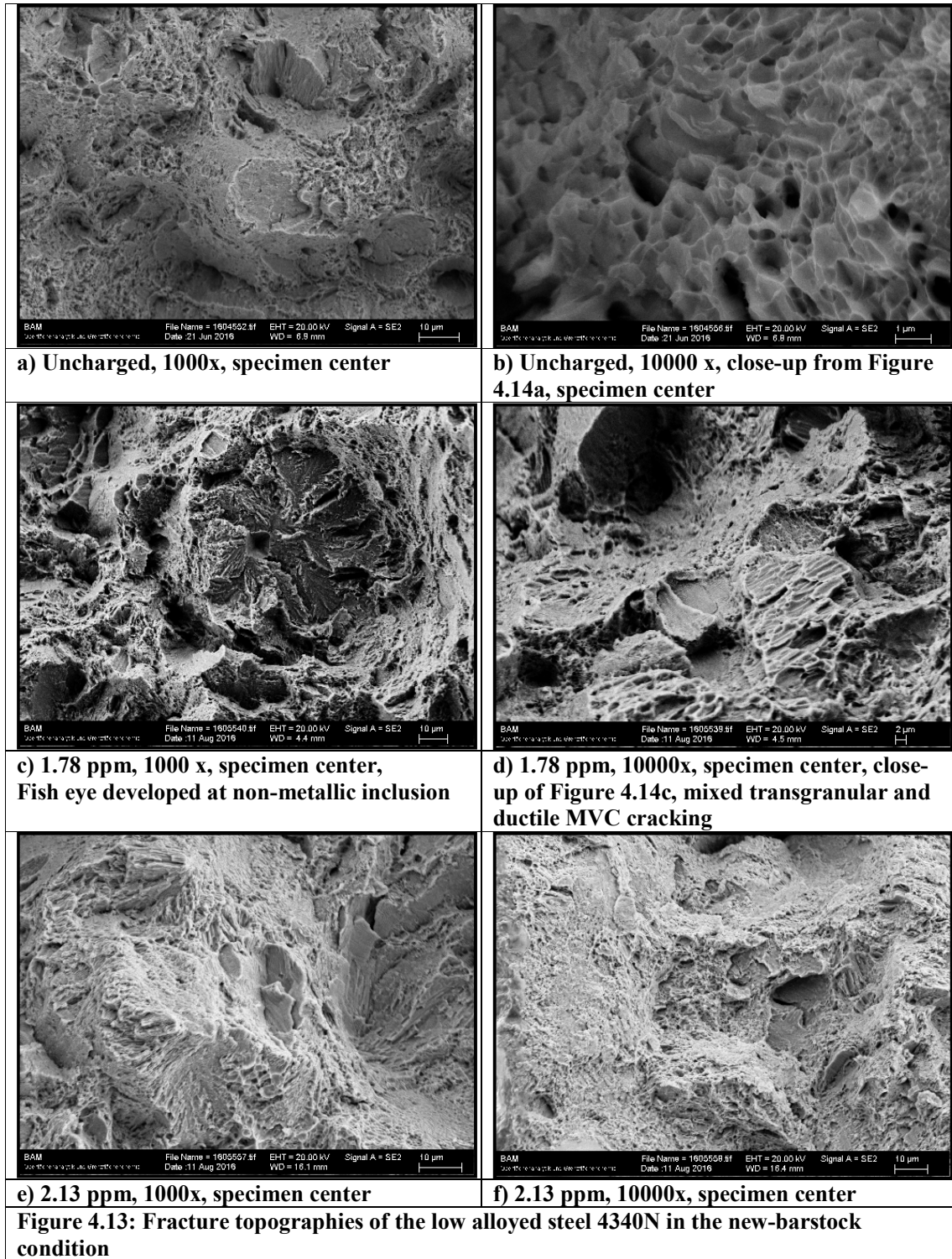
In particular, in the used or service-applied condition, the ultra-high strength design alloy S53 withstands up to 5 times higher hydrogen concentration levels of even above 10 ppm before showing any mechanical property degradation.

However, in the new as-delivered as well as in the ultra-high strength state the S53 steel can also solute much higher hydrogen concentrations than the 4340 steel in both conditions.

Further testing summarized in the Chapter 4.3 will then have to show how much hydrogen is really been taken up in the high-strength processed and service applied steel S53 under service-related conditions and how crack-resistant this material is under more realistic environmental conditions.

4.2.4 Fracture topographies of hydrogen charged tensile test specimens

Before evaluating the hydrogen assisted cracking appearance in the service-applied landing gear S53U steel in more realistic environmental conditions, principal evaluation of the fracture topography in both, the low and the high alloyed materials and in both conditions, i.e. in the new as-delivered and in the ultra-high strength service-applied condition, has been carried out and is summarized here.



Starting with the new-barstock low alloyed landing gear steel, the respective photo-micrographs taken by SEM investigation of the fracture surface are summarized in Figure 4.13. As can be seen from these, the steel 4340N exhibits common ductile fracture by microvoid coalescence

(MVC) in the uncharged condition. As the new-barstock material contained traces of hydrogen between 0.2 and 0.7 ppm such low concentrations clearly do not affect the fracture topography, as indicated by the ductile dimples on the fracture surface at lower (Figure 4.13a) and higher (Figure 14.3b) magnification. Also, the mechanical properties shown in Figure 4.9 seem not to be affected by such low hydrogen concentrations in this material.

At hydrogen concentrations above 1 and close to 2 ppm, this material exhibits increasing transgranular quasi-cleavage fracture, which becomes evident in Figure 4.13c at lower magnification and in Figure 4.13d at higher magnification. Figure 4.13c also shows a typical, if not classical, fish-eye developed at an inclusion in the center which is surrounded by transgranular fracture planes. At hydrogen concentrations below 2 ppm (Figures 14.3c and 14.3d) the predominant fracture type is still MVC with respectively shallower dimples than in the uncharged condition. However, at concentrations above 2 ppm the fracture surface of the tensile specimens exhibits mainly transgranular (TG) quasi-cleavage cracking (Figure 14.3e and 14.3f). Although still some ductile MVC parts remain on the fracture surface, the main transgranular portion is associated by significantly low ductilities, as shown by the area reduction in Figure 4.9a and the true fracture strain 4.9b.

Figure 4.14 represents an assembly of exemplary fracture surface micrographs from the uncharged and hydrogen-charged specimens of the low alloyed steel 4340U in the used service-applied condition. In comparison to the new-barstock material (Figures 4.13a and 4.13b), this material shows much shallower dimples in the uncharged condition which has to be attributed to its up to three times higher strength.

Similarly, to the new-barstock material 4340N, the specimen charged with a quite low hydrogen concentration of 2.39 ppm did not show any necking, i.e. a very brittle behavior, as already indicated by the tremendous decrease of the ductility parameters reduction in area and true fracture strain, shown in the Figures 4.10a and 4.10b, respectively.

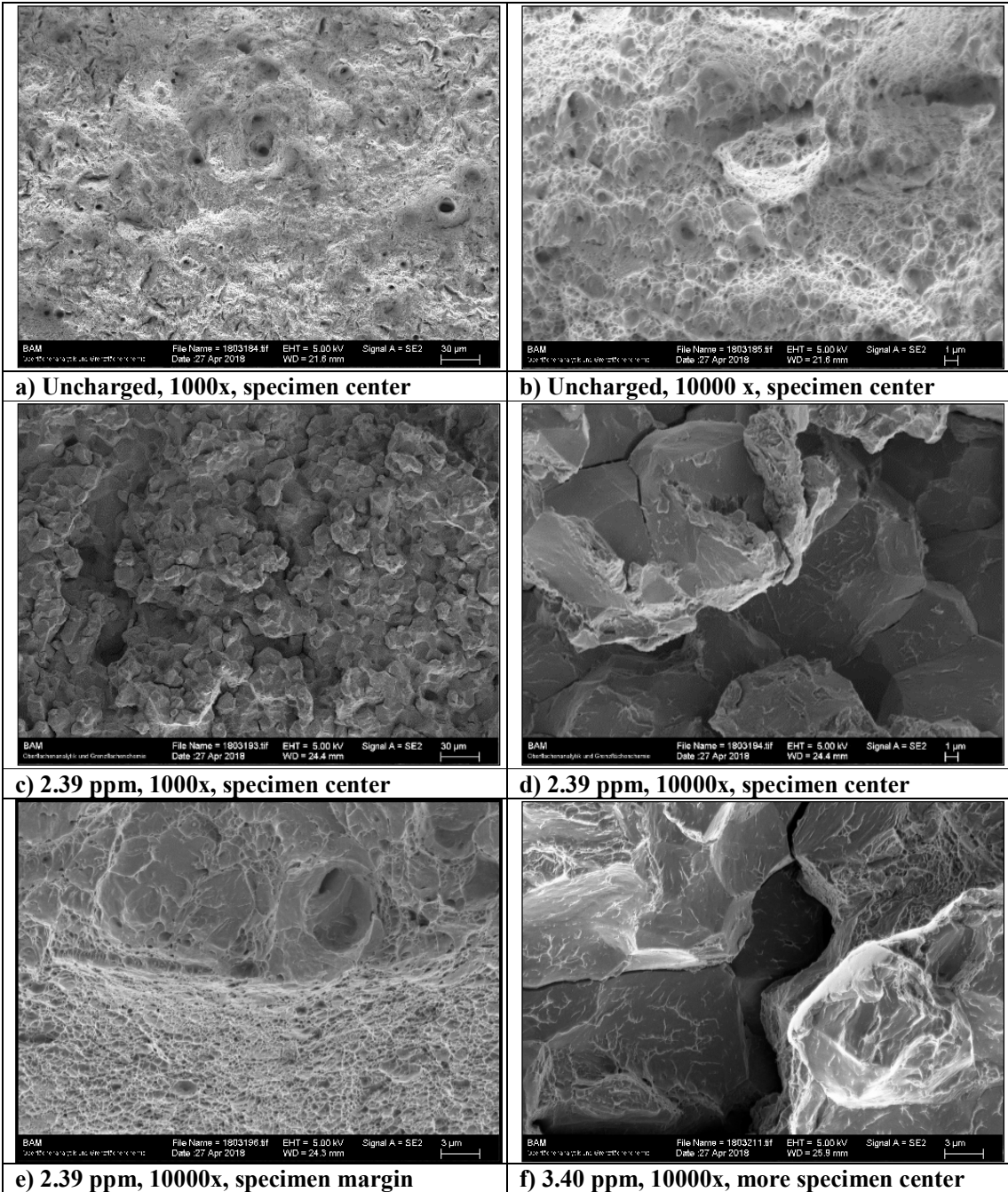
In this context, it should be reflected that in most high strength martensitic steels like the material 4340U the fracture topography changes significantly with increasing hydrogen concentrations. Lower hydrogen concentrations first lead to MVC with formation of much shallower dimples than the hydrogen-free material. With increasing hydrogen concentrations,

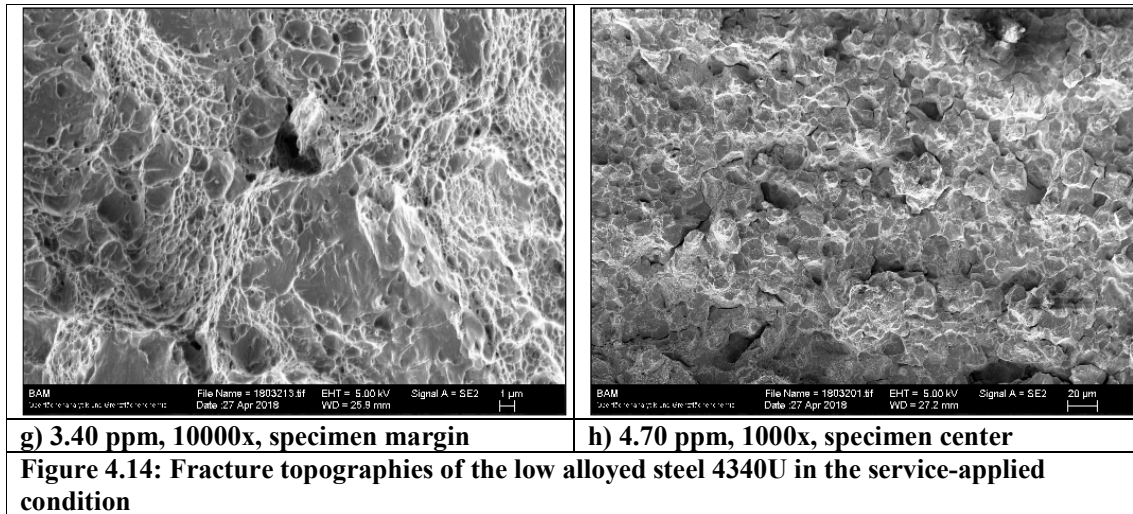
the fracture topography usually turns from MVC into a transgranular, mostly quasi-cleavage, cracking. At respectively high hydrogen concentrations the topography is then changing a second time into very brittle intergranular cracking, predominantly alongside former austenite grains. However, the changing of the fracture topography normally happens gradually and thus, the different types of the topography can be observed on the same specimen and in most cases, are mixed in the same region.

However, in contrast to the new low alloyed material 4340N that exhibited still transgranular cracking associated with shallow MVC at the same concentration of around 2 ppm, the high strength processed steel 4340U shows already at this concentration some portions of intergranular cracking, as shown in the Figure 4.14c taken from the respective specimen center.

Figure 4.14d shows a close-up of the nearly total intergranular region shown in Figure 4.14c and exhibits typical features of intergranular cracking caused by hydrogen like intergranular side-cracks and so-called bird-feet or hair lines on the grain faces. At such concentration, the used steel 4340U still exhibited larger portions with shallower dimples and also with a transgranular cleavage-like topography. Figure 4.14e shows exemplarily a region of transition between dimple and quasi-cleavage cracking, also typically observed in martensitic steels at lower hydrogen concentrations. This micrograph have been taken near the specimen margin and indicate a slight tendency towards a little more ductile cracking which might tentatively be attributed to a small loss of hydrogen evaporating from the specimen surface during tensile testing. However, based on the experiences made elsewhere [24,107], this does normally not affect the respectively measured materials properties to any extent.

However, only slightly increase of the hydrogen concentration up to 3.40 ppm entailed larger sections of intergranular cracking. This is presented in Figure 4.14f at a high magnification which also shows that still some ductile MVC portions alongside the former austenite grain boundaries. Also, the specimen charged with hydrogen at this concentration showed a minimal more ductile fracture topography at the specimen margins (Figure 4.14g). Here, hydrogen seems to have more homogeneously been dissolved in the microstructure, since a sharp transition (Figure 4.14e) between transgranular cleavage-like cracking and MVC was not detected. Instead, a mixed TG and MVC topography appeared at the margins of the specimen charged with

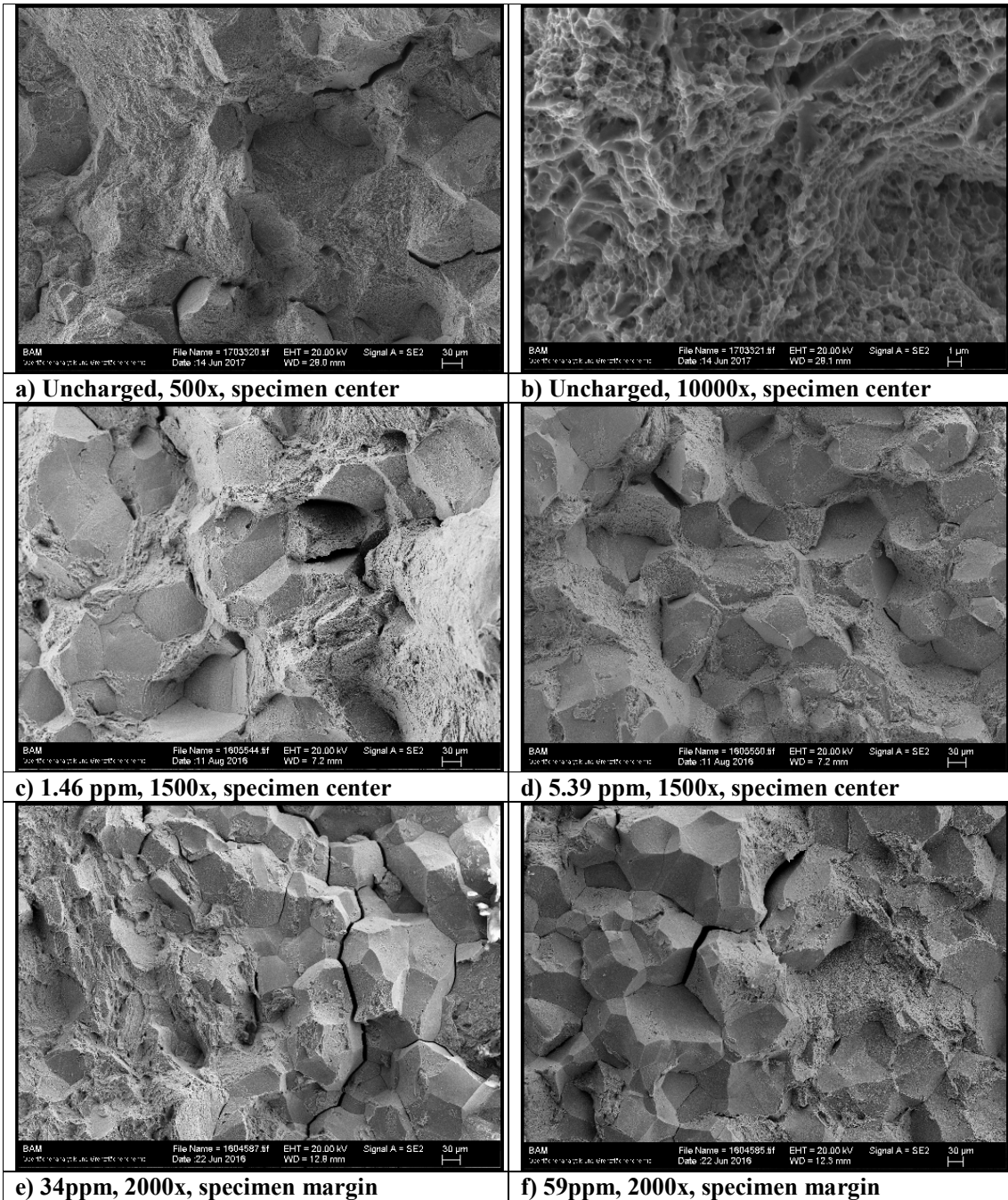


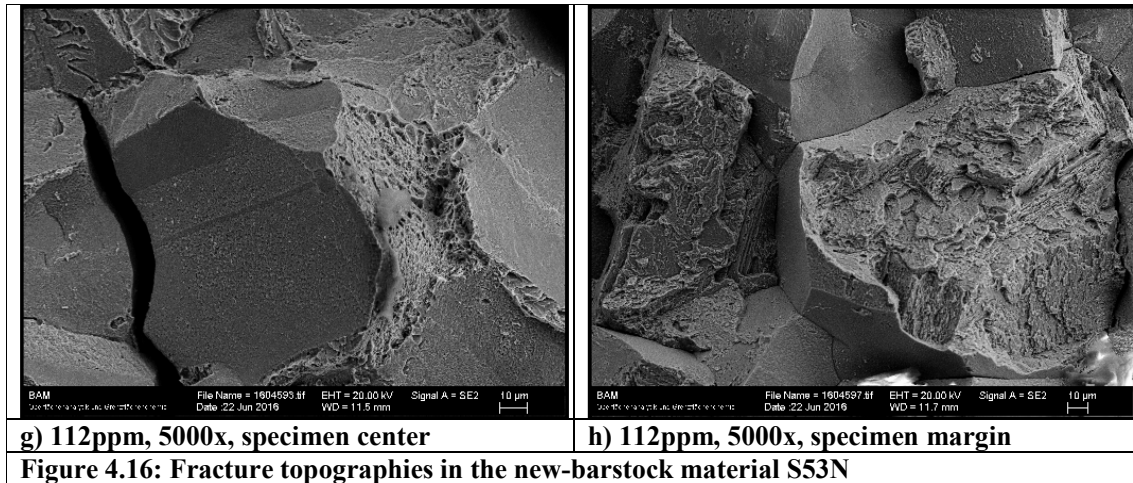


hydrogen at a concentration of 3.40 ppm. As shown exemplarily by Figure 4.14h for a concentration of 4.70 ppm, the intergranular portion of the fracture surface was further increasing with higher hydrogen concentrations in the tensile specimens.

SEM micrographs of the new-barstock steel S53N have been assigned to the Figure 4.15. In the uncharged condition, the material behaves macroscopically ductile. However, already at a lower magnification, some intergranular orientation of the fracture topography can be detected (Figure 4.15a), associated with some side cracking. This intergranular-like fracture surface is probably caused by the already above mentioned high amount of retained austenite in this material. However, at a larger magnification it becomes clear that at least the spaces between the former austenite grains exhibit a ductile topography, characterized by MVC. These dimples appear significantly smaller than in the new-barstock low alloyed steel 4340N in the uncharged condition, reflecting a smaller grain size which might be the reason for the higher strength and a at the same time higher ductility of the S53N material in the as delivered and uncharged condition, as also shown by the Figure 4.9 compared to the Figure 4.11.

Already at low hydrogen concentrations just above 1 ppm such intergranular fracture topographies become more pronounced, exhibiting quite smooth surfaces of the retained austenite grains. With increasing hydrogen concentrations, the intergranular portions on the fracture surface of the respective specimens become larger and it should be anticipated that also





intergranular fracture alongside the former austenite grains in the martensitic parts of the microstructure appears. Already at a medium hydrogen concentration of 34 ppm nearly the complete fracture surface is characterized by intergranular cracking. The ductile parts still being pronounced at a concentration of 34 ppm begin to vanish when the hydrogen concentration is increased to 59 ppm (Figure 4.15f).

However, for another landing gear UHSS, conversion from ductile to severe transgranular fracture surfaces with increasing hydrogen concentrations has been observed and has been attributed to H repartitioning from a high density of homogeneously distributed and reversible M_2C traps to the crack tip at high tensile stresses [6, 11]. Interestingly, the significant intergranular fracture topography at hydrogen concentrations above 30 ppm observed in the presently investigated new-barstock material S53N seems to have not or at least been less investigated for another similar landing gear UHSS [6, 11]. Following the investigations of the hydrogen trapping sites in such materials [6, 11], it should be anticipated that such severe intergranular cracking, on one hand, is associated with much smaller fractions of carbide precipitates in the austenite. On the other hand, hydrogen interactions with austenite-martensite phase boundaries as well as with the higher hydrogen solubility in the austenite phase might be the origin for such effects.

The fracture surfaces alongside the austenite grains are even so smooth that twinning inside the austenite grains can be detected (Figures 4.15f and 4.15g). Increasing the hydrogen concentration above 30 ppm is also associated with severe side cracking (Figures 4.15e to

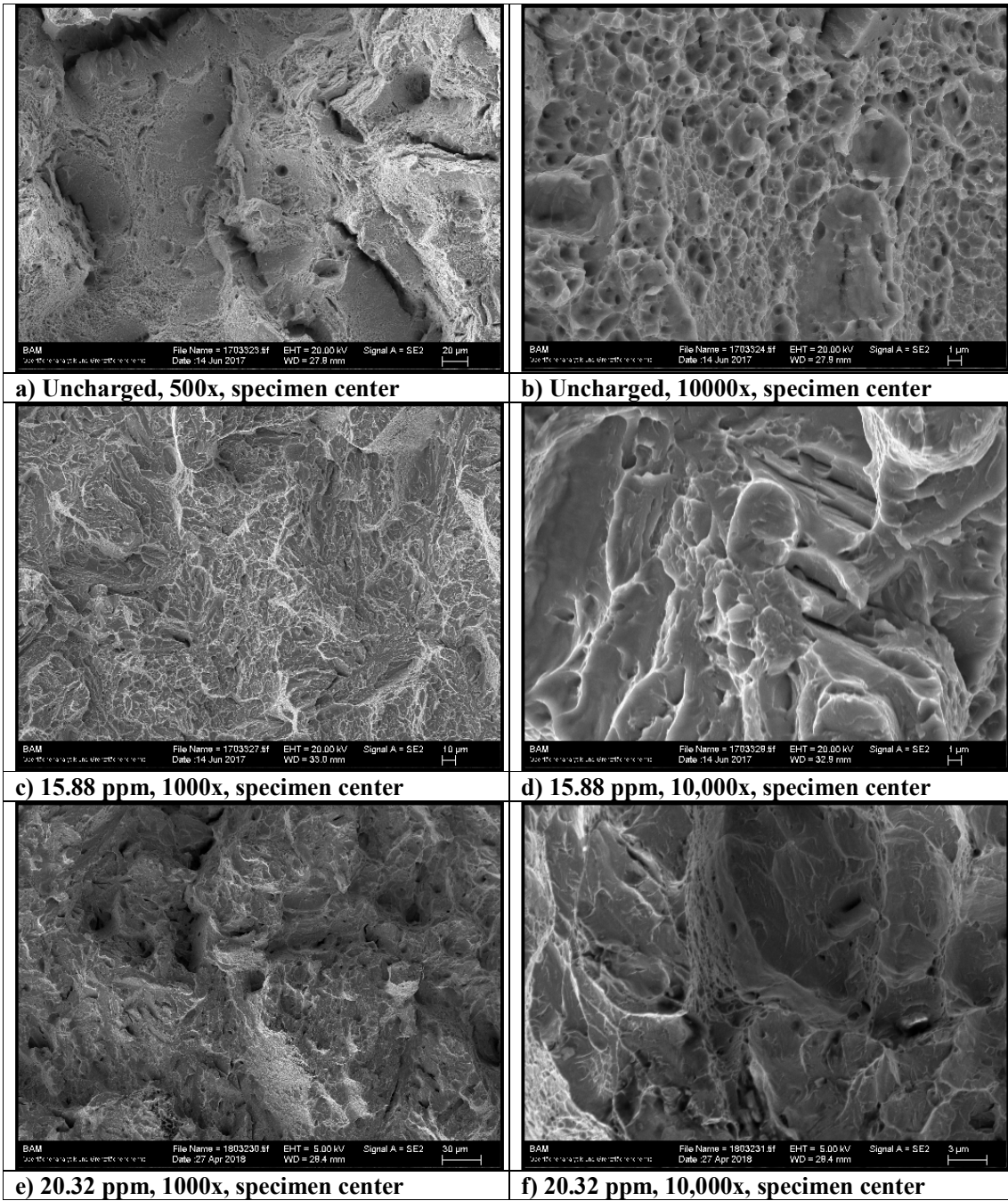
4.15h). At extremely high hydrogen concentrations over 100 ppm the fracture surface is nearly exclusively intergranular. Still, some ductile parts may be found at grain boundary triple points (Figure 4.15g) as well as transgranular cleavage (Figure 4.15h) following the overall fracture direction under plain strain.

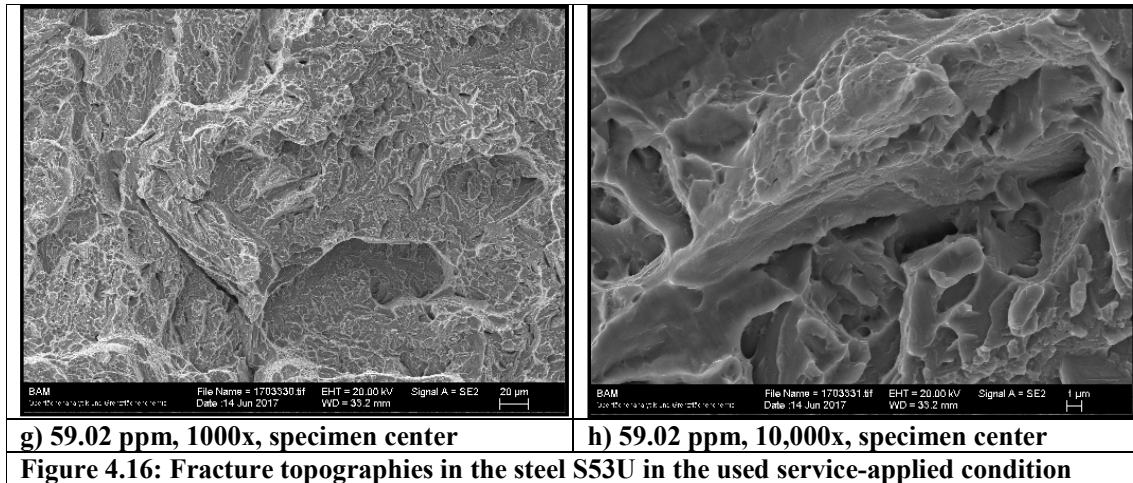
Figure 4.16 shows an exemplary assembly of fracture topographies for the service-applied version of the S53U steel. In contrast to the condition in which the bar-stock material has been delivered, no intergranular portions have been detected in the hydrogen-free state. This becomes immediately evident by a comparison of the Figures 4.15a and 4.15b with the Figures 4.16a and 4.16b, respectively. In the used and service-applied state, the steel S53U exhibits a very ductile fracture topography with a high number of small dimples (Figures 4.16a) that in some cases can also reach a considerable depth (Figure 4.16b).

Increasing the hydrogen concentration in this material to quite a significant level of 15.88 ppm leads to transgranular quasi-cleavage cracking of the tensile specimens, as it is quite typical, if not classical, for a martensitic steel. Nearly no ductile portions could be detected any more on the fracture surface. Increasing the hydrogen concentration to even higher levels slightly above 20 ppm did not reveal any significant changes in the fracture topography (Figure 4.16e).

Still, small portions of feather-like ductile cracking could occasionally be detected at the margins of the transgranular fracture planes, indicating typical quasi-cleavage cracking, as reported elsewhere [Broichausen-Schadenskunde]. By increasing the hydrogen concentration to the maximum level investigated here, i.e. to 59.02 ppm, still a transgranular fracture topography has been observed. However, at such high hydrogen concentrations, any ductile features seem to have vanished from the fracture topography.

As shown by the Figures 4.16g and 4.16h, the fracture topography seems to be totally covered by the transgranular cleavage cracking type. Any features indicating a quasi-cleavage mode have vanished. This even represents a clear indication that transgranular quasi-cleavage cracking does not actually represent a separate cracking topography type, as reported elsewhere [Broichausen-Schadenskunde], and is thus not a special fracture topography type associated with hydrogen assisted cracking.



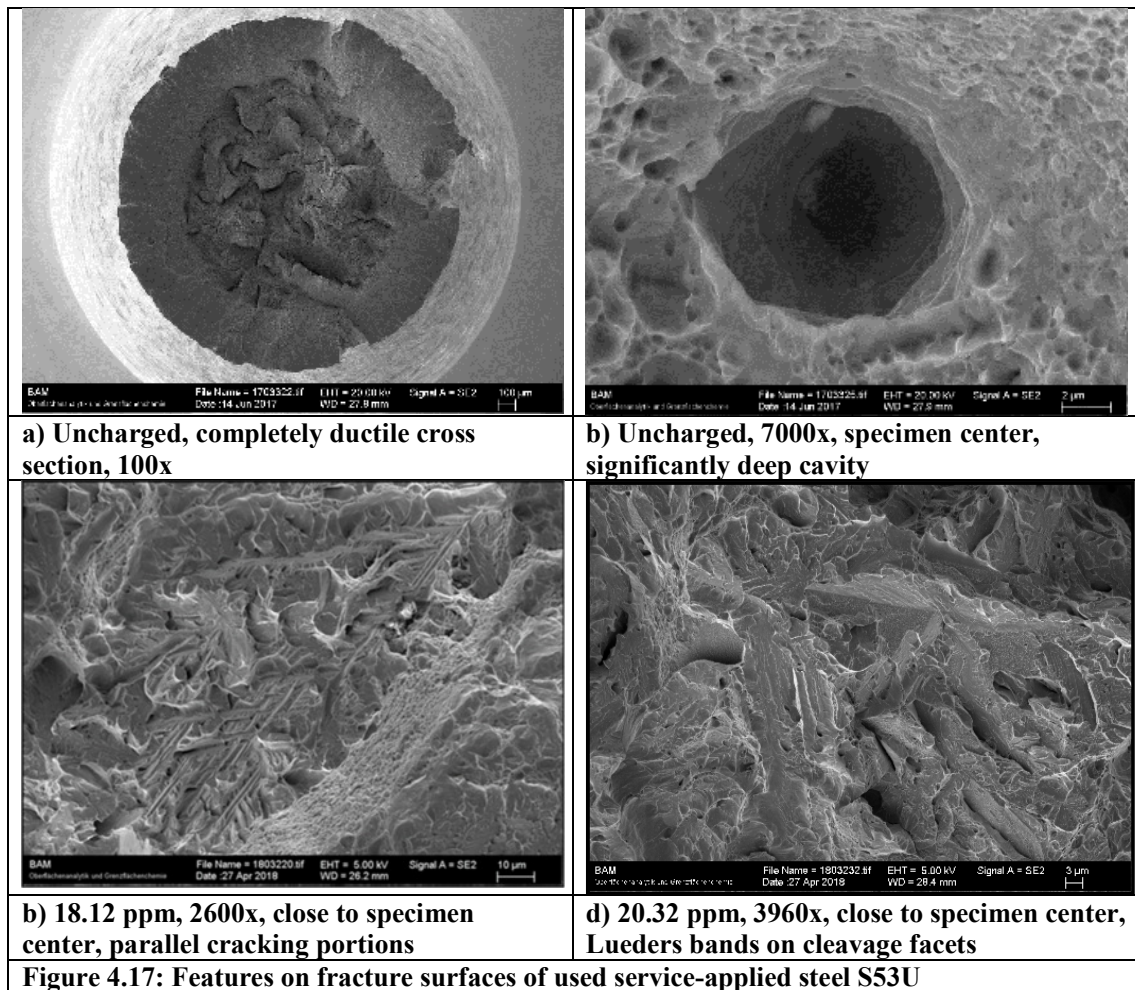


In turn, it can be taken as ascertained by the above considerations that with increasing hydrogen concentrations the fracture mode turns from ductile towards more transgranular cracking with some still ductile portions that are elsewhere assigned to a separate fracture topography type, but actually do not represent such. Increasing the hydrogen concentration thus just leads to an increased portion of transgranular cleavage facets with a decreasing number of ductile sites at the edges of such facets, towards the former austenite grain boundaries in the case of a martensitic steel.

However, no intergranular cracking has been observed in the used and service-applied S53U steel in the un-charged condition. Intergranular cracking, i.e. cracking alongside the former austenite grains in totally martensitic microstructures as exhibited by this material (Section 3.1), represents the last stage of embrittlement indicated by the fracture topography. Since this fracture topography type has not been observed in the used and service-applied steel S53U, it can be anticipated that it behaves much more tolerant against hydrogen than in the new bar-stock condition.

Finally, some remarkably features detected during the fractography of the used steel S53U should be highlighted at this point. First, a very deep dimple has been detected in the uncharged material Figure 4.17a), as shown in the Figure 4.17b). It is anticipated that this does not even represent a typical dimple to be associated with MVC, but rather represents a micro-cavity introduced during the materials processing. If this is actually the case, and considering the

safety-relevant application of such a highly loaded material in landing gear components, it can only be emphasized that any cavities should be avoided during processing of the steel.



As another feature, quite significant parallel cracking has been detected on the fracture surface of the specimen charged with hydrogen at a concentration of 18.12 ppm (Figure 4.17c). It is assumed that these regions represent retained austenite which have been found only occasionally by investigating the fracture surface, since the amount of retained austenite is considerably small in the used S53U steel (Section 3.1). However, it is a well-known phenomenon that twinning, and even martensitic transformation, might occur during observation of such retained austenitic regions and the parallel cracking observed here is thus associated to twinning effects in a small portion of retained austenite in the material.

Figure 4.17d shows a part of the typical transgranular (quasi-) cleavage fracture surface of the specimen charged with hydrogen at a concentration of 20.32 ppm. Here, some parallel features can be observed on the cleavage planes which might tentatively be assumed as Lueders bands. However, it is not clear, if those should be associated to hydrogen or perhaps carbon.

4.3 Investigation of UHSS at Environmental Conditions

As already outlined in the experimental section, the Slow Strain Rate Tests (SSRT) represents a very suitable procedure to investigate the stress corrosion cracking resistance of a material under environmental conditions. In contrast to frequently applied constant load tests, the SSRT provides a continuous straining of a material under the respective environmental conditions. By this, it thus, provides particularly information, if a material shows a brittle or ductile behavior in the respective environmental. This is particularly important, if hydrogen might be absorbed from the environment. However, the SSRT is often performed in too harsh environments for the respective materials to be tested and thus is often assumed as a too sharp test for a respective corrosion system, i. e. for a specific material-environment combination. It is thus important to select an environment that is realistic and representative for the environmental conditions a specific material will be exposed during service.

Airplane landing gear materials are exposed during service to very different climatic conditions. For military applications, marine environments have to be considered. The respective landing gear components might also be subjected to other saline environments, for instance splash water contaminated with deicing salts on runways, however, at respectively lower temperatures. As a worst-case scenario, the exposure of the uncoated, i.e. unprotected, material to sea water in marine environments has to be taken into account which might happen during severe duty service on aircraft carriers.

For such reasons, most of the SSRT described in the following section have been carried out in seawater. As previously described above, the S53 steel has been developed to replace the commonly applied landing gear steel 4340. Since the latter has thoroughly been investigated, this section is concentrating only on investigations of the new design alloy S53 which has not been investigated in detail up to the present. The S53 steel has been investigated in both conditions, as it already has been tested with respect to the hydrogen related mechanical properties. However, the main focus lies in the used service-applied condition by cutting out

the specimens from real landing gear that had been in service for a period of five years. It can only be mentioned that this represents a completely new approach for testing the new landing gear steel S53. To have well-defined and reproducible conditions, most of such tests have been carried out in artificial seawater. However, for comparison, also a test series in natural seawater (Section 4.3.2.2) has been performed.

It should be considered that similar SSRT experiments have not yet been carried out with the conventional landing gear steel 4340 in the used service-applied condition. These results should then be compared to some new as-delivered variant of this low alloyed steel as it has been provided for the hydrogen dependent mechanical properties in the previous section. However, this would go far beyond the scope and size of the present thesis and has thus been left for future research.



Figure 4.18: A new F-35 Multi-role fighter demonstrating Vertical take-off and landing – Ferrium S53 landing gear is in the design process for this new aircraft – designing landing gear will be completely different due to unique load directions [6]

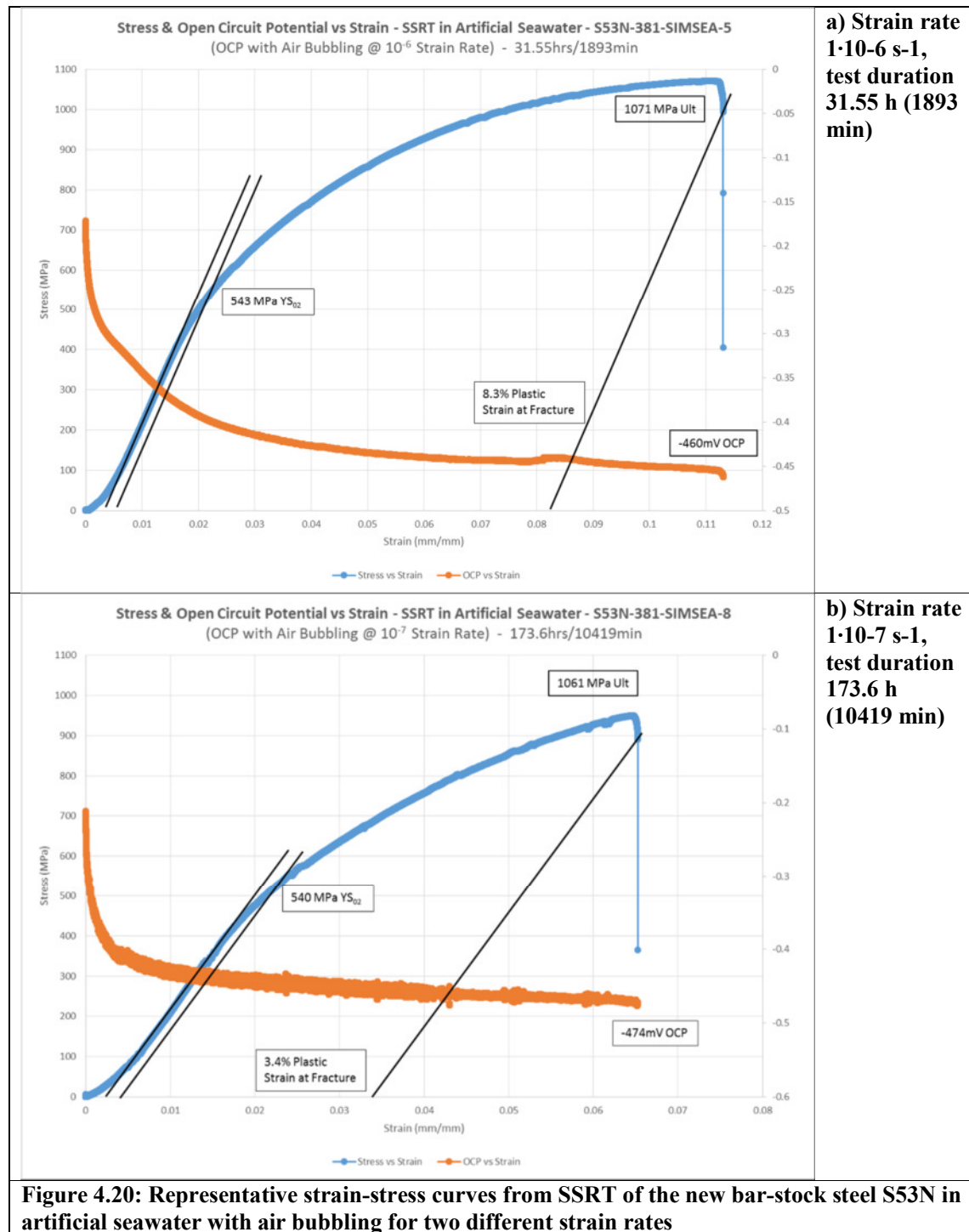
4.3.1 SSRT of the S53 Steel in the New As-Delivered Condition

As a first approach to determine the general behavior of the landing gear steel S53 in general, a series of SSRT has been carried out with the material in the new as-delivered condition in artificial seawater. The strain rate has been varied in these tests between $\dot{\epsilon} = 1 \cdot 10^{-5}$ and $\dot{\epsilon} = 1 \cdot 10^{-7} \text{ s}^{-1}$ for two reasons, i.e. for identification of the suitable strain rate to exhibit potential material degradation in such environments as well as for providing a respective time strain fracture diagram. The latter provides a failure curve by which under knowledge of the accumulated strain in service the potential failure risk of a material in specific environments might be assessed.

Figure 4.19 provides representative stress-strain curves monitored at open circuit potential in artificial seawater for the new bar-stock material at strain rates of $\dot{\epsilon} = 1 \cdot 10^{-6}$ and $\dot{\epsilon} = 1 \cdot 10^{-7} \text{ s}^{-1}$, respectively. The gradients of the curves are different, particularly in the elastic region, although all specimens have been prestressed at 50 N before starting the test. The reason is that the stiffness between the mounting devices, i.e. the machine parts, and the specimen are different. During elastic straining, the specimen behaves stiffer than the mounting devices which are still interfacing with the threads with increasing loading force at the cross head. However, above the yield point, when the material shows uniform plastic deformation and the specimen behaves much less stiff than the mounting devices intrinsic to the machine, there is less influence on the gradient of the stress-strain curves. Such effects are more pronounced at lower straining rates on the material and thus, the elastic ascent of the stress-strain curve is somewhat lower for the SSRT carried out at $\dot{\epsilon} = 1 \cdot 10^{-6} \text{ s}^{-1}$, as compared that performed at $\dot{\epsilon} = 1 \cdot 10^{-7} \text{ s}^{-1}$.

However, all tests exhibited a similarly high yield strength of about 540 MPa and a similarly high tensile strength of about 1070 MPa for the as delivered new bar-stock steel S53N. The yield strength appears as to be somewhat lower than that measured in air which has to be attributed to some measurement uncertainties associated with the gradient of the curves taking into account that the air tests have been carried out at higher strain rates of about $\dot{\epsilon} = 10^{-3} \text{ s}^{-1}$. The tensile strength this material exhibits during SSRT corresponds well to the value determined in air for both strain rates, which is much more important regarding

environmentally, i.e. hydrogen assisted, cracking. Also, the yield strength and the tensile strength range at similarly high values for both strain rates.



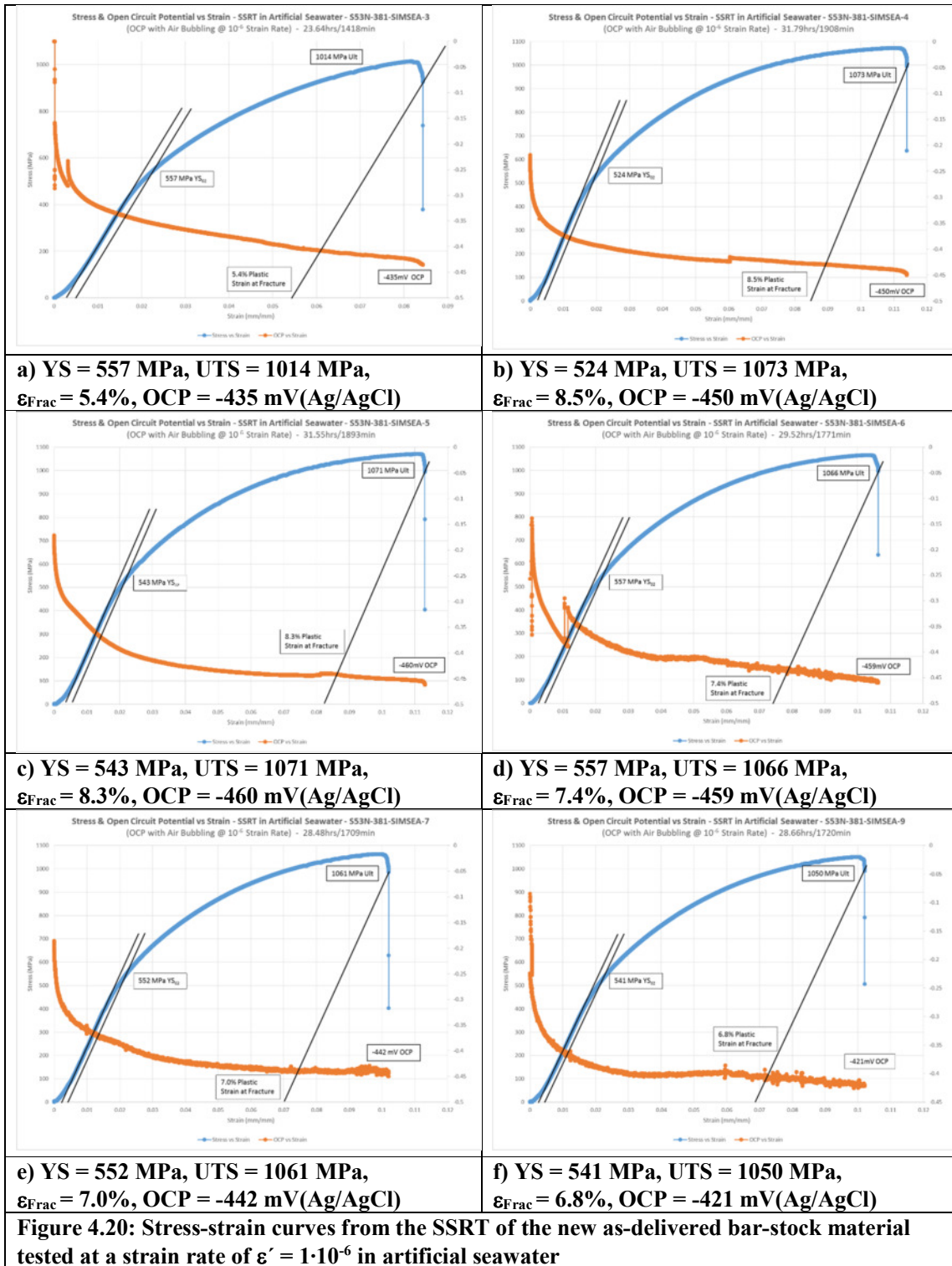
This means that the environment (aerated artificial sea water) specifically affects the mechanical material behavior in terms of necking. Actually, the technical strain at fracture is significantly reduced to from about 8% to about 3%, if the strain rate is decreased from $\dot{\epsilon} = 1 \cdot 10^{-6}$ to $\dot{\epsilon} = 1 \cdot 10^{-7} \text{ s}^{-1}$. The values of all relevant tensile test parameters determined from the SSRT of the new bar-stock steel S53N have been assigned to the Table 4.1.

Specimen No.	Strain Rate (s^{-1})	Yield Strength (MPa)	Tensile Strength (MPa)	Time to Fracture TTF (min)	Technical Strain at Fracture (%)	True Fract. Strain	Final OCP (mV-Ag/AgCl)
S53N-1	$1 \cdot 10^{-6}$	540	1059	1712	7.2	0.0694	N/A
S53N-2	$1 \cdot 10^{-6}$	464	609	1133	4.6	0.0532	N/A
S53N-3	$1 \cdot 10^{-6}$	557	1014	1418	5.4	0.0803	-435
S53N-4	$1 \cdot 10^{-6}$	524	1073	1908	8.5	0.0913	-450
S53N-5	$1 \cdot 10^{-6}$	543	1071	1893	8.3	0.0803	-460
S53N-6	$1 \cdot 10^{-6}$	557	1066	1771	7.4	0.0694	-459
S53N-7	$1 \cdot 10^{-6}$	552	1061	1709	7.0	0.0640	-442
S53N-8	$1 \cdot 10^{-7}$	540	1061	10419	3.4	0.0858	-474
S53N-9	$1 \cdot 10^{-6}$	541	1050	1720	6.8	0.0317	-421

Table 4.1: Mechanical properties determined during the SSRT in artificial seawater at various strain rates

Since no decrease of the tensile properties has been detected by reduction of the strain rate from $\dot{\epsilon} = 1 \cdot 10^{-6}$ to $\dot{\epsilon} = 1 \cdot 10^{-7} \text{ s}^{-1}$, a strain rate of $\dot{\epsilon} = 1 \cdot 10^{-6}$ can be taken as sufficiently low to effectively exhibit the degradation of the steel S53 in seawater environments. Thus, and according to the general standard for SSRT of corrosion resistant alloys (CRAs) [125], it has been decided to carry out most of the subsequent tests, including those of the S53 steel in the used service-applied condition (see Chapter 4.3.2) at the strain rate of $\dot{\epsilon} = 1 \cdot 10^{-6}$. Figure 4.21 shows a compilation of stress-strain curves and respectively on-line monitored open circuit potentials (OCP) for a number of tests carried out at a strain rate of $\dot{\epsilon} = 1 \cdot 10^{-6}$ with very consistent and reproducible results. As confirmed by Table 4.1, no material degradation has been observed at a strain rate of $\dot{\epsilon} = 1 \cdot 10^{-5} \text{ s}^{-1}$. Still, at such strain rate, fracture strain of 12% has been reached, which agrees well to that measured in air at a considerably higher strain rate of 10^{-3} s^{-1} .

Figure 4.21 represents the time-strain fracture (TSF) diagram of the steel S53N in the as-delivered bar-stock condition, evaluated from the various SSRT at different strain rates.



In this diagram, the failure curve is represented the decrease of the fracture strain, i.e. the total technical strain the material ϵ_{Frac} can tolerate in the respective environment which is here

artificial sea water, with increasing exposure time t_{ex} . It follows an exponential function, given by:

$$\epsilon_{Frac} = 2.0346 \cdot t_{ex}^{-0.255}$$

(4.21)

This formula thus be used for a very rough assessment regarding the application of the unprotected and uncoated new bar-stock steel S53N in marine environments: If the total exposure time in totally liquid sea water of the unprotected material is known the also to be accumulated tensile strain during service, as for instance during start and landing operations, of the unprotected exposed material should simply not exceed the value of ϵ_{Frac} given by above formula.

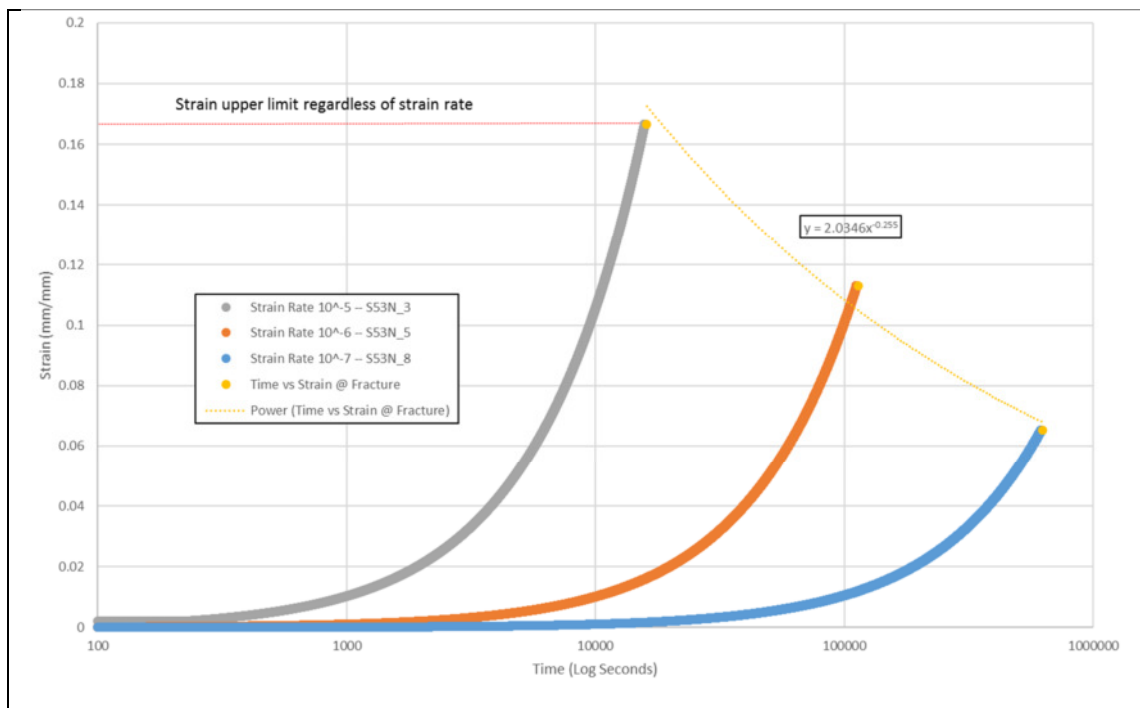
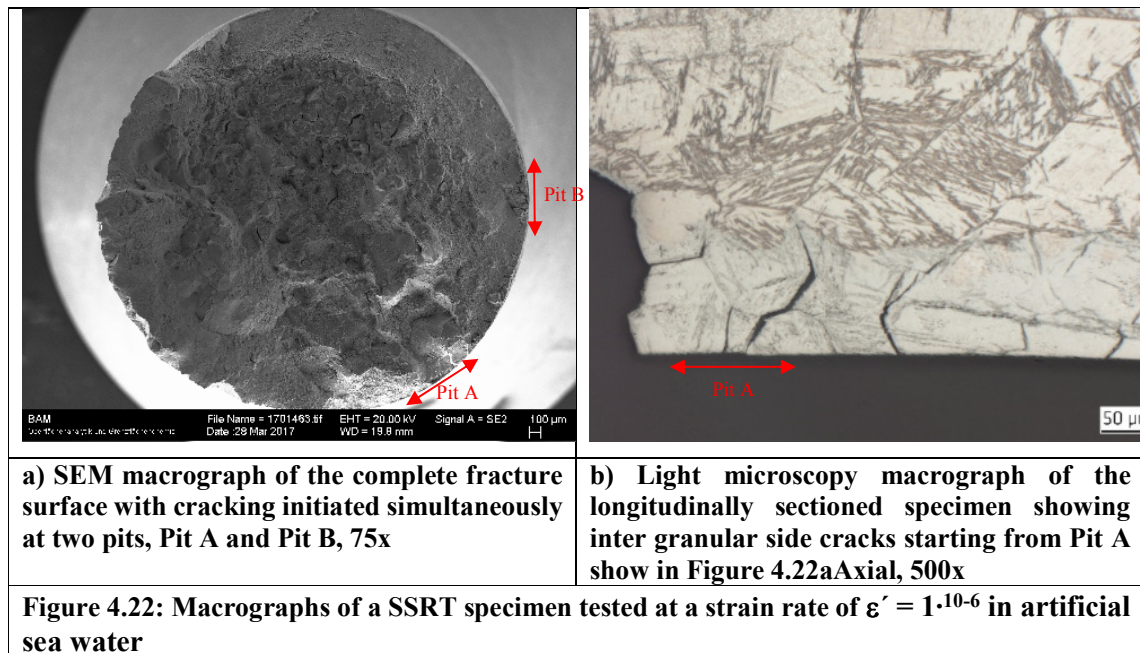


Figure 4.21: TSF diagram for the steel S53N in the as-delivered and commercially available bar-stock condition

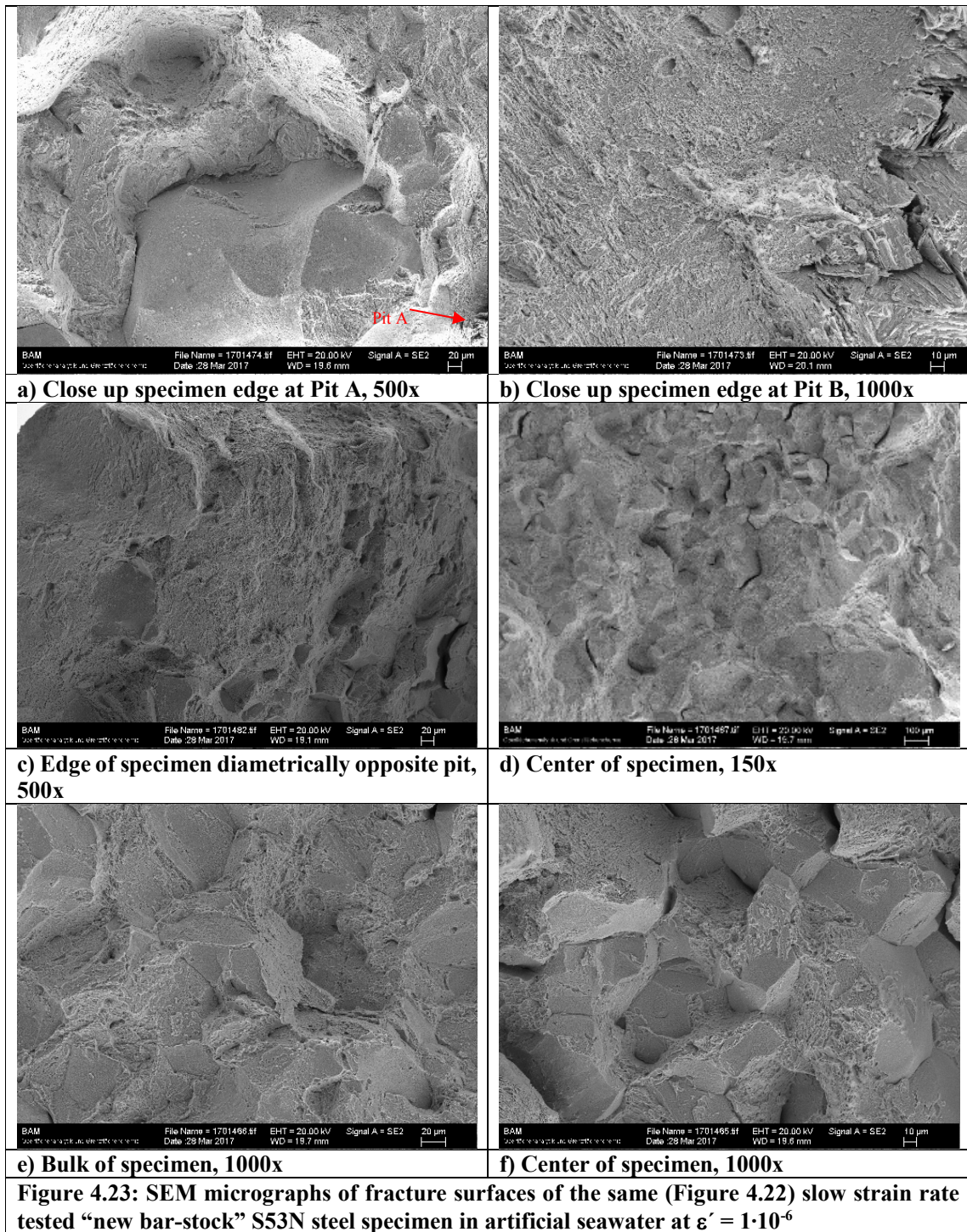
As can also be seen drawn from the diagrams in the Figure 4.20, the open circuit potential (OCP) also monitored during the tests is continuously decreasing after starting the SSRT towards quite negative values of about -450 mV-Ag/AgCl, i.e. against the Ag-AgCl reference electrode. Considering the 258 mV difference of this reference electrode against the standard

hydrogen electrode, the established OCP is somewhat higher. However, the measure electrochemical potential against this reference electrode $E_{Ag/AgCl}$ corresponds very well to those measured with a calomel reference electrode for other martensitic stainless steels having even a slightly higher chromium content, as for instance supermartensitic stainless steels (SMSS) in salt brines [24], considering that the potential difference between calomel and Ag/AgCl reference electrodes is only 8 mV.

As shown by the two SSRT diagrams in the Figures 4.20a and 4.20b, the OCP is decreasing to fairly low values of $E_{Ag/AgCl} < -400$ mV already during elastic deformation of the material, i.e. below reaching the yield point.



This in turn means that the steel S53N already is affected by the environment at lower strength levels, i.e. fairly below yielding. In fact, as shown by the micrographs in the Figure 4.22, severe pitting has been found on the surface of the new S53N material and it has been confirmed that such pitting already started during elastic straining of the material quite considerably below the yield point. It has thus to be emphasized at this point that reaching still the tensile strength at quite low strain rates does not mean that the material is not affected by the environment at mechanical loads below the UTS. This also means that a breakdown of the passive film even happens while loading the material fairly below its original design yield strength. As



exemplarily shown by the macrographs in Figure 4.22, by the SEM micrographs in Figure 4.23, cracking has always started from inside such pits. As shown in these figures, cracking started predominantly intergranularly, with a considerable number of side cracks. Although it has not

been investigated in detail, it is assumed that such cracks developed from the sides of such pits at locations with the highest strains, as it has been observed recently in other martensitic stainless steel types [107].

From Table 4.1, it can be taken that all SSRT specimens also dissolved some hydrogen during the test at strain rates of $\epsilon' = 1 \cdot 10^{-6}$ and below. Clearly, with decreasing strain rate the average hydrogen concentration in the specimens increases (Table 4.1). The specimen tested at a strain rate of $\epsilon' = 1 \cdot 10^{-5}$, in contrast, did not show any pitting nor any hydrogen concentration has been measured in this specimen. On one hand, this means that this strain rate is too high and does not provide enough time to establish a respective potential drop and/or passive film break down in the artificial sea water.

Thus, pitting has also not been observed. The fact that also no hydrogen has been taken up by this specimen allows the assumption that the hydrogen measured in the SSRT specimens tested at up to two orders of magnitude lower strain rates has been absorbed through, i.e. inside, the pits. As damage or environmental degradation mechanism of the new bar-stock steel S53 in artificial seawater has thus to be considered respective pitting corrosion with subsequent hydrogen assisted stress corrosion cracking (HASCC). It can only be emphasized that this is a quite common damage mechanism, particularly regarding martensitic stainless steels usually having a chromium content at the lower limit of corrosion resistance of 10.5 wt.-% [24]. This is the case for above mentioned SMSS with about 12 to 13 wt.-% Cr, and particularly applies to the as-delivered steel S53 tested here, having exactly 10 wt.-% Cr, i.e. even 0.5 wt.-% less than the required lower limit for CRA.

For elucidation of the phenomenology of pitting and subsequent HASCC, the stepwise damage sequence is given here under reflection of the explanations given in modern text-books

1. Local breakdown of the slight passive layer that could be and probably has been established on the surface of the material with 10.0 wt.-% Cr. This is supported also by straining the material below the yield point, since the passive film is much more brittle than any substrate material underneath.

2. Repassivation of the surface is quite slow as compared to other CRA, since the Cr content ranges at the lower required limit. Fresh metal surface is exposed to the environment, i.e. artificial sea water, and local metal dissolution starts at such pit nucleation sites. The local metal dissolution is enforced by Cl ions in the environment, since Cl ions increase the solubility of metal ions in aqueous environments.

3. The rest of the surface is acting as cathodic side, providing electron consumption by a cathodic oxygen reaction (Figure 4.24). This is actually enhancing the pit growth into depth. With increasing pit growth into depth and dissolution of metal into the environment associated with the incomplete repassivation, corrosion products in form of hydroxides and, partly oxides, are formed that actually plug the pit mouth.

4. Plugging of the pit mouth with corrosion products prevents oxygen addition out of the bulk electrolyte into the pit. Instead of repassivation, hydrolysis is initiated by the metal ions. Thus, the oxygen depletion inside the pit is associated with a severe potential and pH drop. The hydrogen produced in the pit is not recombining, but directly absorbed and incorporated as an ion into the metallic microstructure.

5. The mechanical properties, particularly the ductility, is degraded significantly by the hydrogen absorbed inside the pit. Additionally, straining of the material, specifically the direction perpendicular to the growing pit, causes further fresh metal exposure in and outside of the pit and will predominantly lead to crack initiation and brittle propagation inside the pit.

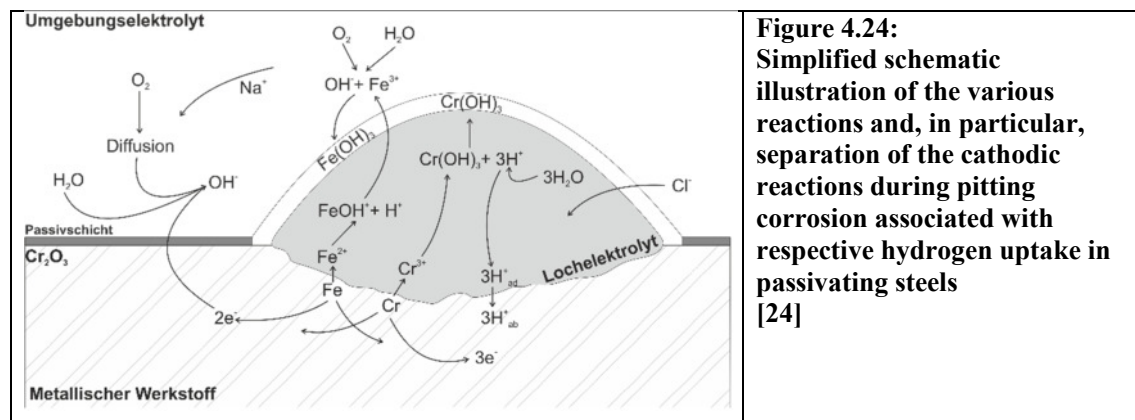
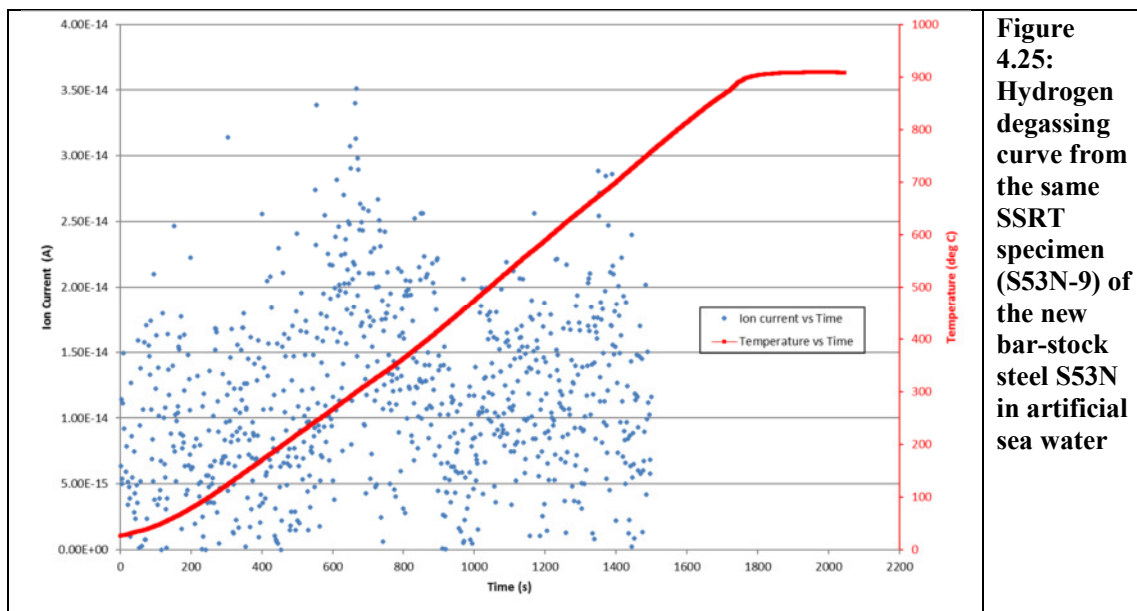


Figure 4.24:
Simplified schematic illustration of the various reactions and, in particular, separation of the cathodic reactions during pitting corrosion associated with respective hydrogen uptake in passivating steels [24]

As can be drawn from the hydrogen degassing diagram in Figure 4.25, again two peaks have been established. It should be mentioned that these curves are much less pronounced than for the hydrogen-charged specimens, due to the fact that not as much hydrogen is introduced in total into the specimens during pitting and cracking during the SSRT as compared to the continuous hydrogen charging over a period of about a week. However, since these peaks occur at the same temperatures of about 550 to 700 °C, then it has been observed for the hydrogen charged specimens, it can be assumed that the hydrogen entering the material during pitting and subsequent cracking in the SSRT from artificial seawater is released in a similar way.

In other words, the hydrogen introduced locally during the pitting and straining of the S53N material is not distributed differently to that in hydrogen charged and completely saturated specimens in sulfuric acid. Aside the fact, that it is again shown that hydrogen is not trapped deeply and irreversibly in this ne bar-stock steel S53N, this consequently means that the degradation of this material by environmentally introduced hydrogen is also reflected very well by the hydrogen-charged specimens investigated in the previous chapter and, that the quantitative results developed there can be taken very well as crack initiation and propagation criterion for respective numerical simulations of hydrogen assisted cracking of this material.



4.3.2 SSRT of the S53 Steel in the “Used Component” Service-Applied Condition

4.3.2.1 Variation of Strain Rate in Artificial Sea Water

The first series with the new as-delivered bar-stock steel S53N was carried out to get a more fundamental understanding of the general corrosion and cracking resistance of such innovative design alloys under environmental conditions which are more service oriented and to identify the principal damage mechanisms, i.e. pitting and subsequent hydrogen assisted cracking. As already shown above, the new S53 steel has a much lower strength and also, somewhat lower ductility than the actually service applied steel S53U. For this reason, but predominantly for investigating the steel in the actual service-applied condition, i.e. with its real mechanical properties and microstructure, SSRT has been carried out on the material taken from a real landing gear system. The SSRT with the real landing gear material have thus also been carried out to a much larger extent, i.e. it has been tested not only at different strain rates in artificial seawater. Already SSRT of the new as-delivered bar-stock material has not yet been carried out like it has been done with similar landing gear steels, like the AerMet 100, for instance [2]. However, it should be emphasized at this point, that the testing of really landing gear-applied S53U that has been in service for more than five years has been carried out for the first time. Thus, the “used component” S53U steel has been tested by SSRT to a much larger extent than in the new as-delivered condition.

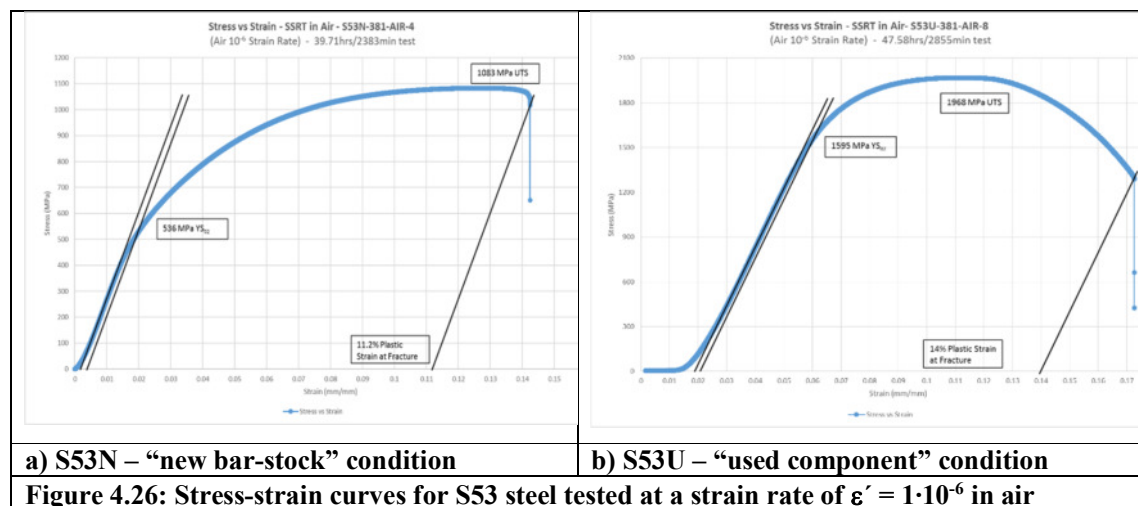


Figure 4.26: Stress-strain curves for S53 steel tested at a strain rate of $\dot{\epsilon} = 1 \cdot 10^{-6}$ in air

Like the new steel S53N, also the used landing gear material S53U has been tested in artificial sea water at different strain rates, as a first approach. The test results have been summarized in

Table 4.2. The Figures 4.27 to 4.29 show exemplary stress-strain curves of the SSRT of the S53U material for three different strain rates between $\dot{\epsilon} = 1 \cdot 10^{-5}$ and $\dot{\epsilon} = 1 \cdot 10^{-7}$. In addition to the also shown potential curve, photographs of the outer specimen surface monitored during the test have been attached to these diagrams.

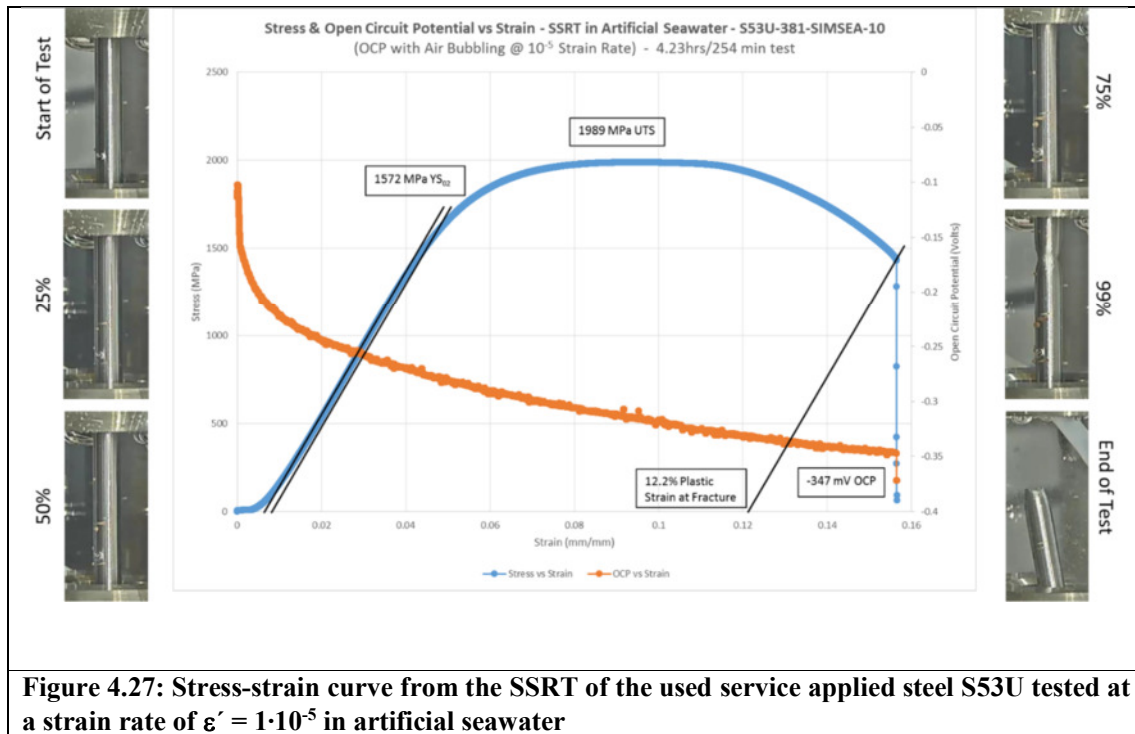
As can be seen from the Figure 4.27, the stress-strain curve at a strain rate of $\dot{\epsilon} = 1 \cdot 10^{-5}$ is very similar to that of the material tested in air at a higher strain rate. The ultimate tensile strength ranges at nearly 2000 MPa above the level of the air-tested material and at about 1600 MPa, the original yield strength of the air-tested material is also matched. In addition, the ductility in terms of the fracture strain seems only be slightly reduced from 14 to about 12.2%.

However, the open circuit electrochemical potential is significantly reduced during the test down to values ranging at about -350 mV(Ag/AgCl). Also, after about one quarter up to half of the testing time, pitting corrosion has been detected by continuous monitoring of the specimen surface. This becomes quite evident from the photos of the specimen surface attached to the left side of the diagram in Figure 4.27.

Such pitting at the lower half of the specimen was clearly growing during the continuation of the test. The bubbles formed at such pits represent hydrogen bubbles at such low potentials, although air has also been purged through the test solution.

Specimen No.	Strain Rate (s ⁻¹)	Yield Strength (MPa)	Tensile Strength (MPa)	Time to Fracture TTF (min)	Technical Strain at Fracture (%)	True Fracture Strain	Final OCP (mV-Ag/AgCl)
S53U-1	1·10 ⁻⁶	1555	1555	777	4.6	0.0211	n. d.
S53U-2	1·10 ⁻⁶	1483	1483	781	4.6	n. d.	n. d.
S53U-3	1·10 ⁻⁷	765	765	4414	2.8	n. d.	-427
S53U-4	1·10 ⁻⁶	1653	1653	827	4.9	n. d.	n. d.
S53U-5	1·10 ⁻⁷	745	745	3789	2.3	n. d.	-425
S53U-6	1·10 ⁻⁶	1548	1548	743	4.4	0.0053	-366
S53U-7	1·10 ⁻⁶	1540	1540	737	4.4	n. d.	-376
S53U-9	1·10 ⁻⁷	658	658	3183	2.1	n. d.	n. d.
S53U-10	1·10 ⁻⁵	1572	1989	254	15.8	0.6962	-347
S53U-11	1·10 ⁻⁶	1432	1432	692	4.2	0.0105	-390

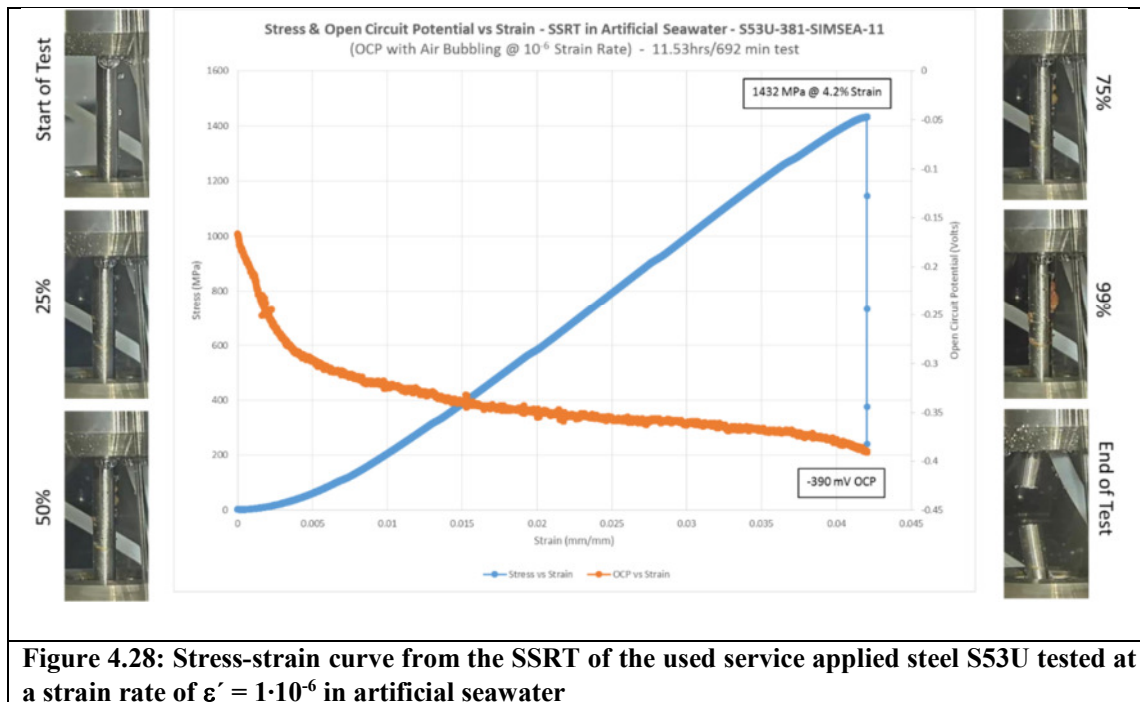
Table 4.2: Overview of SSRT results for the used service-applied steel S53U in artificial seawater



This means, that also the used service-applied steel S53U will be prone to pitting and subsequent hydrogen assisted stress corrosion cracking in chloride environments, like the artificial seawater used in this test solution.

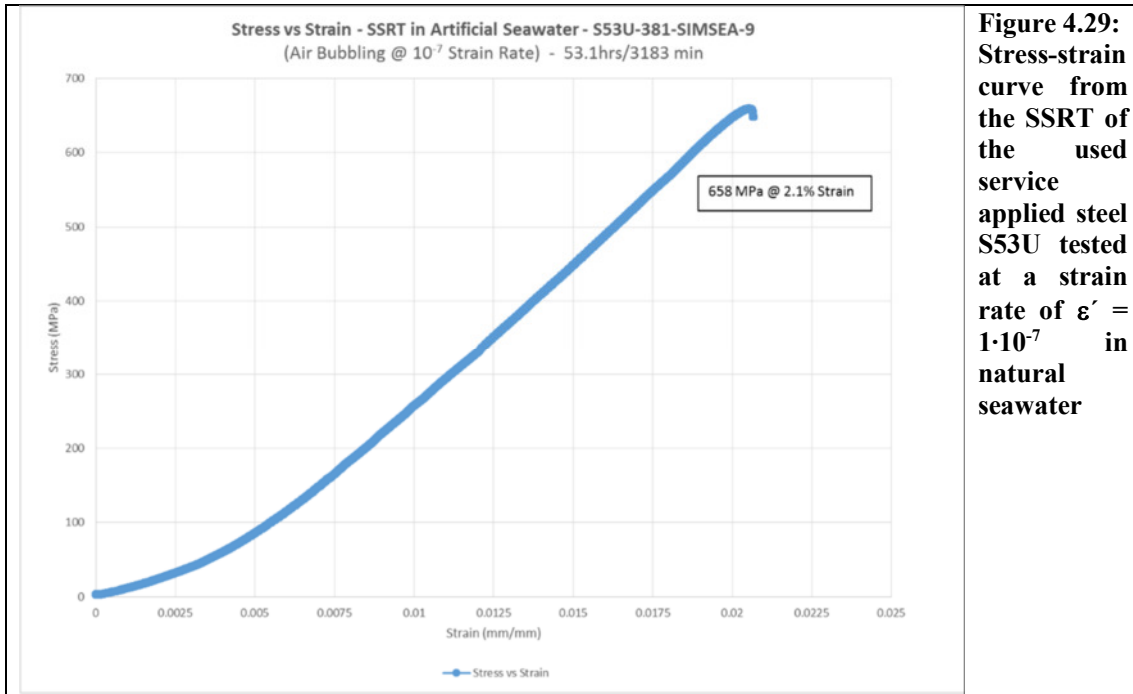
However, necking of the specimen evidently occurred in the upper half of the specimen, i.e. independently from the location of pitting. It can thus already be stated at this point that a strain rate of $\epsilon' = 1 \cdot 10^{-5}$ seems not to be sufficient to exhibit the complete damage mechanisms of this material in the respective environment, i.e. artificial seawater.

Figure 4.28 presents exemplarily the stress-strain curve, electrochemical potential and surface photos of a specimen tested at a lower strain rate of $\epsilon' = 1 \cdot 10^{-6}$ in artificial seawater. However, a series of tests at the same conditions have been carried out for validation. At this strain rate, due to the increased exposure time to the environment, pitting occurs more frequently on the specimen surface and seems also develop more into depth. Additionally, it can be drawn from Figure 4.28 that corrosion products are developed at the pits which might contribute to plugging of the pit mouth, as described in the previous section.



It can also be seen that such corrosion products have a bubble-like shape that might, tentatively assumed, result from the formation and recombination of hydrogen inside those pits. However, as outlined above, most of the hydrogen produced by hydrolysis in the pit will not recombine and will be directly absorbed as ion in the material, leading to subsequent hydrogen assisted stress corrosion cracking starting at the pit. It can be seen in Figure 4.28 that the main crack growth in the upper half of the specimen ruptured at the location of a preceding pit. A closer inspection of the photos shown here exhibits at least one if not more additional cracks starting from pits also in the upper and lower half of the specimen. The open circuit potential ranges at about -400 mV (Ag/AgCl) at these tests and thus, ranges also at about 40 mV lower values than that monitored in the test at a higher strain rate of $\epsilon' = 1 \cdot 10^{-5}$.

Severe pitting has also been observed during straining of the used service applied steel S53U still in the elastic region at a strain rate of $\epsilon' = 1 \cdot 10^{-7}$ during the SSRT. The respective stress-strain curve is shown in Figure 4.29. This time, the material fails already at about a third of the yield strength. Also, significant corrosion products have been observed developing at the pits which are assumed to similarly plugging the pit mouth and, consequently, causing a pH, oxygen and electrochemical potential depletion inside the pit leading to respective hydrogen uptake and brittle cracking. The bulk potential in the test solution has been only slightly reduced as



compared to the SSRT at higher strain rates of $\epsilon' = 1 \cdot 10^{-5}$ and $\epsilon' = 1 \cdot 10^{-6}$. However, from a comparison of the Figures 4.27 to Figure 4.29, it becomes clear that already a strain rate of $\epsilon' = 1 \cdot 10^{-6}$ is sufficiently low to completely exhibit the damage mechanism of pitting and subsequent hydrogen assisted stress corrosion cracking for the used service-applied steel S53U, like it has been for the material in the new bar-stock condition, S53N.

Similar to the Figure 4.21, Figure 4.30 shows the TSF-diagram for the used steel S53U after five years of service. In comparison to the new bar-stock material, the service applied material S53U shows a significantly steeper gradient of the failure curve which is given by the equation

$$\epsilon_{\text{Frac}} = 338.79 \cdot t_{\text{ex}}^{-0.803} \quad (4.2)$$

Although the actual technical fracture strain of the used material (14%), has been higher than that for the steel S53N in the as-delivered condition (12%), this steeper gradient had to be expected, since the yield strength of the used material S53U has been three times higher and the tensile strength has been twice as high than for the new bar-stock material S53N. Due to the much higher strength level, it is thus not surprising that the used material reacts much more

sensitive to a reduction of the mechanical properties as a consequence of hydrogen invading into the microstructure. This has also been observed during the tensile tests of the charged specimens, which in turn. In this context, it has also to be considered that the used material S53U in contrast to the new material S53N did not contain such significant amounts of undesired retained austenite, i.e. only about 2% instead of up to 40%, and thus, any ductility reserves cannot be provided the retained austenite having much more gliding lines and planes, as compared to the martensite phase.

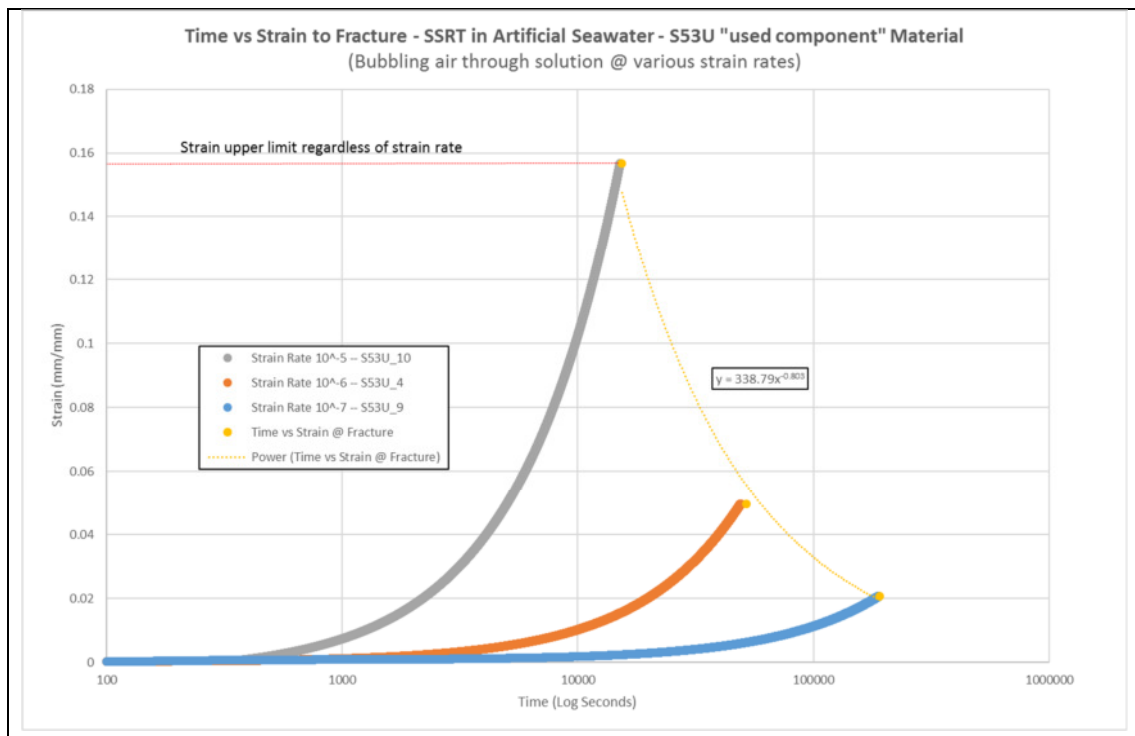
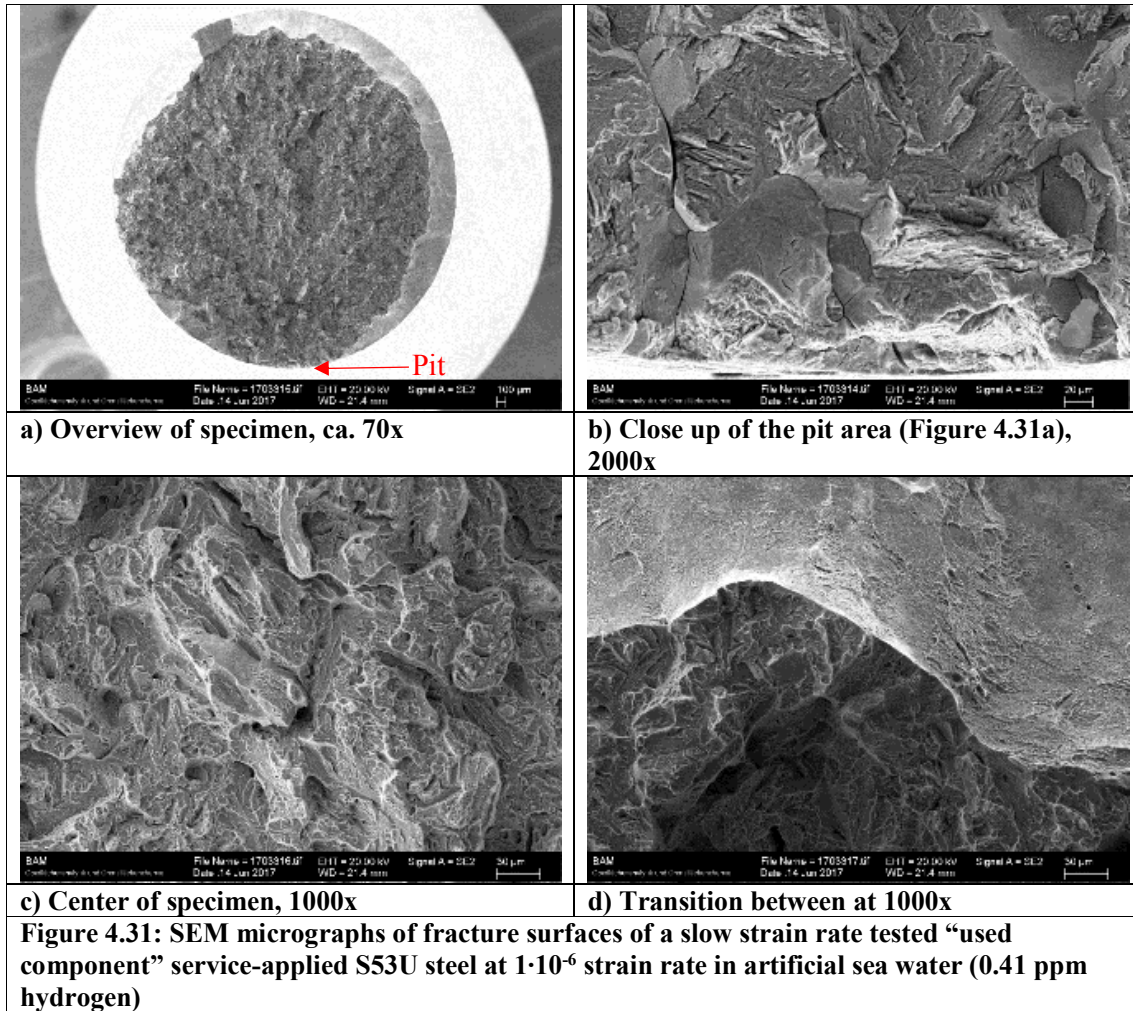


Figure 4.30: TSF diagram for the S53U steel in the service-applied “used component” condition in artificial seawater at various strain rates

Figure 4.31 shows exemplary photographs from the SEM investigation of a specimen of the used and service-applied steel S53U exposed to artificial seawater at a strain rate of $\dot{\epsilon} = 1 \cdot 10^{-6}$. From the overall fracture surface shown in Figure 4.31a the pit serving as a crack initiation site can be clearly identified. A close-up of this region in Figure 4.31b shows that the crack starts from the pit mixed inter- and transgranularly, in contrast to the new as-delivered steel where the crack initiation at the pits has been intergranular with nearly no exception, probably due to the much higher amount of retained austenite in the new material S53N. However, also in contrast to the new steel S53N, the crack propagates over the main part in a transgranular quasi-



cleavage mode, as shown by the photograph in Figure 4.31c taken from the specimen center. Finally, when the rest of the specimen cross section is not capable to carry the increased load due to the advanced crack, the ligament ruptures under a 45° direction, indicating some shear.

Figure 4.32 shows the respective hydrogen degassing curve for the same specimen taken for SEM evaluation of the fracture surface in Figure 4.31. This has been the specimen with the highest hydrogen concentration of 0.41 ppm taken up as an average in the gage length. It has to be emphasized, however, the actual and local hydrogen concentration causing crack initiation in the pit and respective propagation has been much higher than this average value. As already mentioned above, at respectively low hydrogen contents in the specimens, the degassing curve shows a significant scatter, like that in Figure 4.32. The typical peak at 200 to 300 °C, as already

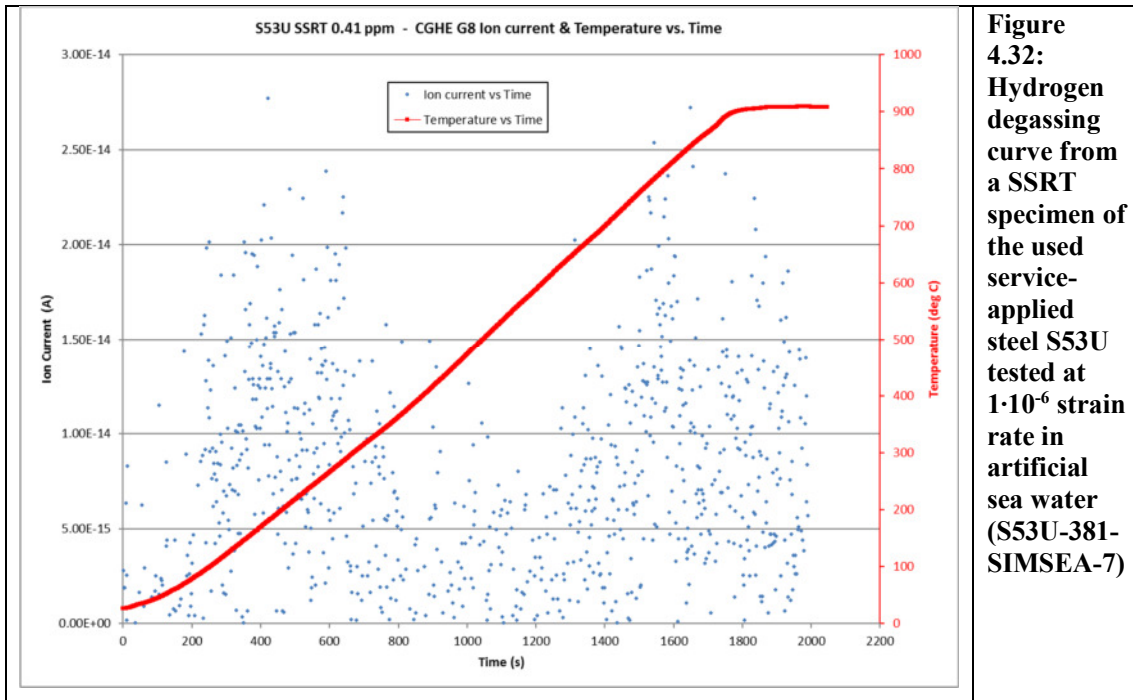


Figure 4.32: Hydrogen degassing curve from a SSRT specimen of the used service-applied steel S53U tested at $1 \cdot 10^{-6}$ strain rate in artificial sea water (S53U-381-SIMSEA-7)

observed for the hydrogen charged tensile specimens at higher concentrations is at least visible in the large scatter of the degassing curve in Figure 4.32. However, there seems also to be a second peak at significantly higher temperatures around 800 to 900 °C, indicating somewhat deeper trapped hydrogen in this material. As such peak has not been observed at the respective hydrogen-charged tensile specimens, it might have been the case that the hydrogen taken up by the used service-applied steel S53U during SSRT inside pits or at the tip of propagating cracks might have been trapped much deeper, perhaps by formation of additional deeper traps in the severe deformed area ahead of the crack tips. However, the large scatter of the degassing curve allows only such vague speculations which will not be followed further at this point.

4.3.2.2 Variation of Strain Rate in Natural Sea Water

It is commonly discussed in the current literature, if corrosion tests, in particular tests for the resistance against stress corrosion cracking should be carried out in standardized artificial seawater instead in natural seawater. On the one hand there are statements in literature [137] that natural seawater is much more aggressive than artificial sea water, particularly due to also providing microbes that might cause additional biofilms and microbiologically influenced corrosion on the surface, i.e. the above recognized localized corrosion in terms of pitting corrosion might be enhanced by respective anaerobic/aerobic biofilms. On the other hand, it

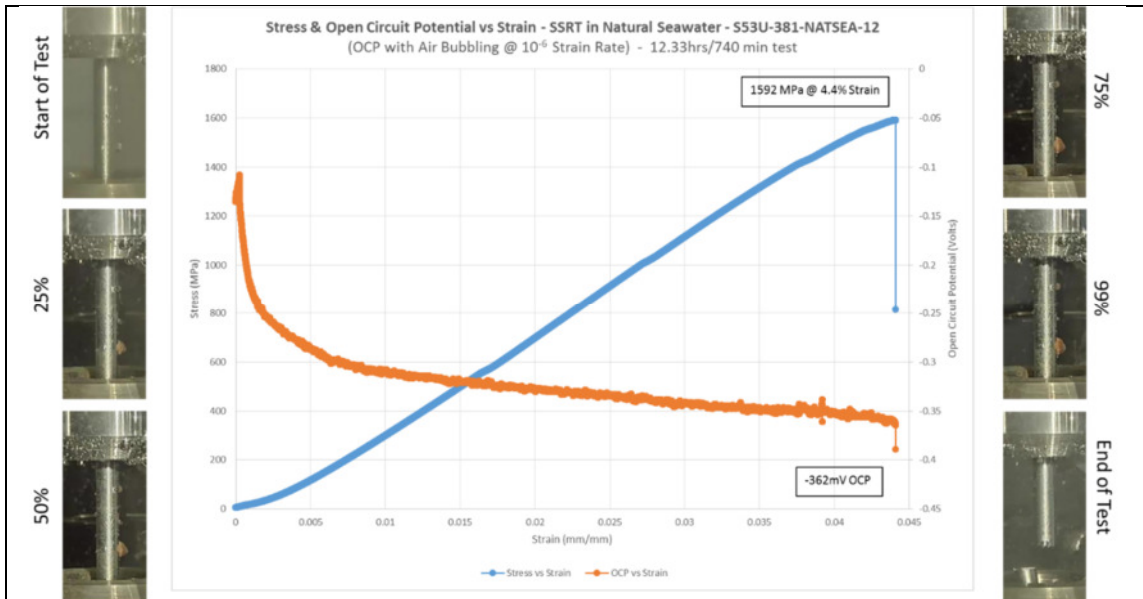
has been anticipated in literature that additional ingredients and perhaps less stable salt compositions in the natural seawater might retard localized corrosion.

The new landing gear steel S53 is intended to be used in marine environments which might entail some seawater contact. Thus, any ambivalent discussion about natural seawater effects as compared to testing in artificial seawater has been avoided by just conducting a small test series of the used and service-applied material in natural seawater taken from the Baltic Sea shore as described in Section 3 and to compare the results with those achieved by SSRT in artificial sea water. Since a strain rate of $\epsilon' = 1 \cdot 10^{-5}$ has already been identified as too high to exhibit the complete damage mechanism of combined pitting and hydrogen assisted stress corrosion cracking of the landing gear steel S53 in the new bar-stock as well as in the used service-applied condition for artificial seawater, the tests with the used steel S53U have only been carried out in natural seawater at a strain rate of $\epsilon' = 1 \cdot 10^{-6}$ and $\epsilon' = 1 \cdot 10^{-7}$. The results of these tests are compiled in Table 4.3.

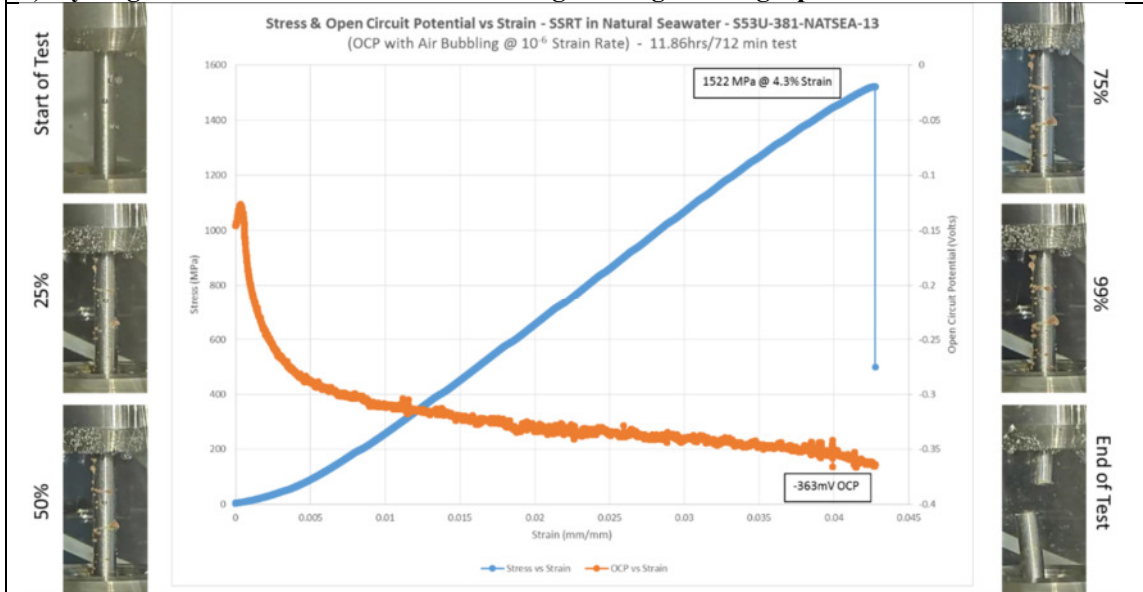
Specimen No.	Strain Rate (s ⁻¹)	Yield Strength (MPa)	Tensile Strength (MPa)	Time to Fracture TTF (min)	Technical Strain at Fracture (%)	True Fract. Strain	Final OCP (mV-Ag/AgCl)	Hydrogen conc. in the gage length (ppm)
S53U-12	$1 \cdot 10^{-6}$	1592	1592	740	4.4	0.0053	-362	n. d.
S53U-13	$1 \cdot 10^{-6}$	1522	1522	712	4.3	0	-363	0.10
S53U-14	$1 \cdot 10^{-7}$	643	643	2989	2.0	0	-424	0.61

Table 4.3: Results of the SSRT in artificial seawater at various strain rates

Figure 4.31 shows two stress-strain diagrams with respective potentials and photographs taken during the SSRT of the used service-applied steel S53U at a strain rate of $\epsilon' = 1 \cdot 10^{-6}$. Both diagrams show that the specimen failed around the yield strength, i.e. did not show any plastic deformation during the test. The first specimen (Figure 4.31a) failed by a single pit developing into hydrogen assisted stress corrosion cracking site on the lower half of the specimen, nearly at the specimen shoulder. However, pitting seems to be randomly occurring on the specimen service and the second specimen (Figure 4.31b) shows numerous pitting sites. At least two of those, one in the lower and one in the upper part of the specimen, developed into hydrogen assisted stress corrosion cracking. The main crack was clearly developing from the pit in the upper half of the specimen and caused final rupture there.



a) Hydrogen assisted stress corrosion cracking starting at a single pit



b) Hydrogen assisted stress corrosion cracking starting at numerous pits

Figure 4.31: Stress-strain curves from the SSRT of the used service applied steel S53U tested at a strain rate of $\epsilon' = 1 \cdot 10^{-6}$ in natural seawater

In comparison of Figure 4.28 with Figure 4.31, it seems that pitting of the used steel S53U is more severe in the natural seawater at a strain rate of $\epsilon' = 1 \cdot 10^{-6}$. Hydrogen assisted stress corrosion cracking also seems to develop at slightly about 30 mV (Ag/AgCl) higher electrochemical potentials in natural seawater as compared to the same test in artificial sea water. Even more pitting seems to develop below the yield strength, if the used and service-applied material S53U is tested at lower strain rate of $\epsilon' = 1 \cdot 10^{-7}$.

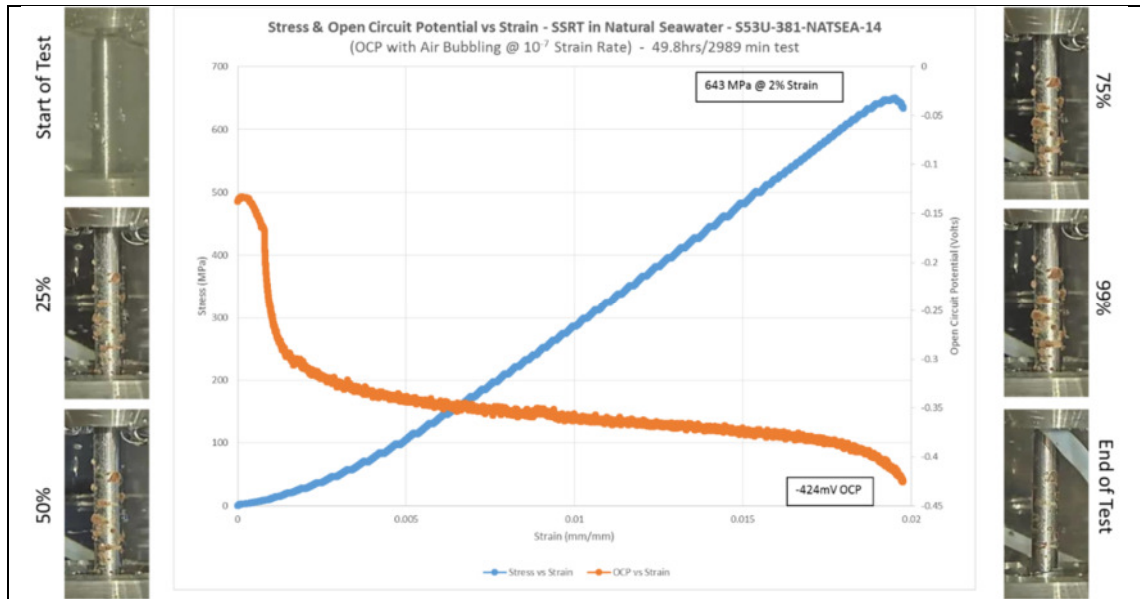


Figure 4.32: Stress-strain curve from the SSRT of the used service applied steel S53U tested at a strain rate of $\epsilon' = 1 \cdot 10^{-7}$ in natural seawater

As shown in Figure 4.32, several large pitting sites are situated on the specimen surface already after a quarter of the total test runtime. While the specimen tested at a strain rate of $\epsilon' = 1 \cdot 10^{-6}$ (Figure 4.31) at least still reached the yield strength, this specimen failed already at a third of the total yield strength. This test result is very similar to that revealing from testing in artificial seawater. However, a strain rate of $\epsilon' = 1 \cdot 10^{-6}$ seems to be sufficiently low to show the complete damaging of the material in natural seawater, as it has been for testing in artificial seawater.

Figure 4.33 finally shows the TSF diagram evaluated from the SSRT of the used service-applied steel S53U in natural seawater. Similar to the tests in artificial seawater, a very steep gradient can be observed towards higher strain rates. As can be seen from the diagram in comparison to Figure 4.30, the gradient is only marginally steeper as that for testing the same material in artificial seawater and the best fit failure curve is given by the equation

$$\epsilon_{\text{Frac}} = 382.91 \cdot t_{\text{ex}}^{-0.824} \quad (4.3)$$

This, again, means that the application of natural seawater as test solution in comparison to artificial seawater does not cause much difference in the failure curve. It appears thus as sufficient, to test the steel S53U in the used condition in artificial seawater without any need for complicated collecting natural seawater from a shore.

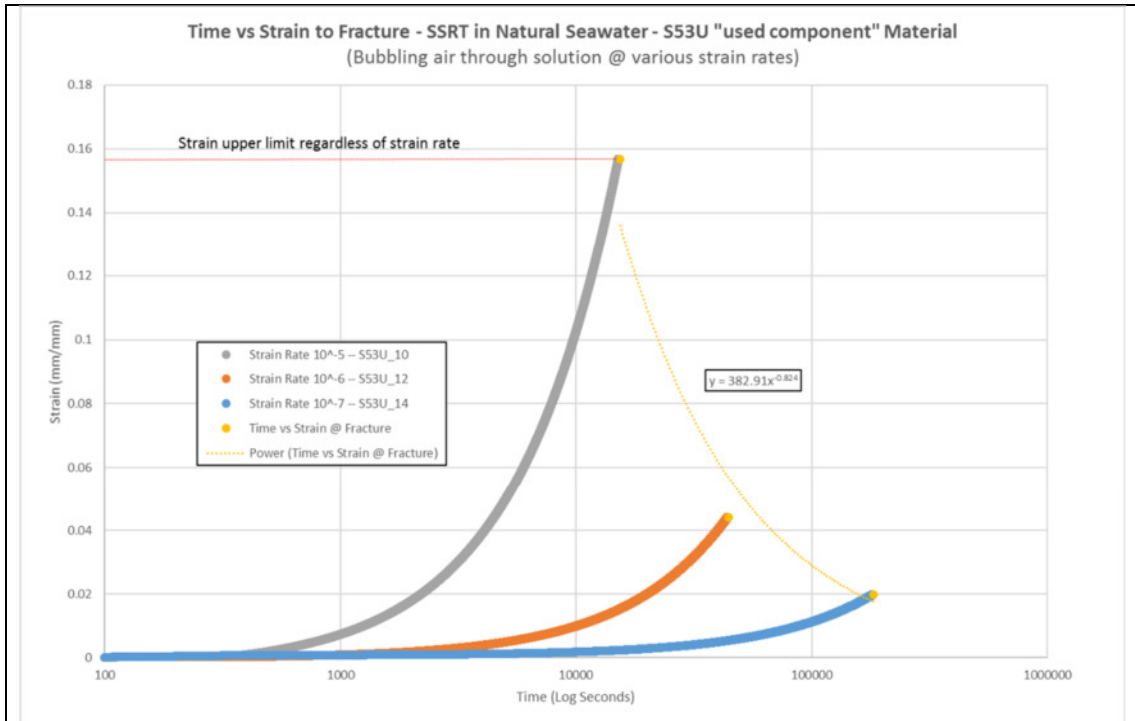
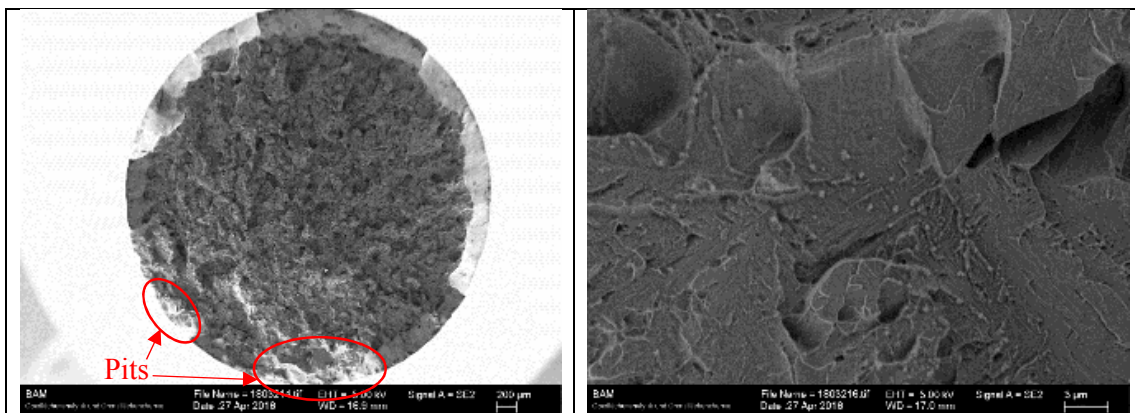


Figure 4.33: TSF diagram for the S53U steel in the service-applied “used component” condition in artificial seawater at various strain rates

Figure 4.34 shows two exemplary photographs of the SEM investigation of the fracture surfaces of this series carried out in natural seawater, here again at a specimen tested at a strain rate of $1 \cdot 10^{-6}$. Similar to the tests in artificial seawater, initiation of cracking from respective pitting corrosion becomes already visible on the overall fracture surface shown in Figure 4.34a.



a) Overview of the specimen at 70x

b) Center of the specimen at 10000x

Figure 4.34: SEM micrographs of the fracture surface of a SSRT specimen of the used and service-applied steel S53U specimen tested with a strain rate of $\dot{\epsilon} = 1 \cdot 10^{-6}$ in natural sea water

Also, rupture of the final ligament under 45° shear can be observed on this specimen, similar to those tested in artificial seawater (Figure 4.31a).

Figure 4.34b shows a close-up of the fracture topography in the center of the specimen. Aside some corrosion products left on the surface, it exhibits classical quasi-cleavage cracking in the very typical form for hydrogen assisted cracking in martensitic steels, as already shown in the literature survey. It is characterized by the elongated facets, showing a leaf-like structure and feather-like edges under 45° shear towards the next cleavage facet. However, nearly no ductile portions exhibiting any MVC could be detected at the edges of the cleavage facets which is an indication for total brittle failure.

Figure 4.35 shows exemplarily a degassing curve of a SSRT specimen of the used service-applied steel S53U exposed to natural seawater a strain rate of $\dot{\epsilon} = 1 \cdot 10^{-7}$. The degassing curve is only little more pronounced than that for the specimen tested in artificial seawater, since the average concentration in the specimen is similarly low than the one shown previously from a test in artificial seawater (Figure 4.32). It has also to be considered that this specimen here has been tested at an order of a magnitude lower strain rate and thus, has had significantly more time to take up hydrogen at the progressing crack tips and inside the preceding pits. In other words, the used service-applied steel S53U does not take up much more hydrogen in natural seawater than in artificial seawater.

As already mentioned, although the hydrogen concentration take up in the vicinity of a pit and at the tip of propagating cracks might be very high, the average hydrogen concentration in the gage length of such SSRT specimens is normally considerably low, in particular if compared to totally saturated tensile specimens investigated in Chapter 4.2. Thus, the degassing curve shown in Figure 4.35 again shows a remarkable scatter.

However, as compared to the totally hydrogen saturated tensile specimens, also this curve seems to exhibit a second peak of hydrogen release at significantly high temperatures between 800 and 900 °C, similar to the investigated specimen tested in artificial seawater (Figure 4.32) which might represent an indication for some deeper trapping of hydrogen during the SSRT than during simple hydrogen charging of tensile test specimens.

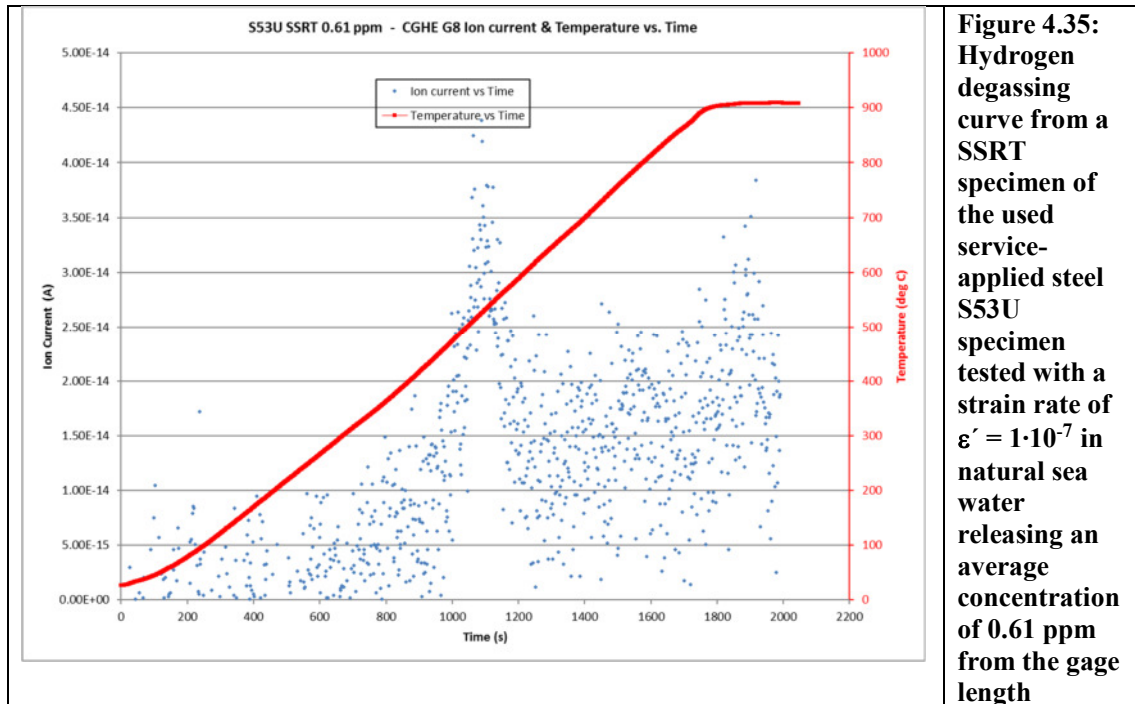


Figure 4.35:
Hydrogen
degassing
curve from a
SSRT
specimen of
the used
service-
applied steel
S53U
specimen
tested with a
strain rate of
 $\epsilon' = 1 \cdot 10^{-7}$
in
natural sea
water
releasing an
average
concentration
of 0.61 ppm
from the gage
length

Again, this provides some evidence for the tentative assumption that this might be caused by significant deformation of the specimen at respective tips of propagating cracks. Again, the scatter of also these curves (Figures 4.32 and 4.35) does not allow much more interpretation at this point.

4.3.2.3 Variation of Electrochemical Potential in Artificial Seawater

In nearly all SSRT, regardless if in artificial or natural seawater and regardless, of testing the new as-delivered bar-stock or the used service-applied steel S53, pitting corrosion with subsequent hydrogen assisted stress corrosion cracking has been developing at an open circuit potential (OCP) between -350 and -400 mV(Ag/AgCl). Thus, and for practical application of this steel for airplane landing gear systems, the question arises, whether the material could be protected by a fixed potential (cathodic protection – CP) to prevent any pitting and sudden rupture during service in severe marine environments, as for instance on aircraft carriers.

Following an indication in a previous work [144] that a cathodic potential of -605 mV (Ag/AgCl) might be helpful to completely prevent failure in saline environments by such mechanisms, a series of SSRT has been carried out in artificial seawater by variation of the specimen potential in steps of 200 mV from -405 to -1000 mV (Ag/AgCl). The complete test

series has been carried out at a constant strain rate of $\epsilon' = 1 \cdot 10^{-6}$ and the results of the evaluable tests are listed in Table 4.4.

Specimen No.	Strain Rate (s ⁻¹)	Yield Strength (MPa)	Tensile Strength (MPa)	Time to Fracture TTF (min)	Technical Strain at Fracture (%)	True Frac. Strain	Applied Potential (mV-Ag/AgCl)	Hydrogen concentration in the gage length (ppm)
S53U-15	1·10 ⁻⁶	1619	1868	650	6.2	0.048	-605	1.83
S53U-18	1·10 ⁻⁶	1613	1965	2509	14.9	0.645	-605	2.05
S53U-19	1·10 ⁻⁶	1630	1960	2570	15.3	0.827	-605	n. d.
S53U-20	1·10 ⁻⁶	1266	1266	599	3.6	0	-1000	3.73
S53U-21	1·10 ⁻⁶	1629	1629	760	4.6	0.026	-805	3.95
S53U-22	1·10 ⁻⁶	1437	1437	652	3.9	0.011	-405	2.03

Table 4.4: Results of the SSRT in artificial seawater at a strain rate of $\epsilon' = 1 \cdot 10^{-6}$ at various constant cathodic potentials

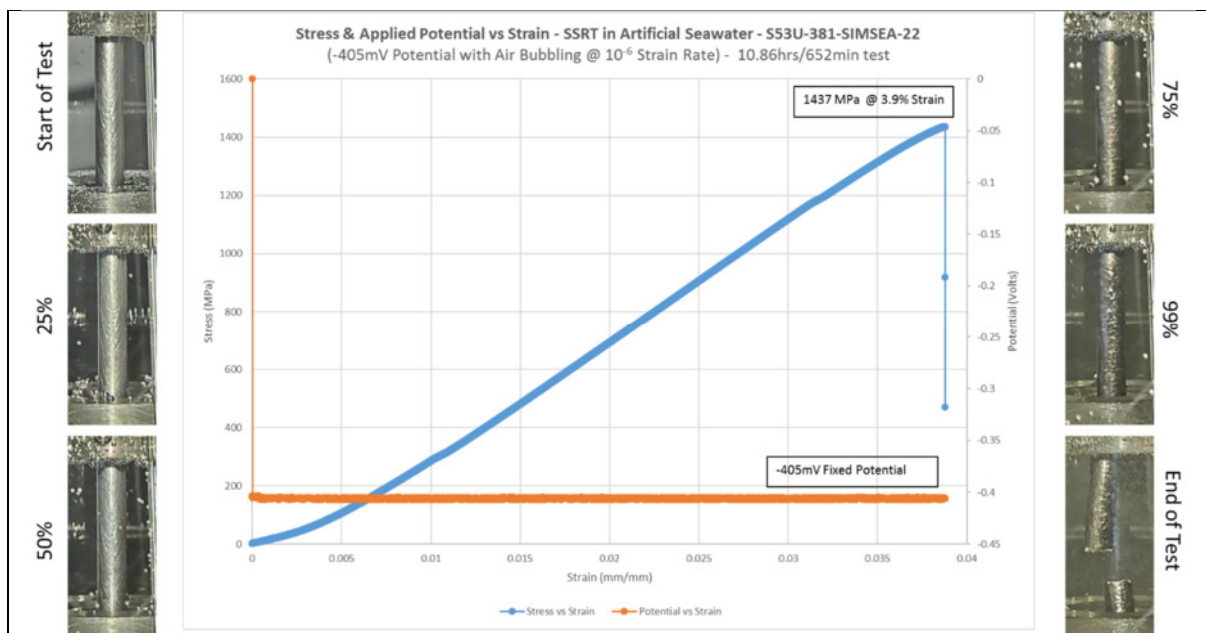
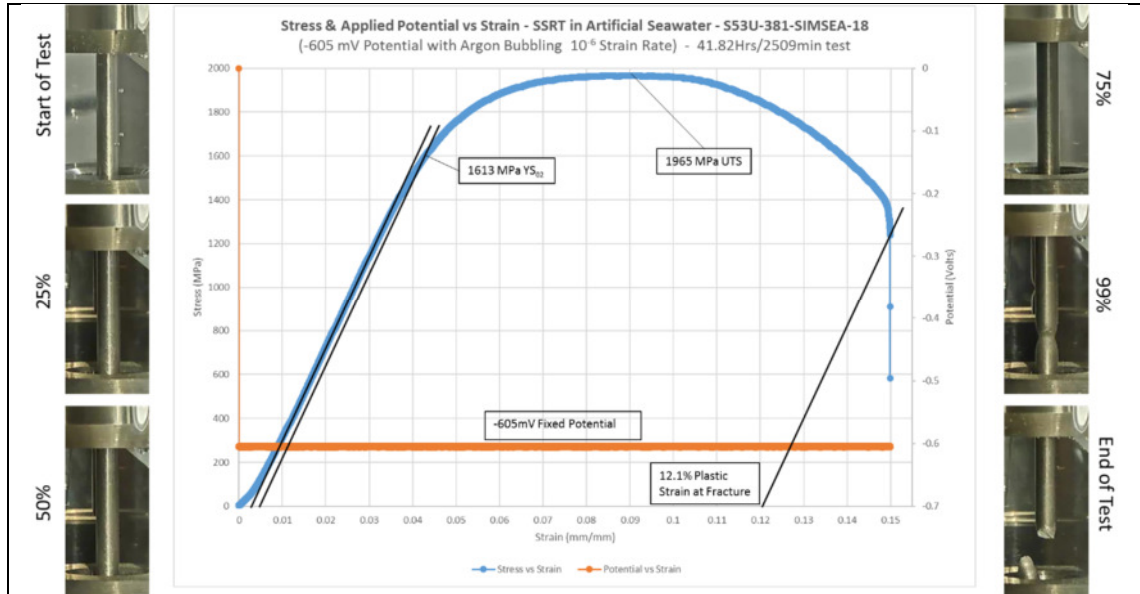


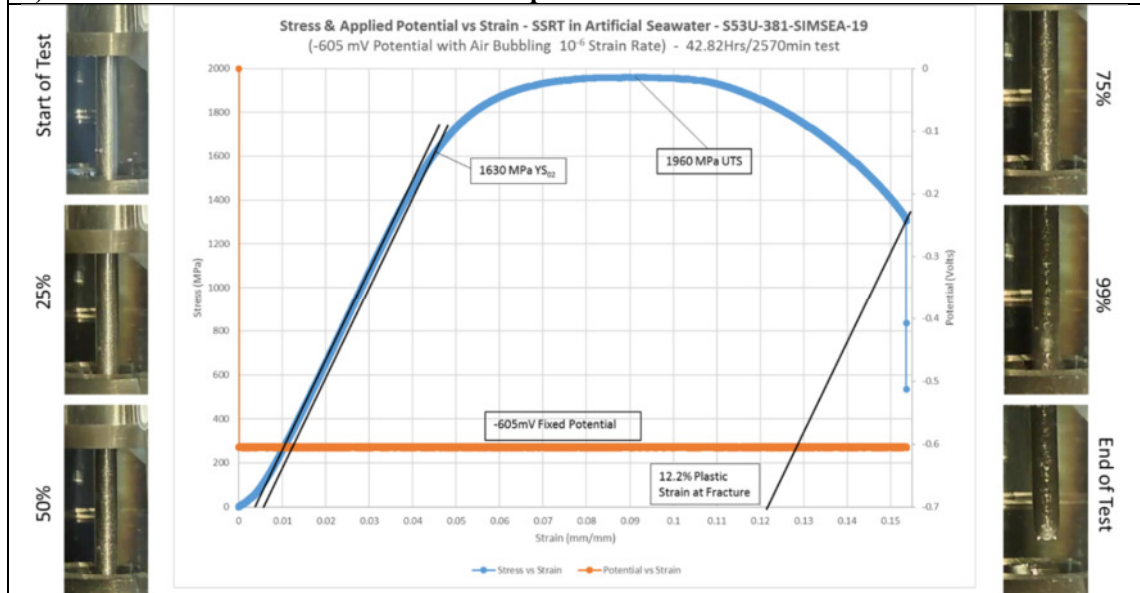
Figure 4.36: Stress-strain curve from the SSRT of the used service applied steel S53U tested at a strain rate of $\epsilon' = 1 \cdot 10^{-6}$ in artificial seawater at a fixed electrochemical potential of -405 mV (Ag/AgCl)

As a first approach, a fixed potential of -405 mV (Ag/AgCl) corresponding to the final open circuit potential measured in the preceding tests has been applied. Figure 4.36 shows the respective stress-strain curve, the constant potential as well as some significant photographs of the specimen surface taken during the test at start, different percentages of the total runtime and at the end of the test. The specimen surface starts to show heavy corrosion after 75% of the total

runtime. This potential, consistent to the tests at OCP, clearly ranges above the critical potential for passive film breakdown in artificial seawater. The specimen failed without showing any ductility in the lower half of the gage length.



a) Ductile fracture in the lower half of the specimen



b) Ductile fracture in the lower half of the specimen

Figure 4.37: Stress-strain curves from the SSRT of the used service applied steel S53U tested at a strain rate of $\epsilon' = 1 \cdot 10^{-6}$ in artificial seawater at a fixed electrochemical potential of -605 mV (Ag/AgCl)

Figure 4.37 shows the stress-strain diagrams of two out of three specimens tested at a cathodic potential of -605 mV(Ag/AgCl) which has been mentioned elsewhere as being protective for a

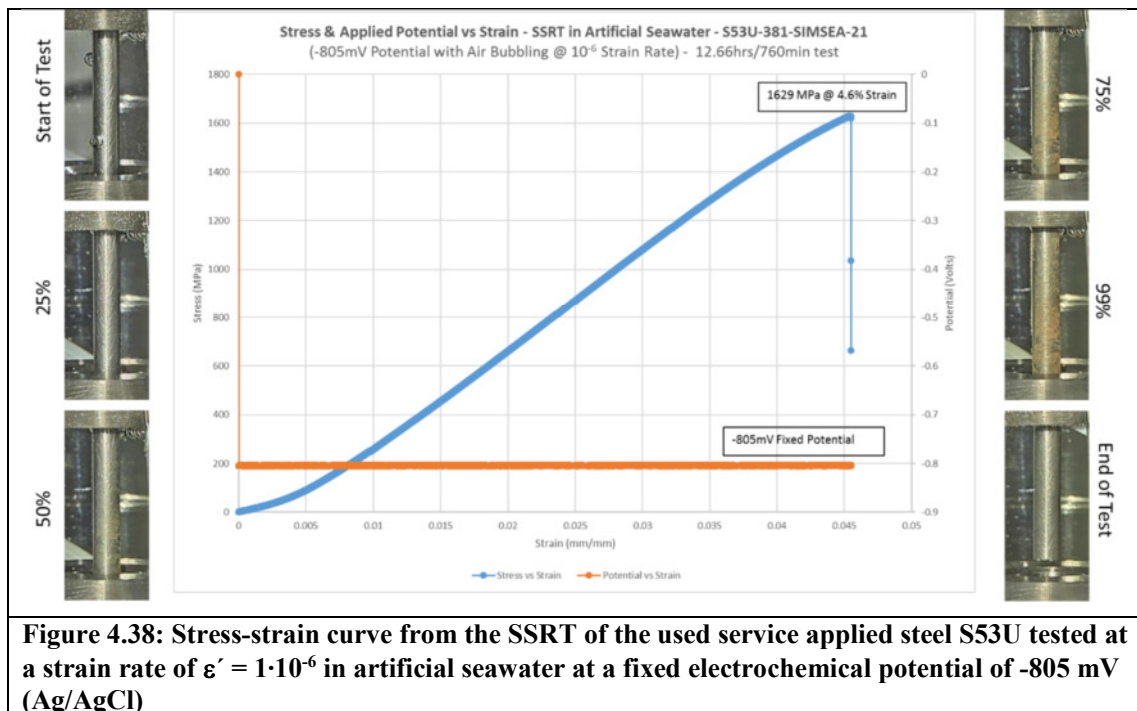
similar steel (AerMet 100) in artificial seawater. Consistent to those results, also the steel S53U in its used and service-applied condition after five years shows quite a ductile behavior in the SSRT at this constant cathodic potential.

In contrast to the investigations carried out by others [144] this result shows quite evidently that a degassing of SSRT specimens after the test is indispensable for proving, if hydrogen might have been absorbed during the test under the respective conditions, or not. At the present state of the investigations, it can thus only be emphasized that application of a cathodic potential of -605 mV(Ag/AgCl) does not mean that the material does not take up some hydrogen via the surface, causing a reduced ductility. Additionally, it has to be expected that the hydrogen concentration in the specimens has not been homogeneously distributed, since the exposure time of the 3.85 mm thick specimen with about 48 hours has been much shorter than the exposure time required for complete saturation of the by 3 mm somewhat thinner hydrogen charged tensile specimens in an even much more hydrogen producing environment. It has thus to be expected that the sub-surface concentration in these specimens has been significantly higher than the about 2 ppm measured as an average during degassing.

In addition, it has to be considered that the tensile testing of the hydrogen charged used and service-applied steel S53U exhibited already a significant reduction of ductility of this material when it is fully saturated by hydrogen with a concentration of about 2 ppm that has been measured here as an average over the gage length volume.

As an anticipated conclusion, further investigations have to show evidently, if hydrogen uptake and subsequent hydrogen assisted cracking can be really avoided by applying a cathodic potential of -605 mV(Ag/AgCl) and that this value given elsewhere cannot be taken as granted to avoid hydrogen assisted cracking of respective landing gear components made of the steel S53 as tested in the used and service-applied condition here. However, such investigations, in particular in comparison with the conventionally applied steel 4340 and others go definitely beyond the frame of this thesis. Anyway, it has to be stated clearly at this point, that application of a cathodic potential of 605 mV(Ag/AgCl) clearly protects the surface of the used and service-applied steel S53U in a way that no passive film and localized corrosion is occurring.

Figure 4.38 shows the stress-strain curve of the used and service-applied steel S53U from SSRT in artificial seawater at an even 200 mV lower potential of 805 mV(Ag/AgCl). While in the first quarter of the test runtime, the specimen surface was maintaining quite shiny, after half of the test duration some hydrogen bubbles seem to develop on the specimen surface. After about 12 hours, the specimen ruptured at the level of its yield strength in air, i.e. without showing any ductility. Table 4.w reveals that hydrogen at significant average concentrations of 3.95 ppm might be taken up, if this material is exposed to artificial seawater at this cathodic potential.

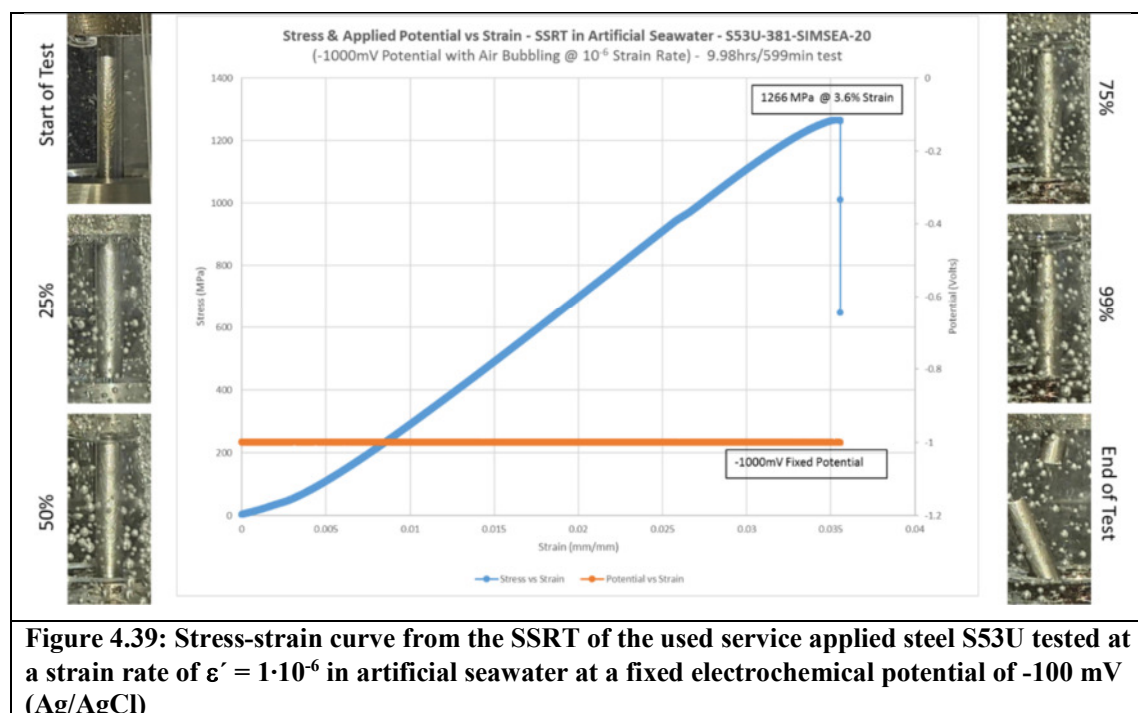


It can thus tentatively be assumed at this point that such a low potential will also prevent the used and service-applied steel S53U from passive film breakdown and localized corrosion in seawater/marine environments, but not from hydrogen uptake and subsequent hydrogen assisted cracking, particularly at long-term exposure.

Figure 4.39 shows that lowering the cathodic potential down to a value of -1000 mV(Ag/AgCl) which is a very common potential applied for corrosion protection of materials subjected to marine environments evidently entails a severe risk for hydrogen assisted cracking. As shown by the stress-strain curve of the SSRT with a strain rate of $\dot{\epsilon} = 1 \cdot 10^{-6}$, at such low potentials severe hydrogen production seems to take place in the artificial seawater, as indicated by the

bubbling shown in all of the photographs taken during the test runtime. Failure of this specimen occurred significantly below the yield point of the used service-applied steel S53U in air, i.e. in inert environments.

Already this represents an indication for severe hydrogen assisted cracking which becomes evident by the high average concentration of 3.72 ppm that has been taken up during the test runtime in this series (Table 4.4).



Interestingly, the hydrogen concentration taken up this potential seems to be slightly lower than that taken up in the specimen tested a 200 mV higher fixed potential (Table 4.w). This might be attributed to the fact that much more hydrogen bubbling indicating recombination to molecular hydrogen has been observed during this as compared to the previous test at a fixed potential of -805 mV(Ag/AgCl) under the consideration that molecular hydrogen evaporates instead being absorbed by the material.

However, it has at least to be mentioned that no localized corrosion has been observed under such a cathodic potential and that the specimen surface remained shiny during the whole test.

However, it can only be concluded from this test that commonly applied potentials of around -1V as corrosion protection for components subjected marine/seawater environments do actually do not prevent the material tested here from hydrogen uptake entailing severe cracking.

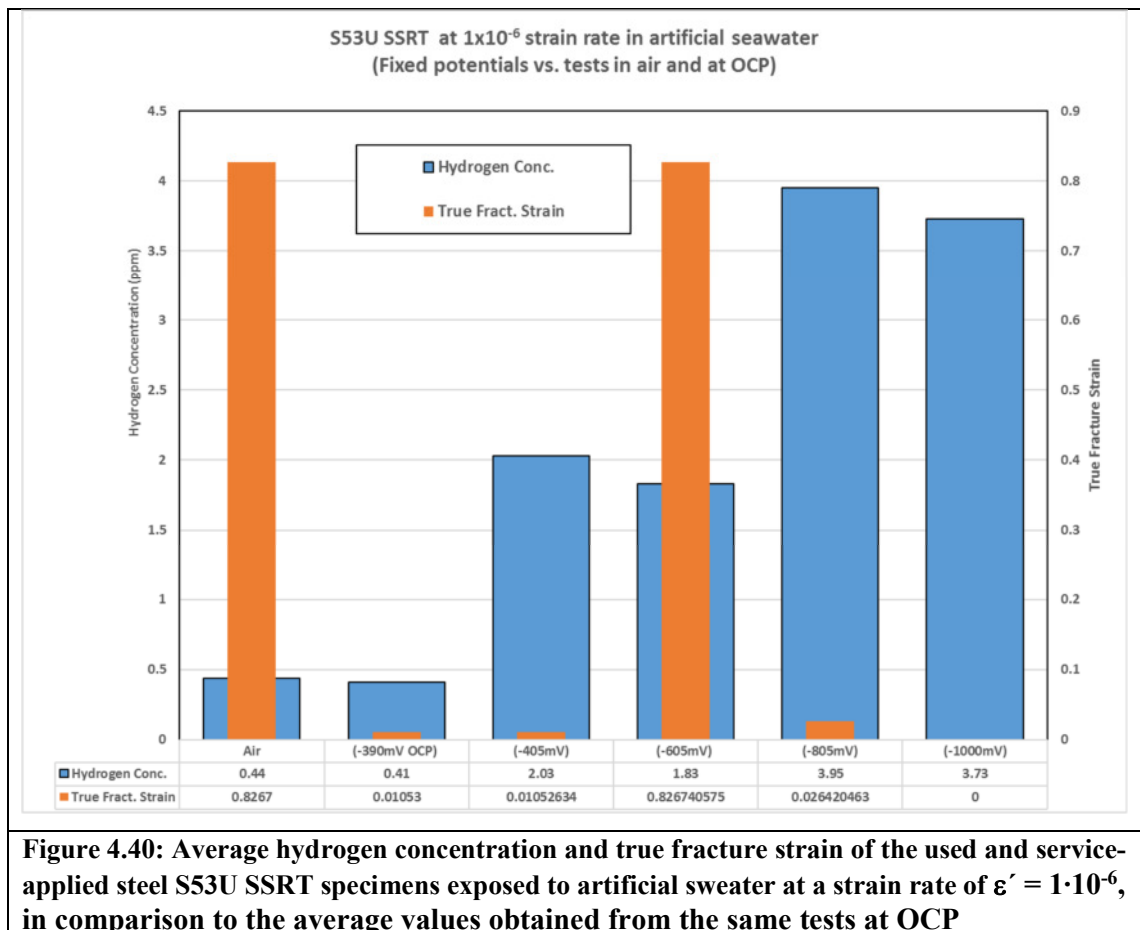
Figure 4.40 summarizes the results of the SSRT of the used and service-applied steel S53U with a strain rate of $\dot{\epsilon} = 1 \cdot 10^{-6}$ in artificial seawater at fixed cathodic potentials in comparison to the average results of the same SSRT at OCP. It can be clearly seen that a cathodic potential of -605 mV(Ag/AgCl) leads to the lowest hydrogen concentrations taken up by the material. Such potential thus seems to be suitable to prevent at least the severe damage mechanism of passive film breakdown and pitting corrosion with subsequent hydrogen assisted stress corrosion cracking starting from such regions of localized corrosion. At the applied strain rate of $\dot{\epsilon} = 1 \cdot 10^{-6}$ this potential also entails the highest ductility values in terms of the true fracture strain, as also shown in the Figure 4.40.

However, it can again only be emphasized at this point, that the average hydrogen concentrations taken up during exposure to artificial seawater at this potential of -605 mV(Ag/AgCl) has not been zero in any of the three tests (Table 4.w). This means that the high ductility values revealed in the SSRT at this strain rate might perhaps cover a potential risk for hydrogen assisted cracking under long-term exposure of landing gear components made of the used and service-applied steel S53U to severe seawater environments.

In contrast, it has to be mentioned here that the submerging of the steel surface to artificial seawater probably represents the most severe environment the uncoated, i.e. unprotected, used landing gear material might experience in service. It is well-known for instance, that salt film coatings represent much less aggressive environments for a steel surface than artificial or natural seawater, for instance, since the ion mobility in more or less dry salt films is much lower than in seawater. In this context, it has to be mentioned also, that such salt films are probably the most frequent saline environments landing gear materials are exposed to in marine climates, like on aircraft carriers.

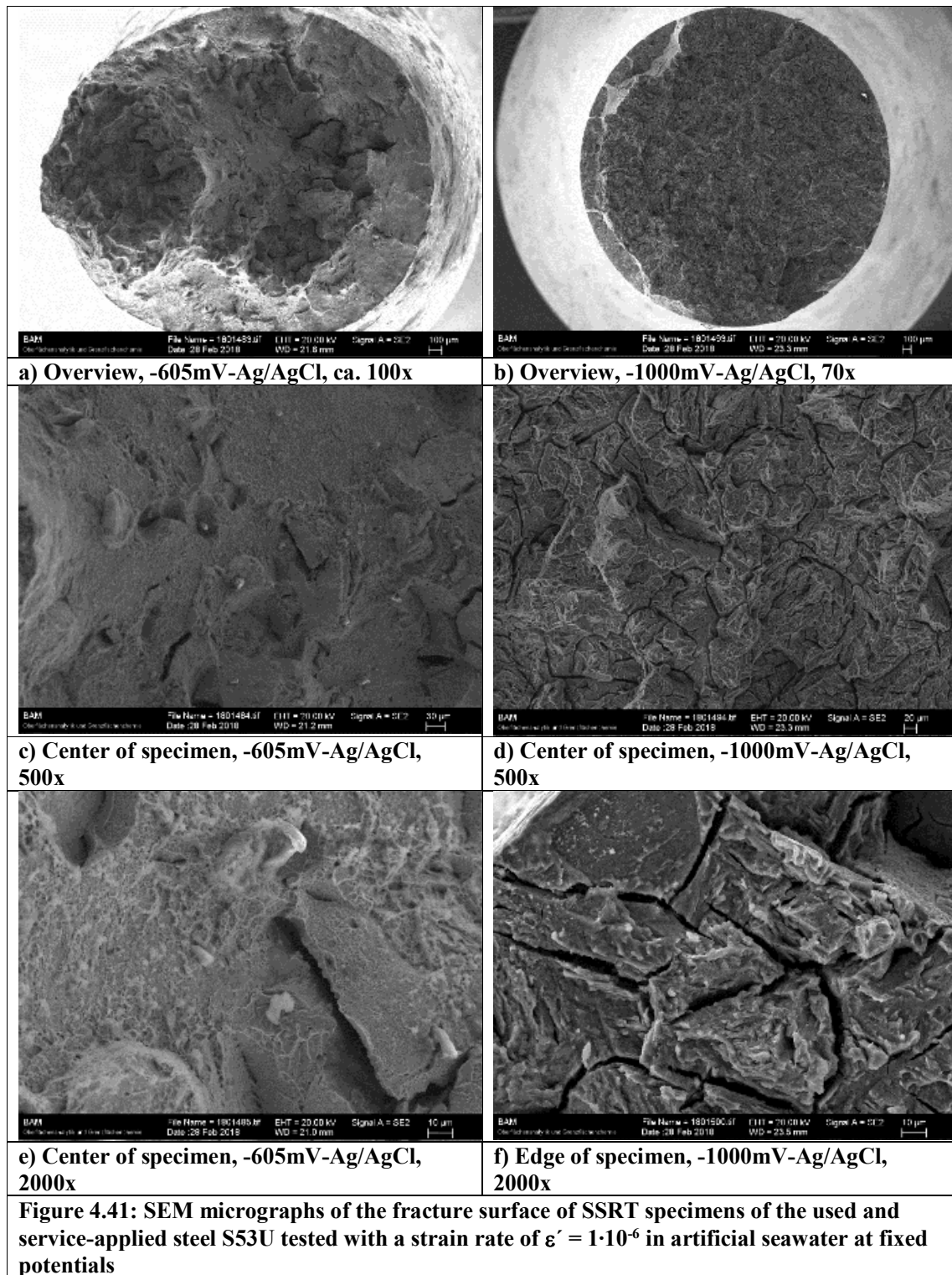
To sum this up here, before proposing application of this potential regime around -605 mV(Ag/AgCl) for protection of this material in marine environments, an embracing test series has to be carried out to evaluate the materials resistance against hydrogen assisted cracking in

such environments at such potentials under long term exposure. This should embrace a complete conclusive test series with the real component at the one end and basic tests for hydrogen transport and mechanical properties of the various microstructures on the other hand. It is suggested at this point that such investigations should include a series of SSRT at lower strain rates in seawater but also in splash zone environments like salt film coverages on the exposed surface, full scale or at least component oriented tests at realistic service-oriented mechanical loads combined with numerical modelling.



As a tentative conclusion, proposed cathodic potentials and corrosion protection measures suggested by limited investigations of different materials elsewhere [144] should not be taken for granted and be applied to other, similar materials and should be controlled by a complete conclusive test series, before it is applied to landing gear components made of the S53 steel investigated here.

Figure 4.41 shows fracture topographies as they had been revealed in the SEM investigations of the SSRT specimens.



Exemplarily, the fracture surfaces of a SSRT specimen tested at a fixed potential of -605 mV(Ag/AgCl) (Figures 4.41a, 4.41c and 4.41e) have been compared to those of the one tested at -1000 mV(Ag/AgCl) (Figures 4.41b, 4.41d and 4.41f). Already a comparison of the complete fracture surface (Figures 4.41a and 4.41b) reveals that the specimen tested at a fixed potential of -605 mV(Ag/AgCl) shows a much more ductile behavior.

This can predominantly be manifested by the ductile shear region at the margins of the specimen tested at a fixed potential of -605 mV(Ag/AgCl). As to be expected and in contrast to the previous specimens tested under OCP, no crack initiation at any pitting sites has been observed in both specimens. A larger magnification at 500x also shows a ductile rupture of the specimen tested at a fixed potential of -605mV(Ag/AgCl) by MVC (Figure 4.41c). In contrast, the fracture topography of the specimen tested at a fixed potential of -1000 mV(Ag/AgCl) shown in Figure exhibited a predominant transgranular cracking with some severe side cracking, partly also intergranular alongside former austenite grains, but mostly also alongside the martensite laths (Figure 4.41d). A close-up of the center of the fracture surface of the specimen tested at a fixed potential of -605 mV(Ag/AgCl) is shown the Figure 4.41e and confirms evidently rupture by MVC and respective ductile behavior. In contrast, transgranular cracking of the specimen tested at a fixed potential of -1000 mV(Ag/AgCl) is evidently exhibited by the larger magnification of the specimen edge shown in Figure 4.41f. It can be clearly seen that this fracture topography is very similar to that observed in the center of the specimens tested in artificial and natural seawater at OCP.

Since failure of this specimen (Figure 4.41f) can only have been caused by hydrogen uptake and subsequent hydrogen assisted cracking. The similarity of this fracture topography to that exhibited by the respective specimens tested at OCP provides enough evidence that also the corrosion cracking starting at preceding pitting sites and propagating slowly through the specimen is actually hydrogen assisted stress corrosion cracking.

Figure 4.42 shows the degassing curve of the specimen tested at a fixed potential of -805 mV(Ag/AgCl) which took up the highest concentration as compared to those of the whole test series. The higher hydrogen concentration provides also a less scattering hydrogen degassing curves, as can be drawn from a comparison of the Figure 4.35 and 4.42. However, this more

pronounced degassing curve now clearly exhibits a significant second hydrogen peak at temperatures above 800 °C, i.e. this peak is a real degassing peak showing some deeper trapping of hydrogen during the SSRT. Also, a quite small additional peak can be observed in this degassing curve at temperature of around 500 °C.

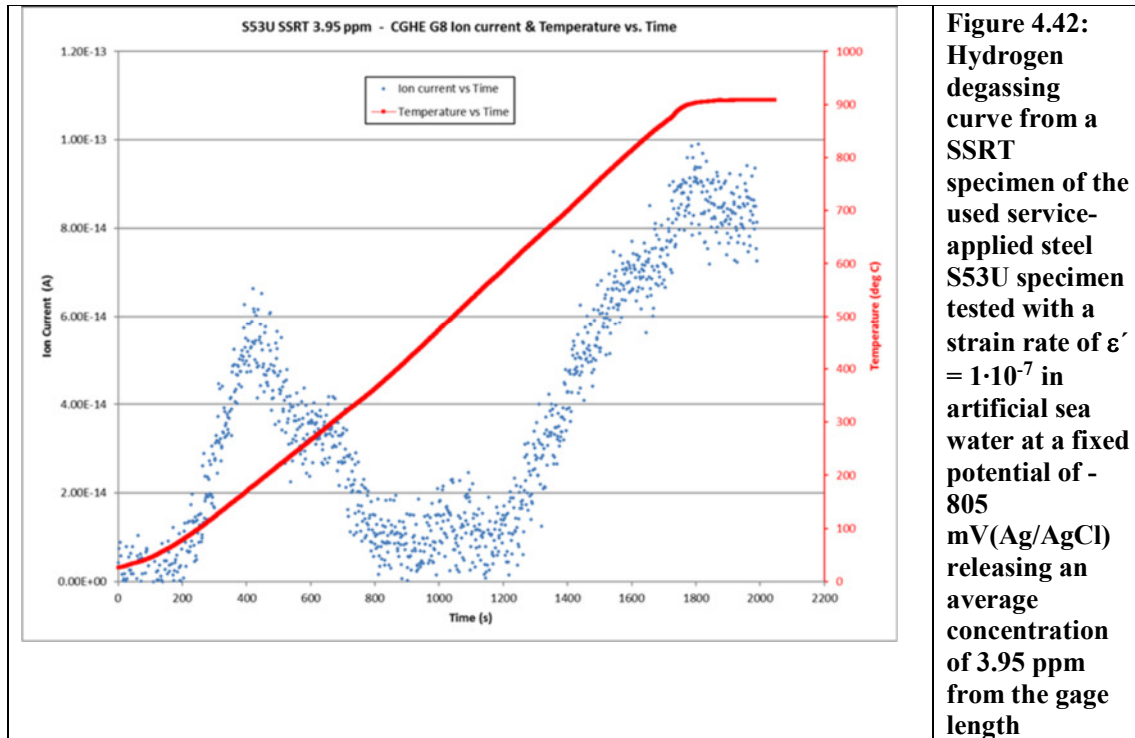


Figure 4.42: Hydrogen degassing curve from a SSRT specimen of the used service-applied steel S53U specimen tested with a strain rate of $\epsilon' = 1 \cdot 10^{-7}$ in artificial sea water at a fixed potential of -805 mV(Ag/AgCl) releasing an average concentration of 3.95 ppm from the gage length

This degassing curve provides some evidence that during straining in the SSRT hydrogen is absorbed and bound to deeper traps than during cathodic charging. However, even such deeper trapped hydrogen should be anticipated to contribute to brittle cracking of the used service-applied landing gear steel S53U and it cannot be expected that the hydrogen dependent material properties, particularly not the ductility relevant parameters, are overemphasizing any brittle behavior of this material at higher hydrogen concentrations, i.e. above about 2 ppm.

4.3.2.4 Variation of Temperature in Artificial Sea Water

Supposing that planes with landing gear made of the steel S53 investigated here might also be used for aircraft carriers in climates with elevated temperatures and also considering that such aircraft may be used on the deck of such carriers in the open sunlight in marine environments, exposure to temperatures up to 60 °C has to be taken into consideration. A small series of tests

Specimen No. and Test Temp.	Strain Rate (s ⁻¹)	Yield Strength (MPa)	Tensile Strength (MPa)	Time to Fracture TTF (min)	Technical Strain at Fracture (%)	True Fract. Strain	Potential mV (Ag/AgCl)	Average hydrogen concentration in the gage length (ppm)
S53U-23 (60 °C)	1·10 ⁻⁶	839	839	429	2.5	0	OCP	6.09
S53U-24 (60 °C)	1·10 ⁻⁶	1610	1912	2606	14	0.546	-605	0.96
S53U-25 (40 °C)	1·10 ⁻⁶	864	864	433	2.8	0	OCP	NR
S53U-26 (40 °C)	1·10 ⁻⁶	1625	1941	1681	10.2	0.075	-605	2.78

Table 4.5: Results of the SSRT of the used and service applied steel S53U in artificial seawater at a strain rate of $\epsilon' = 1 \cdot 10^{-6}$ at various two different temperatures with OCP versus a constant cathodic potential of -605 mV(Ag/AgCl)

has thus also been carried out at 40 and 60 °C, as a first approach towards more realistic and service application oriented testing of the S53 landing gear steel.

To allow a worst-case assessment regarding the aggressiveness of the environment, these tests have also been carried out in artificial seawater, although during real service, rather salt crusts will develop on such materials, if not actually removed during maintenance between take-off and landing. Since the used and service-applied steel S53U did not show any mechanical property degradation at room temperature at a fixed potential, it has also been tested, if this still the case at a temperature of 40 and 60 °C. It has to be mentioned at this point, however, that such tests for the resistance against pitting and hydrogen assisted stress corrosion cracking at higher temperatures than room temperature have not been carried out elsewhere up to the present. The results of this test series are summarized in the Table 4.5.

Figure 4.43 shows the SSRT evaluation diagram for the test carried out at 40 °C at OCP in artificial seawater. The potential is reduced significantly below -435 mV(Ag/AgCl) in this test. The photographs taken during the test show significant corrosion products on the specimen surface. The corrosion products are wiped away from the surface at the time when then specimen ruptured. This means that those corrosion products do not sit firm on the specimen surface, but are only products released into the solution while underneath severe pitting corrosion is taking place. The specimen ruptured finally in the lower half at only about half of the yield strength achieved in air.

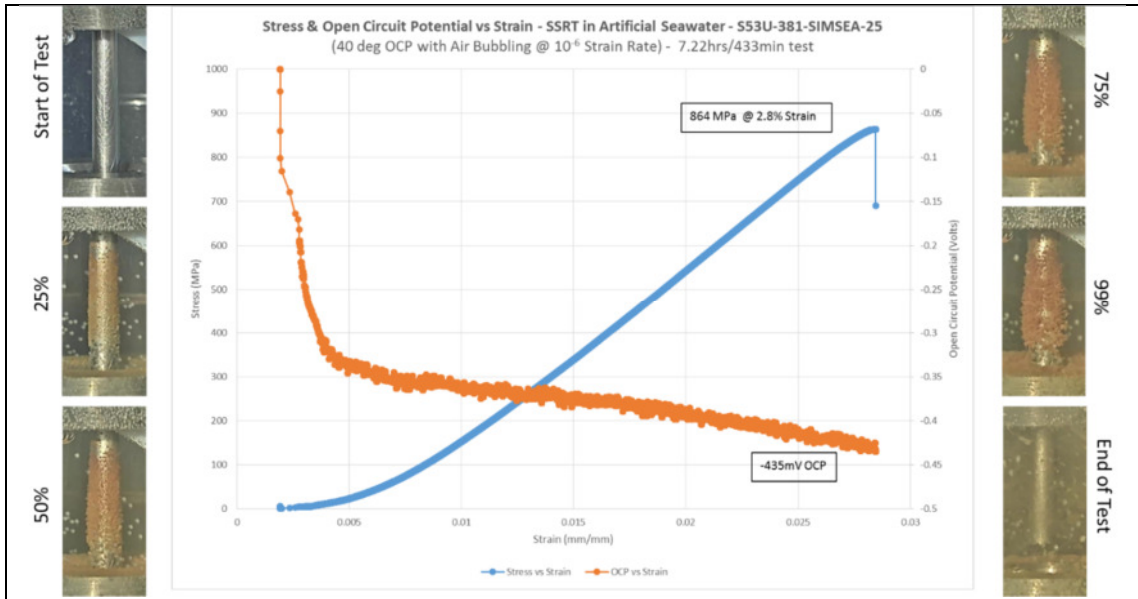
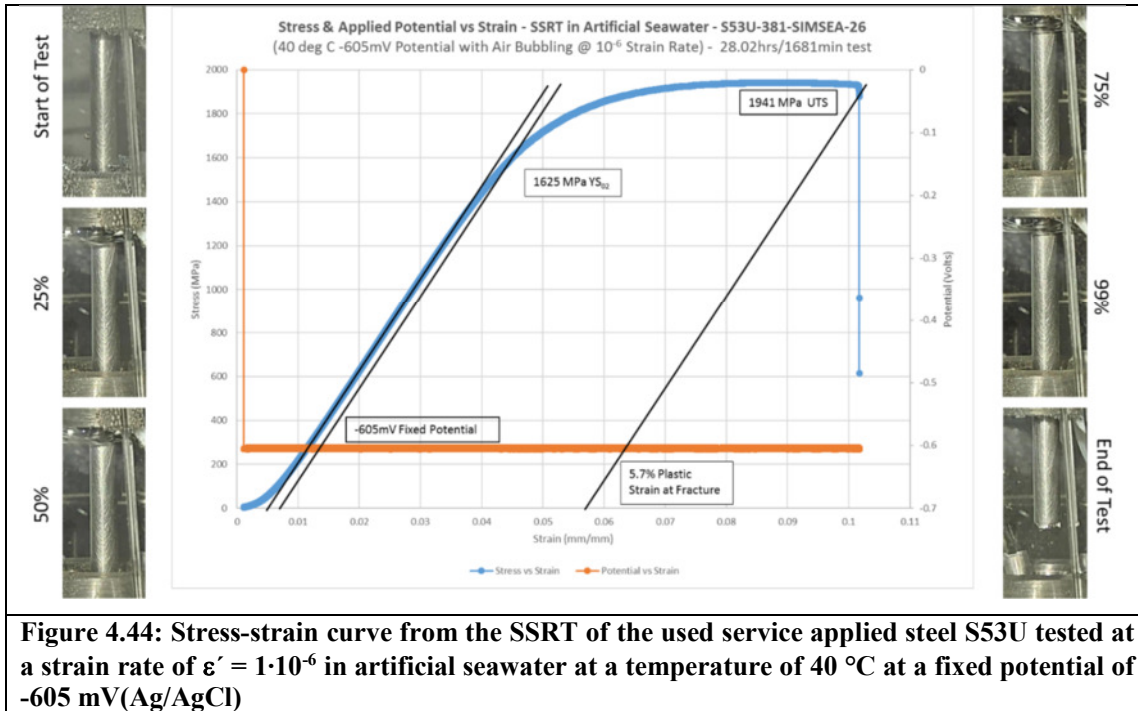


Figure 4.43: Stress-strain curve from the SSRT of the used service applied steel S53U tested at a strain rate of $\dot{\epsilon} = 1 \cdot 10^{-6}$ in artificial seawater at a temperature of 40 °C under OCP

This means that an elevation of the temperature by only about 20 °C above room temperature might cause a much more severe behavior of the material with respect to a passive film breakdown, localized corrosion and subsequent hydrogen assisted stress corrosion cracking. The latter is also indicated by a slightly higher average hydrogen concentration taken up by this specimen as compared to those tested at room temperature under the same conditions.

Figure 4.44 shows the same diagram for the specimen tested at the same condition, but by applying a fixed potential of -605 mV(Ag/AgCl). Under these conditions, the specimen surface stayed shiny and evidently, no pitting corrosion occurred on the specimen surface. Additionally, this specimen exhibited a much higher ductility of the used service-applied steel S53U than the specimen tested in the same environment at the same strain rate and the same temperature under OCP. However, the ductility of this specimen did only last to the ultimate tensile strength, i.e. the specimen exhibited uniform plastic strain, but no necking. Correspondingly, the technical fracture strain of the material in air (about 14%) was reduced significantly in this environment to about 6%.

Table 4.5 shows that quite a significant average hydrogen concentration of 2.78 ppm has been taken up during the test period, probably entailing the reduced ductility in terms of a loss of



necking. Somewhat more hydrogen is thus taken up by the used service-applied steel, if the cathodic potential of -605 mV(Ag/AgCl) is applied at higher temperatures. Application of such potential might thus not be as sufficient as anticipated elsewhere to prevent any hydrogen assisted cracking of the investigated steel S53U, as proposed elsewhere for another material.

Figure 4.45 shows the SSRT evaluation diagram for the test carried out at 60 °C at OCP. It becomes clearly visible, in comparison to Figure 4.43, that the localized corrosion on the specimen surface becomes even worse than it has been observed for a test temperature of 40 °C at the same conditions. The specimen surface seems to be completely covered by corrosion products after 75% of the total runtime. However, these scales are only slightly attached to the surface and immediately released when the liquid is stirred due to the final rupture, exhibiting severe pitting corrosion underneath. The OCP was reduced further to -458 mV(Ag/AgCl) at a test temperature of 60 °C, as compared to the test at 40 °C (-435 mV(Ag/AgCl)) and at room temperature (-360 mV(Ag/AgCl)). The low ductility of the material at this test conditions is associated with hydrogen uptake at a severely high average concentration of 6.09 ppm. It can only be repeated that such high average concentrations in SSRT specimens mean that the concentrations by which hydrogen absorbed underneath the surface and in the propagating

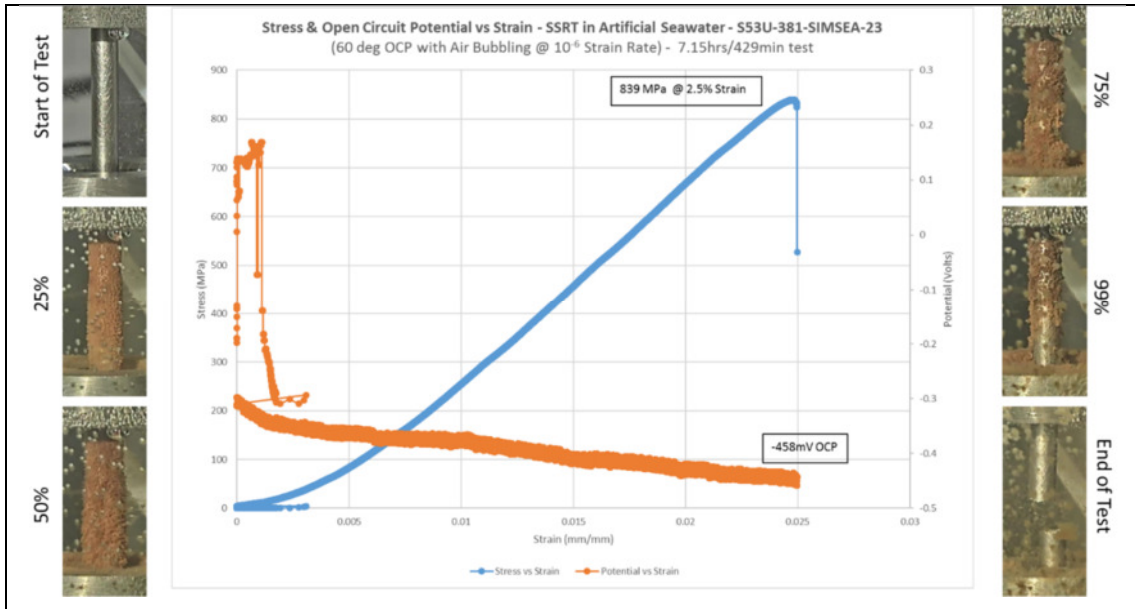


Figure 4.45: Stress-strain curve from the SSRT of the used service applied steel S53U tested at a strain rate of $\dot{\epsilon} = 1 \cdot 10^{-6}$ in artificial seawater at a temperature of 60 °C at OCP

crack must have been much higher, due to the concentration profile at the remarkably low exposition time of about 7 hours in comparison to the complete saturation of such specimens taking probably more than a week.

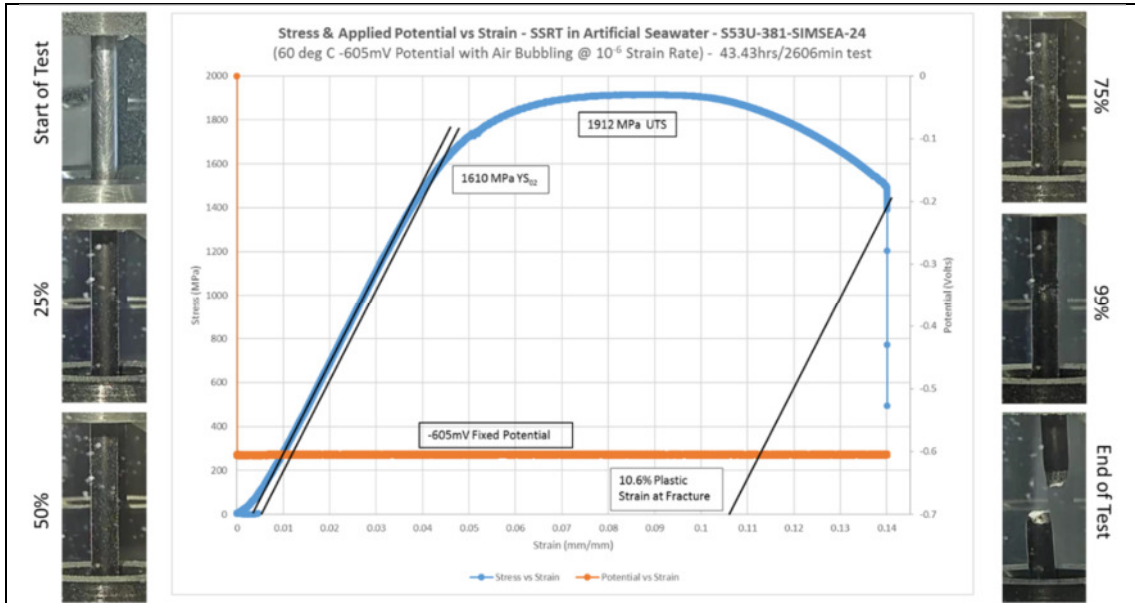


Figure 4.46: Stress-strain curve from the SSRT of the used service applied steel S53U tested at a strain rate of $\dot{\epsilon} = 1 \cdot 10^{-6}$ in artificial seawater at a temperature of 60 °C at a fixed potential of -605 mV(Ag/AgCl)

For comparison, the Figure 4.46 shows the SSRT evaluation diagram for the same test conditions at a fixed potential of -605 mV(Ag/AgCl). Interestingly, this specimen exhibited significantly more ductility than the specimen tested at the same test conditions at a temperature of 40 °C (Figure 4.44). The specimen exhibited a similar ultimate tensile strength than the steel S53U shows in air and also, significant necking could be observed, indicating a high remaining ductility. The specimen finally failed at a technical fracture strain of 10.6% which is slightly reduced to that what is achieved in air. As shown by Table 4.v, this specimen has also taken up hydrogen in a significantly lower concentration in average, i.e. only 0.96 ppm as compared to 2.78 ppm in the specimen tested at 40 °C at the same fixed potential. This actually explains why this specimen shows a larger ductility. It might thus tentatively be assumed that a fixed potential of -605mV(Ag/AgCl) is more beneficial at exposition of the used service-applied steel S53U to artificial seawater at an elevated temperature of 60 °C as compared to 40 °C and room temperature.

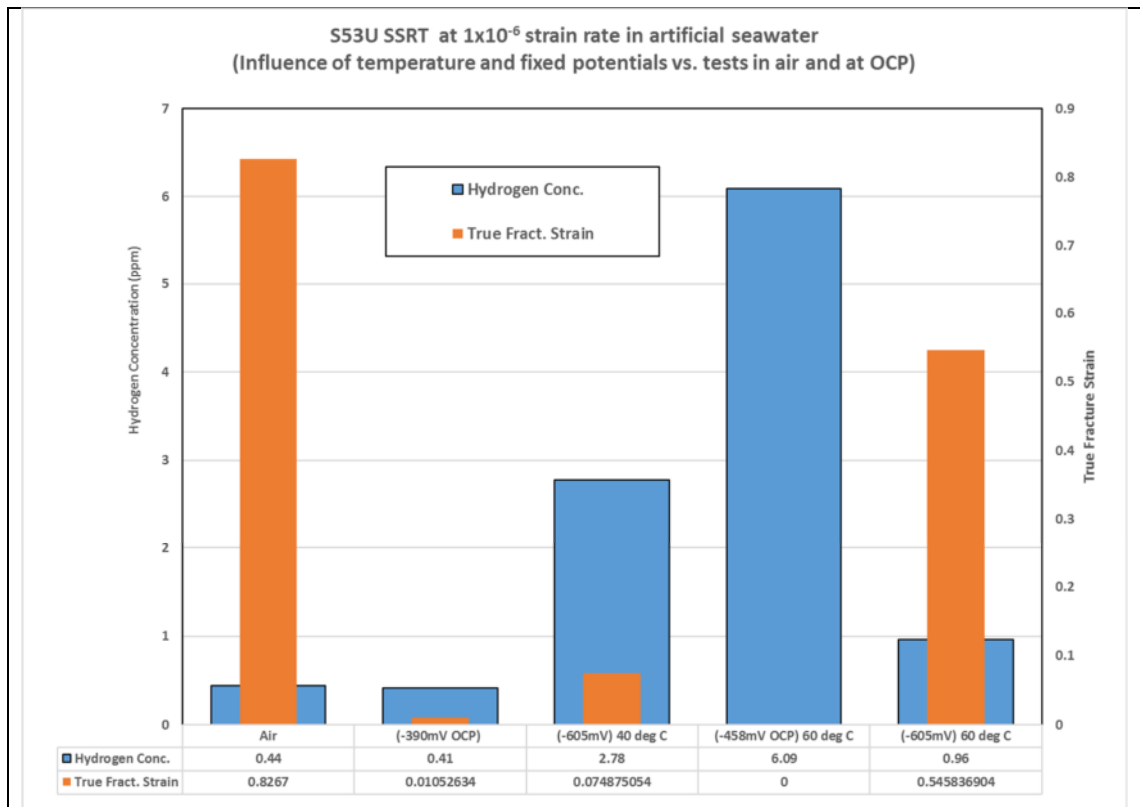


Figure 4.47: Average hydrogen concentration and true fracture strain of the used and service-applied steel S53U SSRT specimens exposed to artificial seawater at a strain rate of $\dot{\epsilon} = 1 \cdot 10^{-6}$ at room temperature, 40 and 60 °C with a fixed potential of -605 mV(Ag/AgCl) and at OCP

The bar chart in Figure 4.47 shows the average hydrogen concentration and the true fracture strain of the specimen tested at elevated temperature as compared to those tested at room temperature.

In general, the results above evidently show that a fixed potential of -605 mV(Ag/AgCl) can prevent localized corrosion in terms of pitting corrosion on the surface of the steel S53U during exposure in seawater at additional mechanical loading, even at higher temperatures up to $60 \text{ }^\circ\text{C}$. But, the bar charts in Figure 4.47 also show evidently that such cathodic protection even at a low fixed potential of -605 mV(Ag/AgCl) might entail hydrogen uptake in the material. This is the reason why the original ductility of the material in air is not been reached in the respective SSRT. It can thus again only be emphasized that further testing has to be carried out to prove if the investigated used and service-applied steel S53U is also resistant against hydrogen assisted cracking in such environments at such potentials under long term exposure. This should especially be carried out under consideration that higher hydrogen concentration in average have been taken up in the gage length at $40 \text{ }^\circ\text{C}$ than at $60 \text{ }^\circ\text{C}$.

Figure 4.48 exemplarily summarizes the results of the SEM investigation of the fracture topographies of the two specimens tested at $60 \text{ }^\circ\text{C}$ at OCP (Figures 4.48a, 4.48c and 4.48e) and at a fixed potential of -605 mV(Ag/AgCl) (Figures 4.48b, 4.48d and 4.48f). Already from a comparison of the overall fracture surface it becomes again clear that cracking started in the specimen tested at OCP at a pit and propagated through slowly the specimen cross section (Figure 4.48a). Actually, this specimen does not show any characteristic 45° shear zone at the margins, like it has been observed in other specimens tested at OCP for rupture of the final ligament. In contrast, the specimen tested at a fixed potential of -605 mV(Ag/AgCl) shows a much better ductility with a very 45° pronounced shear zone nearly round the complete margin (Figure 4.48b). A closer look at the center of the specimen tested at a temperature of 60°C at OCP exhibits the typical inter- and transgranular fracture surface, as already observed on other specimens. Cracking evidently propagated through the martensite in the former austenite grains, but also shows significant side cracking alongside the former austenite grains (Figure 4.48c). In contrast, the fracture surface of the specimen tested at the same temperature under a fixed potential of -605 mV(Ag/AgCl) shows a complete ductile topography by MVC also at this magnification.

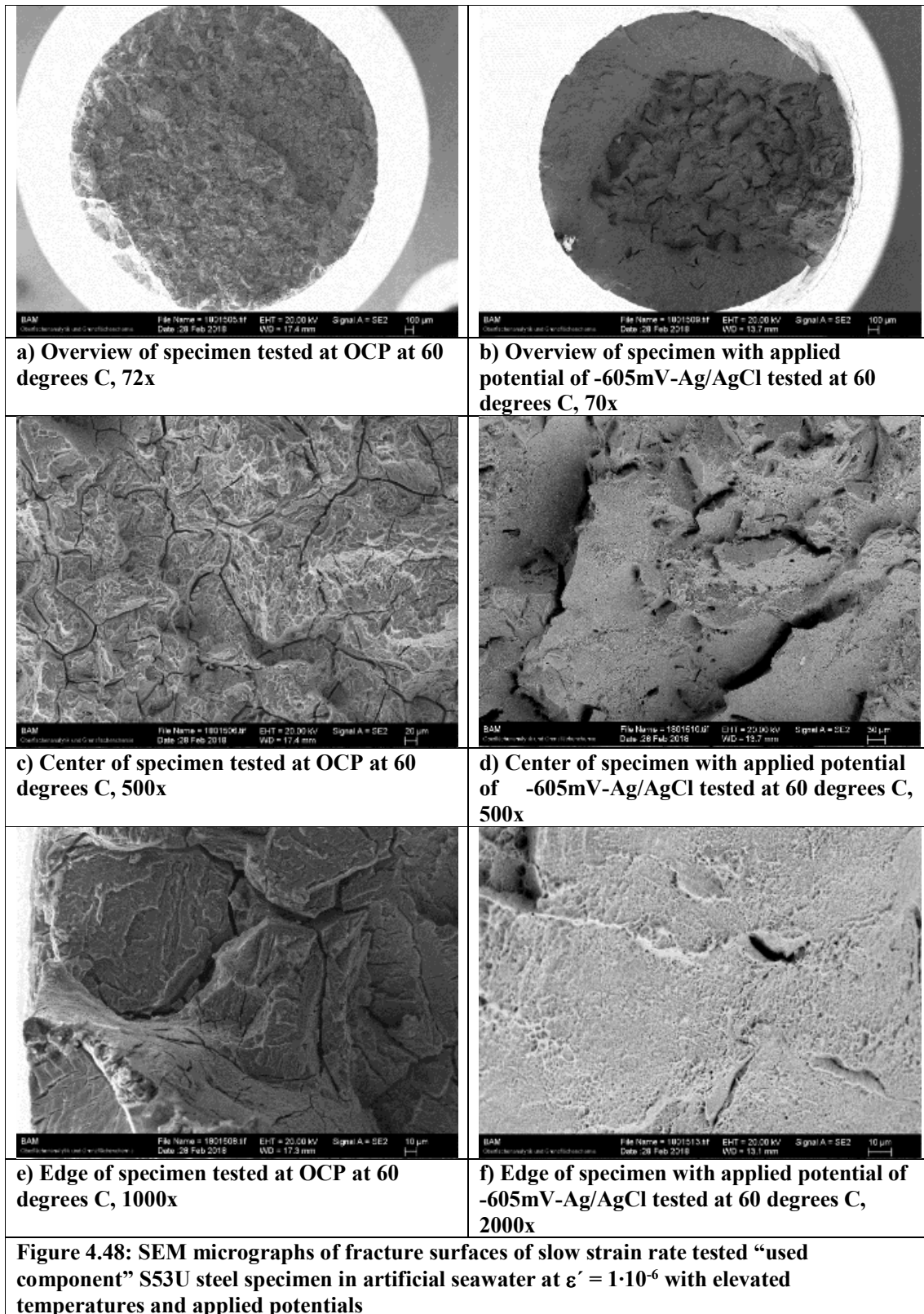
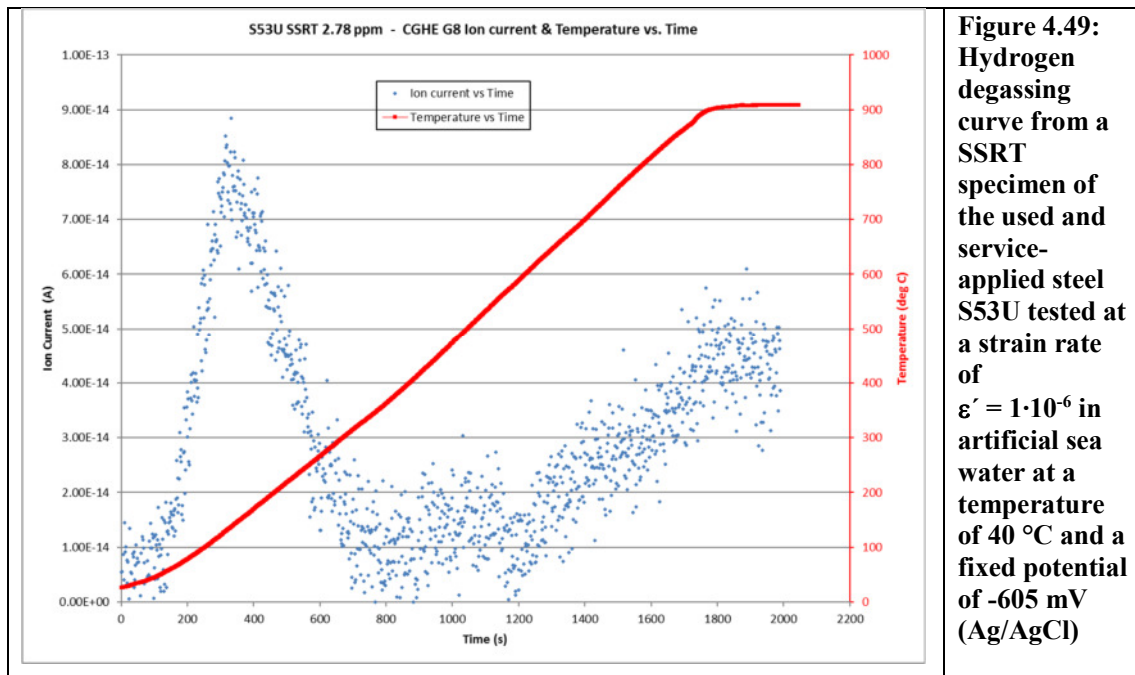


Figure 4.48e confirms the typical inter- and transgranular cracking of the used and service-applied steel S53U at OCP and a temperature of 60 °C. It can only be emphasized that such mixed inter- and transgranular cracking is quite typical for martensitic steels. However, any ductile zones could not be detected at the margins of the transgranular facets. It is thus assumed that, in contrast to the previous SSRT, the increased temperature evidently causes hydrogen uptake at higher concentrations levels in the vicinity of the pit and the propagating crack at OCP, entailing really brittle inter- and transgranular cleavage cracking, while at room temperature, for instance, still some quasi-cleavage cracking has been observed under the same test conditions (Figure 4.31c). Figure 4.48f, for comparison, shows a close-up of the ductile 45° shear zone at the specimen margins of the specimen tested at 60 °C at a fixed potential of -605 mV(Ag/AgCl).

Figure 4.49 shows the degassing curve of the specimen tested at a fixed potential of -605 mV(Ag/AgCl) and at a temperature of 40 °C which took up hydrogen in an average concentration of 2.78 ppm (Table 4.v). Due to the lower hydrogen concentration, this degassing curve again shows a larger scatter than that taken for the specimen tested at room temperature at -805 mV(Ag/AgCl) (Figure 4.42). However, also in Figure 4.49 the second hydrogen release peak at high degassing temperatures of 800 to 900 °C is quite pronounced. Again, this peak confirms some deeper trapping of hydrogen during the SSRT in the used service-applied steel S53U, as compared to the hydrogen-charged tensile test specimens, exhibiting much higher concentration levels, which might be attributed to the hydrogen accumulation at severely deformed regions due to straining. Again, it is confirmed that significant levels of hydrogen are taken up during cathodic protection of the material at a, in comparison to common practice in marine technologies, quite low potentials of -605 mV(Ag/AgCl).

A comparison of the Figures 4.35, 4.42 and 4.49 allows the tentative assumption that the second hydrogen release peak becomes higher than the first release peak, if the average hydrogen concentration exceeds 2 ppm in the specimens. This, consequently, confirms that the first hydrogen release peak is probably associated with the release of hydrogen from the martensitic lattice, usually having a solubility of up to 2 ppm hydrogen, while the second peak represents a hydrogen release from deeper traps in the strained and deformed microstructure.

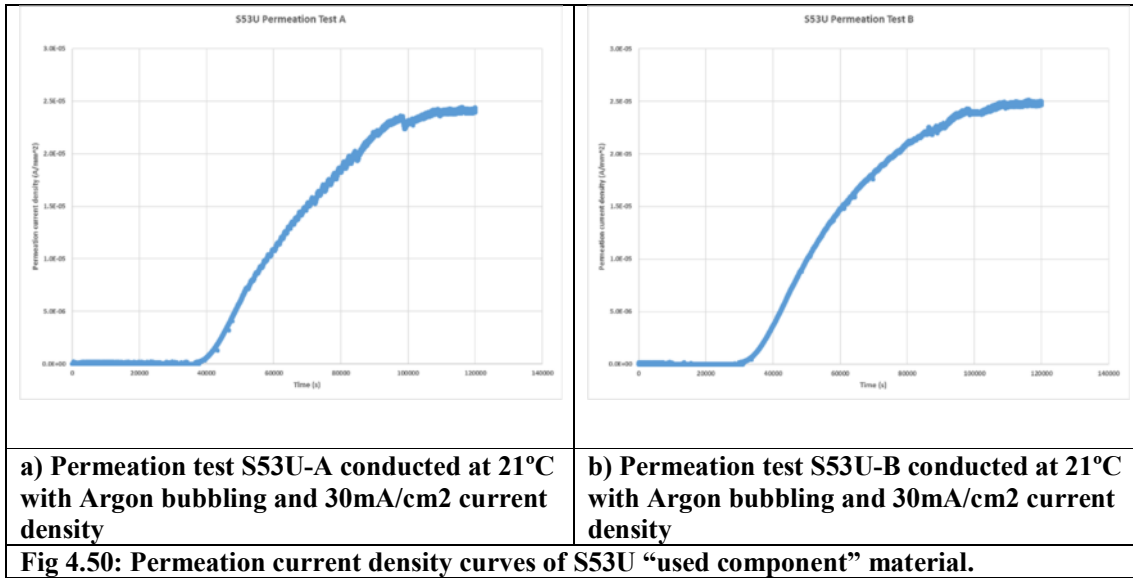


4.4 Hydrogen Diffusion Kinetics

4.4.1 Permeation Test results

Hydrogen diffusion was examined in the S53U “used component” service-applied material by using electrochemical Devanathan experiment, as outlined in Chapter 3. The solution used was 0.1M H₂SO₄ with an added quantity of NaAsO₂ for a recombination poison in the charge cell. A 0.1M aqueous solution of NaOH was used in the detection cell. The tests were run at 21°C with Argon bubbling on the charge cell to reduce surface oxidation and keep the solution in a mixed state. A 30mA/cm² current density was applied to the charge cell to cathodically charge the 0.5mm thick metallic membrane specimen. Tests were monitored until the data showed a steady state permeation current density.

In Fig 4-50a, a subtle staircase can be seen in the curve – this phenomenon is caused by bubbles forming at the membrane charging surface. As a result, the detection of the charge falls and then rises back to the measured permeation current density. This occurred outside of the inflection point area, therefore it did not affect the results. The calculation methods used were the “time-lag” and “inflection point” methods outlined in Chapter 3. There is about a five times difference in the results from each method, but each diffusion coefficient represents a different characteristic of the material.



With the D_{lag} calculation, the material must reach the 63% steady-state permeation current density, therefore filling the material which is devoid of hydrogen to begin with, before it can diffuse through the membrane. With the D_{IP} calculation, the value is derived from the slope of the line at the inflection point after 24.4% of hydrogen flux is reached, which has less effect from the initial uptake of the hydrogen into the material [107].

Specimen	i_{max} (A/mm ²)	t_{lag} (s)	a_{ip} (A/mm ² *s)	D_{lag} (mm ² /s)	D_{IP} (mm ² /s)
S53U-A	2.41×10^{-5}	69961	6.195×10^{-10}	5.96×10^{-7}	1.09×10^{-6}
S53U-B	2.48×10^{-5}	62626	7.491×10^{-10}	6.65×10^{-7}	1.28×10^{-6}

Table 4.6: Hydrogen diffusion data and diffusion coefficients collected from permeation tests of S53U at room temperature

5. Conclusions and Perspectives

From the present study of the hydrogen assisted cracking of two aircraft landing gear steels in the as delivered condition and, particularly in the used service-applied condition the following conclusions can be drawn:

1. Similar to other martensitic steels, even similar to any type of steel, hydrogen affects the material properties of the two investigated steels in both, the as-delivered and in the use-service applied condition predominantly by a reduction in ductility.

2. Since both steel types represent heat-treatable that means hardenable alloys which are delivered and machined in the not finally heat-treated and softer condition, the full strength and ductility is that of the used service-applied condition. In the as-delivered condition, especially the steel AISI 4340 cannot not even match the strength and ductility requirements of a typical landing gear material. Also, the new steel S53 has a far lower strength than in the used service-applied condition. In this soft as-delivered condition, both steels exhibit no reduction of their yield strength, if saturated by hydrogen even at high concentration levels. However, considerable ductility reductions appeared at hydrogen concentrations above 1 ppm in 4340 and above 2 ppm in S53, respectively. Although it can solute much more hydrogen, the tolerance of the new alloy S53 against hydrogen dependent degradation of the mechanical properties is generally higher, although it has a higher strength and respectively lower ductility than the steel AISI 4340 in the as delivered and uncharged state.

Shortly, in the as-delivered non-hardened state the tolerance of the new steel S53 against hydrogen in the microstructure is higher which might also be attributed to a high amount of retained austenite.

3. In the used service-applied condition the yield strength of the alloy S53 is about 200 MPa higher than that of the used and service-applied landing gear steel AISI 4340. Similarly, the tensile strength of the design-alloys S53 is around 100 MPa higher. However, as evaluated by the reduction in ductility and the true fracture strain, the ductility of the novel steel S53U in the used and service applied condition is also higher than that of the conventional steel AISI 4340. Consequently, the tolerance against hydrogen dissolved in the microstructure is similarly higher

in the used than in the new service applied condition. While the steel AISI tolerates in this state only about 2 ppm without any degradation of properties, the steel S53 might withstand even higher concentration. This becomes even more pronounced by considering the strength levels. In contrast to the new as-delivered condition, both materials exhibit severe reductions of even the yield strength, if hydrogen is dissolved in the microstructure. This is already the case at 2 ppm in the used service -applied steel AISI 4340, while concentrations of up to 10 ppm are needed to significantly reduce the yield strength of the novel landing gear steel S53U. The hydrogen tolerance of the nearly complete martensitic microstructure in the novel landing gear S53 steel is considerably higher in the used and service-applied condition than that of the conventional AISI 4340 steel.

However, the reduction of the yield strength at saturation with increased hydrogen concentrations is a behavior that has not yet been observed in any other type of martensitic steels, as reviewed by the literature.

4. Fracture topography changes with increasing hydrogen concentration levels represent a classical feature for any type of martensitic steels. The materials investigated here are no exception to this respect and both materials exhibit fracture topography changes from MVC towards transgranular cleavage-like towards transgranular cleavage cracking and finally towards intergranular cracking at significantly high hydrogen concentration levels.

In the new as-delivered condition, the low-alloyed steel 4340 showed only transgranular cleavage-like fracture at increasing hydrogen concentrations. In contrast, the novel steel S53 shows significant intergranular fracture alongside the austenite phase as well as alongside former austenite grains in the as-delivered state. However, in the used service-applied condition, the steel AISI 4340 exhibited severe intergranular cracking at hydrogen concentration levels above 2 ppm, also indicating a very low ductility, while the novel steel S53U fractured always transgranularly, even at very high hydrogen concentrations.

Thus, hardening of the low alloyed steel AISI 4340 clearly results in a fracture topography change from trans- towards intergranular with increasing hydrogen concentrations. In contrast, hardening of the novel design-alloy S53 changes the fracture topography from inter- to transgranular, if hydrogen is present in the microstructure in higher concentrations.

5. In general, determination of hydrogen dependent material properties, as evaluated here, allows a general insight into the tolerance of steels against hydrogen dissolved in the microstructure. They particularly represent valuable material data for respective modelling of hydrogen assisted cracking and life cycle assessments of components.

6. The steel S53 can solute in the new as-delivered as well as in the hardened and service-used condition much more hydrogen than the conventional low alloyed steel AISI 4340, partly up to more than 50 times more in the as delivered condition. It can be assumed that in that microstructure hydrogen has been dissolved at higher concentrations in the retained austenite and might also have been slightly trapped at the austenite-martensite interface.

However, none of the hydrogen charged specimens exhibited any deep trapping of hydrogen, as determined from degassing experiments. In the hardened and service-applied condition, no second hydrogen release peak has been observed in both steels. Numerical modelling of hydrogen distributions in both steels in the as-delivered and in the hardened condition can thus be carried out based on Fick's second law utilizing effective diffusion coefficients.

7. SSRT of the novel steel S53 in the as-delivered as well as in the hardened service-applied condition showed evidently that the damage phenomenology of this material in seawater is represented by pitting and subsequent hydrogen assisted stress corrosion cracking. For practical application of the steel as landing gear material for airplanes that are servicing in marine heavy-duty environments, as for instance on aircraft carriers, such damage has thus to be paid attention to and respective avoidance measures should be taken into account.

8. The respective failure curves in the TSF diagrams evaluated from the SSRT exhibit a more drastic reduction of the ductility of the used material as compared to the as-delivered condition, as indicated by the gradient of the fracture strain versus the time-to-fracture. This has to be attributed to the higher strength and, in particular, the higher ductility level, the hardened and used material exhibits in air and which is thus more severely reduced in severe environments. TSF diagrams allow also a tentative life time evaluation for components made of the novel steel S53 in similar environments, if the accumulated strain in service is recorded.

9. As shown by a respective SSRT series, the behavior of the steel S53 in artificial and natural seawater is not much different. It is thus sufficient and conservative to carry out investigations of the corrosion cracking resistance of such materials in artificial seawater at more defined and reproducible environmental conditions.

10. In contrast to the SSRT at open circuit potentials, SSRT at fixed potentials exhibited a similarly ductile behavior of the used and service-applied steel at a slight cathodic protection at about -600 mV(Ag/AgCl) , as already recommended elsewhere. However, the degassing of the specimens performed in contrast to other studies revealed average hydrogen concentration levels of about 2 ppm in the gage length of the specimens. Under consideration that the sub-surface concentration at the specimen surface and inside a propagating crack might be considerably higher, it has to be evaluated in further studies, how much hydrogen might be taken up under such slight cathodic protection under long-term conditions. This also evidently shows that degassing of the specimens tested by SSRT after the finishing the test is inevitable to avoid any overinterpretations.

11. The damage appearance with respect to pitting and subsequent hydrogen assisted cracking of the used and service-applied steel S53 in artificial seawater becomes even more severe at increased temperature of 40 and 60 °C, simulating even harsher environmental conditions as for instance on deck of aircraft carriers in tropical regions. However, it also turned out again in the SSRT that slight cathodic protection at the same potential of -600 mV(Ag/AgCl) can drastically improve the behavior of the material under such conditions.

In total, it can be derived from the present contribution that the novel Ferrium S53 steel exhibited a better resistance against hydrogen assisted cracking than the conventional AISI 4340 steel, in the “new barstock” as-delivered as well as in the “used component” hardened and service-applied condition. However, potential damage of used and service applied Ferrium S53 steel in the hardened condition by pitting and subsequent hydrogen assisted cracking should be paid attention to. Respective avoidance measures should be accounted for, in particular with respect to harsh salty marine and environments, and have to be evaluated by further full scale and long-term testing.

References

- [1] <http://www.kathrynsreport.com/2011/11/> Image from news article by *The Kathryn Report*, Nov 10, 2011 (Accessed Sept 2015).
- [2] C. Kern, R. Kooy, C. Keuhmann, “Design, development, qualification and insertion of corrosion-resistant, ultra-high strength Ferrium S53 steel for aircraft sustainment and airworthiness” *Proceedings from the 2011 Aircraft Airworthiness and Sustainment Conference* (2011).
- [3] <http://aviationweek.com/awin/eu-chemical-ban-effects-european-mros> Image from news article by *Aviation Week*, Feb 11, 2013 (Accessed Sept 2016).
- [4] <https://media.defense.gov/2008/Mar/05/2000648509/213/142/0/080306-F-3927S-026.JPG> Image from Air Force Archive (Accessed April 2018).
- [5] <https://www.dfrc.nasa.gov/Gallery/Photo/SR-71/Small/EC95-43075-2.jpg> Image from Nasa Dryden photo collection (Accessed April 2018).
- [6] <https://media.defense.gov/2018/Jan/12/2001865274/888/591/0/170428-F-YG608-900.JPG> Image from Air Force Archive (Accessed April 2018).
- [7] A. Schmitt, “High-speed T-38A landing gear extension loads,” *NASA technical memorandum 58226* (1980).
- [8] G. Roloff, “Aircraft landing gear: the evolution of a system,” *Presentation to DGLR-Bezirksgruppe*, Hamburg (2002).
- [9] J Roskam, *Airplane Design Part IV: Layout Design of Landing Gear and Systems*, DAR corporation (1986).
- [10] U.S. Department of Transportation - Federal Aviation Administration, “AMT Airframe Handbook Volume 2 (FAA-H-8083-31),” pp. 13.6 - 13.9 (2012).
- [11] M. Neubauer, G. Günter, “Aircraft loads (ADP010772),” *Excerpt from the report Aging Aircraft Fleets: Structural and Other Subsystem Aspects* (2001).
- [12] S. Findlay, N. Harrison, “Why aircraft fail,” *Materials Today*, vol 5, issue 11, pp. 18-25 (2002).
- [13] Environmental Security Technology Certification Program, “Development of Ferrium S53 high-strength, corrosion-resistant steel – Cost and performance report” (2009).
- [14] E. Herzberg, T. Chan, S. Guo, “Estimated impact of corrosion on cost and availability of DoD weapon systems,” *LMI report to DoD* (2018).
- [15] V. Agarwala, “Aircraft corrosion control and maintenance,” *Naval Technical Order RTO-MP-AVT-144* (2011).
- [16] W. Ko, “Prediction of service life of aircraft structural components using the half-cycle method,” *NASA Technical Memorandum 86812*, (1987).
- [17] G Shoales, Personal interview, (April 2015).

- [18] W. Johnson, "On some remarkable changes produced in iron and steel by the action of hydrogen and acids," *Proceedings of the Royal Society*, London, UK, vol. 23, pp. 168–179 (1875).
- [19] Th. Boellinghaus, M. Bauer, "Investigation of Iron Containers for Storage of Hydrogen Gas – Translation of Adolf Martens' Spectacular Failure Investigation Report published in 1896," *Engineering Failure Analysis*, vol. 43, pp.11-46 (Aug 2014).
- [20] A. Martens, "Results of the investigations of fractured iron bottles for storage of hydrogen gas," *Mittheilungen aus den königlich-technischen Versuchsanstalten zu Berlin*, vol. 14, No.1, pp. 2–36 (in German) (1896).
- [21] A. Martens: "Investigation of iron containers (bottles) for storage of hydrogen gas," *Zeitschrift des Vereins Deutscher Ingenieure*, vol. 40, no. 26, pp. 717–723 (in German) (1896).
- [22] Th. Boellinghaus, "Materials informatics for HAC," *Plenary lecture for SMAI*, Tokyo, Japan, (Feb. 2016).
- [23] J. Hirth, "Effects of hydrogen on the properties of iron and steel," *Metallurgical Transactions A*, vol. 11 pp. 860-891 (1980).
- [24] Th. Boellinghaus, "Hydrogen assisted failures in metallic structural materials," *Habilitation treatise*, Helmut-Schmidt University of the German Armed Forces, Hamburg Germany (in German) (1999).
- [25] T. Mente, "Numerical simulation of hydrogen assisted cracking in austenitic-ferritic duplex steels," *Dissertation*, BAM Bundesanstalt für Materialforschung und -prüfung, Berlin, Germany (in German) (2015).
- [26] O. Grong, "Metallurgical Modelling of Welding," Maney Publishing, London, UK (1997).
- [27] R. Oriani, "The physical and metallurgical aspects of hydrogen in metals," *Proceedings of The Fourth International Conference on Cold Fusion*, Maui, Hawaii, vol. 1, no 18-1 (1993).
- [28] B. Baranowski, "Metal-hydrogen systems at high hydrogen pressures," *Hydrogen in Metals II*, Springer-Verlag, pp. 157-200 (1978).
- [29] Y. Fukai, "The metal-hydrogen system," Berlin, Heidelberg, Springer-Verlag (2005)
- [30] A. Pundt, "Nanoscale metal-hydrogen system," *Dissertation*, University of Göttingen (2005)
- [31] T. Mütschele, R. Kirchheim, "Hydrogen as a probe for the average thickness of a grain boundary," *Scripta Metallurgica* vol. 21, no. 8, pp. 1101-1104 (1987).
- [32] H. Mehrer, "Diffusion in solids" Berlin, Heidelberg, Springer-Verlag (2007).
- [33] J. Völkl, G. Alefeld, "Diffusion of hydrogen in metals," *Hydrogen in Metals I*, Springer-Verlag pp. 321-348 (1978).

- [34] G. Pressouyre, "A classification of hydrogen traps in steel," *Metallurgical Transactions A*, vol. 10, no. 10, pp.1571-1573 (1979).
- [35] A. McNabb, P. Foster, "A new analysis of the diffusion of hydrogen in iron and ferritic steels," *Transactions of the Metallurgical Society of AIME*, vol. 227, no.6, pp. 618-627 (1963).
- [36] R. Oriani, "The diffusion and trapping of hydrogen in steel," *Acta Metallurgica*, vol. 18, no.1, pp. 147-157 (1970)_
- [37] R. McLellan, "Thermodynamics and diffusion behavior of interstitial solute atoms in non-perfect solvent crystals," *Acta Metallurgica*, vol. 27, no. 10, pp. 1655-1663 (1979).
- [38] I. Maroef, D. Olson, M. Eberhart, "Hydrogen trapping in ferritic steel weld metal," *International Materials Review*, vol. 47, no.4, pp. 191-223 (2002).
- [39] A. Cottrell, B. Bilby, "Dislocation theory of yielding and strain aging of iron," *Proceedings of the Physical Society – Section A*, vol.62, no. 1, pp. 49-62 (1949).
- [40] J. Tein, A. Thompson, I. Bernstein, "Hydrogen transport by dislocations," *Metallurgical Transactions A*, vol. 7, no. 6, pp. 821-829 (1976).
- [41] Th. Boellinghaus, H. Hoffmeister, A. Dangeleit, "A scatterband for hydrogen diffusion coefficients in micro-alloyed and low carbon structural steels," *Welding in the World*, vol. 35, no. 2, pp. 83-96 (1995).
- [42] I. Kaur, Y. Mishin, W. Gust, "Fundamentals of grain and interphase boundary diffusion," John Wiley & Sons Ltd, (1995).
- [43] A. Oudriss, J. Creus, J. Bouhattate, "Grain size and grain-boundary effects on diffusion and trapping of hydrogen in pure nickel," *Acta Materialia*, vol. 60, no. 19, pp. 6814-6828 (2012).
- [44] Y. Yazdipour, D. Dunne, E. Pereloma, "Effect of grain size on the hydrogen diffusion process in steel using cellular automaton approach," *Materials Science Forum*, vol. 706-709, pp. 1568-1573 (2012).
- [45] Y. Yazdipour, J. Haq, K. Muzaka, "2D modelling of the effect of grain size on the hydrogen diffusion of X70 steel," *Computational Material Science*, vol.56, pp. 49-57 (2012).
- [46] M. Dadfarnia, P. Sofronis, I. Robertson, "Numerical simulation of hydrogen transport at the crack tip in a pipeline steel," *Materials and Joining; Pipeline Automation and Measurement; Risk and Reliability*, vol. 3, parts A and B, pp. 193-199, ASME, Alberta, Canada (2006).
- [47] S. Chou, W. Tsai, "Effect of grain size on the hydrogen-assisted cracking in duplex stainless steels," *Materials Science and Engineering A*, vol. 270, no. 2, pp. 219-224 (1999).

- [48] G. Pressouyre, I. Bernstein, "A quantitative analysis of hydrogen trapping," *Metallurgical Transactions A*, vol. 9, no. 11, pp. 1571-1580 (1978).
- [49] M. Stevens, I. Bernstein, "Microstructural trapping effects on hydrogen induced cracking of a microalloyed steel," *Metallurgical Transactions A*, vol. 20, no. 5, pp. 909-919 (1989).
- [50] E. Riecke, B. Johnen, H. Liesegang, "Influences of Mo, V, Nb, Ti, Zr and their carbides on the corrosion and hydrogen absorption of iron in sulfuric acid," *Materials and Corrosion/Werkstoffe und Korrosion*, vol. 39, no. 11, pp. 525-533 (in German) (1988).
- [51] J. Leblond, D. Dubois, "A general mathematical description of hydrogen diffusion in steels-I - Derivation of diffusion equations from boltzmann-type transport equations," *Acta Metallurgica*, vol. 31, no. 10, pp. 1459-1469 (1983).
- [52] Th. Boellinghaus, H. Hoffmeister, C. Middel, "Scatterbands for hydrogen diffusion coefficients in steel having a ferritic or martensitic microstructure and steels having an austenitic microstructure at room temperature," *Welding in the World*, vol. 37, no. 1, pp. 16-23 (1996).
- [53] R. Wilson, E. Aifantis, "On the theory of stress-assisted diffusion, I," *Acta Mechanica*, vol. 45, no. 6, pp. 273-296 (1982).
- [54] D. Unger, E. Aifantis, "On the theory of stress-assisted diffusion, II," *Acta Mechanica*, vol. 47, no. 1-2, pp. 117-151 (1983).
- [55] R. Kirchheim, "Interaction of hydrogen with external stress fields," *Acta Metallurgica*, vol. 34, no. 1, pp. 37-42 (1986).
- [56] R. Balluffi, A. Ruoff, "On strain-enhanced diffusion in metals, I – Point defect models," *Journal of Applied Physics*, vol. 34, no. 6, pp. 1634 (1963).
- [57] A. Ruoff, R. Balluffi, "Strain-enhanced diffusion in metals, II – Dislocation and grain-boundary short circuiting models," *Journal of Applied Physics*, vol. 34, no. 7, pp. 1848 (1963).
- [58] A. Ruoff, R. Balluffi, "Strain-enhanced diffusion in metals, III – Interpretation of recent experiments," *Journal of Applied Physics*, vol. 34, no. 9, pp. 2862 (1963).
- [59] S. Piekarski, "Stress-assisted diffusion and the modified Fick law," *Journal of Technical Physics*, vol. 46, no. 1, pp. 3-7 (2005).
- [60] A. Troiano, "The role of hydrogen and other interstitials in the mechanical behavior of metals," *Transactions of ASM*, vol. 52, pp. 54-80 (1960).
- [61] K. Kiuchi, R. McLellan, "The solubility and diffusivity of hydrogen in well-annealed and deformed iron," *Acta Metallurgica*, vol. 31, no. 7, pp. 961-984 (1983).
- [62] O. Sobol, "Hydrogen Assisted Cracking and Transport Studied by ToF-SIMS and Data Fusion with HR-SEM," *Dissertation*, BAM Bundesanstalt für Materialforschung und -prüfung, Berlin, Germany (2018).

- [63] M. Louthan, G. Caskey, J. Donovan, "Hydrogen embrittlement of metals," *Materials Science and Engineering*, vol. 10, pp. 357-368 (1972).
- [64] H. Birnbaum, P. Sofronis, "Hydrogen-enhanced localized plasticity – A mechanism for hydrogen-related fracture," *Materials Science and Engineering A*, vol. 176, no. 1-2, pp. 191-202 (1994).
- [65] I. Robertson, "The effect of hydrogen on dislocation dynamics," *Engineering Fracture Mechanics*, vol. 68, no. 6, pp. 671-692 (2001).
- [66] U. Draugelates, A. Schram, C. Kedenburg, "Hydrogen uptake in the droplet stage during metal inert gas welding of low-alloyed fine-grain structural steel," *Schweissen & Schneiden*, vol. 49, no. 9, pp. 693-699 (in German) (1997).
- [67] P. Hart, G. Evans, "Hydrogen content of single and multipass steel welds," *Welding Journal, Research Supplement*, vol. 76, no. 2, pp. 74s-80s (1997).
- [68] Th. Boellinghaus, "Determination of crack-critical hydrogen distributions in welded connections by means of numerical modelling," *Dissertation*, Helmut-Schmidt University of the German Armed Forces, Hamburg Germany (in German) (1995).
- [69] T. Michler, J. Naumann, "Microstructural aspects upon hydrogen environment embrittlement of various bcc steels," *International Journal of Hydrogen Energy*, vol. 35, no. 2, pp. 821-832 (2010).
- [70] K. Lo, C. Shek, J. Lai, "Recent developments in stainless steels," *Materials Science and Engineering R – Reports*, vol. 65, no. 4-6, pp. 39-104 (2009).
- [71] H. König, K. Lange, "Model ideas for hydrogen transport from iron, taking into account the interactions of gases with metal surfaces," *Archiv für das Eisenhüttenwesen*, vol. 46, no. 4, pp. 237-243 (in German) (1975).
- [72] H. König, K. Lange, "Experimental verification of the influence of the boundary conditions on the determination of the coefficient of diffusion of hydrogen in iron alloys," *Archiv für das Eisenhüttenwesen*, vol. 46, no. 4, pp. 269-275 (in German) (1975).
- [73] R. Song, S. Pyun, R. Oriani, "Hydrogen permeation through the passivation film on iron by time-lag method," *Corrosion Science*, vol. 137, no. 6, pp. 1703-1706 (1990).
- [74] P. Bruzzioni, R. Garavaglia, "Anodic iron oxide films and their effect on the hydrogen permeation through steel," *Corrosion Science*, vol. 34, no. 10, pp. 1751-1752 (1993).
- [75] C. Zapffe, C. Sims, "Hydrogen embrittlement, internal stress and defects in steel," *American Institute of Mining and Metallurgical Engineers*, Technical Publication no. 1307, pp. 225-261 (1941).
- [76] I. Robertson, et. al., "Hydrogen Embrittlement Understood," *Metallurgical and Materials Transactions A*, vol. 46A, no. 6, pp. 2323-2341 (2015).
- [77] Y. Fukai, H. Sugimoto, "Diffusion of hydrogen in metals," *Advances in Physics*, vol. 34, no. 2, pp. 263-326 (1985).

- [78] R. Oriani, "Mechanistic Theory of Hydrogen Embrittlement of Steels," *Berichte Der Bunsen-Gesellschaft Fur Physikalische Chemie*, vol. 76, no. 8, pp. 848-857 (1972).
- [79] H. Birnbaum, P. Sofronis, "Hydrogen-Enhanced Localized Plasticity - a Mechanism for Hydrogen-Related Fracture," *Materials Science and Engineering A*, vol. 176, no. 1-2, pp. 191-202 (1994).
- [80] J. Lufrano, P. Sofronis, H. Birnbaum, "Modeling of hydrogen transport and elastically accommodated hydride formation near a crack tip," *Journal of the Mechanics and Physics of Solids*, vol. 44, no. 2, pp. 179-205 (1996).
- [81] A. Oudriss, et al., "Meso-scale anisotropic hydrogen segregation near grain-boundaries in polycrystalline nickel characterized by EBSD/SIMS," *Materials Letters*, vol. **165**, pp. 217-222 (2016).
- [82] V. Olden, C. Thaulow, R. Johnsen, "Modelling of hydrogen diffusion and hydrogen induced cracking in supermartensitic and duplex stainless steels," *Materials & Design*, vol. 29, no. 10, pp. 1934-1948 (2008).
- [83] J. Furtado, F. Barbier, "Hydrogen Embrittlement-Related Issues and Needs in the Hydrogen Value Chain," *Proceedings of International Hydrogen Conference 2012*. ASME Press (2014).
- [84] R. Gangloff, B. Somerday, "Gaseous Hydrogen Embrittlement of Materials in Energy Technologies, Vol 2: Mechanisms, Modelling and Future Developments," *Gaseous Hydrogen Embrittlement of Materials in Energy Technologies*, Cambridge Woodhead Publ Ltd., vol 2 (2012).
- [85] W. Gerberich, "Gaseous hydrogen embrittlement of materials in energy technologies," Woodhead Publishing Ltd., Cambridge, UK (2012).
- [86] C. John, W. Gerberich, "The effect of loading mode on hydrogen embrittlement," *Metallurgical Transactions*, vol. 4, no. 2, pp. 589-594 (1973).
- [87] R. Oriani, "Hydrogen - the Versatile Embrittler," *Whitney Award Lecture 1987 Corrosion*, vol. 43, no. 7, pp. 390-397 (1987).
- [88] T. Tabata, H. Birnbaum, "Direct observations of hydrogen enhanced crack propagation in iron," *Scripta Metallurgica*, vol. **18**, no. 3, pp. 231-236 (1984).
- [89] I. Robertson, H. Birnbaum, "An HVEM study of hydrogen effects on the deformation and fracture of nickel," *Acta Metallurgica*, vol. 34, no. 3, pp. 353-366 (1986).
- [90] I. Robertson, H. Birnbaum, P. Sofronis, "Hydrogen effects on plasticity," *Dislocations in solids*, vol.15, pp. 249-293 (2009).
- [91] C. Beachem, "New Model for Hydrogen-Assisted Cracking (Hydrogen Embrittlement)," *Metallurgical Transactions*, vol. 3, no. 2, pp. 437-451 (1972).
- [92] A. Tetelman, W. Robertson, "Direct observation and analysis of crack propagation in iron-3% silicon single crystals," *Acta Metallurgica*, vol. 11, no. 5, pp. 415-426 (1963).

- [93] S. Lynch, "Hydrogen embrittlement phenomena and mechanisms," *Corrosion Reviews* (2012).
- [94] M. Nagumo, "Function of hydrogen in embrittlement of high-strength steels," *ISIJ international*, vol. 41, no. 6, pp. 590-598 (2001).
- [95] J. Song, W. Curtin, "A nanoscale mechanism of hydrogen embrittlement in metals," *Acta Materialia*, vol. 59, no. 4, pp. 1557-1569 (2011).
- [96] J. Song, W. Curtin, "Atomic mechanism and prediction of hydrogen embrittlement in iron," *Nature Materials*, vol. 12, pp. 145-151 (2013).
- [97] D. Westlake, "The habit planes of zirconium hydride in zirconium and zircaloy," *Journal of Nuclear Materials*, vol. 26, no. 2, pp. 208-216 (1968).
- [98] A. Barnoush, H. Vehoff, "Recent developments in the study of hydrogen embrittlement: Hydrogen effect on dislocation nucleation," *Acta Materialia*, vol. 58, no. 16, pp. 5274-5285 (2010).
- [99] R. Francis, "Paper K4," *Conf. Proc. Duplex Stainless Steels '94*, Glasgow, Scotland (1994).
- [100] E. Owczarek, T. Zakroczymski, "Hydrogen transport in a duplex stainless steel," *Acta Materialia*, vol. 48, no. 12, pp. 3059-3070 (2000).
- [101] A. Turnbull, R. Hutchings, "Analysis of Hydrogen-Atom Transport in a 2-Phase Alloy," *Materials Science and Engineering A*, vol. 177, no. 1-2, pp. 161-171 (1994).
- [102] E. Wendler-Kalsch, "Hydrogen and corrosion," Kuron, (2000).
- [103] C. Zhao et al., "JMST vol. 30, no. 10, pp. 1155 – 1159 (2014).
- [104] H. Nelson, "Hydrogen Embrittlement," *Treatise on Materials Science and Technology*, ed. B. C.L. and B. S.K., New York: Academic Press, vol. 25 (1983).
- [105] E. Sirois, H. Birnbaum, "Effects of hydrogen and carbon on thermally activated deformation of nickel," *Parkins Symposium on Fundamentals Aspects of Stress Corrosion Cracking*, The Minerals, Metals and Materials Society, pp. 173-190 (1992).
- [106] S. Lynch, "Progress towards understanding mechanisms of hydrogen embrittlement and stress corrosion cracking," *CORROSION 2007*, NACE International (2007).
- [107] M. Rhode, "Hydrogen diffusion and effect on degradation in welded microstructures of creep-resistant low-alloyed steels," *Dissertation*, BAM Bundesanstalt für Materialforschung und -prüfung, Berlin, Germany (2016).
- [108] R. Kirchheim, "On the solute-defect interaction in the framework of a defactant concept," *International Journal of Materials Research*, vol. 100, no. 4, pp. 483-487 (2009).
- [109] G. Han, et al., "Hydrogen environment embrittlement of austenitic stainless steels at low temperatures (study on low temperature materials used in WE-NET 7)," *Hydrogen Energy Progress Xii*, vols 1-3, pp. 1863-1872. (1998).

- [110] P. Wongpanya, Th. Boellinghaus, G. Lothongkum, H. Hoffmeister, “Numerical Modelling of Cold Cracking Initiation and Propagation in S 1100 QL Steel Root Welds,” *Welding in the World*, vol. 53, no. 3-4, pp. R34-R43 (2009).
- [111] G. Dieter, “Mechanical metallurgy, 3rd Edition” McGraw Hill, New York, NY, USA, (1986).
- [112] T. Mente, Th. Boellinghaus, M. Schmitz-Niederau, “Heat treatment Effects on The Reduction of Hydrogen in Multi-Layer High-Strength Weld Joints,” vol. 56, no. 7-8, pp. 26-36 (2012).
- [113] E. Steppan, T. Mente, Th. Boellinghaus, “Numerical investigations on cold cracking avoidance in fillet welds of high-strength steels,” *Welding in the World*, vol. 57, no. 3, pp. 359–371 (2013).
- [114] T. Falkenreck, “High strain rate behaviour of high-strength steel welds,” *Dissertation*, BAM Bundesanstalt für Materialforschung und -prüfung, Berlin, Germany (2018).
- [115] H. Hoffmeister, Th. Boellinghaus, “Modeling of Combined Anodic Dissolution/Hydrogen-Assisted Stress Corrosion Cracking of Low-Alloyed Power Plant Steels in High-Temperature Water Environments,” *Corrosion – Houston TX* vol. 70, no. 6, pp 563-578 (2014).
- [116] L. Marchetti, E. Herms, P. Laghoutaris, “Hydrogen embrittlement susceptibility of tempered 9% Cr – 1% Mo steel,” *International Journal of Hydrogen Energy*, vol 36, no. 24, pp. 15880-15887 (2011).
- [117] <http://usa.arcelormittal.com/~media/Files/A/Arcelormittal-USA-V2/what-we-do/steel-products/plate-products/9-percent-nickel.pdf> , Information on 9% Nickel steel (Accessed May 2018).
- [118] L. Vollmer, “The behavior of steels in hydrogen sulfide environments,” *Corrosion*, vol. 14, no. 7, pp. 324-328 (1958).
- [119] C. Bowers, W. McGuire, A. Wiehe, “Stress corrosion cracking of steel under sulfide conditions,” vol. 8, no. 10, pp. 333-341 ((1952).
- [120] C. Hudgins, R. McGlasson “The effect of temperature (75-400°F) on the aqueous sulfide stress cracking behavior of an N-80 type steel,” *H₂S Corrosion in Oil and Gas Production*, NACE, Houston, TX, pp.90-94 (1994).
- [121] R. Treseder, “Field experience with cracking of high strength steels in sour gas and oil wells,” *A Report of Technical Practices Committee I-G*, NACE, Houston, TX, pp. 57-60 (1994).
- [122] R. Treseder, T. Swanson, “Factors in sulfide corrosion cracking of high strength steels,” *Corrosion*, vol. 24, pp. 31-37 (1968).
- [123] J. Alkire, S. Cialraldi, “Failures of martensitic stainless steels in sweet and sour gas service,” *Corrosion* 88, paper 210.

- [124] R. Thompson, G. Kohut, D. Canfield, "Sulfide stress cracking failures of 12Cr and 17-4PH stainless steel wellhead equipment," *Corrosion* 90, paper 53.
- [125] NACE TM0177-2005, "Laboratory testing of metals for resistance to sulfide stress cracking and stress corrosion cracking in H₂S environments," NACE International
- [126] M. Bonis, J. Crolet, "Experience of 13% Cr tubing II: 10 years and 1 million feet later," *Corrosion* 94, Paper 7.
- [127] J. Combs, J. Kerr, L. Klein, "13Cr tubulars solve corrosion problem in the Tuscaloosa Field," *Corrosion Resistant Alloys in Oil and Gas Production*, NACE, Houston, TX, pp. 91-95 (1996).
- [128] C. Hudgins, Jr., "Practical aspects of hydrogen damage at atmospheric temperature," *H₂S Oil & Gas Production*, NACE, Houston, TX, pp152-158 (1994).
- [129] R. Jones, "Stress Corrosion Cracking," *ASM*, Ohio (1992).
- [130] M. Tanimura, "Development of corrosion resistant OCTG and its application to corrosive wells," *Corrosion Resistant Alloys in Oil and Gas Production*, vol. 1, pp. 226-236.
- [131] S. Asano, A. Kiatmura, R. Otsuka, "The hydrogen dislocation interaction in 17% Cr steel," *Scripta Metallurgica*, vol. 12, pp. 805-808 (1978).
- [132] R. Kane, M. Watkins, J. Greer, "The improvement of sulfide stress cracking resistance of 12% Chromium stainless steels through heat treatment," *Corrosion*, vol. 33, no. 7, pp. 231-235 (1977)
- [133] L. Klein, "H₂S cracking resistance of 420 stainless steel tubulars," *Corrosion* 84, paper 211.
- [134] D. Vitale, H. Ebert, "Austenitizing temperature effect on SCC resistance of 410 stainless steel," *Corrosion* 93, paper 139.
- [135] M. Watkins, E. Rosenberg, "Sulfide stress cracking resistance of weld repairs in wellhead alloys," *Corrosion* 83, paper 159.
- [136] A. Yoshitake, M. Teraoka, T. Torigoe, "The application & field experience of high strength 12% Cr centrifugally cast pipe for gas gathering system," *Corrosion* 95, paper 86.
- [137] M. Saenz De Santa Maria, A. Turnbull, "The effect of H₂S concentration and pH on the cracking resistance of AISI 410 steel in 5% brine," *Corrosion Science*, vol. 29, no. 1, pp. 69-88 (1989).
- [138] A. Turnbull, A. May, "Effect of temperature and H₂S Content on the cracking resistance of a 13% Chromium martensitic stainless steel in acidified NaCl," *NPL-Report DMA(A) 173* (1988).
- [139] J. Gonzalez-Rodriguez, V. Salinas-Bravo, A. Martinez-Villafane, "Hydrogen embrittlement of type 410 stainless steel in sodium chloride, sodium sulfate and

- sodium hydroxide environments at 90°C,” *Corrosion*, vol. 53, no. 6, pp. 499-504 (1997).
- [140] Y. Ishizawa, T Shimada, M. Tanimura, “Effect of microstructure on the sulfide stress corrosion cracking resistance of AISI 410 and 420 steels,” *Corrosion* 82, Paper 124.
- [141] F. Shawesh, E. Agdel, “Hydrogen embrittlement of martensitic stainless steels,” *Proceedings of the International Conference EuroCorr98, Utrecht* (1998).
- [142] J. Enerhaug, S Eliasson, “Kvalle: Qualification of welded super 13% Cr martensitic stainless steels for sour service applications,” *Corrosion* 97, Paper60.
- [143] B. Somerday, P. Sofronis, “Material Performance in Hydrogen Environments,” *Proceedings from 2016 International Hydrogen Conference, Moran, Wyoming* (2016).
- [144] G. Pioszak, “Hydrogen Assisted Creacking of Ultra-High Strength Steels,” *Dissertation, University of Virginia, USA* (2015).
- [145] Y. Lee, R. Gangloff “Measurement and Modeling of Hydrogen Environment–Assisted Cracking of Ultra-High-Strength Steel,” *Minerals, Metals & Materials Society, ASM International*, (2007).